Refill Friction Stir Spot Welding of Casting AM50A Mg Alloy to Zn Coated DP600 Steel Dissimilar Joints

[blank page]

Refill Friction Stir Spot Welding of Casting AM50A Mg Alloy to Zn Coated DP600 Steel Dissimilar Joints

Filipe Amorim Gonçalves Giesteira

Supervisor at HZG: Banglong Fu

Co-advisor at HZG: Jorge dos Santos

Co-advisor at FEUP: Paulo Manuel Salgado Tavares de Castro

Master Thesis

Integrated Master Degree in Mechanical Engineering

October 2018

"Now this is not the end. It is not even the beginning of the end. But it is, perhaps, the end of the beginning."

"Continuous effort - not strength or intelligence - is the key to unlocking our potential"

Winston Churchill

"…Nothing worth gaining is ever gained without effort…"

Theodore Roosevelt

"Intelligence is the ability to adapt to change"

Stephen Hawking

Abstract

The present report was carried out under ERASMUS+ student exchange program, and submitted in partial fulfillment for the degree of Integrated Master in Mechanical Engineering, by Faculty of Engineering of University of Porto (FEUP).

The aim of this report is to investigate an alternative to the conventional spot joining techniques for Magnesium (Mg) to steel dissimilar joints. The automotive industry is being forced to rapidly increase the amount of high strength, high energy absorption and lightweight materials in each vehicle. Advanced High Strength Steels (AHSS) and casting Mg alloys proved to be relevant options to meet the stringent requirements of weight reduction and safety increase.

The feasibility of welding casting AM50 Mg alloy with Zn coated DP600 AHSS by Refill Friction Stir Spot Welding (Refill-FSSW) in sleeve plunge mode was evaluated. A particular technique was employed to weld in lap joint configuration the Mg soft material (upper sheet) and the steel hard material (lower sheet); the tool was only plunged into the Mg sheet enabling the Zn coating to act as an interlayer. The joint bonding exclusively relayed in pure metallurgical bonding between the two sheets. Two different variants of Refill-FSSW were studied, Conventional Rotation Refill-FSSW (CR Refill-FSSW) and Differential Rotation Refill-FSSW (DR Refill-FSSW). In CR Refill-FSSWed dissimilar joints, the effect of different welding parameters such as Plunge Depth (PD), Rotation Speed (RS), Plunge Time (PT), Dwell Time (DT) and Retract Time (RT) on Lap Shear Strength (LSS) was analyzed through Design of Experiments (DoE). Metallographic analysis by Optical Microscopy (OM) and Scanning Electron Microscopy (SEM) backed with Energy-Dispersive X-ray Spectrometry (EDS), were used to study the Mg/steel interface and fracture surfaces. The thermal cycle during welding experienced by the center of the spot was recorded using a thermocouple based apparatus. In order to study the influence of the Zn coating, the fracture surface of dissimilar joints of Mg and bare steel (same base material without coating) was analyzed.

For CR Refill-FSSW technique, the ANOVA methodology indicated that the most significant and dominant welding parameter was sleeve PD, with a positive correlation between the increase in PD and the increase in joint strength. The best set of parameters was a 2.8 mm sleeve PD, 1500 rpm for RS of both sleeve and probe and a total Welding Time (WT) of 3.5 s. The welding cycle was composed by: null DT, and a PT and RT of 1.5 s and 2 s respectively. For these parameters defect free welds with up to 6.07 kN average LSS were achieved. The strengthening mechanism was ascribed to the increase in the length of the weld-brazed interfacial region. The fracture was asymmetric in the welded spot, and since the steel lower sheet wasn't plunged and the Mg and steel matrixes are insoluble and non-reactive, mainly interfacial failure with shear fracture was observed.

DR Refill-FSSW was used to try to further increase the LSS of the joint. The PD window was initially limited by the occurrence of a Stir Zone (SZ) pull-out defect. After several unsuccessfully approaches to try to avoid the presence of this defect, DR Refill-FSSW by reduction of the probe RS was studied. The process window was increased along with the level of surface finishing. A desired increase in joint strength for LSS higher than 6.5 kN was achieved. Higher mechanical performance was achieved with a 600 rpm probe RS, 1800 rpm sleeve RS, 2.9 mm sleeve PD and a total WT of 2.5 s. The strengthening mechanism was ascribed to the growth of the Fe-Al IMC's layer. No relevant changes in the fracture surface were observed.

Keywords

Refill Friction Stir Spot Welding, Refill-FSSW, RFSSW, conventional rotation, differential rotation, dissimilar welding, solid-state welding, automotive industry, AM50A, Magnesium Alloy, casting Magnesium, DP600, dual phase steel, advanced high strength steel, AHSS, HDG Zn coating, design of experiments, DoE, factorial design, ANOVA, mechanical properties, lap shear strength, metallographic analysis, fracture surface analysis, SEM, EDS, thermal cycle

[blank page]

Acknowledgements

I would like to express immense gratitude, for the opportunity of doing this thesis in HZG, Germany, and its success to:

Prof. Dr. Paulo Manuel Salgado Tavares de Castro, co-advisor of this thesis at FEUP, Portugal, for giving me the opportunity to produce my master's thesis at HZG. For all the support, contribution and enlightenments.

Dr. Jorge dos Santos, co-advisor of this thesis at HZG, Germany, and head of the WMP department, for opening the possibility of working in WMP department at HZG. For the kindness that always demonstrate and the confidence placed in me. This was a great opportunity for the development of my skills as a researcher and as an engineer, and I am grateful for it.

Banglong Fu, supervisor of this thesis at HZG, Germany, for all the mentoring and step by step guidance in my experimental work. Without its patience and promptitude, my experimental work would not be possible, as well as the results derived from it.

Inês Giesteira, for the help in overcoming the linguistic barrier, by the precious tips and comments concerning the English writing revision.

All my colleagues and co-workers at HZG that made my work easier, with their countless precious comments and tips, and their invaluable knowledge and experience.

All HZG staff, Dagmar Koschek, Menno Peters, Natalia Manente, Alesssandro Barbini, Martin Reimann, for their dedication and help, in the innumerous times I need it.

The ERASMUS+ program and HZG, for making my staying in Germany financially possible.

Finally, I would like to express my gratitude to my friends, girlfriend and family, for their encouragement, support and patience and for helping me going through my stay in Germany.

[blank page]

Contents

List of Acronyms

AA – Aluminum Alloy
AHSS – Advanced High Strength Steel
ANOVA – Analysis of Variance
ASTM – American Society for Testing and Materials
AWS – American Welding Society
BB – Box-Behnken
BIW – Body-in-white
BM – Base Material
BoF – Body on Frame
CCD – Central Composite Design
CDF – Cumulative Distribution Function
CNC – Computer Numerical Control
ColdR – Cold Rolled/Rolling
CR Refill-FSSW – Conventional Rotation Refill Friction Stir Spot Welding
DF – Degree of Freedom
DIC – Digital Image Correlation
DoE – Design of Experiments
DP – Dual Phase
DR Refill-FSSW – Differential Rotation Refill Friction Stir Spot Welding
DT – Dwell Time
FEA – Finite Element Analysis
FEM – Finite Element Method
FEUP – Faculty of Engineering of the University of Porto
FRW – Friction Welding
FSpW – Friction Spot Welding
FSSW – Friction Stir Spot Welding
FSW – (Linear) Friction Stir Welding
FW – Fusion Welding
FZ – Fusion Zone
GHG – GreenHouse Gas
HAZ – Heat Affected Zone
HDG – Hot-dip galvanization/galvanized
HE – Hole Expansion
HotR – Hot Rolled/Rolling
HSLA – High Strength Low Alloy steel
HSS – High Strength Steel
HZG – Helmholtz-Zentrum Geesthacht

IF – Interfacial Failure

IMC – Intermetallic Compound

LCA – Life Cycle Analysis

LM – Low Magnification

LOF – Lack-of-Fit

LW – Laser Welding

NDT – Non-destructive Testing

NZ – Nugget Zone

OM – Optical Microscope/Microscopy

PD – Plunge Depth

PF – Pullout Failure

PT – Plunge Time

Refill-FSSW – Refill Friction Stir Spot Welding

RS – Rotation Speed

RSW – Resistance Spot Welding

RT – Retract Time

RW – Resistance Welding

SCF – Stress Concentration Factor

SEM – Scanning Electron Microscope/Microscopy

SF – Stretch Flangeability

SSW – Solid State Welding

SZ – Stir Zone

TEM – Transmission Electron Microscope/Microscopy

TMAZ – Thermo-mechanically Affected Zone

TRIP – Transformation-induced Plasticity

TWI – The Welding Institute

UP – University of Porto

USW – Ultrasonic Spot Welding

UTS – Ultimate Tensile Strength

WMP – WerkstoffMechanik Projekte / "Materials mechanics project" (Solid State Joining Process Department of HZG)

WS – Welding Speed

WT – Welding Time

WZ – Welding Zone

YS – Yield Strength

List of Figures

[blank page]

List of Tables

[blank page]

1 Introduction

1.1 Context of the Project and HZG Institution

The project results from an initial partnership between *Helmholtz-Zentrum Geesthacht* (HZG) - *Zentrum für Material und Küstenforschung* and Volkswagen group. Due to an error from VW regarding the material supply and the subsequent booming of the "Dieselgate" scandal, VW withdrew its financial supporting, consequently becoming a self-funded project. However, the interest of the VW group remained. The financial support came from HZG's internal funds, and the Magnesium base material was supplied by MagIC (Magnesium Innovations Centre) division from the institute of Materials Research.

The specific goal of the project was to study the feasibility of joining casting AM50 Magnesium (Mg) alloy to Zn coated DP600 dual phase Advanced High Strength Steel (AHSS) by Refill Friction Stir Spot Welding (Refill-FSSW). These dissimilar joints are to be implemented in a new Hybrid body structure mixed design concept, illustrated in Figure 1. The original specifications of the project: DP600 Zn coated steel; 3 mm thick bare plate casting AM50 Magnesium alloy; and total welding time below 6 s were kept the same. In order to study the correlation between the mechanical and microstructural properties and each parameter, essentially two basic approaches can be followed (Fanelli, Vivio, and Vullo 2012): numerical simulation – necessary to build a parametric free model of the joint in order to determine the optimal set of parameters; or experimental study – empirical research of the optimal set of parameters. Increasing attention is being dedicated to the area of numerical simulation in Refill-FSSW (Muci-Küchler, Kalagara, and Arbegast 2010). However, numerical results must always be validated by experimental data, highlighting the value of this dissertation. Thus, the present report consists of an experimental study and optimization of some of the Refill-FSSW process parameters of the dissimilar welding between these two materials.

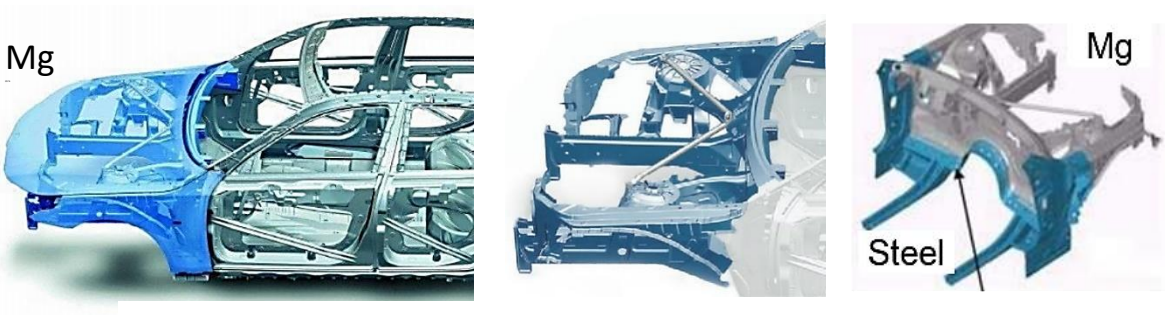

Figure 1- Mixed-material body structure design with Magnesium and Steel joints.

This project is part of the PhD program of Banglong Fu, the supervisor in HZG of this dissertation. The PhD program is divided in four main topics, which aim to study the feasibility of Refill Friction Stir Spot Welding (Refill-FSSW) of: wrought AZ31 Mg alloy to Zn coated DP600 steel, casting AM50 to AM50 Mg alloys, casting AM50 Mg alloy to Zn coated DP600 steel, and hypothetically casting AM50 Mg alloy to Titanium (alloy not defined yet). The feasibility of welding the first two material combinations was already studied at the date of this dissertation. Part of this data and acquired knowledge was used to substantiate some decisions during the experimental work. However, the results will be part of his doctoral thesis and future papers, which are yet to be published in manuscript version (so confidentiality is required). Thus, only a small fraction of this background data will be released in this dissertation, sometimes insufficient to explain in detail every decision adopted.

The author was integrated in an on-going work, specifically the preparation of Banglong Fu's doctoral thesis. During this curricular internship, the author divided his focus and working hours between researching topics presented in this master dissertation as well as topics covered exclusively in Banglong Fu's dissertation. Several experimental tasks were conducted and two scientific papers partially revised regarding different topics within his doctoral thesis, but outside the scope of this dissertation. Non-scientific tasks such as presentations and demonstrations to visiting potential industrial partners were also conducted; detailed information about the overall work done is given in subchapter 1.5.

HZG is a German scientific federal institution, dedicated to materials and coastal research, located in Geesthacht, Germany. It is composed by five main institutes: Coastal Research, Climate Service Center (GERICS), Polymer Research, Biomaterial Science and Materials Research. The project was developed in the Solid-State Joining Process department (WMP) from the Materials Mechanics main division of the Materials Research institute, HZG. The institute of Materials Research has five main divisions: Materials Mechanics, Materials Technology, Materials Physics, Magnesium Innovations Centre (MagIC), and Metallic Biomaterials. The experimental work was conducted in the Friction Stir Spot Welding group within the Solid-State Joining Processes department WMP (*Werkstoffmechanik Projekte*). WMP is composed of four main groups: Friction Stir Welding based processes, Friction Stir Spot Welding, Local Modification and Metal-Polymer Joining group.

1.2 Societal Relevance and Project Motivation – Automotive Industry

Automobiles are complex systems formed essentially by: chassis or frame (load bearing member), body (protective outer hull or skin, with aesthetic function and possible bearing capacities as in unibody chassis), powertrain system (engine, transmission, drive shaft. differential, drive wheels) and other subsystems. Sometimes the term chassis encompasses the frame and powertrain system, also referred in that case as rolling chassis (Giancarlo and Lorenzo 2009). A common car steel frame incorporates different structural members to support different loads. Rail members are important elements in the majority of chassis types, adopting several configurations such as longitudinal members, cross members and side members. They are usually classified by their geometry in: channel section (I, C, U, etc.) - typically long members optimal for vertical load bearing; and tubular beams and box sections (squared, rectangular, etc.) – commonly short members optimal for torsional load bearing. Stressed skin members such as welded hollow sheet components, panels (e.g. quarter panel), shear panels (e.g. roof and inner wings), and pans (e.g. floor) are also incorporated in modern unibody chassis design (Crolla 2009). During this report, several mentions to car components and its materials will be made, thus in Figure 2, some nomenclature of a typical unibody car frame design is illustrated.

In order to understand the trends and choices of materials for different car frame components (helping to clarify subchapter 2.1 and 2.2), some basic safety design concepts need to be outlined. Typical passenger vehicles have zones with different structural functions: two crush or crumple zones (front and rear regions) – areas intentionally engineered to collapse in a predetermined mode, designed with high energy absorbing materials and geometries; and a safety or anti-intrusion cage – designed with high stiffening geometries, and high stiff materials with high strength, to avoid intrusion or penetration of the passenger cockpit in both longitudinal and side loading (providing protection from different angles). Figure 3 illustrated the safety design concepts previously mentioned.

During this chapter and throughout the literature review chapter, the author will try to answer different questions outlined in Figure 4. The goal is simply to uncover the motivations behind the project, and understand its main requirements. The choice of materials – casting Magnesium and Advanced High Strength Steel – and their surface condition is explained in subchapters 2.1 and 2.2. The reasons for welding these two materials and its current technological background are summarized in subchapter 2.3. The joints studied in this report were produced using Refill Friction Stir Spot Welding (Refill-FSSW). Generic reasons for using this process to join Mg-steel, are outlined throughout subchapter 2.4, and several details and advantages of this process over different fusion and solid-state technologies are also advanced. Refill-FSSW was also a project requirement because it is a spot welding technique. Thus, later in the current subchapter, the reasons behind studying spot welding in lap joint configuration and its relation to the automotive body/frame assembly field are finally explored.

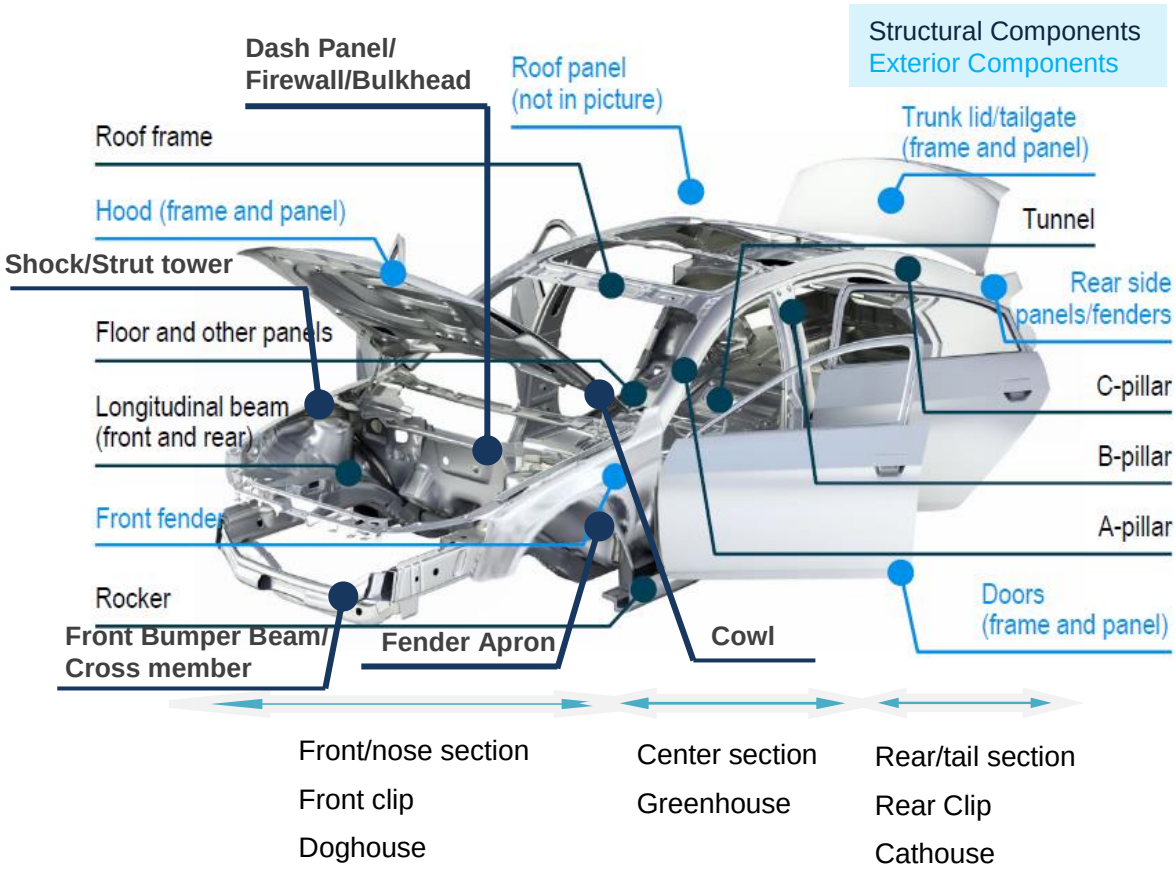

Figure 2- Main automobile structural components in a typical unit body chassis type. Image adapted from (Prém, Bézi, and Balogh 2017).

Figure 3- Scheme of the basic car zones regarding safety functions (Zhao and Jiang 2017).

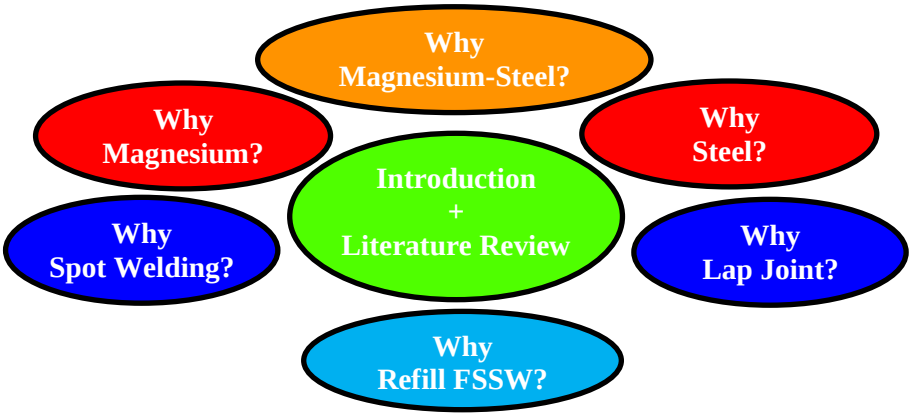

Figure 4- Illustration of the main goals aimed with the introduction and literature review chapter.

The choice for a lap joint configuration and a spot welding technique was motivated by the intended application. The project initially was ordered by VW group, one of the biggest automotive manufactures in Germany. History evolution dictated the success of unibody car construction design, in which the number of spot joints ranges from 7000-12000 spot welds, depending on the size of the vehicle; corresponding to about 90% of the total chassis assembly work (Manladan et al. 2017).

Body on frame (BoF) were the dominant car structures until early 1930, short after the introduction of the European model Lancia Lambda, 1922, which resembled a current unibody design (Giancarlo and Lorenzo 2009). The bolted body is connect to the frame on body mounts that are usually constituted by: frame bracket, body-side structure, bolt, and rubber bushings and a retainer (Huang 2002). Bolt assemblies required time and good technical knowledge, incompatible with nowadays mass production demands. However, this frame construction continues to be used in vehicles with towing function (National Research Council 2013). The unibody design is a 3D structure optimized for generic loading, whereas in the specific case of towing loading, BoF design has higher twisting stiffness.

Frames of modern mass-produced passenger vehicles are almost exclusively unibody designs. Unibody frames or unitized construction frames mean that the body parts provide both structural and other functions (primary enclosure, aesthetics, crash protection, etc.), in opposition to the body-on-frame concept, in which a non-structural body is simply assembled to the load carrying frame. It is produced with metal sheet pressings, spot welded together to form an integral 3D structure. The multiple curvatures make the panels stiffer, allowing the skin to bear part of the loads. The redundancy and space depth improve the general stiffness of the structure. Both the roof and floor pan, in conjunction with the side frame shell, can contribute to the vehicle bending and torsional stiffness. The unibody high bending and torsional stiffness, enables to reduce the chassis weight by reducing metal thickness. Only with Finite Element Method (FEM) is possible to compute the mechanical behaviour of the structure due to its geometrical and three dimensionality complexities. To what concerns steel body/frame, there are no true *monocoque*, single shell, structural skin or stressed skin construction. True *monocoque* body construction is only used in some high performance sports cars, mainly with Carbon Fiber Reinforced Polymers (CFRP) or some niche products of Aluminum skin and casting components (Crolla 2009). The main features and applications of different steel car frame/body types are summarized in Table 1 from Annex A, and some examples are illustrated in Figure 5.

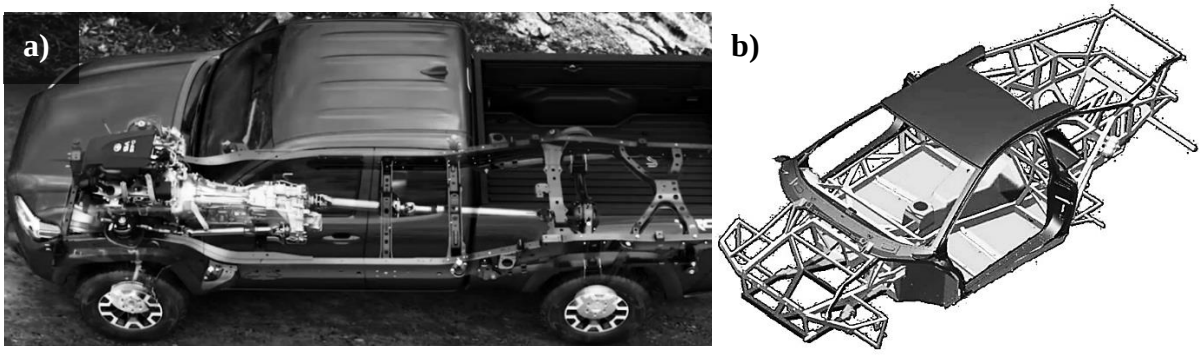

Figure 5- Examples of typical applications of different vehicle body types. a) Body-on-frame Toyota concept for all non-crossover SUV's and Pickup trucks (Toyota Canada Inc. 2016). b) Tubular steel frame of the 2005 Lamborgini Murcièlago model, along with the CFRP exterior panels (Feraboli and Masini 2004).

The unibody chassis requires a high investment in sheet metal working tooling, being only compatible with mass production to amortize the high initial capital. Sheet-intensive structures require technologies that are economic, robust, and are relatively insensitive to fit-up variations, geometric tolerances, clearances, etc.). Thus, the boom of unibody cars is intrinsically related with advances in spot welding techniques in lap joint configuration. Lap joints are easily aligned by industrial robots, require almost no joint/surface preparation, are compatible with spot joining process, and metal sheet components are easily designed for lap welding. In addition, in spot welding the clamping technology is already integrated with the welding system, carrying almost no additional costs due to the spot nature (only exception is the laser spot welding, not frequently used). Considering the process intrinsic features, spot welding is a quick, easily automated, highly reproducible and with high work rate method. Spot welding techniques have high energy density, allowing short welding cycles. Currently, there are a significant number of cost-effective spot welding processes, either by fusion or solid-state spot welding techniques.

As already stated, spot welding in lap joint configuration is widely used throughout the assembly process, and in the production of sheet metal components for the automotive industry. However, other types of joint configurations and seam welding processes not only have their space in auto manufacturing, but also saw the recent spreading of their usage. Seam welding enables to weld different configurations and different structural components. In addition, the more significant load transfer area can offer improved crash performance, greater durability and improved torsion and bending stiffness. Due to its increasingly importance in the automotive industry, Laser Beam Welding (LBW) will be highlighted when characterizing seam welding features in vehicles production.

Regarding lap seam welding, Laser welding enables short flanges, which translates in weight savings and additional freedom for design. Single-sided accessibility and contact-free joining enabling invisible joints and elimination of access windows (higher torsion stiffness), in combination with a highly efficient productivity (Katayama 2013). It also satisfies high volume automotive production requirement for different parts with its inherent flexibility (a beam from one laser source can easily be switched to several workstations). Typical automotive application of LBW includes welding of roof to the side panels of car body structure. Tighter dimensional and geometric tolerance requirements for parts and positioning, and separated cells from the main body shop line are some drawbacks in comparison with spot welding. According to the state of art of this emerging joining technology, no short-term replacing is envisioned, rather a more realist position as a complementary process is predicted (Graudenz and Baur 2013).

Considering its geometric features, butt joints are often associated with seam welding. Butt joints have better mechanical performance and are optimized in terms of material consumption and weight addition (no overlap region). However, they require extensive joint preparation and are hard to align. Tailor Welded Blanks (TWB) are semi-finished products that will be subjected to deep-drawing or stamping, and are produced by butt welding metal sheets of different thickness, compositions, strengths or coatings. The majority of TWB are produced by laser cutting, and joined by laser welding, and allow for structural optimization (Kinsey and Wu 2011). However, Friction Stir Welding (FSW) is already been used for seam welding of Aluminum Tailor Welded Blanks (Hovanski et al. 2015).

The recent evolutions in LBW (Katayama, Kawahito, and Mizutani 2012), (Acherjee 2018), enabled the spread of edge and hem joints in the automobile body. This type of joints have many advantages compared to lap seam welding, such as higher welding speed, lower thermal deformation, smaller flanges, the possibility of omitting the use of anti-corrosion coating on the edge of the steel sheet, and continuous water tight joint can also eliminate the use of sealants (Uchihara 2011).

Even if spot welding continues to play an important role in joining of stamped sheet base steel components, novel design approaches may change the balance in favor of other techniques. Table 1 illustrates a probable future evolution of vehicle steel body frames, with a double hybrid approach. It is advisable that this happens, if steel ought to be competitive with promising lightweight materials body frames, such as Al, Mg, polymers and composites based. New structural lightweight materials such as Al and Mg will replace steel in: low stressed locations, and were different manufacturing processes such as casting, extrusion, and hydroforming provide cost-effective design freedom and optimal performance. In addition, a hybrid construction is expected to revolutionize the passenger vehicle body frame, by blending the current unibody design with space frame (concept imported from Al frame designs) (Overbagh 1995). These design modifications would increase design flexibility, reduce the number of stamped parts and in its turn cost, improve stiffness by introducing load-carrying profiles, and boost the use of lightweight materials (Böhler et al. 2008).

Table 1- Hybrid concept for future steel body-frames (Böhler et al. 2008).

Hybrid Steel Design	Multi-material	Stamped Sheet skins	Steel
		Panels	Al, Steel
		Casting components	Mg, Al
		Extruded profiles	Al
		Hydroformed profiles	Al, Steel
	Hybrid Construction	Uniboby Space Frame (Al concept)	Unibody/Space-frame

1.3 Project Objectives and Current Knowledge gap

This dissertation is integrated into a partnership R&D project (itself part of the PhD thesis from this work's supervisor) whose content and experimental work wasn't exhausted with this report. Considering the time during which this thesis was developed, its conclusion wasn't viable. The project is intended to be further explored by at least one future student. The main objectives of the project can be divided as follows:

- Scientific view
    - Characterize the microstructure and metallurgical reactions in the Mg-steel interface, and establish the relationship between interface features and different welding parameters. Correlate the microstructure/interface features and mechanical properties. Correlate the microstructure evolution with the thermal cycle data recorded. Study the development of Al-Fe intermetallic layer by SEM and EDS analysis;
    - Understand the welding mechanism between casting Mg and Zn-coated steel - Characterize the role of the Zn coating and Al-Fe intermetallic layer in the bonding process. Understand the influence of the main alloying elements keeping the remaining composition the same, and changing the Al content of the Mg alloy (by welding Mg plates with 0, 3 and 9 Al wt.%), and the Zn content (wt.% undetermined);
    - Understand the fracture mechanism in static, low cycle and high cycle loading conditions.

- Technical view
    - Achieve sound Refill-FSSWed joint between AM50 Mg alloy to Zn-coated steel, with good surface appearance;
    - Define the process window and develop optimized welding parameters;
    - Evaluate static mechanical properties – lap shear strength and strain development during lap shear test by Digital Image Correlation (DIC);
    - Evaluate dynamic behavior – lap shear fatigue strength and preliminary damage tolerance

To the best of the author's knowledge, taking in account the existing literature, all experimental studies of dissimilar welding between Mg and steel were based on wrought Mg plates. Scanning from advanced fusion welding to solid state welding, and seam welding to spot techniques, there are still no reports about casting Mg alloy to Zn-coated steel dissimilar welding. In addition, welding of Mg alloys to Zn-coated steel is still challenging and the published research is limited. In the particular case of Refill-FSSW, the only conducted studies published so far used wrought ZEK100 Mg sheets (Chen et al. 2015), (Shen, Ding, et al. 2016). In contrast to ZEK100 Mg alloy, commonly used series such as AM and AZ are mainly alloyed to Al. Mg-Al alloys are the most widely casted (Zheng et al. 2006) and a lot of work on its behavior of alloy phases is being made (Pan et al. 2005). Regarding dissimilar welding of Mg-Al series to steel, the welding process should be more challenging considering the unavoidable Mg-Al eutectic reaction.

1.4 Project organization and Workflow

The evolution of the project, and eventual difficulties, were assessed by periodic department meetings, a total of three during the project course. One month after the beginning of the project, a first kick-off presentation was arranged. Its main goal was to ensure that all the important topics of the project and background research were understood, and that all the technical training - laboratory operation and maintenance; cutting, tensile and welding machine operation; and health and safety regulations - was properly received. The intended time schedule, and its feasibility, was also validated. Two months after the kick-off presentation, a mid-term presentation was held. It ensured that there were no technical nor bureaucratic tangles delaying the work (broken machine or in maintenance, broken tool, lack of material, etc.). Preliminary results and the update of the time schedule were also required. One week after the end of the project a final presentation took place. Its main goal was to present the final results and outline the necessary future work, as well as to suggest future research topics about the remaining knowledge gaps. The time schedule followed during the project is presented in Figure 6.

1.5 Work Outline and Dissertation Structure

This dissertation presented in fulfillment of the thesis requirement for the degree of Master in Mechanical Engineering, had the particularity of being conducted in an industrial placement. The data used in the present report was produced from a 6 months curricular internship (from 05/02/2018 to 03/08/2018) at HZG institution. The work performed directly for HZG during the internship, which wasn't fully used in this report, can be summarized as:

- Literature review of the different welding techniques successfully applied to Mg-steel joining (subchapter 2.3), particularly competitive fusion welding and other solid-state welding techniques not studied in HZG – in contrast to the remaining literature review topics from chapter 2, this specific topic (with significant dimension) was assigned as a task from this thesis' supervisor. The information gathered is intended to be used in the future to produce visual material to be used in presentations and internal workshops;
- Definition of the Design of Experiments (DoE) – it was necessary to adequately and justifiably choose the best standard design, tune the different design features, and establish the inference window for the experiment;
- Experimental work – study the influence of different welding parameters in the joint strength, influence of differential rotation in the joint strength and metallurgical features. In addition, non-related work to this thesis was conducted - welding the fatigue test specimens (not tested due to time limitations) and other lap joints relevant to Banglong Fu's work;
- Technical work – assembly of the tool head, setting up the welding and temperature recording apparatus; welding operation and set up of the machine; metallographic sample preparation by standard techniques (sample cutting, embedding and polishing), observation and recording of macrostructures and microstructures by optical microscope; lab maintenance routine; assembly of the tensile tests apparatus and operation of the tensile machine; Data analysis – statistical analysis of the DoE, generate spreadsheets from data recorded during welding (force, torque, travelling displacements, rotation speeds, etc.), during tensile testing (force, displacement), temperature recording, and finally organize a spreadsheet with the welding parameters and relevant information gathered in each weld along with internal reference number;
- Non-scientific work – presentations and demonstrations to visiting potential industrial partners (confidential), about the state of art of Refill-FSSW, were quite frequent. Maintenance routines of the metallographic Lab were also part of the student work.

One natural important task as HZG researcher is to properly document all generated experimental data in a final internship report. However, in the case of master students, the final internship report is replaced by the final dissertation. In addition, an extensive review of the state of art regarding the background of each project must also be done in its beginning. Even though the project already received other students, the author was the first master student. Thus, some chapters have slightly differences from the classic dissertation structure. This document is divided in 5 main chapters, being this introductory chapter the first one, in which a brief introduction to the project, to the receiving organization and to the automotive industry is made.

Throughout Chapter 2, the literature review and current state of art is exposed. This chapter is significantly different from the classic dissertation structure, since an extensive literature review was assigned at the beginning of the internship as first work task. As usual in any master thesis, the mechanical behavior, technological aspects and applications of the base materials are explored – Mg alloys and advanced high strength steels are detailed in subchapter 2.1 and 2.2 respectively. Then, the background on dissimilar welding of Mg to steel is unveiled in subchapter 2.3. However, these subchapters were elaborated in more detail than what is usually required since HZG plans to use the information gathered in the future (projects, events, etc.). An overview of the Refill Friction Stir Spot Welding (Refill-FSSW) process is made in subchapter 2.4. Finally, the last subchapter (2.5) outlines the basic concepts of design of experiments. The last two subchapters were developed entirely in the scope of this thesis and therefore are not related to the work developed for HZG. As a result, these resemble more (in terms of detail and length) what it is expected to see in a master thesis state of art review.

Chapter 3 – 'Experimental Procedure', first characterizes the base materials used. A brief introduction of the two base materials characteristics (chemical composition, metallographic analysis, and mechanical properties) is quickly discussed and exposed. Then, a description in detail of the equipment set-up, techniques and procedures adopted during the experimental work is given. More relevant, are the assumptions outlined in the design of experiments. The working plan for the experimental approach is also presented.

Chapter 4 – 'Results and Discussion', summarizes the main results derived from the experimental work, followed by its discussion. It also contains a preliminary analysis to the project in hands and also systematizes some procedures for future industrial optimization experiments.

Chapter 5 – 'Final Remarks', enumerates the final conclusions of this thesis, and outlines the remaining knowledge gap as well as recommended guidelines and unexplored topics for future works

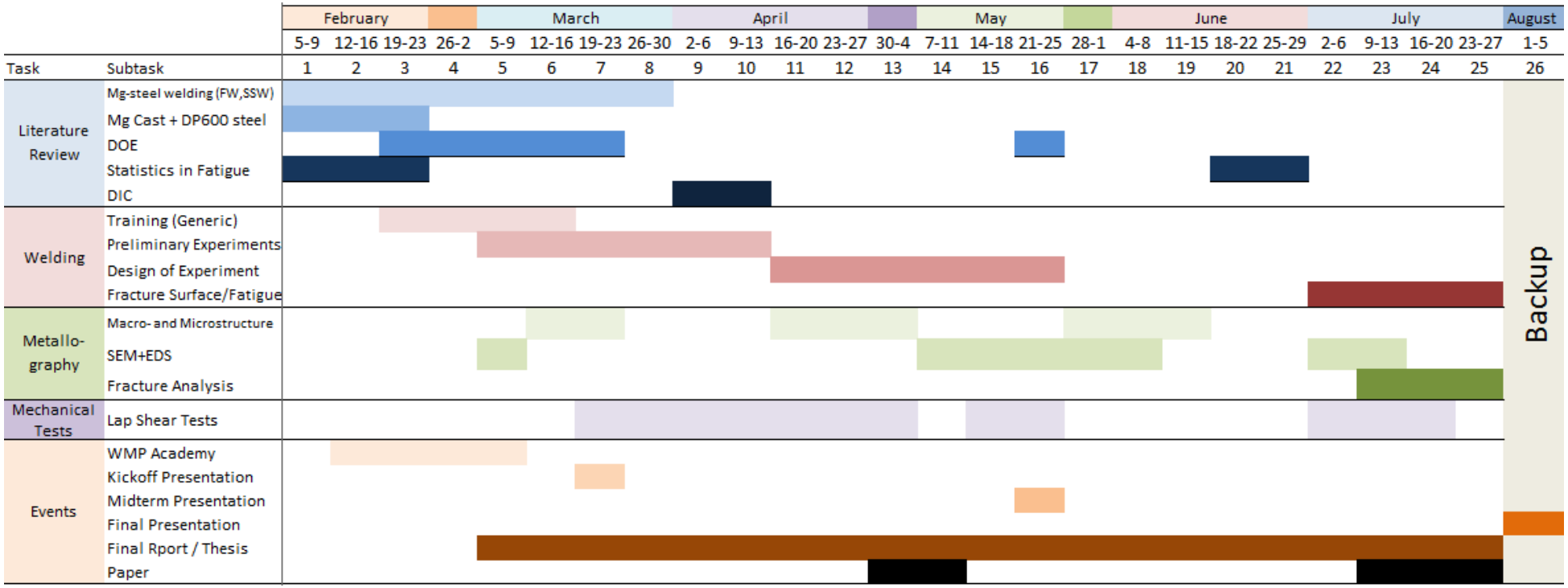

Figure 6- Time schedule followed during the internship from which this report was produced.

2 Literature Review

2.1 Magnesium and Magnesium Alloys

2.1.1 Classification and properties

Magnesium and its alloys are usually classified as commercially pure Magnesium, wrought alloys and casting alloys. Commercially pure Magnesium doesn't have structural applications. It is essentially used for alloying nonferrous metals (Al, Zn, Pb), steel desulphurization, as nodulizing element (production of nodular cast Iron), as reduction agent (Titanium and Zirconium production) and as chemical for a variety of process. In addition to these chemical related functions, it can also be used for flash photography, flares and some small office equipment. One important physical property is its flammability, present in sheeted and powdered Magnesium (Friedrich and Mordike 2006), (GrantaDesign 2017).

Magnesium alloys don't have such a well standardized designation, in comparison to other alloys like Aluminum alloys and steel. Efforts from ASTM, in the early 2000s, are now getting the intended outcome. The ASTM B 275 - 05 designation is the most widely used, reason why it will be adopted during this report (ASTM International Standards 2005). As opposed to the designation of Aluminum, specified by the Aluminum Association, the ASTM standard for Mg is applicable for both wrought and casting Mg. According to the ASTM codification system, the first two or three capital letters refer to the main alloying elements, and the following numbers indicate their respective average mass compositions. The letter corresponding to the element present in greater quantity is used first, if they are equal, they are listed alphabetically. In order to acknowledge future modifications of the base composition, an additional capital letter after the numbers is introduced, starting in A and following the chronological order of registration. Further codifications using both letters and numbers, separated by a dash, define the fabrication code (Hussey and Wilson 2013). Table 2 defines the relation between the capital letter and the chemical element, as established in (ASTM International Standards 2005). Table 3 defines the designation for different material conditions.

Wrought Magnesium alloys often have a more homogeneous microstructure and enhanced mechanical properties, as illustrated in Figure 7. Wrought alloys come as forged, extruded, rolled sheet, drawn products, etc. Although they have superior mechanical properties, their cumbersome production - poor formability (r-value and n-value), edge cracking, and asymmetric yielding - and lack of suitable alloy composition, justify their small usage comparing with casting Magnesium alloys, Figure 8 (Bettles and Barnett 2012). Due to their Hexagonal Close Packed (HCP) crystal structure, ductility is limited at room temperature, restricting plastic forming processes. Contrary to FCC (Face Centered Cubic) and BCC (Body Centered Cubic) crystal structures, only the basal slip system can initiate the slipping in the Magnesium HCP crystal structure. Its critical resolved shear stress (CRSS) is much lower than those of the non-basal system, at room temperature. Thus, plastic deformation relies more on the combining action of the slip and twin process movements of basal system. Consequently, cold-working of wrought alloy is often prone to create crack defects and anisotropic plastic deformation behavior due to enhanced texture development (Huang et al. 2011), (Wang, Qiao, et al. 2013). Only two independent slip systems are present in the basal slip mode. The fulfillment of the von Mises condition (more than 5 independent slip systems must operate for polycrystals deform uniformly and without failure at the grain boundaries) would also require the activation of non-basal slip and twinning modes (Styczynski et al. 2004). With increasing temperature, activity of non-basal systems also increases, resulting in higher alloy ductility. However, costs of high temperature forming tools, grain size growth (deteriorating the mechanical properties) and poor surface finish are some of the drawbacks that limit the production of wrought Magnesium alloys (Huang et al. 2011).

Table 2- Codification of the capital letter in the standard designation of Mg alloys (Friedrich and Mordike 2006).

A	Aluminum	**F**	Iron	**M**	Manganese	**R**	Chromium	**W**	Yttrium
B	Bismuth	**H**	Thorium	**N**	Nickel	**S**	Silicon	**X**	Calcium
C	Copper	**J**	Strontium	**P**	Lead	**T**	Tin	**Y**	Antimony
D	Cadmium	**K**	Zirconium	**Q**	Silver	**V**	Gadolinium	**Z**	Zinc
E	Rare earths	**L**	Lithium						

Table 3- Basic fabrication states codification (Friedrich and Mordike 2006).

Letter	Designation
F	As fabricated
O	Annealed, recrystallized – wrought products only
H	Strain-hardened – wrought products only. Different subdivisions
W	Solution heat-treated – unstable temper
T	Thermally treated – stable tempers. Series of subdivisions

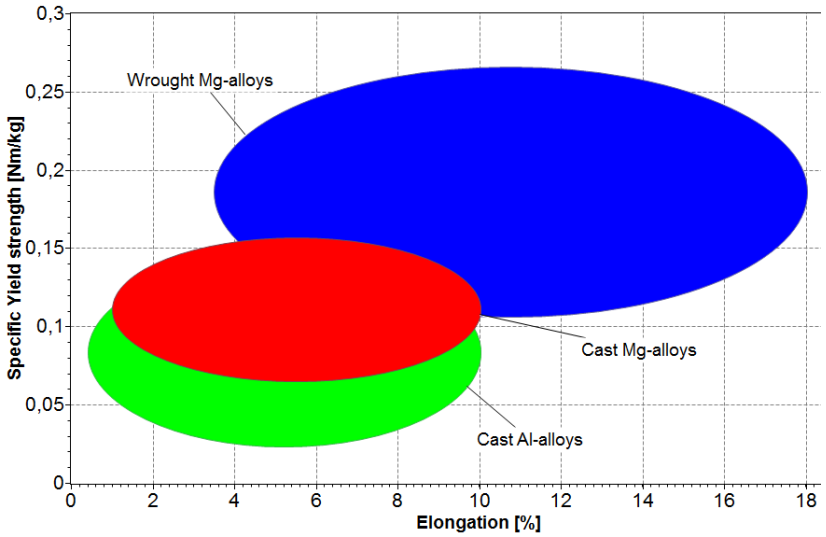

Figure 7- Comparison of some mechanical properties of wrought and casting Mg alloys (GrantaDesign 2017).

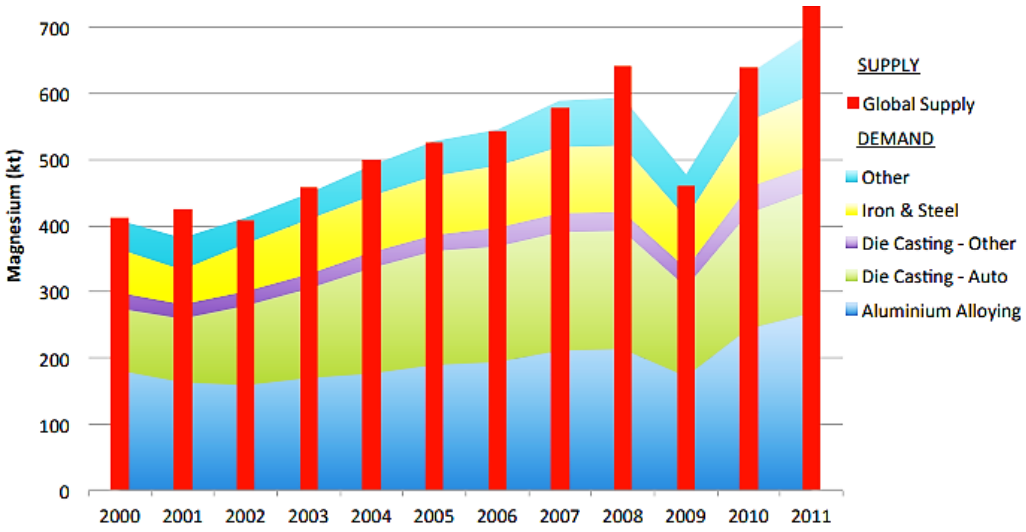

Figure 8- Consumption of Magnesium and Magnesium alloys by application (IMA 2012).

Casting Magnesium alloys account for nearly 75% of Magnesium alloys consumption (GrantaDesign 2017), representing about 98% of their structural applications (Luo 2013). Nearly 93% of casting Magnesium alloys are produced by die casting process, being one of the most efficient methods in the automotive industry (Friedrich and Mordike 2006). The main casting methods used are die-casting (particularly high pressure) and gravity casting (essentially sand and permanent mold casting). Magnesium alloys have an excellent castability, mirrored in their:

- Low melting point (447-649 ºC) (GrantaDesign 2017);
- Good mold filling – high viscosity and fluidity (Khan et al. 2008);
- Low porosity – in contrast with casting Al alloys, Mg alloys do not suffer highly from hydrogen porosity, since the difference between the solid and liquid solubility of Hydrogen is smaller;
- Relative low heat content (955-1060 J/kg.ºC) and low density (1750-1870 kg/m^3) – reduced thermal distortion, enabling close tolerances and complex features (GrantaDesign 2017), (Friedrich and Mordike 2006);
- Low die soldering proclivity – molten Al has high affinity to Iron, so attacks Iron crucibles, die casting machines, etc. more than molten Mg does (Luo 2013),(Bowles, Han, and Horton 2016).

In addition to the low formability of Mg alloys, there are a series of specific features that hampered their industrial implementation. Table 4 summarizes some aspects that justified the recession in the Magnesium alloys usage since the world war II (Mishra, De, and Kumar 2014).

Table 4- Main drawbacks of wrought and casting Mg alloys (Wang, Eliezer, and Gutman 2003), (Dahle et al. 2001), (Kulekci 2008), (Potzies and Kainer 2004).

Disadvantages	**Justification**
Corrosion resistance	Quickly corrosion in salty environments and inorganic acids (however not by alkalis neither soda caustic) Poor galvanic corrosion resistance Stress corrosion, susceptibility to intergranular stress corrosion cracking
Creep Resistance	Weak creep resistance is related to the occurrence of low-melting point phases (grain boundary sliding), e.g. $Mg_{17}Al_{12}$ phase
Coarse grain size	There's no reliable, easy to use, commercial grain refiner Permanent molding and sand casting of Mg-Al don't exhibit the fine grain size of others alloy systems
Fatigue Behavior	Engineering fatigue behavior (S-N curves) similar to steels (pronounced fatigue limit) in benign environmental conditions as concluded in the first studies. Fatigue performance highly dependent of corrosive media, service temperature, manufacturing process and the presence or not of defects
Inflammability	Fire hazard during fabrication (melting, machining and grinding) and usage (burn near the melting point)
Service Temperature	Limited max. service temperature by strength, creep resistance, corrosion problems and inflammation risk

2.1.2 Casting Magnesium Alloys in the Automotive Industry

The history of Magnesium in the automotive industry begins in 1921, United States, where Dow Chemical® developed the first Mg based racing engine pistons for "Indy 500". Since then, structural applications such as pistons, crankcases housings, air-cooled engines, and gearbox castings, began to use Mg alloys. However, due to their limited corrosion and creep resistance, and increase in power requirements (load and temperature service conditions worsened), their application suffered a drastic reduction during the 1970s (Luo 2013). Its price volatility and lack of processing knowledge are also outlined as important factors by (Blawert, Hort, and Kainer 2004). There were several major driving forces for the reborn of the structural applications of Mg alloys in the automotive industry, all somehow backed in the car weight concerns (detailed further in Page 19). Technological breakthroughs such as the development of "high-purity" Mg alloys (excellent chemical stability), high creep resistance alloys, and the introduction of the high-ductility and energy absorption alloys of the AM-series, also had their share in the Mg recurrence process. Nowadays, around 90% of the total Mg alloys are consumed by the automotive industry (Kulekci 2008). Figure 9 a) - c) illustrates, and Table 5 summarizes, some real and practical applications of casting Mg alloys in the automotive industry.

Gravity sand and permanent mold processes are less prone to porosity and metallurgic defects for large Mg alloys components. It is usually the first choice for manufacturing creep resistance Magnesium alloys. However, production rates are lower and cost per piece is higher. Thus, they are used more often in specialized applications such as racing wheels, engine blocks, and in aircrafts and helicopters components (Luo 2013), (Elsayed et al. 2011), (Friedrich and Mordike 2006).

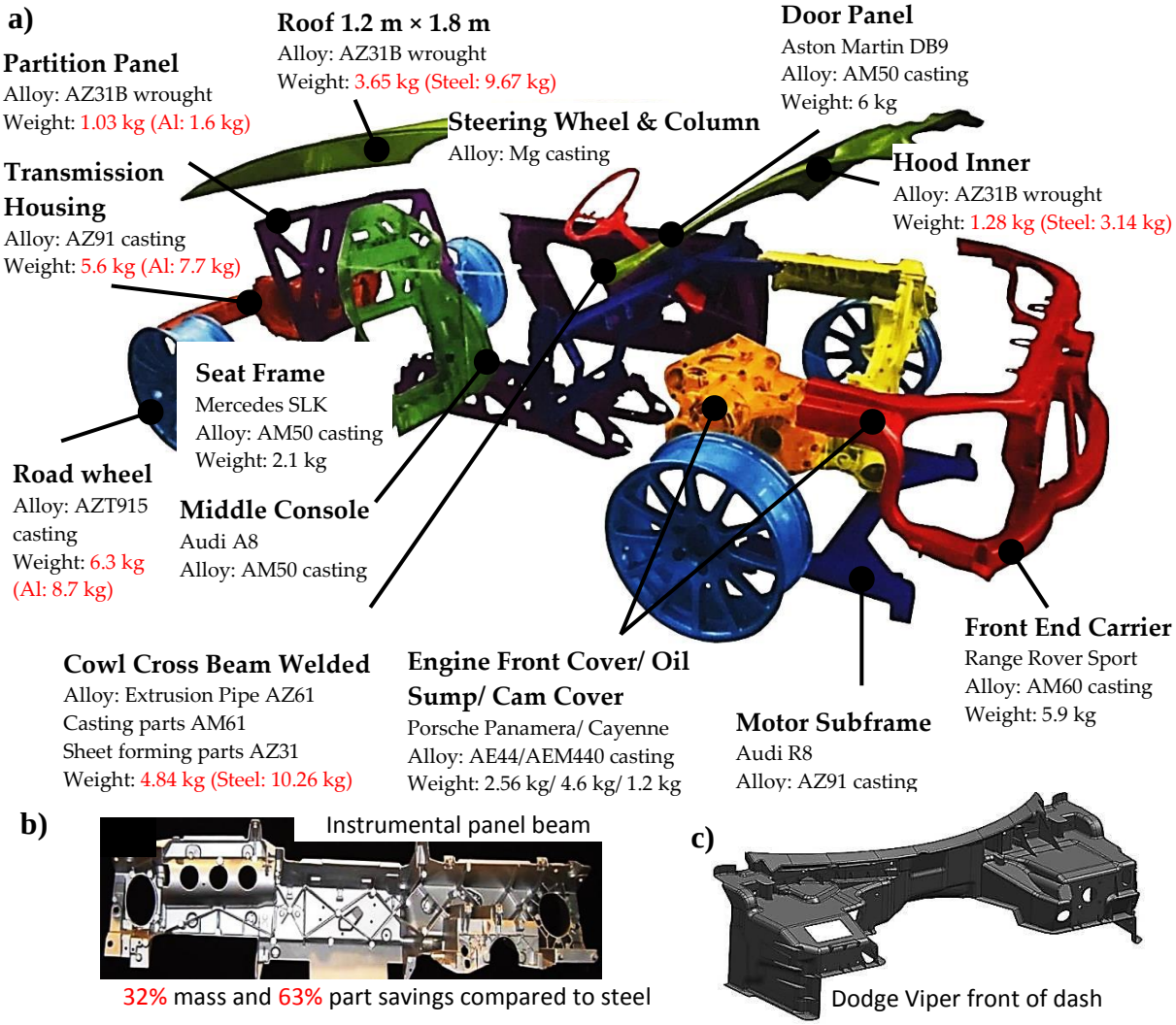

Figure 9- a) Illustration of several applications of casting Magnesium alloys in the automotive industry. b) Instrumental panel beam. c) Dodge Viper front of dash. All images provided by the MagIC department from HZG.

Table 5- Global Magnesium alloys applications in the automotive industry (Luo 2013).

System	Component	North America	Europe	Asia
Interior	Instrument panel	Yes	Yes	Yes
	Knee bolster retainer	Yes		
	Seat frame	Yes	Yes	Yes
	Seat riser	Yes	Yes	Yes
	Seat pan	Yes	Yes	
	Console bracket	Yes		
	Airbag housing	Yes		
	Center console cover	Yes	Yes	
	Steering wheel	Yes	Yes	Yes
	Keylock housing	Yes		
	Steering column parts	Yes	Yes	Yes
	Radio housing	Yes	Yes	
	Glove box door	Yes		
	Window motor housing	Yes	Yes	
Body	Door inner panel		Yes	
	Liftgate inner panel	Yes	Yes	
	Roof frame	Yes	Yes	
	Sunroof panel	Yes	Yes	
	Mirror bracket	Yes	Yes	
	Fuel filler lid	Yes	Yes	
	Door handle		Yes	Yes
	Spare tire carrier	Yes		
	Cross car beams		Yes	Yes
Chassis	Wheel (racing)	Yes	Yes	Yes
	ABS mounting bracket	Yes		
	Brake pedal bracket	Yes		Yes
	Brake/accelerator bracket	Yes		
	Brake/clutch bracket	Yes		
	Brake pedal arm	Yes		
Powertrain	Engine block		Yes	
	Valve cover/cam cover	Yes	Yes	Yes
	4WD transfer case	Yes		
	Transmission case		Yes	Yes
	Clutch housing & piston	Yes		
	Intake manifold	Yes	Yes	
	Engine oil pan		Yes	Yes
	Alternator/AC bracket	Yes		
	Transmission stator	Yes		
	Oil filter adapter	Yes		Yes
	Electric motor housing	Yes		

2.1.3 Mg-Al-Mn alloy system

Most commercial Magnesium alloys are based on the Mg-Al system (Dahle et al. 2001). In addition of their relatively lower price (compared to others magnesium alloys), they are readily castable. Unlike Aluminum die casting, Magnesium parts usually constitute structural members, which must fulfill stricter requirements, instead of being just cost cutting alternatives. According to (Friedrich and Mordike 2006), the renascence of Magnesium die cast usage is in part attributed to the development of the low Aluminum AM series. Casting Magnesium components can replace low stressed multi-part welded steel parts.

AM50A Magnesium alloy is commonly used for die-casting process, particularly by high pressure. It has high-energy absorption and damping capacity (impact strength and ductility) and elongation at high strength. Features that justify its applications in components with complex geometry such as steering wheels, dashboards, instrument panels, brackets, fans, font end support assemblies, cylinder head covers, etc. (Kiełbus, Rzychoń, and Cibis 2006), (Friedrich and Mordike 2006), (Kulekci 2008), (Kumar et al. 2015). The effect of typical alloying elements is given in Table 6.

Table 6- Main effect of alloying elements in Magnesium alloys based on the Mg-Al system, specifically present in the AM50A alloy used (Kiełbus, Rzychoń, and Cibis 2006), (Zheng et al. 2006), (Friedrich and Mordike 2006).

Alloying Element	**Effect**
Al	Enhances both tensile strength, hardness and grain refinement
	Improves castability and reduces the oxidation rate of the melt, but decreases ductility, due to the brittleness of the $Mg_{17}Al_{12}$ phase
	Also increases corrosion resistance – prevents α-phase dendrites from building big networks
Mn	In the presence of Al, Mn_5Al_8 compound is formed
	Increases slightly the yield strength
	Enhances corrosion resistance to sea water and controls iron detrimental effect by reducing FE solubility forming Fe-Mn compounds
Zn	With Zn/Al ratio < 1:3, is dissolved mainly in the $Mg_{17}Al_{12}$ phase; for greater ratios the $Mg_{17}Al_{12}$ phase is transformed to $Mg_{32}AlZn_{49}$
	Improves strength at room temperature
	Increases fluidity of the melt, intrinsically connected to castability
	Higher Zinc content promotes weld cracking (brittleness and hot cracking)
Si	Improves creep resistance by forming stable silicide compounds with Magnesium (Mg_2Si) and other alloying elements (Al, Zn)
	Decreases castability
Be	Reduces the reactivity of the molten metal. It tends to precipitate out of the liquid and segregate to the surface, being incorporated into the surface oxide.

For the most Magnesium alloys, Aluminum content typically range from 3-9 wt.% Al. According to the equilibrium phase diagram in Annex I Figure 4, they are all hypoeutectic alloys. So, their equilibrium microstructure is 100% α-Mg matrix, with precipitates of γ-intermetallic compound (phase) by maximum solubility limit (Dahle et al. 2001). In real-practice solidification phenomenon, a non-equilibrium, metastable (heat treatable) eutectic structure always develops. (Kiełbus, Rzychoń, and Cibis 2006) state that even down to about 2 wt.% Al content, an intermediate eutectic is present. There are several parameters that influence the eutectic morphology and distribution. In permanent mold casting, (Dahle et al. 2001) stated that the Mg-Al eutectic changes progressively from lamellar, fibrous, granular, partially divorced to fully divorced with the increase in Zn content and cooling rate, and decrease in Al content.

2.2 Advanced High Strength Steels

2.2.1 Automotive Industry Steel Classification

Steel is the world's most commonly used alloy, and the automotive industry is no exception. It continuous to be the primary material used for vehicle body structures (BIW[1], exterior panels, etc.) and other subsystems (power train, moving parts, trim subassemblies, etc.). No other alloy provides its unique combination of different features:

- Mechanical properties – YS/UTS, stiffness, ductility and fatigue behavior;
- Performance flexibility and versatility – by alloying and heat treatment;
- Technological properties at high cost efficiency – formability, weldability, machinability and recyclability

(Baluch, Udin, and Abdullah 2014)

There are different types of steel classification throughout the world and field of applications (general construction, tooling, automotive industry, etc.). Steel is usually classified by their standard composition, defined in national and international standards such as ASTM, ISO, DIN, etc. In the automotive field, steel can be classified according to their tensile strength in: low strength (YS: < 210 MPa), high strength (YS: 210-550 MPa), advance high strength (YS: 550-780 MPa), ultra high strength (YS: 780-1000 MPa), and GigaPascal steel (YS: >1000 MPa) (Tamarelli 2011). With the continuous development of the Advanced High Strength Steels (AHSS) 1st, 2nd and 3rd Generations, this nomenclature no longer makes sense. There is a constant overlap of mechanical strength between different grades, Figure 10. Currently, the most common designation in the automotive industry classifies steels according to their microstructure/metallurgical differences, providing also some process information:

- Mild steel – IF, Mild;
- Conventional High Strength Steel (HSS) – IF-HS, IS, BH, CMn, HSLA;
- Advanced High Strength Steel (AHSS) – 1st, 2nd and 3rd Generation.

A brief summary of mild and high strength steels is presented in Table 1 from Annex B. According to their historical evolution, there are currently three generations of AHSS. The 1st Generation (FB, DP, CP, TRIP, MS, PFHT, and PHS), has well rooted industrial implementation and will be further detailed in Table 2 from Annex B. Only a superficial insight of the 2nd (L-IP, TWIP, and HMn TRIP) and 3rd Generation (Q&P, TBF, NanoSteel and MMn Steel) of AHSS will be given in Table 3 from Annex B. Designation developed by the Ultra-Light Steel Automotive Body-Advanced Vehicle Concept (ULSAB-AVC) consortium (Shaw and Roth 2002), (Thorpe and Adam 2002), (Zuidema et al. 2001), and used in Future Steel Vehicle (FSV) reports (Ten Broek, Singh, and Hillebrecht 2012), identifies steels as "XX aaa/bbb" or only "XX/bbb" [1)]. The nomenclature is used throughout this report for 1st Generation AHSS, and its meaning is explained in Table 7.

(Khedkar et al. 2016)

Table 7- Designation used to classify the steel grade, main microstructure and mechanical properties.

Codification	XX	aaa	bbb
Meaning	Type of steel [2)]	Minimum YS in [MPa]	Minimum UTS in [MPa]

[1)] When only one number is used, it refers to the (Ultimate) Tensile Strength

[2)] The abbreviations for each steel grade are given in Table 2 and Table 3 from Annex B

[1] In-white refer to the stage of a structural product before the painting and assembling of non-structural subsystems (power-train, trim components, etc.). Commonly used as body-in-white in the automotive industry.

The "banana diagram" is a typical property envelope plot, used in the automotive industry. It results from the balance between mechanical strength and elongation. Yield strength is sometimes used instead of the ultimate tensile strength. The result is the steel design sheet illustrated in Figure 10.

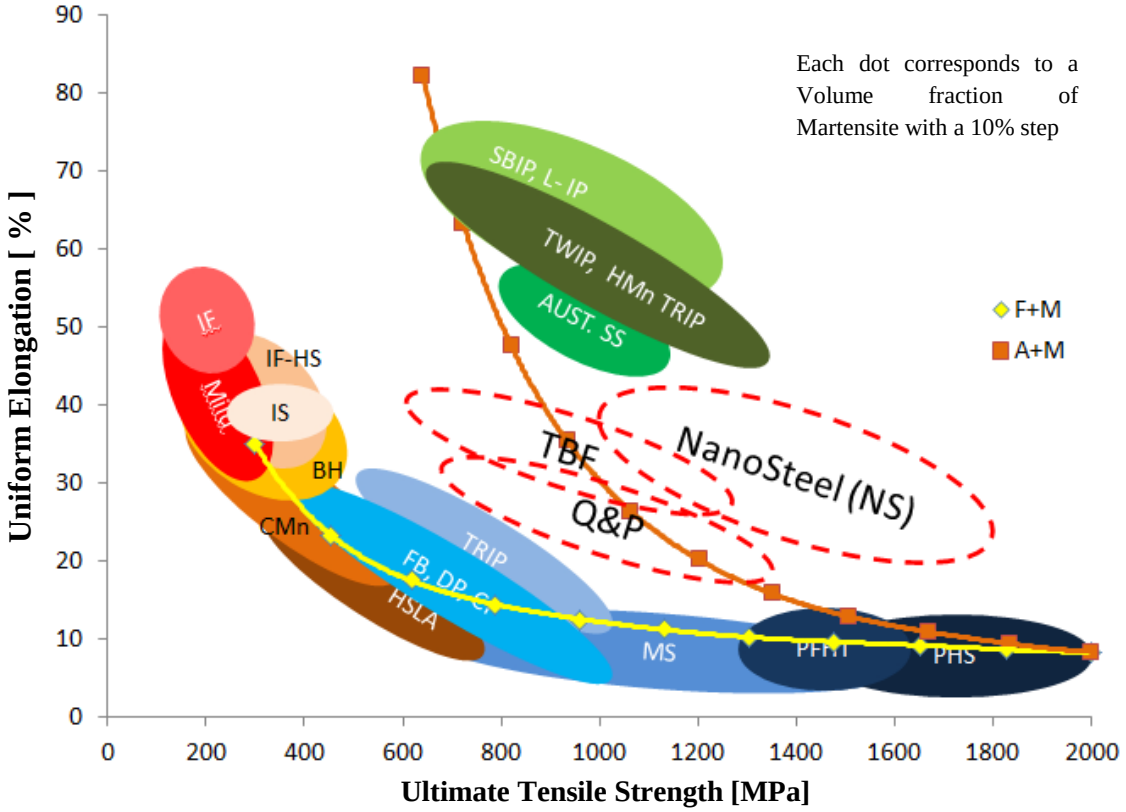

Figure 10 - Elongation and tensile strength envelop of the major steels used in automotive industry. Image produced by the author, from data collected from different sources: (Fonstein 2015), (Baluch, Udin, and Abdullah 2014), (Kuziak, Kawalla, and Waengler 2008), (Demeri 2013), (Chatterjee 2017), (Matlock et al. 2012), (Ozturk et al. 2013).

Mild steel, conventional HSS and the 1st Generation of AHSS lie down over the conventional banana curve. The increasing in mechanical resistance is followed by a decrease in uniform elongation. With the 2nd Generation, the main goal was to brake the banana curve behavior and increase the ductility of the steel, without lose its tensile strength. The 3rd Generation of AHSS claims to be able to have an intermediate mechanical behavior between the two, in expense of reduction of the alloying content and production cost. It is a real challenge for more complex strip compositions to ensure high levels of product uniformity and repeatability achieved with HSS and 1st Generation of AHSS. The superimposed curves, yellow and orange, from Figure 10, result from the modeling of the steel mechanical behavior based on its microstructure. A model from composite modelling theory was used, in Annex C is illustrated the physical background and mathematical procedure used to compute the two curves mentioned above. The data used to model the microstructure design is given in Table 8. Thus, it is clear that both HSS and the 1st Generation of AHSS are based on a Ferrite microstructure with continuous increasing of Martensite hardening phase (see yellow curve). An interesting conclusion withdrawn from the orange curve (A+M), is that this combination of phases can be an attractive approach to reach the 3rd Generation goals (base of Q&P and Medium Mn Steels).

Table 8- Mechanical properties data form each phase, used to model the microstructure design (Demeri 2013).

Phase	Uniform True Strain	Ultimate Tensile Strength [MPa]
Ferrite (F)	0.3	300
Austenite (A)	0.6	640
Martensite (M)	0.08	2000

(Fonstein 2015), (Shome and Tumuluru 2015)

2.2.2 Evolution and applications of Steel in the Automotive Industry

Mild steel was the first ferrous material to be used in the automotive industry. For almost one century, it was used without significant changes for passenger vehicles in structural elements and exposed parts. Technological aspects like formability, weldability, paintability and repairability required the steel to be as soft as possible. Its technological advantages allowed it to be the material of choice for auto chassis until the first oil crisis, 1973. The rise in fuel prices made economically viable and appealing to implement car weight reduction measures in order to reduce fuel consumption. Automakers resorted to higher strength steels that could allow thinner profiles and stamped parts as main lightweighting approach. During almost three decades (Korchynsky and Stuart 1970) until the current millennium, HSS were developed and common steel grades such as IF-HS, IS, BH, CMn and HSLA - saw their commercial expansion.

Dual phase (DP) steels were pioneers in the AHSS development, they were first studied in the 1970s (Meyer, Heisterkamp, and Mueschenborn 1975). However, their solid industrial implementation didn't start until late 1990s, with the creation of the international steel consortium responsible for ULSAB (Shaw and Roth 2002). The first attempts to commercially produce other 1st Generation AHSS already started in 2000s, and coincided with the first studies of the 2nd Generation of AHSS. Currently, a 3rd Generation of AHSS is being developed. The recent evolution of the usage of the three steel types previously mentioned is shown in Figure 11 a). It can be observed a continuous replacement of mild steel by both HSS and AHSS in auto body manufacturing, with a steeper growth for AHSS. The two last columns of Figure 11 a) show the relative share of AHSS by vehicle design, indicating the importance of unibody design on the development of AHSS. Figure 11 b) details the average mass of AHSS incorporated in an average passenger vehicle, also pointing out a continuous growth.

(Demeri 2013), (Kuziak, Kawalla, and Waengler 2008), (Fonstein 2015)

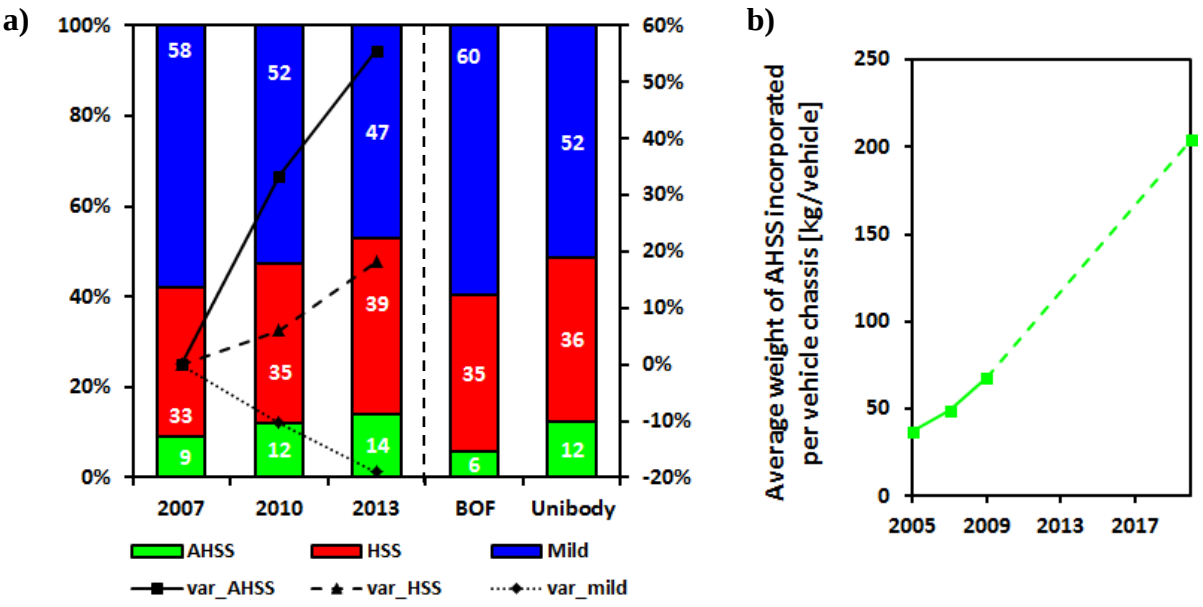

Figure 11- a) Evolution of the share of each type of steel in the body and closure of average passenger vehicles (Tamarelli 2011), and type of steel by car construction design for the year 2007 (Bhat 2011). b) Average mass (in kg) of AHSS used in mid-size passenger vehicles and future expectations, based on data from (WordAutoSteel 2009).

Yet, only the 1st Generation of AHSS has a solid industrial implementation for now. Thus, some typical commercial applications of the 1st Generation of AHSS, in the automobile industry, are summarized in Table 9. It is important to notice the correlation between the safety concept illustrated in Figure 3 and the vehicle component from Table 9, the steel grade to produce the component (Table 9) and its location in the strength-ductility space (Figure 10), and finally the relation between the steel properties and microstructure (Table 2 from Annex B).

Table 9- Applications of AHSS steels, with main focusing in the automotive industry (Billur and Altan 2013), (Khedkar et al. 2016), (Billur and Altan 2013), (Zhang and Ding 2013), (Chatterjee 2017), (Demeri 2013).

AHSS Grade	Component
Ferrite-Bainite (FB)	Rim
	Brake pedal, control and suspension arms
	Seat cross members
	Bumper and rear twist beams
	Chassis parts
Dual phase (DP)	Crash boxes/cans and sock towers
	Bumpers, beams and cross members
	A and B pillars
	Roof, front and rear rails
	Sill and rocker reinforcements
	Body, roof, door, closure panels
	Wheel webs
Complex-Phase (CP)	Rear suspension bracket
	Fender, bumper and Transverse beams
	Car bodies/chassis
	Rocker outer and panel
	Tunnel stiffer
	Sill, A and B pillars, real frame rail reinforcements
	Frame rails
Transformation-Induced Plasticity (TRIP)	Bumper and other cross members
	Longitudinal beams
	Sill, B-pillars and bumper reinforcements
	Front, rear, roof, side and frame rails
	Crash box
	Dash panels
	Engine cradle
Martensitic Steel (MS)	Medical Tools
	Cutlery Industry
	Cross members
	Side intrusion/impact and bumper beams
	Side sill and bumpers reinforcements
	Rocker outer and panels reinforcement
Press-Hardened Steel (PHS) and Post-Forming Heat Treated (PFHT)	Floor Panels
	Sill structure
	Bumper and fender beams
	Floor, door and roof reinforcements
	A and B pillars reinforcements

The increasing development and use of AHSS had three fundamental goals or purposes:

- Improve car safety and reliability (crash worthiness behavior) – high strength steels have higher ductility, higher specific tensile strength, and higher energy absorption capacity - requirements for crumple zones; and higher yield strengths - requirements for passengers safety cage; increasing the crashworthiness of the vehicles, subchapter 1.2, Figure 3;
- Decrease life cycle impact computed from Life Cycle Analysis/Assessment (LCA) – When comparing to conventional steel, AHSS allows reducing the amount of raw material consumed, by simply reduce the total material incorporated in the vehicle (see what allowed weight reduction). This increases the overall output score in LCA tools. When comparing to Al, AHSS during production, have lower energy consumption, Figure 12, and higher recyclability that offset the small increase in vehicle weight, raising lower life cycle impact in LCA (Kim and Wallington 2013);

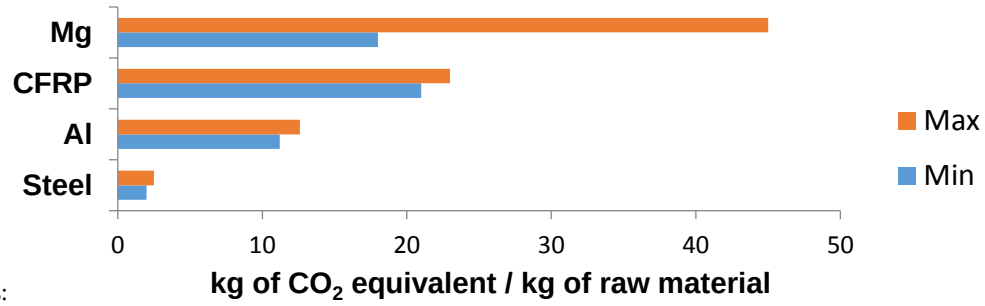

Notes:

- All steel and Al grades included in ranges
- Difference between AHSS and conventional steels is less than 5%
- Al data: global for ingots, European only for process from ingot to final products

Figure 12- GHG (Greenhouse Gas) emissions during primary production of different raw materials (Demeri 2013).

- Reduce the vehicle curb (kerb, UK) weight, Figure 13 (blue area), either through increase in specific strength or improved stiffness by design freedom (formability and manufacturing process). Lowering the vehicle mass is driven among other factors by:
  - Reduction in fuel consumption;
  - Reduction in greenhouse emissions (by reducing fuel consumption);
  - Stimulate the implementation of newly designed powertrains (electric, plug-in hybrids, fuel cell vehicles, etc.) – as a result of the ability to reduce storage battery and motor size for the same autonomy and power;
  - Offset the progressive weight addition due to the stringent car safety and pollution regulations (imposed by the governments, European directives, global treats and even by consumer requirements), Figure 13 (green and red area). The weight add can be found - in safety structural components (door intrusion beams, stiffening reinforcements, etc.), safety systems (air bags, anti-lock brakes, stability control, etc.) and emission control systems (exhaust gas recirculation system, evaporative control system, catalytic converter, etc.) (Gilles 2015);
  - Compensate for continuous additional car weight by other forms, Figure 13 (purple area). The weight add can be introduced for passengers' comfort (air conditioning, automatic transmission, power steering, etc.) and convenience (infotainment systems, connectivity, navigation systems, sound system, etc.);
  - Compete with low density materials (mainly Al alloys but also Mg alloys and plastics in specific applications) – the development of AHSS with high formability advantages is essential to keep steel as the major choice for carmakers, or at least maintain a representative share of steel in future automobiles, Figure 14;

(Shaw and Roth 2002), (Shome and Tumuluru 2015), (Demeri 2013)

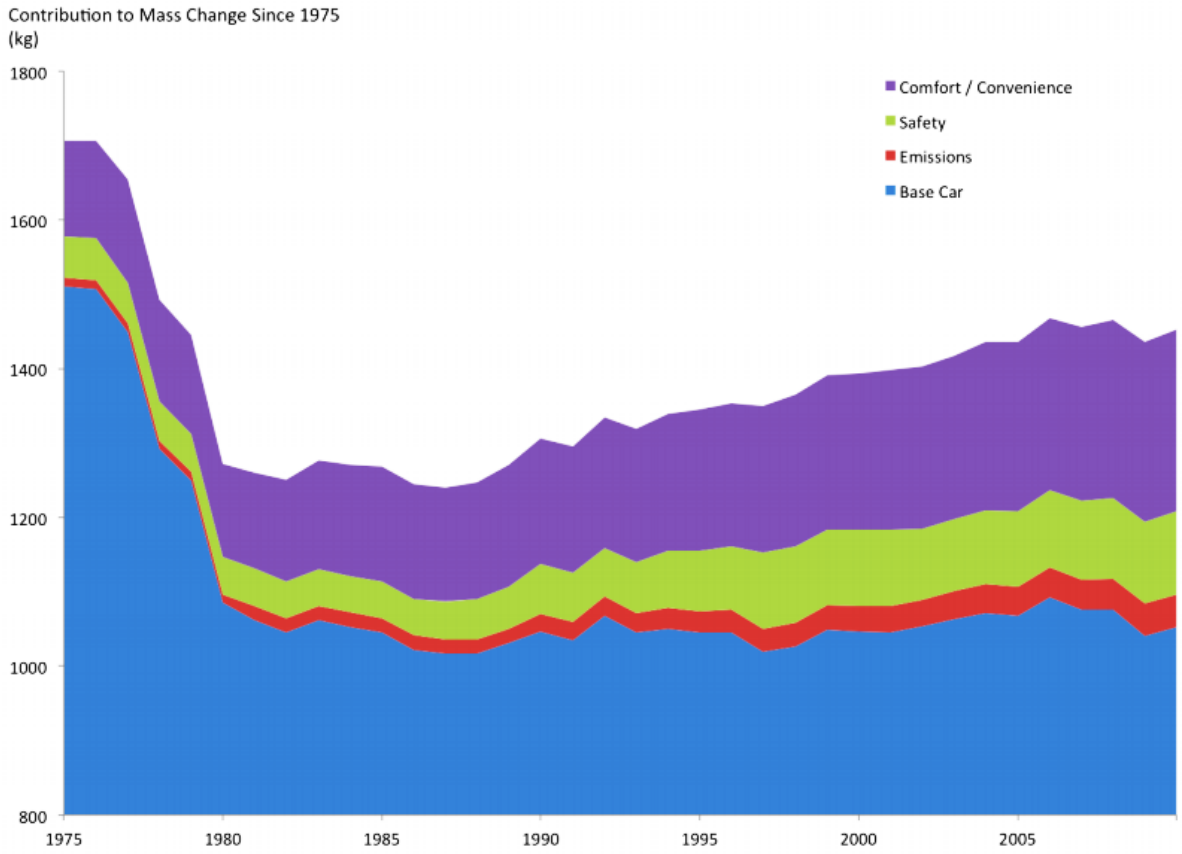

Figure 13- Different contributions for the evolution of the US average vehicle weight (MacKenzie, Zoepf, and Heywood 2014).

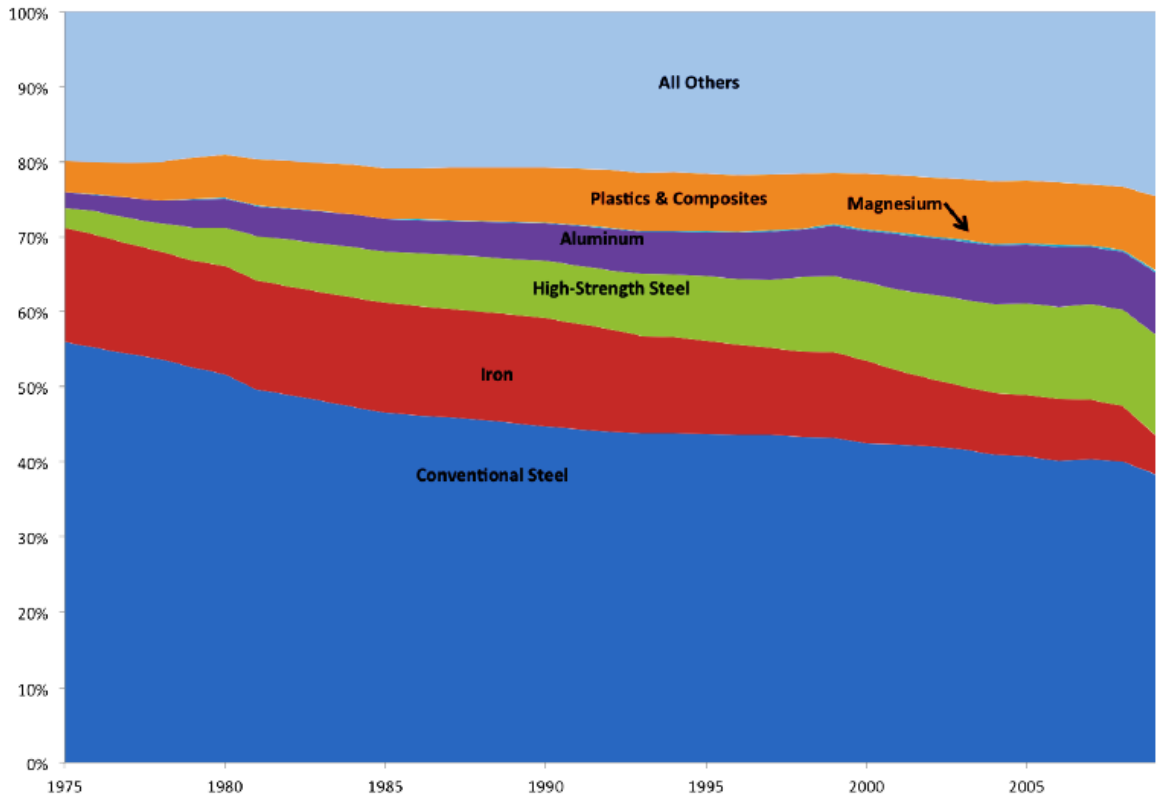

Figure 14- Evolution of the material usage in an average US vehicle. Adapted from (MacKenzie, Zoepf, and Heywood 2014).

2.2.3 Dual Phase Steel

Dual-Phase (DP) steels consist of a ductile and soft ferritic matrix, with fined dispersed hard martensitic second phase in the form of small islands (percolate or elongated bands structures are not desirable). The martensitic secondary phase volume content, usually ranges between 10-40 vol.%. This type of AHSS is a low-carbon and low-alloy system. Carbon content used is between 0.06–0.15 wt.%, it strengthens the martensite and also determines the phase distribution (influencing the final ductility). In addition to Carbon, DP steels are essentially alloyed to Mn (1.5–3 wt. %) - is a ferrite solid solution strengthener but retards ferrite formation, and Si - promotes ferritic transformation and portioning of carbon to austenite during annealing. Small amounts of Cr and Mo, used up to 0.4 wt.%, can retard pearlite and bainite formation, while Al, P and N may also be present. Additional strengthening mechanisms, such as grain refinement, are used to reach the higher strength DP grades. This is accomplished by microalloying to V, Nb, and Ti that are also precipitation strengtheners.

(Demeri 2013), (Tasan et al. 2015)

Dual phase steels combine high strength and good formability at low production costs, due to the lean alloying and relatively straightforward thermomechanical processing. Thus, they are the widest AHSS used in the automotive industry, as depicted in Figure 15 a) and more detailed in b). In addition, they were the first AHSS to be studied and industrial implemented (Gupta and Chang 1984), (Southwick et al. 1985). Typical applications of DP steels in BIW structure are illustrated in Figure 16. In subchapter 2.3, it can be noticed the importance for the auto industry of the dual phase steel by its relevance in the research field. The majority of research papers about Mg-steel dissimilar welding, whether fusion welding or solid-state welding, used some grade of dual phase steel (usually DP600).

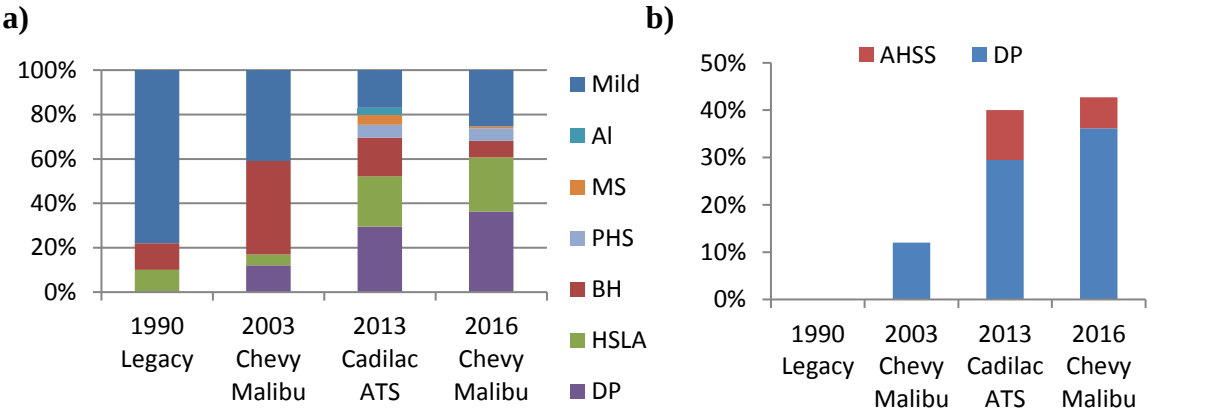

Figure 15- a) Evolution of the share in mass percentage of different metals in cars of Generals Motors®. b) Isolation of the data concerning DP steels and the remaining AHSS. Plot based on data from (Rana and Singh 2016).

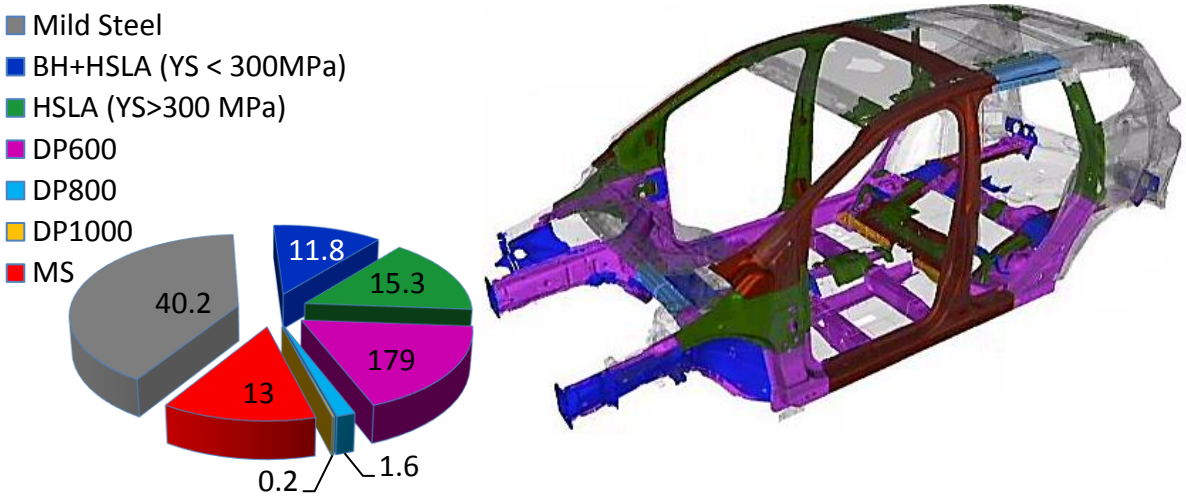

Figure 16- Applications of DP steels in passenger vehicle chassis (Tasan et al. 2015).

The mechanical behavior of DP steel can be designed by controlling volume fraction of martensite and its dispersion, by tuning C content and thermomechanical processing. Increasing the volume fraction of the hard second phase and grain refinement of ferrite grains, increases the alloy strength. Ductility is enhanced by fine and small martensite dispersion in the ferritic matrix; small vol. fraction of martensite phase, and by achieving the optimal point for ferrite refinement (Calcagnotto, Ponge, and Raabe 2010). Typical mechanical behavior of DP steels can be summarized as:

- High performance flexibility – UTS values in the regime of 400-1200 MPa and elongation varying between 10-35 %
- Low YS/UTS ratio (around 0.5) – relative high UTS (enabled by martensite phase) and low YS (enabled by ferrite phase). Usually doesn't exhibit pronounced yield point elongation;
- High work-hardening/strain hardening (n) rate – particularly initial rates, function of volume fraction and size of the second phase. High n-values lead to high uniform strain and total elongation;
- Continuous yielding behavior - macroscopically homogeneous plastic flow (enabled through the absence of Luders effects);
- Good response to static and dynamic strain aging (Bake-hardening effect) – Snoek ordering, Cottrel atmosphere, carbide precipitation and relaxation of internal stresses by martensite tempering;
- Excellent fatigue crack propagation resistance – Low carbon content;
- Strain rate sensitivity (positive and with strain rate sensitivity coefficient almost constant) - flow stress increases with increasing strain rate (Ozturk et al. 2013);
- Low strain ratio – high difference between the ferrite and Martensite lead to relative poor SF and HE;

(Chatterjee 2017), (Tasan et al. 2015), (Rana and Singh 2016)

There are two common routes to produce DP steels used in the automotive industry - controlled cooling from the austenite phase (hot band products) and intercritical annealing (cold rolled products). The heat treatment underwent by each is illustrated in Figure 17.

- Hot Rolling (HotR) process – continuous casting slabs, reheating, rolling in rough mill, coil boxed, rolling in finishing mill, cooling in run-out table, coil boxed, and several intermediate surface cleansing stages;
- Cold Rolling (ColdR) in continuous annealing lines or batch annealing facilities – coiled steel, cold rolling, reheating (heating section/bell furnace), cooling (cooling section/cooling hood) and recoil boxed (for the continuous annealing line);

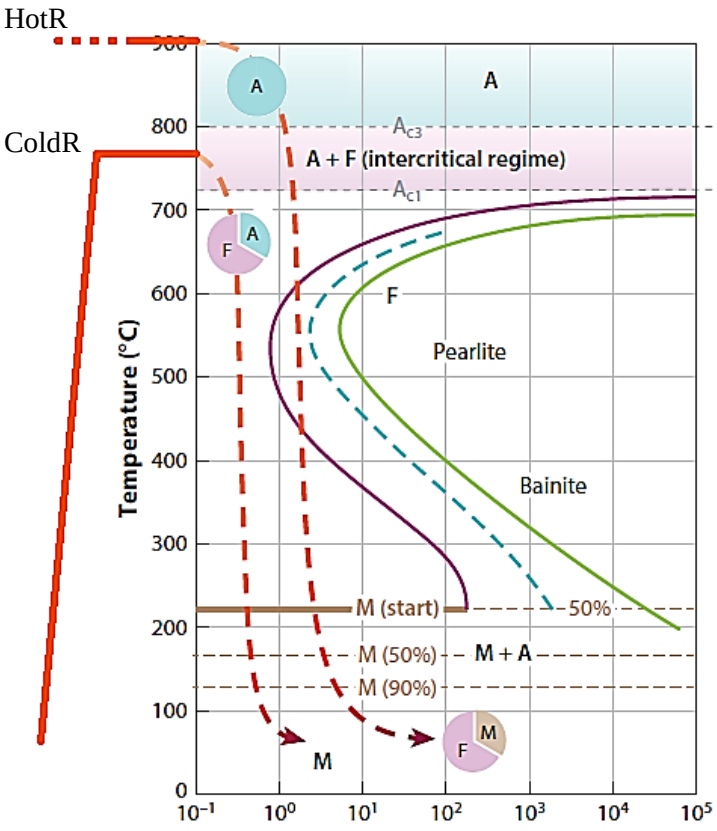

Figure 17- Heat treatment methods used to obtain DP steel by the two common processing routes (hot rolling and cold rolling). Adapted from (Tasan et al. 2015).

2.3 Research Background – Joining Magnesium to Steel

This subchapter tries to summarize the current known technologies successfully applied to produce dissimilar joints of Mg-steel, either by fusion welding or solid-state welding. Some particularly relevant results will be presented as well as some comparisons will be made. Regarding the less known (to the average college engineer student) and more advanced welding process, a brief explanation of the process will also be given. In this review, the author will mainly focus on the features of the chosen technology, which are:

- Geometry – spot joining technique. However, whenever a seam welding process is considered of relevance for the automotive industry, a brief mention will also be made;
- Nature – solid-state joining technique. However, since fusion welding is still the dominant process in the automotive industry, several fusion welding processes will be also explored. The most notorious absence was the laser and hybrid-laser welding technologies, which due to report length limitations weren't explored.

Other solid-state techniques successfully applied in dissimilar welding of Mg-steel, but with less applicability in the automotive industry, won't be discussed in this report, e.g. Diffusion Bonding – (Elthalabawy and Khan 2010), (Elthalabawy and Khan 2011), (Yuan et al. 2013); and Transient Liquid Phase (TLP) bonding – (Araki et al. 2011), (Koba et al. 2012), (Shuangming, Yang, and Jie 2016).

An ideal component should have a continuous construction without joints. The bonding point or edge of two or more workpieces is inevitably a source of mechanical performance reduction, and also insecurity for the designer. However, two main technological features inhibit the production of ideal single-part structures:

- Each primary process has size limitations, and geometric limitations in thickness and/or in shape – it might be easier or necessary to produce individual components - with compatible size, less complexity, and manufactured by the optimal process - and assemble them to produce the integral final structure;
- Multi-material structures with different alloys and even different materials in nature (metals, ceramics, polymers, composites), most of the times require some type of dissimilar joining technology[2].

In order to tackle the hot issue in the automotive industry of reducing Greenhouse emissions, continuous efforts are being made to develop technologies for improving powertrain efficiency (Manzie, Watson, and Halgamuge 2007) and for lightweighting the vehicle body (Schubert et al. 2001). Powertrain efficiency has an inescapable thermodynamic plateau, given by the ideal Carnot machine and illustrated in the Sankey diagram of internal combustion engine (ICE) of common passenger vehicles (Campbell 1985), (Milton 1995). The overall energy efficiency of mass-produced ICE for automobiles is below 40% (Gupta 2006). A possible approach is to change directly the source of energy from typical fossil fuel to electricity, biofuel, etc. However, these strategies have a predicted mass-implementation in the long term, and there are still debatable topics concerning them (Egbue and Long 2012), (Sovacool and Hirsh 2009), (Pleanjai, Gheewala, and Garivait 2007), (Escobar et al. 2009). In contrast, vehicle lightweighting approaches can benefit directly with the massive introduction of lightweight materials and designs. As the author tried to outline in chapter 2.1 and 2.2, both AHS Steels and casting Magnesium alloys are very good candidates to what concerns the automotive industry. Aspects like car weight reduction, crashworthiness and occupant safety, can be addressed simultaneously and/or individually by both materials.

Hybrid structures have the potential of bringing design freedom and structural optimization for the automotive industry. This can be translated in increasing the weight-to-strength structural performance of transportation vehicles. The simple introduction of these two materials is just the beginning stage of the process; the issue of joining Mg alloys to steel cannot be avoided if these two

[2] Joints made by two components constituted with either: different alloys (same base material), different metals, sheet thickness or surface conditions are designated by dissimilar joints. Contrariwise, joints made of sheets from the same alloy and with the same thickness, are called similar joints. (Sinha, Kundu, and Chatterjee 2016)

alloys ought to be applied in the same structures. Effective bonding technologies for Mg-Steel dissimilar joining, and techniques to control and/or predict galvanic corrosion, must be developed for hybrid structures to thrive. Figure 18 a) - b) and Figure 19 a) - c) illustrates several results from different projects involving the design and testing of Magnesium-steel hybrid structural concepts. Dissimilar welding was identified as a main priority in materials joining technologies by recent surveys conducted by the Joining and Welding Research Institute (JWRT) of Japan (Nakata and Ushio 2002) and the Edison Welding Institute (EWI) in the United States (Conrardy 2008) (Firouzdor and Kou 2009). Dissimilar joints between Al-Mg underwent great progress and research effort, systematized in (Liu, Ren, and Liu 2014), (Al-Zubaidy 2017), (Shah, Othman, and Gerlich 2018). Aluminum to steel welding also received great attention by the scientific community (Shah and Ishak 2014), (Wang et al. 2016), (Ding, Shen, and Gerlich 2017), (Suhuddin et al. 2017). The metallurgical nature of the Al-Fe and Al-Mg couples facilitates its welding. Both dissimilar combinations of Mg-Al and Al-steel form IMC's, bi-phase structures or solid solutions. However, the welding mechanism between Mg-Fe is different considering the multiple particularities of Mg and steel alloys. Thus, the ability to join Magnesium to steel (the most common metal in modern industry) is the key to widen the application of Magnesium alloys.

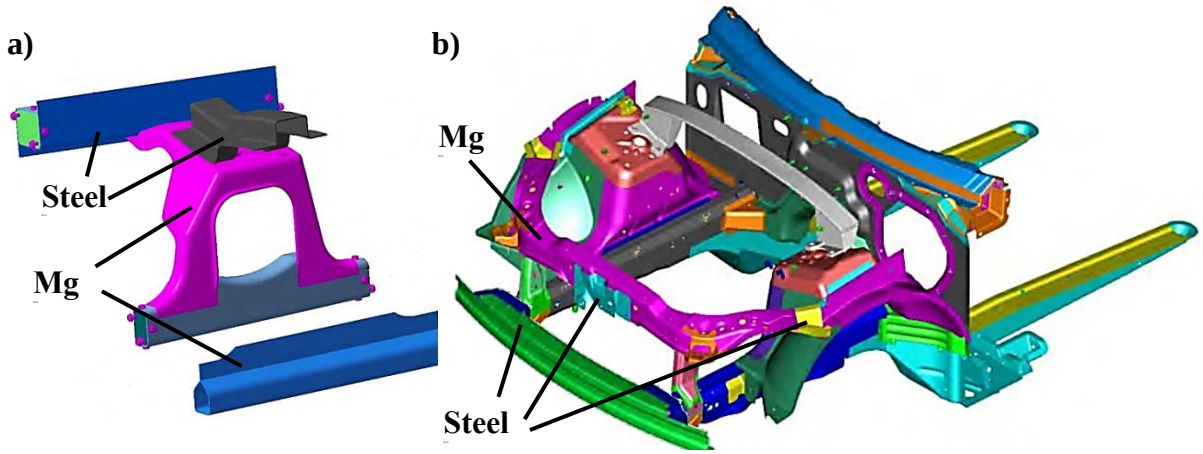

Figure 18- Results from the project "Development and demonstration of a Mg-intensive vehicle front-end substructure" that resorted on the Mg-steel hybrid material concept. a) Detail of shock tower; b) front end structure (Logan, Forsmark, and Osborne 2016).

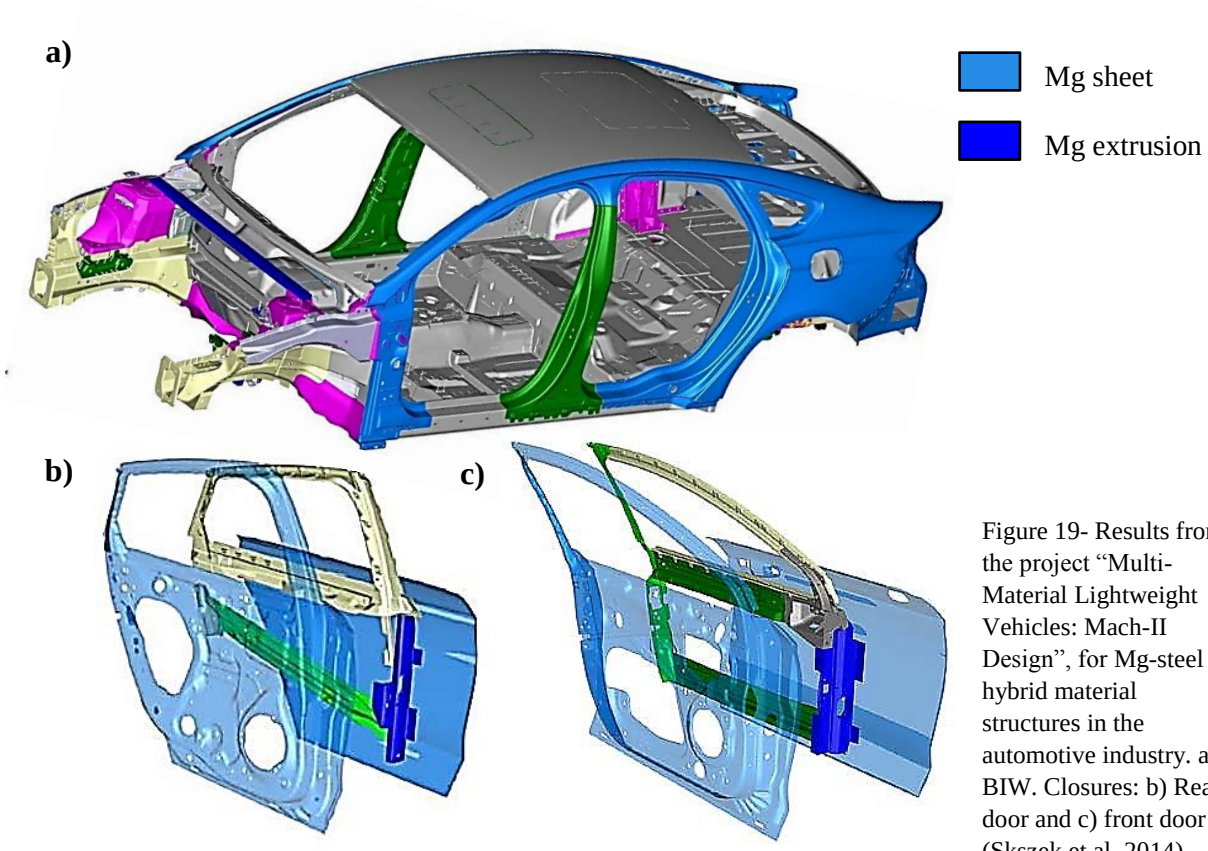

Figure 19- Results from the project "Multi-Material Lightweight Vehicles: Mach-II Design", for Mg-steel hybrid material structures in the automotive industry. a) BIW. Closures: b) Rear door and c) front door (Skszek et al. 2014).

The dissimilar welding of Mg-steel has some particularities that are also present in the similar welding of Mg-Mg joints. The Mg nature dictates that way. Magnesium welding requires taking generic cautions like:

- Low and controlled power input – Mg alloys have low melting and boiling temperature;
- High affinity with oxygen – 1) in liquid state, Mg welding requires shielding gases to protect the liquid weld from the environment atmosphere; 2) although in solid-state it also reacts with oxygen - forming a thermodynamically stable natural oxide layer on the Magnesium surface - it doesn't require shielding gases.

(Czerwinski 2011)

Fusion welding (FW) of Magnesium to steel is limited by two main reasons: high difference in physical, thermal, electrical, and chemical properties, and the nature of the Mg-Fe couple (metallurgical incompatibility), making it problematic to obtain strong bonding. Usually, conventional Fusion Welding processes are not applicable for producing dissimilar joints from these two materials. However, the feasibility of using advanced FW process was extensively studied. A brief summary of the properties differences previously outlined, and some consequences of those gaps are given in Table 10. The issue related to the nature of the binomial Mg-Fe is addressed in Table 11.

Table 10- Outline of the difference in thermal and electrical properties of Magnesium alloys and Steel, particularly the materials used in this experiment (DP600 and AM50A) (GrantaDesign 2017), (Liu 2010a).

Property	**DP600**	**AM50A**	**Related Problems**
Density [kg/m^3]	7800-7900	1800-1810	Immiscibility in the liquid state, hindering the wetting
Melting Point [ºC]	1420-1510	440-625	Loss of Mg element by evaporation Change of chemical composition in the weld zone Penetration of Mg into the grain boundaries
Thermal Conductivity [W/m.ºC]	42-50	61-63	Influence the thermal gradient and crystallization phenomenon - low melt wettability and grain coarsening
Specific Heat Capacity [J/kg.ºC]	447-500	1050-1060	Necessary using powerful heat source (High heat power)
Thermal Expansion Coefficient [μstrain/ºC]	11-13	25.9-26.2	Different stress states on each side of the bed/spot (residual stress) Micro-cracking at the interface of the HAZ and BM Low fatigue performance
Electrical Resistivity [μΩ.cm]	19-29	12.3-12.6	Difference in heat generation during Resistance Welding (RW) Formation of cracks, pores and segregation in the fusion zone if symmetric techniques are employed
Galvanic Potential [V]	(-0.51)–(-0.43)	(-1.61)–(-1.53)	Galvanic cell effect in the boundary between the two dissimilar metals Oxidation of Mg with formation of MgO brittle phase – fracture initiation site
Magnetic Type	Magnetic	Non-magnetic	Instability of electric arc in Arc Welding

Dissimilar metals can be divided into reactive and non-reactive couples. Reactive couples (such as Ti–Al, Fe–Al and Cu–Sn), form IMC layers at weld interfaces. Also called transition or bridge layer, they act as a buffer to accommodate the bonding between two dissimilar materials. Non-reactive couples, the bonding is ensured by solid solubility and multi-phases with high lattice-matching. Regarding solid solution, a good example is the couple Cu–Ni, two metals that are completely miscible in the entire mixture spectrum, and as a result of that, can be easily welded. Even immiscible metal elements under room temperature (Cu–Fe) can be welded due to small lattice mismatching between them. (Yao et al. 2012), (Liu et al. 2016). In addition to the difficult in forming solid-solutions (are mutually insoluble), and mixing in liquid state, Mg and steel do not react to form intermediate phases. As a direct conclusion from Table 10 and Table 11, the production of dissimilar Mg-steel (particularly in butt or T joints) by fusion welding techniques is rather cumbersome.

Table 11- Metallurgical properties of commercially pure Fe and Mg (Liu 2010a), (GrantaDesign 2017).

Property	**Fe**	**Mg**	**Related problem**
Atomic radius	126	160	Incompatible metallurgical parameters
Lattice type	*	HCP	High lattice mismatching
Lattice parameters	a=286.65	a=320.94 c=521.08	Mg and Fe are not mutually completely soluble in the liquid state
Solid Solubility [wt.%] **	0.00043	0	Almost impossible to form a solid solution from the two metals

* Lattice type change according to temperature and composition

** Solubility of the material in the heading of the column, in the other material

Throughout the present report, the bonding mechanisms will be classified in metallurgical and mechanical bonding. Depending on the degree of mechanical bonding, partial or full mechanical bonding can be observed. From a physics point of view, the metallurgical bonding can be achieved by different mechanisms illustrated in Figure 20 and listed below:

- Liquid-State welding – fusion welding in which both metals melt, forming a molten bath mixture of the two parent materials;
- Liquid/Solid-State welding – brazing (when a filler material is added); weld-brazing (products form the reaction between the two metals or with the coating interlayer partial liquefy during welding - usually forming new eutectic phases; or partial liquation of the coating); and soldering (in which the only difference for brazing is the melting point temperature of the third melted alloy that must be less than 450 ºC);
- Solid-State welding – solid-state diffusion leads to the formation of solid-solutions and/or IMC's.

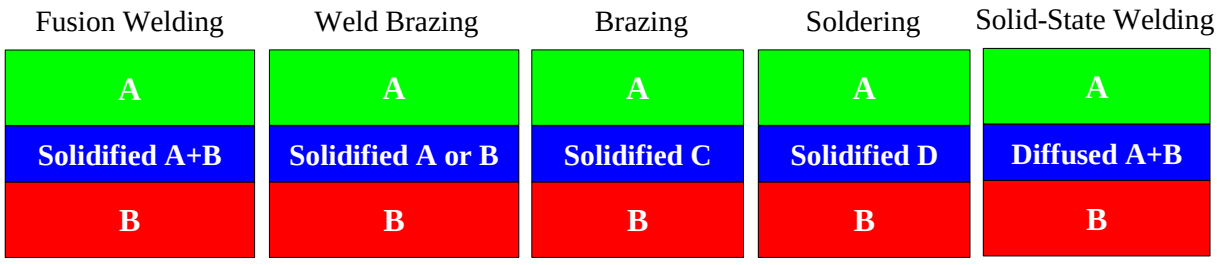

Figure 20- Illustration of the different mechanisms of metallurgical bonding.

2.3.1 Fusion Welding

Gas Metal Arc Welding (GMAW)

Gas Metal Arc Welding (GMAW), particularly Metal Inert Gas Welding (MIG), was also employed to join Magnesium to steel. This arc welding process was the object of some research that involved its individual application; in contrast with the Gas Tungsten Arc Welding (GTAW) or Tungsten Inert Gas (TIG) arc welding process that only saw its application combined with the Laser beam Welding (LBW) in a hybrid process (Liu and Zhao 2008), (Liu and Qi 2010), (Qi and Song 2010), (Zeng et al. 2011), (Tan et al. 2013), (Song et al. 2017), (Song et al. 2018). Table 12 summarizes the main arc welding process with different industrial applications. Regarding the automotive industry, GMAW is from the arc welding processes the most used (Teker 2013). Cold Metal Transfer (CMT) will also be briefly approached; however, it will be classified as a different process, and not as a variant. On the other hand, (Kah, Suoranta, and Martikainen 2013) described different advanced GMAW based processes, and CMT was classified as a technological improvement of the conventional GMAW.

Table 12- Summary of common arc welding process.

Arc Welding (AW)	Shielded Metal Arc Welding (SMAW)	
	Submerge Arc Welding (SAW)	
	Flux-Cored Arc Welding (FCAW)	
	Gas Metal Arc Welding (GMAW)	Metal Inert Gas (MIG)
		Metal Active Gas (MAG)
	Gas Tungsten Arc Welding (GTAW) or Tungsten Inert Gas (TIG)	
	Plasma Arc Welding (PAW)	

Regarding seam welding of Mg to steel, (Wang et al. 2015) and (Wang, Sun, and Sun 2016) studied the feasibility of dissimilar butt welding of these two metals. (Wang et al. 2015) studied the MIG welding of AZ31B to Q235 with different filler electrode wires (AZ31 and AZ61) in butt joint configuration. Two bonding mechanisms were observed in the butt joint, fusion welding of the Magnesium plate with the molten bath, and brazing in the steel side. Increasing the Al content of the bath (using AZ61 filler alloy), enabled the formation of a continuous transition reaction layer of Fe-Al IMC's. Hence, the better mechanical strength of the joint made with AZ61 filler material.

(Wang, Sun, and Sun 2016) studied the effect of using Cu interlayers of different thickness in MIG welding of AZ31B to Q235 mild steel, also in butt configuration. As stated previously by (Wang et al. 2015), the bonding mechanism was composed of fusion welding in the Mg side, and brazing in the steel surface. The optimum thickness was in the middle of the study space. For thickness over 0.2 mm, coarse eutectic Mg-Cu structures and ternary phases of Mg-Al-Cu were formed.

Spot welding feasibility of GMAW Mg to steel was first studied by (Ren and Liu 2014). They took a different arrangement to weld AZ31 Mg alloy to Q235 mild steel. In this technique, the upper part was the steel plate and a low carbon ER50-6 electrode wire was used. The effect of using a 0.1 mm thick pure Copper foil as interlayer was also studied. Without Cu interlayer, no successful weld joint was achieved, with almost null Lap Shear Strength (LSS). In the GMAW with Cu foil, the bonding region was made of two different mechanisms: middle region – where Mg and steel are bonded by a transition layer of ternary Al-Cu-Fe and binary Fe-Cu compounds, formed in the interface center and within the joint; and peripheral region – where the bonding mechanism was weld-brazing of Mg and steel by the Cu transition interlayer. Brittle fracture with interfacial mode was observed for all specimens during static lap shear test. Voids and cavities were observed at the center of the nugget. When compared with RSW of similar materials combination (Liu et al. 2016), the author suggests that the lack of welding time and pressure result in the unsuccessful direct GMAW spot of Mg-bare steel.

Cold Metal Transfer (CMT) Spot Welding

Cold Metal Transfer is a modified MIG process (Selvi, Vishvaksenan, and Rajasekar 2017). It is based on a short-circuiting technology that combines an innovative wire feed system and a high-speed digital control system. The beginning of the welding cycle is similar to a conventional MIG process. It can be divided into three main phases:

- Peak current – A high pulse current with constant voltage enables the arc ignition and heats the electrode wire, then a droplet starts to form;
- Background current – To prevent globular transfer mode, the current is decrease and kept constant until the droplet formed at the wire tip close the electric circuit;
- Short-circuiting phase – when the molted filler material dips into the weld pool the arc is extinguished and the voltage drops to zero. In this moment the feeding system applies a back-drawing force (triggered by the return signal) that helps in the metal transfer by liquid fracture.

Regarding CMT for seam welding, (Cao et al. 2013) first studied the feasibility of welding AZ31 to HDG Zn coated mild steel. The influence of different coating methods and compositions for the steel plate were studied by (Kang, Kim, and Kim 2017). Cold rolled bare steel, HDG steel, HDG steel with post annealing treatment (Galvannealed) and Aluminized steel were tested. Surprisingly, the dissimilar joints between AZ31 Mg alloy to bare steel and the Aluminized steel achieved the best mechanical performance. The better performance in static loading was attributed to a thinner and controlled Fe-Al IMC's layer developed for the bare and aluminized coating conditions. Weaker bonding between the Mg-Zn layer and Fe-Al IMC's and thicker coating layers are also advanced as a reason for the poorer LSS of dissimilar joints with HDG and the Galvannealed steel.

To the author knowledge, there is only one research work regarding CMT technology applied to spot welding. (Chen, Amirkhiz, and Zhang 2017) compared CMT spot welded AZ31 dissimilar joints to both Zn coated and Bare steel. A filler wire of AZ61 Mg alloy was used. The LSS was almost three times higher for the dissimilar joint with Zn coated steel (2.8 kN) when compared with bare steel (0.9 kN). In the first case, the Fe-Al layer formed during HDG probably melted during welding, indicated by the presence of ZnO in the fracture surface. Thus, the molten AZ61 reacted with the molted Fe-Al to form a nanoscale Al_2Fe continuous transition layer by diffusion of Al of both molted alloys to Fe surface. When Zn wasn't present, only discrete islands of Al_2 Fe formed. The absence of the Fe-Al melted film hindered the wetting of the steel surface by AZ61, decreasing the Al diffusion. This low diffusion process promoted the formation of Al_2Fe islands rather than the continuous layer formed when Zn coating is preset, hence its lower mechanical strength.

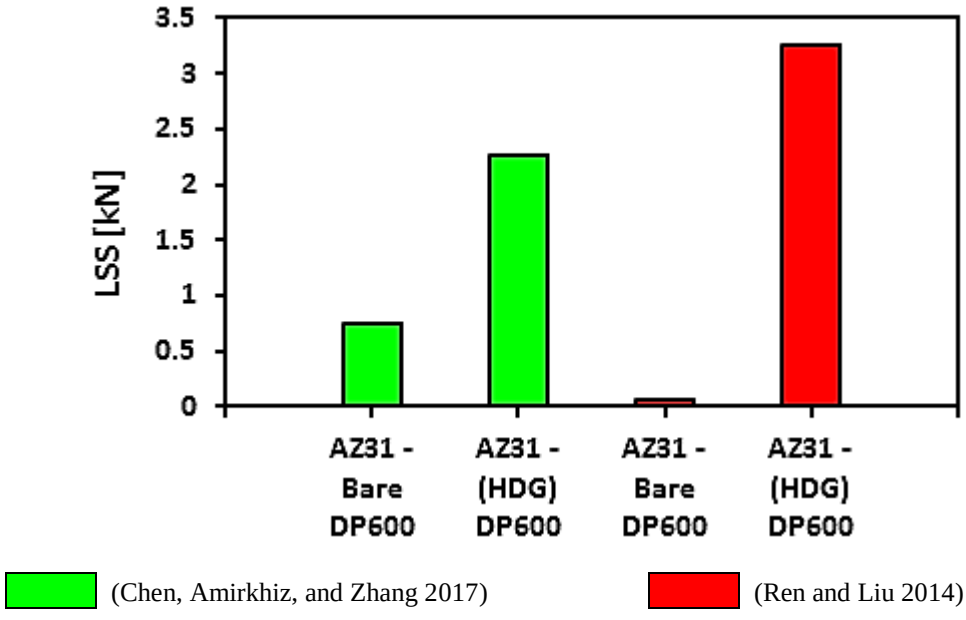

Figure 21- Lap shear strength for CMT and GMAW/MIG spot welding of Mg-steel dissimilar joints.

Resistance Spot Welding (RSW) and Resistance Spot WeldBonding (RSWB)

The mechanisms of Resistance Spot Welding (RSW) of Magnesium to steel were first studied by (Liu et al. 2010), using twin-roll strip cast AZ31B Mg alloy, and Hot-dip galvanized Zinc coated DP600 steel sheets. In order to promote electrode life and ensure weld strength (remove MgO surface oxides), the faying surfaces of the Mg coupons were treated with a solution of 2.5 %. (wt./vol.) Chromic acid. A relevant technological aspect must be noted. In order to balance the heating generation and its transfer, a domed electrode in the Mg side and a flat electrode against the steel surface were used. The maximum LSS achieved was around 5 kN for an increasing welding time. During lap shear test, all specimens failed in an interfacial failure mode, indicating a through the fusion zone crack propagation. The welding was accomplished by a combination of welding mechanisms: weld brazing combined with solid-state bonding in the middle region; in the periphery, only solid-state bonding was observed; and in the most outer region a soldering bonding by the molten Zinc and Zn-Mg phases (formed by the reaction between the Zinc coating and the Mg) allowed the mechanical sealing of the nugget. No melted regions were found in the steel plate.

In a further work, (Liu et al. 2011) studied the effect of a nanoscaled Fe_2Al_5 transition layer, coated onto the steel (Fe) plate surface. Hot-dip galvanized Zn coated DP600 steel was used. The free Zn and Zn–Fe layers from the as-received coating were removed by fuming nitric acid (HNO_3), leaving naked the Al–Fe IMC's layer. The goal was to improve the bonding by reducing the interfacial energy of the Fe and Mg immiscible phases. This was achieved by using the semi-coherent (with both surfaces) nanoscaled Fe_2Al_5 transition layer.

Surface treatment is very important for adhesive bonding of Mg, especially in bonding of Mg to other metals due to the corrosion behaviors (Liu 2010b), (Lazarz et al. 2009). There is only a small number of researches of purely adhesively bonded joints of Magnesium to steel (Lai and Pan 2014). The closest application of adhesives is in Resistance Spot Weld Bonding (RSWB) and Ultrasonic Spot Weld-Bonding (USWB) research fields. RSWB is a hybrid technique, very attractive to the automotive industry that combines Resistance Spot Welding (RSW) with Adhesive bonding.

The feasibility of the hybrid Resistance Spot Weld-Bonding (RSWB) process was first studied by (Xu et al. 2012). A comparison between the microstructure, static and dynamic mechanical properties of the RSWed and RSW-Bonded AZ31 Mg to Zn coated HSLA steel dissimilar joints were evaluated. A short study on the fatigue properties of RSWed joints of AZ31 Mg alloy to HDG Zn coated steel had already been done by (Miyamoto et al. 2012). (Xu et al. 2012) reported improvements (relative to RSW) in mechanical strength and energy absorption during lap shear test were achieved. In addition to the mechanical properties, the adhesive layer had a significant influence in the microstructure. During static lap shear test all specimens fractured at the interface, with an improvement from 5 kN (RSW) to 11.5 kN (RSWB) in the maximum carrying load. Fatigue load strength was also increased (roughly 2 times) by changing the failure mode from nugget (lower loads) and interface failure (higher loads), to mainly steel base material failure. The adhesive also decreased the cooling rate of the spot, allowing retaining the original microstructure of the steel sheet confirmed by the formation of $Mg_7 Zn_3$. In spite of the promising results, an extensive surface treatment and curing process was necessary. Both steel and Mg specimens were ultrasonically cleaned for 5 min in acetone. The faying surfaces of Mg plates were, prior to welding, cleaned with a solution of 2.5% (w/v) chromic acid to remove surface oxides. The post weld curing of the adhesive was at 180 ºC for 30 min. A more detailed fatigue studied regarding the same material combination was conducted by (Liu et al. 2013). SEM analysis of the fractured surfaced show crack initiation sites in the Mg-steel interface. Since the failure was in the Mg base material, this indicates that the crack propagation properties from the joint are better than the Mg base material.

Magnesium and bare steel was first studied by (Liu et al. 2016). Its feasibility and further comparison with Zn coated steel was also done. For that, two combinations of materials were used: commercial pure Mg to IF (Interstitial Free) mild steel, and AZ31 Mg alloy to Zn coated DP600 steel. In spite of the lower mechanical properties, a successful welding of Mg-bare steel was achieved. Since no intermetallic transition layer was present, to accommodate the bonding between the two immiscible metals, a new mechanism of dissimilar welding was unlocked. TEM analysis indicated that the bonding of bulk Mg and Fe grains was achieved by the formation of Mg nano grain layer with 100–200 nm thickness.

The first approach to welding Mg to Stainless Steel (SS) was studied by (Min, Yong, and Jie 2016). A different welding apparatus was used; AZ31B Mg alloy was welded to 443 Ferritic SS using a steel cover plate of the same material, Figure 1 a) from Annex E. In this low-heat input process, the heat is produced by resistance to the flow of localized current (from the workpieces and the interfaces). In the nugget zone interface, different bonding regions were observed: Mg wetting of steel, IMC's Fe-Al layer and Mg wetting the Fe-Al IMC's. Even though the feasibility was ensured, poor mechanical performance due to the presence of internal stresses that ultimately led to hot cracking.

Different coating methods for the steel were also studied. (Feng, Li, Luo, et al. 2016) studied the benefits of using a 0.6 mm thick HDG Q235 steel interlayer to weld AZ31 Mg alloy to Electro-galvanized (EG) DP600 steel. The benefits of using HDG Zn coating in steel plates dissimilar joints, aren't present when electro-plated Zn coating is used. The microstructure, static mechanical properties, and weld mechanisms were analyzed and compared for the RSW with and without the interlayer. In contrast to previous works, the steel melted forming a nugget in both sides (Mg and steel plate). The (EG) coating wasn't squeezed out in the initial stages of welding, and the soldered region reported in previous HDG Zn coated dissimilar joints, didn't form. With the addition of the HDG steel interlayer, the Zn coating was squeezed out of the nugget and a peripheral soldered region formed during welding. As already stated in this section, this soldered region creates a mechanical sealing that improves the solid-state bonding and braze-welding in the joint. Reasons why when an interlayer was used, the LSS increased by 32.6% and the energy absorption by 117.0%.

The feasibility of welding Mg-steel dissimilar joints by the novel Resistance Element Welding (REW) process was studied by (Manladan et al. 2017a). In addition to the novel REW process, the feasibility of welding Mg-austenitic SS was also studied. The process was first described by (Meschut, Janzen, and Olfermann 2014) and its feasibility to weld aluminium to steel was studied and compared with different solid-state process by (Meschut et al. 2014). The process is illustrated in Annex E, Figure 1 b)). The materials used were AZ31 Mg alloy and AISI 316L Austenitic Stainless Steel (ASS) coupons and a Q235 steel solid rivet was used in the REW process. Also, instead of the spherical electrode tip used for RSW, a conical tip was used in REW to decrease current density. As already reported in previous works, RSW of Mg-steel was accomplished by weld-brazing technique, in which only part of the Mg melts. In the case of REW spots, the fusion zone (FZ) was composed by two regions: a peripheral FZ on the ASS side, and the main FZ. The LSS was 63% higher and the maximum energy absorption was 9 times higher for the REW when comparing with the RSW. What correlates well with transition from interfacial failure (IF) to pull-out failure with increase in welding current, and general IF failure for RSW joints. To conclude the review of RSWed joints of Mg-Steel, a brief comparison of LSS achieved by different process is given in Figure 22.

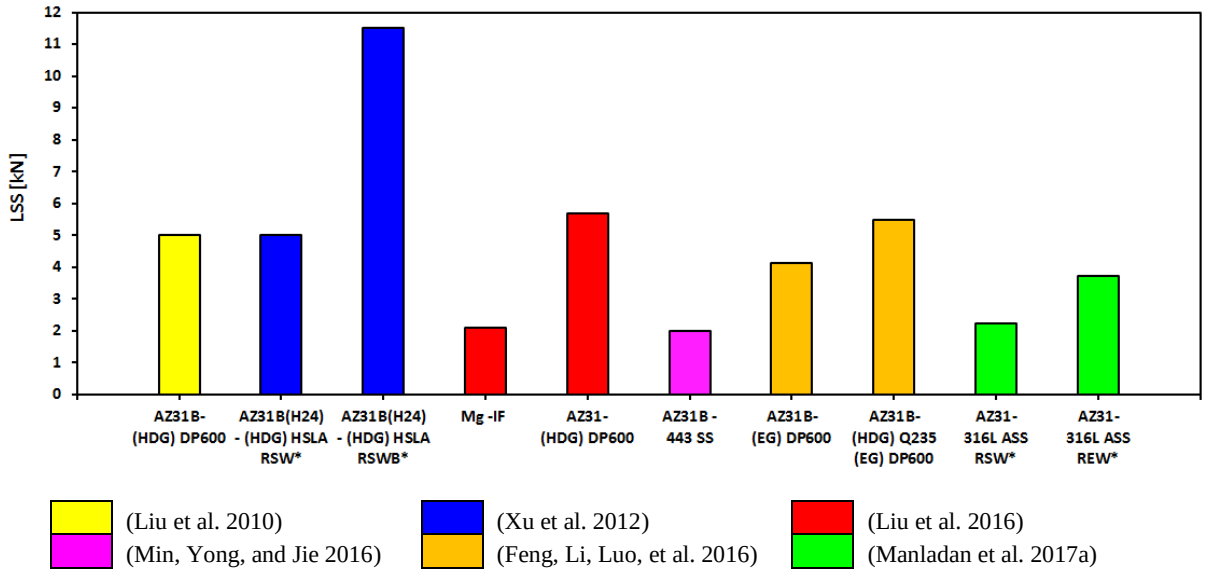

Figure 22- Lap shear strength for different material combinations of RSWed and RSWBed joints.

2.3.2 Solid State Welding

Friction Stir Welding

Friction Stir Welding (FSW) is a solid-state joining process, invented at The Welding Institute (TWI), UK, in 1991. It is capable of welding butt joints, T-joints, and also lap joints (penetration and fillet), sometimes referred as Friction Stir Lap Welding in that case. A non-consumable rotating tool is inserted into the gap between the two metal sheets (butt joint) or penetrating through the upper sheet (lap joint) and subsequently traversed along the joint line or overlap direction (Mishra and Mahoney 2007b). The rotating tool is made of a specially designed pin and shoulder. The process is illustrated in Figure 23.

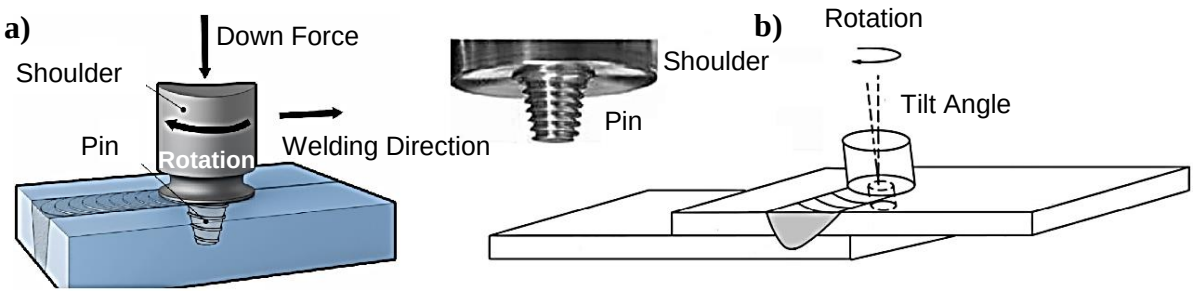

Figure 23- Illustration of the FSW process. a) Butt joint configuration; b) Lap joint by penetration (Fadaeifard et al. 2014), (Pasha et al. 2014), (Bergmark, Bergmark, and Eliasson 2015).

Several advantages are depicted in (Swarnkar et al. 2016), together with the influence of different welding parameters for Al alloys FSW. Tool design was extensively discussed in (Zhang et al. 2012). Different variants of friction stir technologies were extensively developed Bobbin Tool FSW (BT-FSW) – (Li, Fu, et al. 2014), Self-Reacting Bobbin Tool FSW (SRBT–FSW) – (Neumann 2009), Stationary Shoulder Bobbin Tool FSW (SSBT-FSW) – (Hilgert 2012), Semi-Stationary Shoulder Bobbin Tool FSW (SSSBT-FSW or S3BT-FSW) – (Goebel et al. 2017); Stationary Shoulder FSW – (Martin, Stanhope, and Gascoyne 2011); Self-Support FSW – (Huang et al. 2013).

The feasibility of welding Magnesium to steel was first studied by (Watanabe et al. 2006). In butt joint configuration, AZ31 was welded to SS400 mild steel by FSW. They employed a pin offset technique toward the steel (closer to the Mg side). Ignition of Mg was observed for higher rotation speeds and scattering of steel fragments for higher offsets.

The weldability and effect of Zinc coating in the steel plate was first studied by (Nakata 2009). FSWed lap joints were produced by welding AZ31 to Zn coated steel. (Chen and Nakata 2009) and (Chen and Nakata 2010) further studied the influence of welding parameters in two different coating conditions for the steel. Magnesium AZ31 alloy was lap welded to bare (brushed finish) and Zn coated mild. The effect of different Zn coating process on the mechanical performance and microstructure of FSWed joints were studied by (Jana, Hovanski, and Grant 2010). For that, AZ31B Mg alloy was welded to both HDG Zn coated steel and Electro-galvanized (EG) Zn coated steel. Superior lap shear strength was achieved by with the HDG coating.

(Schneider et al. 2011) demonstrated that the mechanical interlocking, achieved by plunging through the AZ31B Mg alloy into the Zn coated steel, could enhance mechanical strength. Similar results were achieved by (Wei et al. 2012). They studied the feasibility of FSW of SUS302 Stainless Steel (SS) to AZ31 Mg alloy. A different tool design was used, with a cutting pin of rotary burr. It enabled to produce bonding mechanisms of nail effect in a millimeter scale and saw-tooth structure of zipper effect in micron scale. The fatigue behavior of AZ31 to Zn coated HSLA and mild steel was studied by (Jana and Hovanski 2012). Lap joint configuration with Mg on top was used.

By looking at the Mg alloy series alloyed mainly to Al (AZ, AM, AS, AE, AJ), one can say that Al is one of the most popular alloying elements for Mg. Thus, (Kasai, Morisada, and Fujii 2015) studied the influence of the Al content of the Mg alloy in dissimilar FSWed joints. All fractures occurred in the Mg side. The LSS increased with the increasing Al content of the Mg alloy, because it could accommodate the depletion of Al at the Mg side near the interface (consumed in the formation of Fe–Al IMC's layer).

Ultrasonic Spot Welding (USW) and Ultrasonic Spot Weldbonding (USWB)

Ultrasonic Spot Welding (USW) can be defined as a solid-state joining process whereby materials are held together under pressure (by a normal force), at the same time a high-frequency shear vibration is applied by the sonotrode tip (Horn in the USA) (Al-Sarraf and Lucas 2012). . A typical lateral ultrasonic system is illustrated in Figure 24.

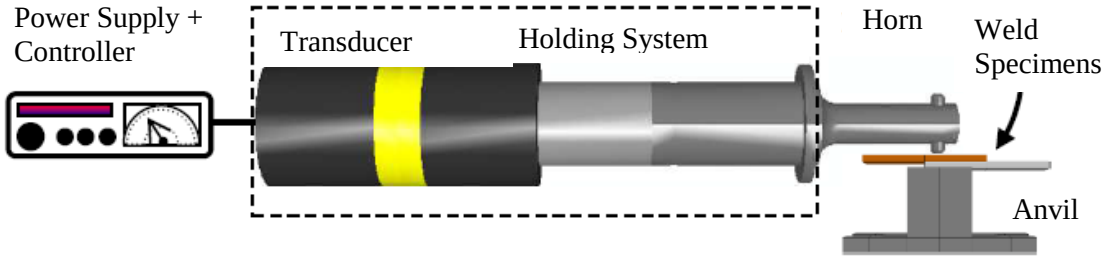

Figure 24- Illustration of a typical ultrasonic spot welding system. The horn is tuned to operate in the longitudinal mode (Al-Sarraf and Lucas 2012).

The weld joining is achieved by vibration deformation and shearing. The oscillatory movement also flattens surface asperities (increasing the contact area), and scatters interstitial oxides and contaminants. The first soldering applications, evolved to give rise to welding of polymers, softer and harder metals and a wide combination of dissimilar metals and materials (metals-polymers, metals composites, etc.), (Ahmed 2005). The weldbonding concept in RSW, already with some industrial applications, can also be applied to USW (Feng, Li, Zhao, et al. 2016).

(Pan et al. 2010) performed ultrasonic spot welds between sheets of 0.8-mm-thick hot-dip-galvanized mild steel and 1.6-mm-thick AZ31B-H2, with sonotrode engaged to the Mg plate. Lap-shear strengths of 3.0-4.2 kN were achieved with weld times of 0.3-1.2 s. The Zn coating was essential to the bonding mechanism, since when it was removed from the steel surface the joint bonding proved to be significant weaker. The temperatures at the AZ31-steel interfaces reached at least 344 °C in less than 0.3 s, these conditions promoted chemical reactions between Magnesium alloy and the Zn coating. Some of the authors further continue this study in (Pan and Santella 2012b), with the same material combination but with the sonotrode engaging steel specimen. The joint strength was similar, reaching over 4.2 kN at 1.8 s welding time. Mg-Zn eutectic structures at the interface ensured metallurgical bonding. The process was shown to be insensitive to metal arrangement of either the AZ31 or steel engaged with the sonotrode.

The eutectic reaction and the interfacial welding mechanisms were further studied in (Santella et al. 2012) and (Patel, Bhole, and Chen 2013). According to (Santella et al. 2012) during USW two Mg-Zn layers at the interface of AZ31B-HDG Zn coated steel was formed. The 9 µm was replaced by a 22 µm relatively uniform double layer formed in 0.3 s. Both layers were at least partially melted. During static lap shear test the facture propagated through the Mg sheet (0.5 s). For greater welding times, about 1 s, Mg–Zn phases were completely squeezed from the spot weld region, remaining only an Al_5 Fe_2 intermediate layer. Since the fractured also propagated through the AZ31 sheet, the metallurgical bonding strength of the joint can be attributed to this layer. (Patel, Bhole, and Chen 2013) identified a thin IMC layer in the Mg side and a pure Zn layer in the steel side during USW of also AZ31B-H24 to Zn coated HSLA steel. Due to plastic deformation induced by the vibration, the basal plane aligned in the interface direction. The strengthening of the basal texture was observed by texture analysis.

The effect of an interlayer were studied later by (Patel, Chen, and Bhole 2014). Sound dissimilar lap joints were achieved via ultrasonic spot welding (USW). The addition of Sn interlayer during USW effectively blocked the formation of brittle Al_{12} Mg_{17} intermetallic compound in the Mg-Al dissimilar joints without interlayer, and led to the presence of a distinctive composite-like Sn and Mg_2Sn eutectic structure. The lap shear strength of the joints with a Sn interlayer was significantly higher than that of the corresponding dissimilar joints without interlayer. During static test, two different fracture modes were observed in the Mg-HSLA steel dissimilar joints: partial cohesive failure, and partial nugget pull-out. The lap shear results are compared in Figure 25.

The fatigue behavior of Magnesium to steel joints was also studied by (Franklin et al. 2011) in USW, and by (Lai et al. 2013) and (Lai and Pan 2015) in USWB. According to (Franklin et al. 2011), the dissimilar joints from AZ31B-H24 and Hot-dip Galvanized (HDG) Zn coated mild steel failed mainly from kinked fatigue growth through the Mg sheet. Transversal do other material combinations and spot welding process, the failure mode changed from partial nugget pullout mode (low-cycle loading) to transverse crack growth mode (high-cycle loading). Closed-form stress intensity factor and even a structural stress model based on the closed-form structural solution and the stress-life data was developed. Ultrasonic spot welded, adhesive-bonded, and weld-bonded lap-shear specimens were made to study the effect of the adhesive in joints of the same material (Lai et al. 2013), (Lai and Pan 2015). In spite of the change in the failure mode, no significant variation was reported in the quasi-static and fatigue strengths of adhesive-bonded and weld-bonded lap-shear specimens. (Franklin 2013) in partnership with some of the authors developed closed-form stress intensity factors and a kinked crack growth life estimation model. For that, finite element methods, analytical solutions and experimental data to corroborate the results were used.

Galvanic corrosion in dissimilar metal joints is physically inevitable, however not properly quantified. (Pan and Santella 2012c) and (Pan and Santella 2012a) studied the corrosion of ultrasonic spot welded joints of Magnesium alloy to galvanized steel, in lap joint configuration. No specific corrosion protection was applied in order to study worst-case conditions for corrosion behavior. To assess corrosion behavior, the Ford Arizona Proving Ground Equivalent (APGE) (Blanchard et al. 2016) corrosion automotive cyclically test was used. This corrosion test includes three different cycles, namely salt bath dipping, air drying, and then holding in constant humidity environment. A linear decreasing relation between lap-shear strength of the joints and the exposure cycles was observed. The corrosion of the AZ31 was localized and non-uniform. The most severe corrosion occurred not at the intersection of AZ31 and the steel but rather 15-20 mm away from the spot welds, which indicates good corrosion properties of the spot. In further works of (Pan et al. 2013) and (Pan et al. 2014), the feasibility of USWB of Magnesium to steel and the corrosion behavior of its joints was studied. For that, Ford L-467 automotive cyclic corrosion test (NaCl less concentrated and lower times for each stage). Lap shear strengths of 1.3 kN (with 1.8 s) and 6.4 kN were achieved in prior to cure (pasty) and cured state respectively. The strength was relatively independent of the welding time (load carried essentially by the adhesive).

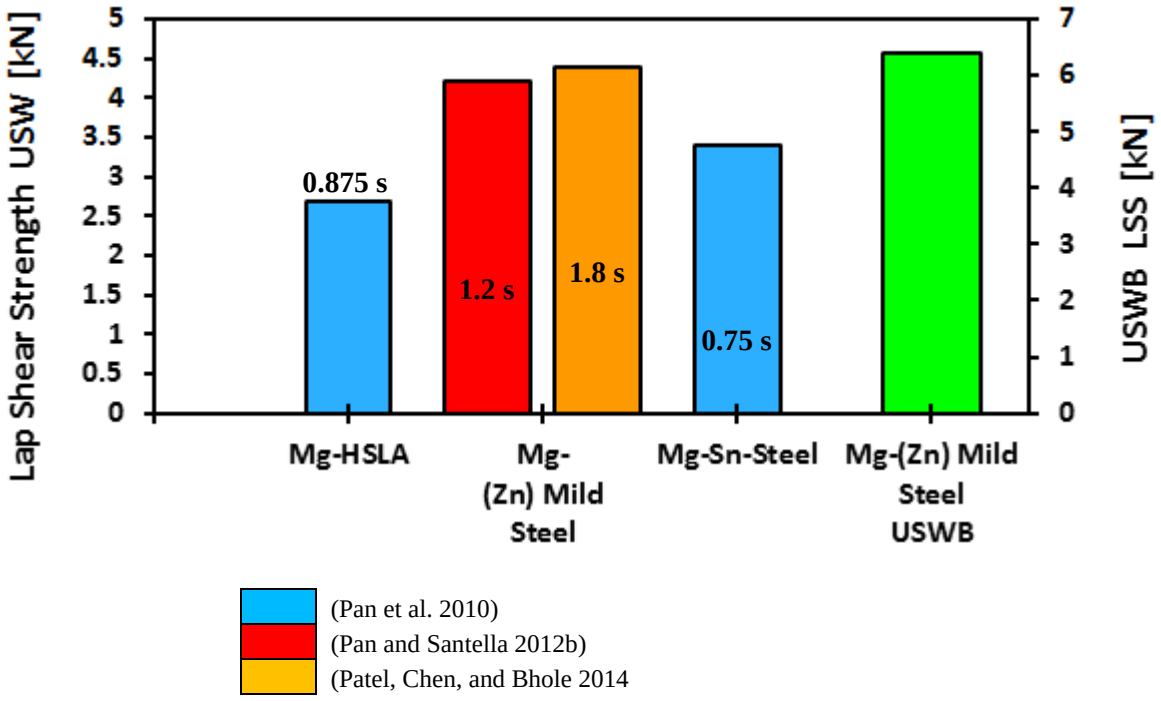

Figure 25- Lap shear strength data collected from the literature of different joints produced by Ultrasonic Spot Welding and Ultrasonic Spot WeldBonding.

Friction Stir Spot Welding (FSSW) based technologies

Conventional FSSW was invented by Mazda Motor Corporation in 1993 (Fujimoto et al. 2001), to replace common spot joining process like Resistance Spot Welding (RSW) and mechanical fastening. Technologies like FSW and FSSW received considerable attention from the automotive, aerospace, aeronautics, and generally in-white industries[3]. According to (Fanelli, Vivio, and Vullo 2012), it is in part due to the increasing use of the hard-to-weld lightweight Aluminum and Magnesium alloys. Whereas traditional fusion welding (FW), Resistance Welding (RW) and Resistance Spot Welding (RSW) technologies can't response properly to the task, FSW and FSSW manage to do so. Not only lightweight alloys like Aluminum and Magnesium brought new welding challenges. Since the High Strength Low Alloy steels (HSLA), to the different generations of Advanced High Strength Steel (AHSS), high strength steels underwent profound evolutions. RSW achieved poor results in welding AHSS of different grades and thickness, features that are increasingly common in the automotive industry. This led to a growing number of projects with the aim of applying this technique in similar and dissimilar (both in thickness and material) welding of AHSS. Some authors, such as (Buffa, Fratini, and Piacentini 2008) also state as a critical advantage of these two solid state welding techniques is their ability to weld sheets of different materials.

(Tamarelli 2011)

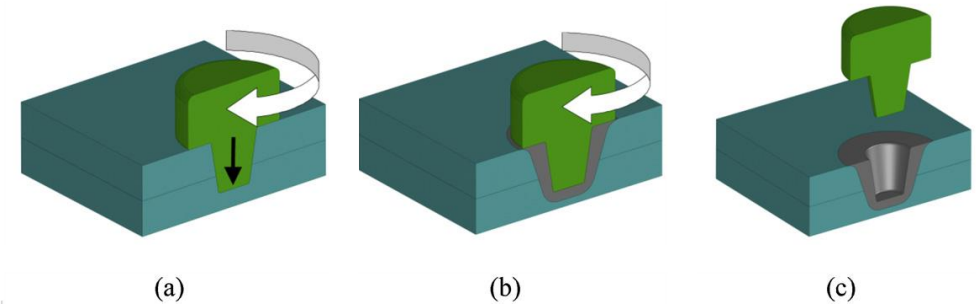

Figure 26- Different stages of FSSW: a) Plunging, b) Stirring, c) Retracting (Tier et al. 2013).

FSSW process is divided in three main stages, Figure 26 a) - c): Plunging – the spinning tool is plunged into the workpiece; Stirring – the rotating tool stays at a fixed vertical position (can occur a small displacement for welding machines with force control mode) for an certain dwell time and a metal flow is achieved by the frictional heat that softens the material; Retracting – .the tool is retracted leaving a keyhole in the center of the spot (Arul et al. 2008). In order to overcome the main drawback represented by the keyhole, different refilling techniques were proposed and continue to be proposed until now. Refill Friction Stir Spot Welding (Refill-FSSW) was the only one that thrived and for that reason, is the technique used in the present report. In Annex F the author tries to summarize the different refilling techniques that emerged throughout the years in literature. The author tried to gather as much techniques as he could find. If some particular technology wasn't mentioned, it definitely does not mean that it is not worth mentioning, but the simply that the author didn't have the ability to find it. A final comparison with all results documented in this section is done in Figure 27.

(Liyanage et al. 2009) studied the feasibility of FSSWed joints of AM60 / DP600 steel. The lap joints were produced with AM60 as the upper sheet. Unsatisfactory results were observed when steel was the upper sheet, it resulted in a cutting operation rather than a spot welding operation. Mechanical bonding was achieved by steel clinching resulting from the upward extrusion of steel material. No evidence of intermetallic formation was shown, and removing the Zn coating was advanced as a possible approach to avoid the cracking. Since the tool penetrated the lower steel sheet, significant wear of the W–25Re tool was also observed, Tungsten rich particles from the powder sintered tool were entrapped in both AM60 and DP600.

[3] In-white refer to the stage of a structural product before the painting and assembling of non-structural subsystems (power-train, trim components, etc.). Commonly used as body-in-white in the automotive industry.

The feasibility of FSSW AZ31B to Zn coated DP600 steel was studied by (Wang, Zhang, et al. 2011). A novel designed pinless tool was used to join the Mg (as upper sheet) to steel (as lower sheet) in a lap joint configuration. Taguchi orthogonal method was used to study the effects of rotation speed, plunge depth, shoulder diameter and welding time. Welding time and rotation speed came out to be the most significant ones. From SEM and composition analysis it was stated that LSS of the joint significantly depended on the extent of diffusion between Zn and Mg. A thin layer in the MG-steel interface accommodated the weld. Non-pin inserting FSSW of AZ31B to Zn coated DP600 was further studied by (Wang, Wu, et al. 2013). Only rotation speed was study, with the remaining welding parameters kept the same. But this time, a lap joint configuration with the steel plate as upper sheet was used. Metallurgical bonding was achieved by Mg-Zn reaction phases from the Zn coating. Interfacial fracture in cleavage mode was observed with SEM analysis.

(Wang, Li, and Zhao 2014), based on the optimization results from (Wang et al. 2012), studied the bonding mechanisms and microstructure in the FSSW of AZ31B to Zn coated DP600 steel without keyhole. A lap joint configuration was adopted, in which the steel plate is over the Mg plate. Both mechanical and metallurgical was observed. Main bonding achieved mechanically by steel "nail" embedding into the Mg with complete mixed between the two. Different compound and phases such as Fe-Al, Mg-Al and Mg-Zn ensured metallurgical bonding. Also using a variant without keyhole of FSSW, Friction Stir without Keyhole Spot Welding FSKSW), was applied to weld AZ31B Mg alloy to Zn coated Q235 mild steel by (Zhang et al. 2014). In lap joint configuration, the stacking sequence was studied (Mg over steel and steel over Mg). A tool made of WC−Co alloy and produced by powder metallurgy was used to be able to plunge the steel sheet without severe wear. The design of experiments was used to optimize the pin diameter, rotation speed and shoulder plunge depth. Pin diameter was found to be the most influential process parameter. Main mechanical bonding (fully stirring of Mg and steel) was complemented with metallurgical bonding confirmed by the presence of IMC's in the MG-steel interface.

(Liyanage et al. 2014) studied the feasibility of welding AM60 Mg alloy to DP600 Zn coated steel by using conventional FSSW. A tool made of W-25Re alloy with a 10 mm diameter shoulder and a 4 mm diameter pin of 1.6 mm length was used in the study. The Mg plate was the upper sheet, however significant wear of the tool was observed. Mechanical bond was achieved by extruding the steel of the lower sheet into the upper AM60 sheet. The LSS increased with increasing rotation speed and welding time. Metallurgical bonding was verified by the presence of melted αMg + Mg-Zn eutectic. The eutectic structures weren't close nor aligned to the initiation site, fractures always occurred through the AM60 upper sheet. Thus, Zn coating did not influence fracture propagation.

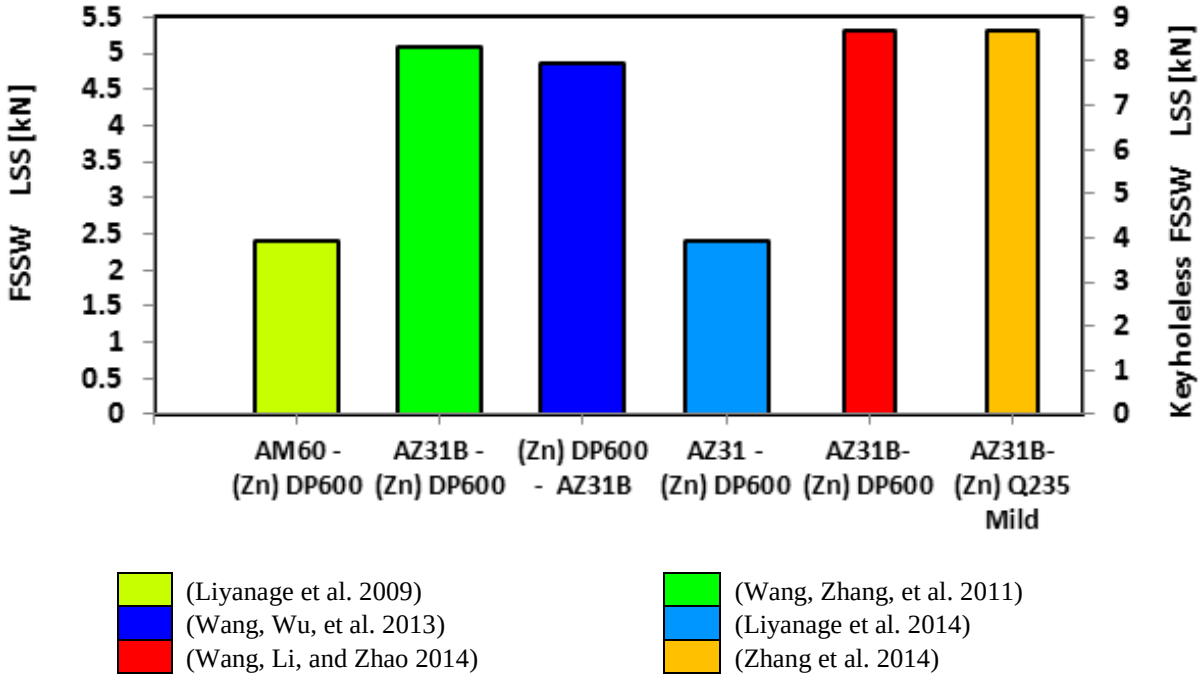

Figure 27- Lap shear strength for different material combinations welded by FSSW and Keyholeless FSSW.

2.4 Refill Friction Stir Spot Welding

2.4.1 General Overview and Historic Introduction

Friction Spot Welding (FSpW) is a solid-state joining process for spot welding in lap joint configuration of structural or non-structural components. It was developed in 1999 by *Helmholtz-Zentrum Geesthacht Forschungszentrum* (HZG), formerly GKSS, Germany (Gonçalves et al. 2016). The technique is described in the 2004 US Patent 6,722,556 B2 (Schilling and dos Santos 2004), (Mishra and Mahoney 2007a). The original name was kept in numerous published works, from German and particularly from HZG researchers. Currently, is more commonly referred by the international scientific community as Refill Friction Stir Spot Welding (Refill FSSW or Refill-FSSW), name and acronym candidates in best place to be standardized. Possible also used acronyms are RFSSW (Shen et al. 2013) or FSSW-R (Tier et al. 2013). In order to avoid further misconceptions, hereinafter it will only be referred as Refill Friction Stir Spot Welding (Refill-FSSW). Born in the development line of Friction Stir Spot Welding (FSSW) and initially considered as a refilling technique of the original process, can now be searched as an independent process in the technical literature (Yang, Fu, and Li 2014). Refill-FSSW has several features and generic advantages inherent to its solid-state nature. Similar to USW, FSW and FSSW, Refill-FSSW overall features are (Mishra and Ma 2005), (Mishra, De, and Kumar 2014), (Kubit et al. 2018), (Suhuddin et al. 2013):

- Ecologic and "Green" – reduces material waste by using a non-consumable tool, exempting the use of electrodes, fluxes, filler material, shielding/cover gases, and interlayers. It has also high energy efficiency (low heat input so less energy consumption) than fusion spot welding processes (Amancio-Filho, Camillo, et al. 2011);
- Safe and user friendly – there are no production of harmful and toxic fumes or vapors, no liberation of gases during welding, no spatter of molten material nor radiation emissions;
- Versatile – is capable of welding dissimilar material, dissimilar metals and/or coated metal sheets joints (Anodized, Chromate conversion coatings, HDG, etc.) (Ding, Shen, and Gerlich 2017). In addition, it can be used in hybrid technologies with adhesives (part of a project from HZG partnered with Ford Motor Company®) or with faying sealants (Kubit, Wydrzynski, and Trzepiecinski 2018). Also, a single tooling set-up can join a wide range of metal sheet thicknesses and material combinations, being able to weld nearby spots due to low heat input;
- No addition of third bodies (nut- screw/bolt system, riveting, clinching, self-piercing riveting, etc.) and no addition of filler material – there are no weight penalty, and no surface modification, since a flat spot weld without keyhole is obtained i.e. the weld do not protrude the original surface. Thus, there are no need to accommodate additional geometric features, e.g. weld bed, rivet or screw head, etc., relevant for design, drag, and fatigue purposes. It also reduces the cost and corrosion potential, eliminating the usage of sealants isolators (necessary in mechanical joints), and finally reduces deburring and other final operations;
- Low production cost technique high production rate – has lower non-recurring assembly costs such as tooling, tool wear and maintenance; and lower operational costs (lower energy consumption) when compared to RSW and other FW techniques (Hancock 2004). It has also high automation capacity, low welding cycle, and reduces the number of activities in the assembly line (particularly pre-cleaning and post weld activities) (Suhuddin et al. 2013);
- Enhanced Mechanical Properties – since there is no solidification involved (the materials do not melt during the procedure), defects typical from fusion welding process (cold cracking, hot cracking, liquation cracking, inclusions, gas inclusions, porosity, element segregation, etc.) are avoided, thin IMC's growth is controlled (brittle phases) (Olson et al. 1993), and reduced SCF (mechanical fastening introduces material discontinuities that are preferential sites for crack initiation and are particularly critical for long fiber composites).

Compared to the variations of FSSW mentioned in section 2.3.2 and Annex F, Refill-FSSW has several advantages mirrored in its clear domain in terms of research effort. The welding time is a lot shorter than the other refilling procedures (is a single process with multiple stages), and since it uses a single tool, makes it suitable for high-automation demand applications with industrial robots. However,

some drawbacks when compared with the well rooted FSSW process delayed its industrial implementation. The fabrication of the welding tool is costly and more complex, which present difficulties in implementing high wear-resistance materials. Additionally, implementing the process requires a dedicated machine, which should be able to handle several independent linear and rotation movements. Virtually, all applications where FSSW broke through, Refill-FSSW is equally or more competitive. Aircraft fuselage (stringer to skin) and automotive body panels are some of the applications for which joining thin section aluminium components using Refill-FSSW can be used. In addition, several dissimilar joining concepts are being developed and implemented in both aeronautics and automotive industry, as illustrated in Figure 28 a) - f).

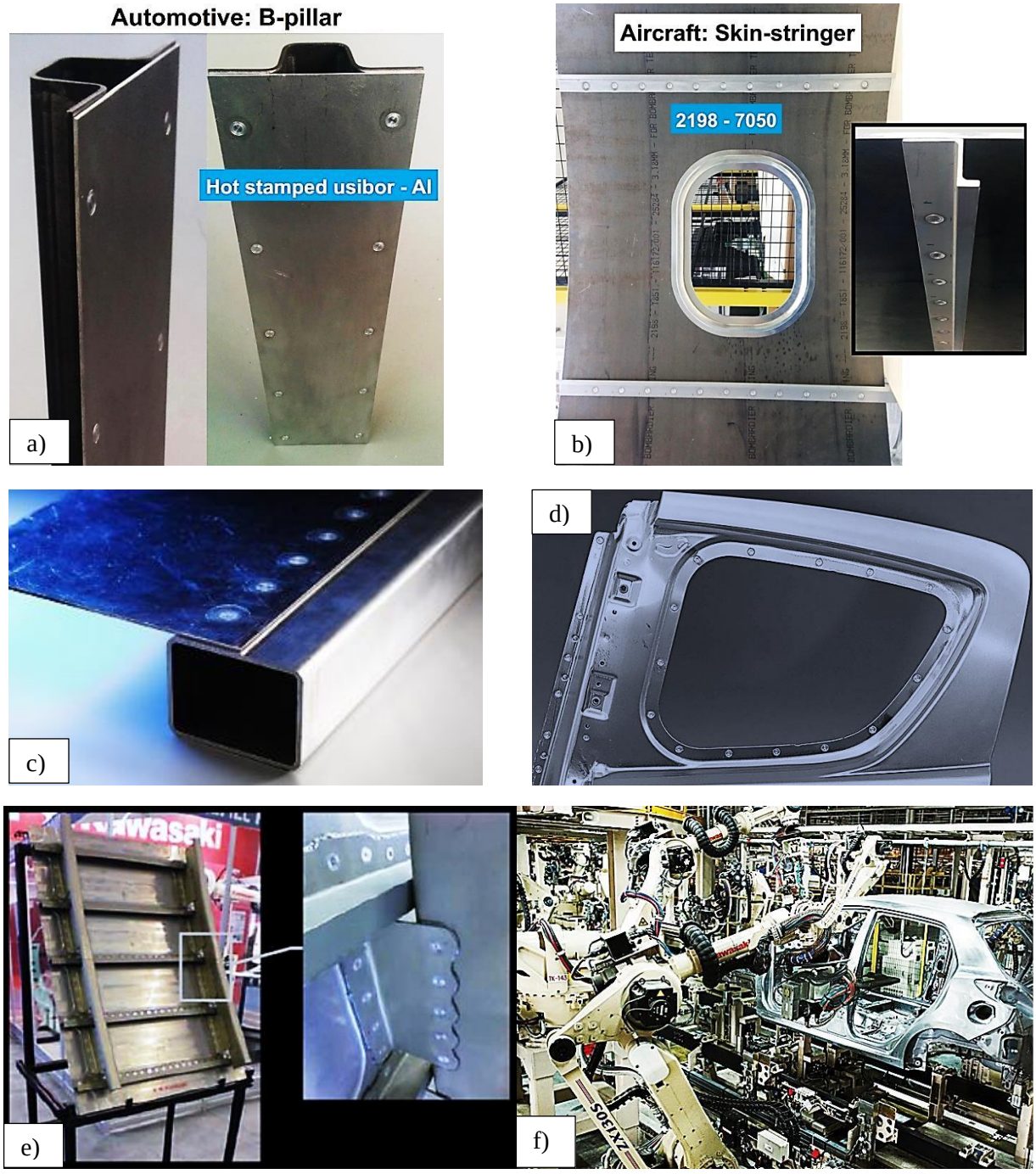

Figure 28- a) B-pillar prototype produced by Refill-FSSW of dissimilar welding between hot-stamped steel and Al. b) Example of aeronautics application of Refill-FSSW to replace the use of rivets in the aircraft fuselage. c) Part of BMW 5 series model (Kolba 2016). d) Part of door from the R8 Mazda model showing several FSSW joints. e) Applications of Refill-FSSW in aeronautics (TWI 2017). f) Assembly line of Mazda showing the FSSW robots (Sprovieri 2016).

2.4.2 Working Principles, Tool and Machinery

In Refill Friction Stir Spot Welding (Refill-FSSW) at least two similar or dissimilar sheets of materials are joined in lap configuration (Suhuddin et al. 2013). Similar to FSSW, this technology relies on the localized forging at the spot. Heat generation has two main sources: friction between sleeve/probe surfaces and plasticized material, and plastic deformation of the stirred material. The Refill-FSSW tool or stirring head is a non-consumable rotating tool, consisting of two rotating independent parts (at constant speed) - probe and sleeve; and one stationary element - clamping ring. This three-piece tool system illustrated in Figure 31, is more complex than the FSSW tool since each part should move independently in the vertical axis. Throughout the development of Refill-FSSW, a wide number of process variants appeared (Rosendo et al. 2011), these can be classified as illustrated in Table 13.

Table 13- Schematic representation of the different variations of the Refill-FSSW process, regarding the plunging component and the relative rotation. Virtually, there are four combinations of different process configurations.

Refill-FSSW	Plunging Element	Sleeve Plunge
		Probe Plunge
	Relative Rotation	Conventional rotation (CR Refill-FSSW)
		Differential Rotation (DR Refill-FSSW)

Contingent upon which part of the tool set is the plunging element, the process can be divided into two variants or cycles: sleeve plunge and probe plunge. The probe plunge variant of Refill-FSSW, requires less torque, plunge force and power consumption. However, the sleeve plunge variant is often used. It enables larger weld areas, enhancing the joint mechanical properties (Shen, Hou, et al. 2016). Thus, it was the process used in the experimental work described in this report and most of the times the mention to this variant will be omitted (typical in the literature). The description of each step will be made considering the possibility of using the two variants, so the superscript $^{I)}$ refers to sleeve plunge, and $^{II)}$ to probe plunge variant. The two variants are illustrated in Figure 29 and are essentially a six step processes (Suhuddin et al. 2014): 1) preparation stage in which a downward fixing force on the overlapped sheets is executed by the clamp (not illustrated); 2) downward movement of both probe and sleeve simultaneously to the surface of the top sheet, and generation of friction-heating by rotational movement of both probe and sleeve bottom surface, with constant angular velocity and for a certain dwell time; 3) first extrusion with plunge movement of the sleeve $^{I)}$ / probe $^{II)}$ and simultaneous retracting movement of the probe $^{I)}$ / sleeve $^{II)}$ to create a cavity/chamber for where the displaced

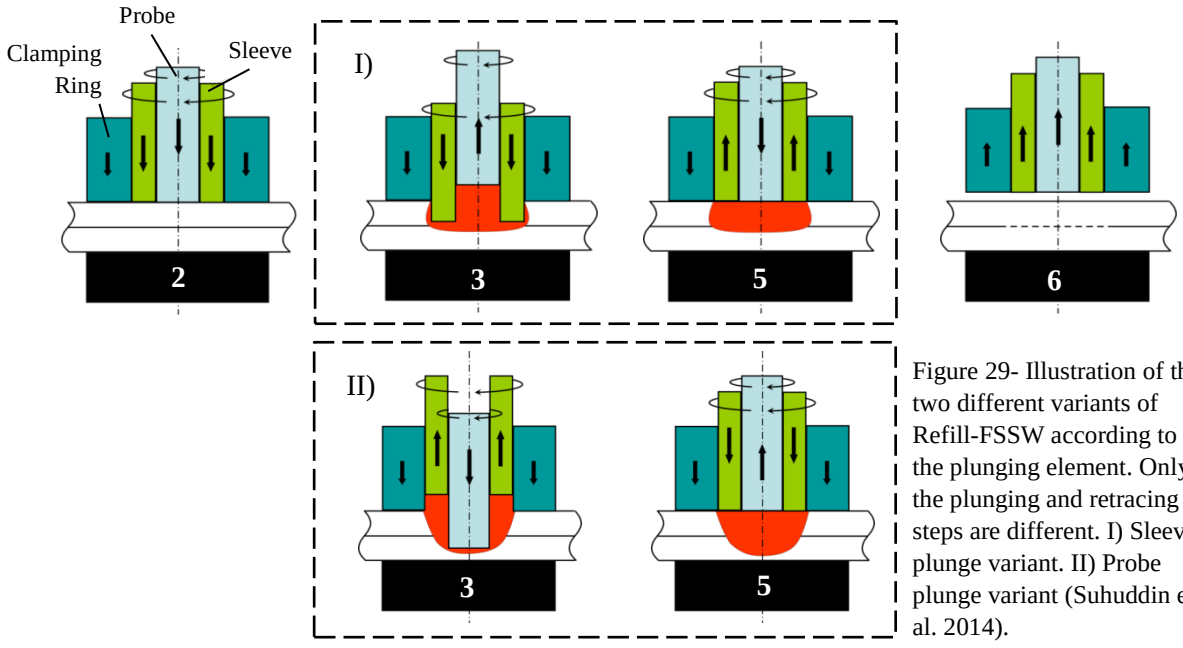

Figure 29- Illustration of the two different variants of Refill-FSSW according to the plunging element. Only the plunging and retracing steps are different. I) Sleeve plunge variant. II) Probe plunge variant (Suhuddin et al. 2014).

material is forced to flow into, by the relative axial motion; 4) dwell time stage in which both the probe and sleeve hold their previous position after the plunged element reaches the preseted depth, in some cases, this stage can be omitted (not illustrated); 5) second extrusion or refilling stage with reverse or returning movement of the sleeve [I)] / probe [II)] to the top sheet, while simultaneously the probe [I)] / sleeve [II)] consolidates the weld material by plunging until the top sheet, all linear movements whilst rotating; 6) pull-out or withdraw stage with tool extraction from the surface of the material that corresponds to the final joint formation.

Currently there are no standard designation and classification of the differential rotation technique. However, the normative process is being conducted in association of HZG institution. As indicated by the name, DR Refill-FSSW is characterized by different angular velocities for the probe and sleeve. The relative rotation movement between the probe and sleeve, Figure 30, can be: a) in the same direction (with different angular velocity magnitude), b) with the same magnitude (in different rotation directions) and c) a combination of both (opposite directions with different absolute velocity). In the case illustrated in Figure 30 c), the sleeve RS can be higher or lower than the probe RS. Internal works conducted in HZG already studied both conditions. A particular case of DR happens when only the plunging element (sleeve [I)] / probe [II)]) is animated with rotational movement, while the retracting element (probe [I)] / sleeve [II)]) does not rotate and only moves along the axial direction. Its successful implementation could reduce the complexity of the machine and consequently the non-recurrent costs.

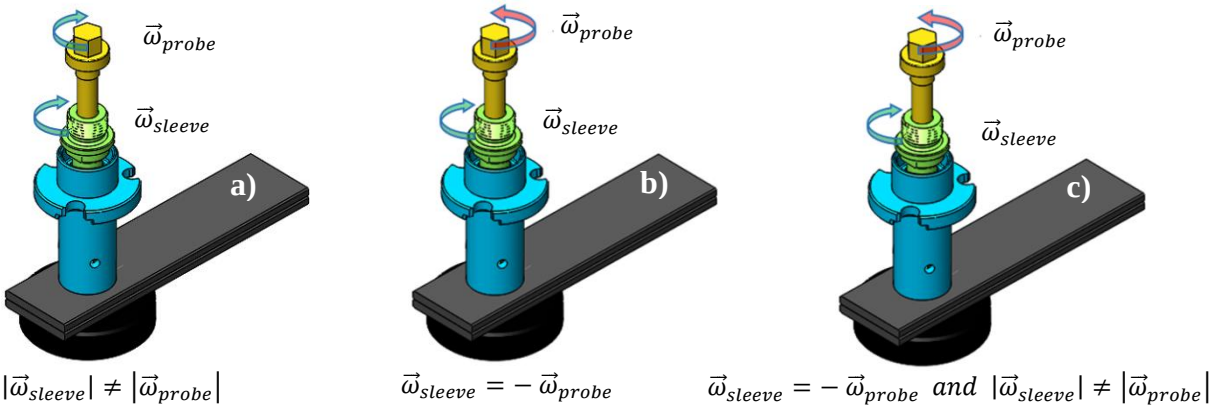

Figure 30- Illustration of the different possible cases of differential rotation Refill-FSSW.

The tool set and basic components of the welding system are illustrated in Figure 31, and generically consist of a:

- Backing support – prevents denting the materials by supporting the back side of the joint. This can be provided by a C-frame, a backing bar/table or an external fixture;
- Back anvil – Local support that give stiffness to the spot region;
- Clamping ring or Clamp – fixes the metal sheets (upper and lower) against the backing support, preventing sheet separation and lifting. It consists in a physical constraint that forces the material, extruded by the sleeve, to flow towards the cavity created by the probe retraction. Also prevents loss of material by expulsion and spitting as flash (Tier et al. 2008);
- Stirring/Rotational Sleeve or Shoulder – threaded outer rotating part that plunges into the material (in sleeve plunge variant) being responsible for plastically deforming the material and provide frictional heat. During the plunging stage, squeezes the plasticized material to fill the cavity left by the relative probe movement. According to (Montag et al. 2014), in sleeve plunge mode the sleeve is the tool part with the most wear, Figure 29 a);
- Stirring Probe or Pin – grooved inner projection component, with its upward retracting movement creates a cavity for which the material flows (in sleeve plunge variant). During the refilling stage the probe is responsible for extruding the material back to the center of the spot.

The tool set is usually manufactured with typical tool steel: High Carbon-Chromium D-series (Cold-working steel) (Kamal et al. 2017), HSS/HS Molybdenum M-series (High Speed Steel) and H series (Hot-Working steel) (Nasiri et al. 2018). According to (Shen, Hou, et al. 2016), tool wear occurs mainly during the plunge stage. Thus, tool wear in the spot version (Refill-FSSW) is significantly higher when compared to Friction Stir Welding (FSW). In order to reduce tool wear, and be able to plunge in hard materials such as steel, Titanium or Nickel/Titanium superalloys, ceramic based tools are required (Dong et al. 2016). Different tools materials, namely W-25 Re, WC-Co Tungsten Carbide (Liu et al. 2005), Si_3N_4 ceramics (Kim et al. 2014), Polycrystalline Cubic Boron Nitride (PCBN) (Sierens et al. 2014), and ultra-high temperature ceramics (TiB_2, ZrB_2, HfB_2, etc.) are gradually applied in FSW and FSSW (Khan et al. 2007), (Kennard 2015). In Refill-FSSW the application cases are sparser and mainly by single order.

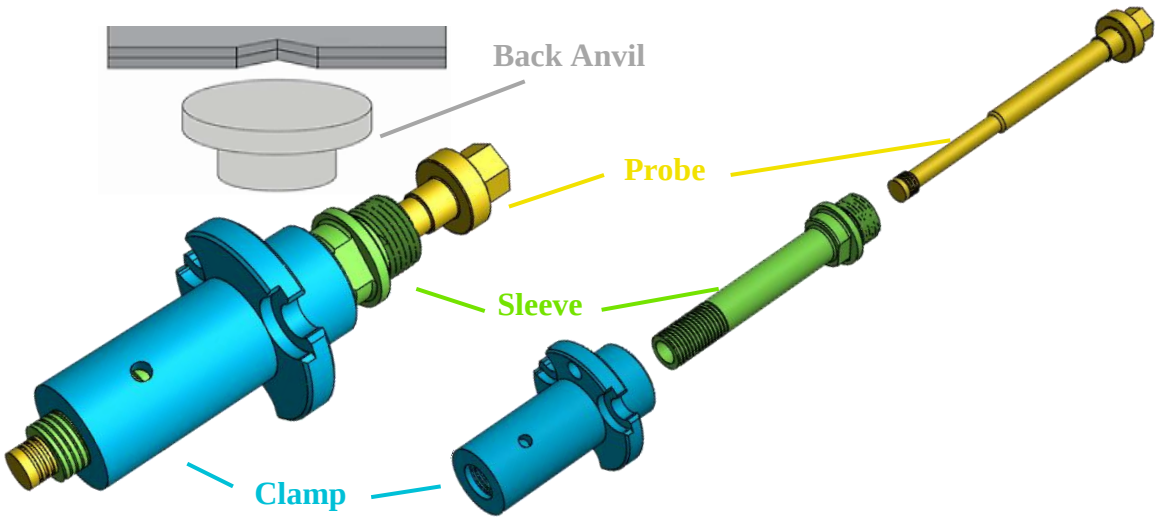

Figure 31- 3D model of the Refill-FSSW tool set used during the experimental study.

According to (Mishra and Ma 2005), the primary functions of the tool are to supply heat and mechanical energy to the spot. The tool essentially induces rapid heating, and promotes material flow by stirring movement, as done by FSSW tool. The real difference to FSSW, is that also constrains the natural overflow of plasticized material with the probe and sleeve axial movement, ensuring the proper refill of the spot. At the early stages of the process research, the feasibility of different tool dimensions was checked and the performance of the joint evaluated. For research and common industrial applications, the standard dimensions stabilized within the interval proposed in Table 14. HZG itself after some preliminary tool design studies and together with some industrial partners, defined a standard tool for research purposes, also detailed in Table 14. However, different dimensions can also be applied when dealing with particular alloys and when it's necessary to meet industrial requirements.

Table 14- Typical tool dimensions values used in several published works.

Outer Diameter [mm]	Clamping Ring	Sleeve	Probe
Typical Dimensions	14-18	8.5-9.5	5-6.5
HZG Standard	14	9	6

Tool design is far from the research level achieved for FSW (Dubourg and Dacheux 2006) and FSSW. In addition, aggressive features such as flutes, non-cylindrical profiles, implementation of scribes, etc., are hard to introduce due to concerns about incomplete refilling, optimize stroke factor, and cylindrical tolerances (required by the concentric movement). However, different tool designs start to be aim of some preliminary studies, and a few to appear in the literature. The main approaches focus on three essential features of the tool: outer cylindrical surface, bottom surface and inner cylindrical surface. Since the sleeve variant is most of the times used, the majority of design modifications are related to sleeve. Regarding the sleeve/probe outer surface, features such as plane, grooved (cylindrical groove) and threaded surface were evaluated. Usually in the most common arrangement the sleeve is threaded and the probe grooved (Plaine et al. 2015), Figure 32 a). However, plane surface sleeve was

successfully used to reduce the amount of heat input in small Refill-FSSWed spots of thin dissimilar Al sheets (internal project at HZG to test sleeves with external diameter of 5 mm). The standard Refill-FSSW tool features both sleeve and probe with a plane bottom surface, Figure 32 a). However, (Shen, Ding, et al. 2018) reported that introducing three notches in the sleeve tip improved metallurgy bonding, material intermixing and mechanical inter-locking at the weld interface, Figure 32 b). The sleeve and clapping ring inner surface design is more related to tool wear, which consequently influences the quality of the weld. Sleeves or clamping rings with plane inner walls are progressively featuring inner grooves. (Montag et al. 2014) stated that during the welding cycle, the small gaps between the parts concentric walls of the tool are continuously filled with plasticized stirred material. The inner grooved notches provide additional small chambers for where the material can pile up; creating a protection layer that generates abrasive tool wear, otherwise given by frictional wear between the concentric parts of the tool.

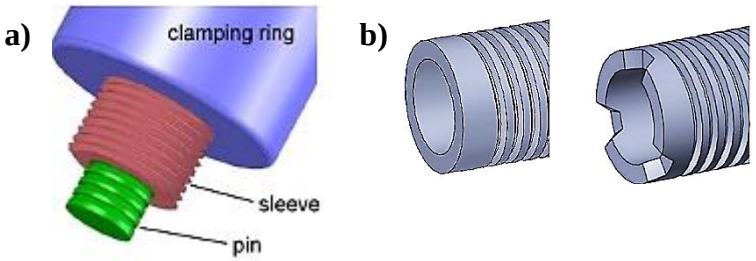

Figure 32- a) Detail of the features of the standard Refill-FSSW tool (Tier et al. 2013). b) Design modification of the sleeve bottom surface tip (Shen, Ding, et al. 2018).

In order to perform FSSWed joints, the welding machine must be capable of moving the tool head in at least two degrees of freedom, and other can be implemented by the workholding table or the welding head. Three linear degrees of freedom in space: two to position the spot accordingly, by moving the tool/table in the xy horizontal plane, and a third plunging perpendicular movement of the head (basic degree of movement); and an angular degree of freedom to animate the tool with rotational motion (basic degree of movement). Thus, a common CNC milling machine is perfectly able to perform spot welding. This may implies no additional investments in dedicated machinery (Wang, Wu, et al. 2013). Robotic arms may have additional rotational movements to increase manufacturing and assembly freedom. However, Refill-FSSW requires dedicated specially designed machinery. The two elementary movements (axial and rotation) of the FSSW tool, are replaced by: three independent linear actuators for the clamp (responsible for the axial movement of the entire welding head against the work pieces), sleeve, and probe; and if Differential Rotation (DR) is desired two more independent angular actuators for the independent rotation of the sleeve and probe. If only Conventional Rotation (CR) is available, the probe and sleeve are controlled by one shared motor spindle, so that they rotate simultaneously at the same speed. Figure 33 illustrates Refill-FSSW machines available in the facilities of HZG. Figure 33 a) and b) are Refill-FSSW machines only capable of performing conventional rotation in lightweight alloys, and are mainly used for experimental research as well as primary industrial production integrating with an industrial robot, for example Figure 33 c).

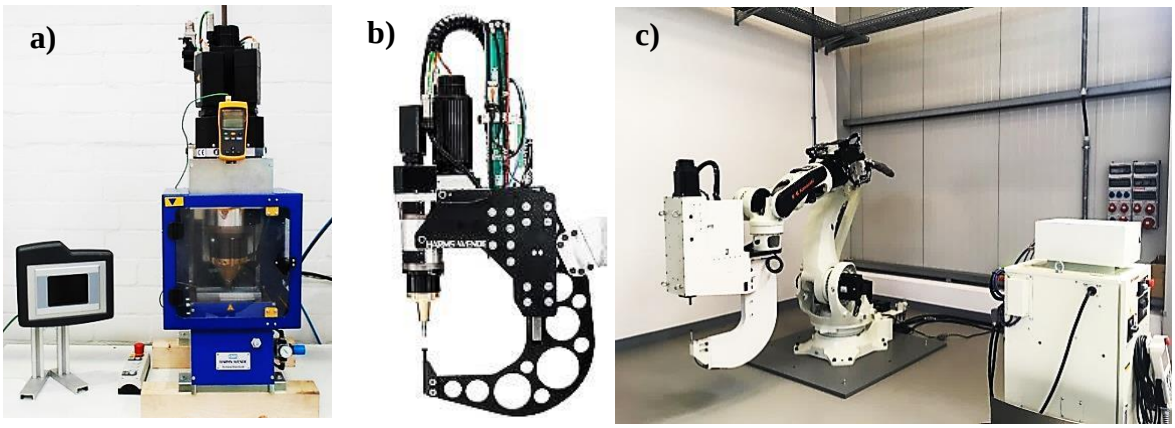

Figure 33- Welding machines with different levels of automation. a) RPS100 machine developed in a technology transfer project between HZG, Harms&Wende® and RIFTEC. b) RPS100 commercially available machine produced by Harms&Wende®. c) Industrial robot with Refill-FSSW head manufactured by Kawasaki Heavy Industries®.

2.4.3 Comparison with FSSW and Application Spectrum of Refill-FSSW

The main difference between FSSW and Refill-FSSW techniques, is the keyhole that the original FSSW technology leaves in the joint, Figure 34 a). This characteristic keyhole usually has the same size of the rotating pin of the FSSW tool, and remains at the joint center after the joining process, Figure 34 b) (Shi et al. 2017).

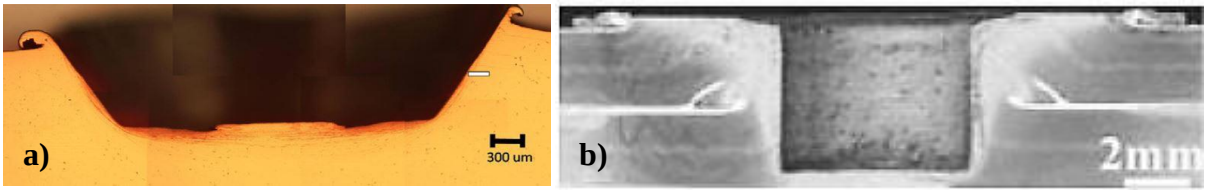

Figure 34- a) Low magnification overview of the pin-plunging detail, of a single crystal austenitic steel welding (Jeon et al. 2011). b) Macrostructure of similar welding of 2024-T3 Al alloy with RS=1200 rpm, PR=8 mm/min, PD=4.6 mm and DT=4 s (Karthikeyan and Balasubramanian 2010).

The more obvious disadvantages of FSSW are precisely their surface finish (to be taken with account for dimension tolerance, post-machining and aerodynamics aspects) and visual or cosmetic appearance (critical for example regarding the exterior panels of vehicles). (Shen et al. 2013) even considered the keyhole a welding defect detrimental to the mechanical properties. In addition, one most also consider:

- Resistant area reduction and thinning of the upper sheet– in the pin-plunging step, the stress will be higher than the remote applied stress, decreasing the resistance of the joint (Shen et al. 2013);
- Stress concentration factors – the joint continuity is destroyed by the keyhole, depending of the area reduction and the borders geometry, the SCF's can't be neglected in cyclic loading;
- Corrosion and sealing properties – primary coatings and further body paint can't reach the keyhole bottom properly, deteriorating the join corrosion resistance and also the paint work visual appearance. In addition, also acts as deposit site for debris and rain water (Uematsu et al. 2008);
- Less conducive for welding dissimilar materials such as metal/composite, metal/polymer and dissimilar metal in nature such as Mg/steel or Al/steel (Chen et al. 2015);

(Shi et al. 2017),(Yang, Fu, and Li 2014)

Every advantage that FSSW has over conventional spot welding techniques is transversal to Refill-FSSW. However, FSSW has an important advantage over Refill-FSSW, their already robust and well rooted knowledge. A good evidence of that, is its industrial implementation (Schwartz 2010). In addition, its welding equipment and machine control systems are much simpler (Zhang et al. 2014). Compare to the 3 (for CR) or 4 (for DR) degrees of movement required for Refill-FSSW head, FSSW only requires a typical CNC machine with one degree of freedom for traveling movement and other for rotation movement, Although large companies like Kawasaki®, Harms & Wende®, ColdWater Machine®, etc. already manufacture Refill-FSSW machines, much still needs to be done in the Refill-FSSW research field: filling gaps like fracture and fatigue properties, corrosion resistance, tool design, tool wear, etc. (detailed explanation in subchapter 5.2).

Refill-FSSW is not only an upgrade of the original FSSW technique. Its first applications were in fact focused on the welding of similar lightweight alloys (Amancio-Filho, Camillo, et al. 2011), particularly Al alloys hard to weld by RSW, similar to FSSW. However, the spectrum of scientific and technological applications is constantly being widened. The currently major applications of Refill-FSSW technology are summarized in Table 15. Several more scientific related applications such as dissimilar welding of metal, polymers, composites and even the dissimilar joining of the previously referred materials, were already developed. Technology transfer enabled applications complementary of other solid-state process such as FSW, or regarding different fields such as structure repairing or battery manufacturing.

Table 15- Review of some scientific and technological applications of Refill-FSSW stated in the literature and being currently developed in HZG.

Application	**Description**
Hybrid Joining of dissimilar materials Patented as Friction Spot Joining (FSpJ) (Santos and Filho 2013)	Metal-Composite: (Amancio-Filho, Bueno, et al. 2011) studied the feasibility of joining AZ31 wrought Magnesium alloy to short glass fiber reinforced PPS and woven carbon fiber reinforced PPS Polymer-Composite: Natalia Manente[1] successfully welded PA polymer to CFRP Composite-Composite (Gonçalves et al. 2015) evaluated the feasibility of similar welding of CFRP laminate based on polyamide 66 Polymer-metal: (Filho et al. 2010) showed the feasibility of joining thermoplastics to metals by FSpJ
Welding Polymers	The feasibility of welding thermoplastics by Refill-FSSW was first studied by (Oliveira et al. 2010). The joint strengths were comparable to other welding techniques (suitable for polymer welding), with shorter or equal joining time
Non-weldable Al alloys	Extensive research work was done in the study of hard to weld Al series by fusion welding process: 2XXX (Li et al. 2016), (Amancio-Filho, Camillo, et al. 2011); and 7XXX (Shen et al. 2013), (Kubit et al. 2018), (Shen et al. 2015)
Welding of dissimilar metals	Welding dissimilar joints in thickness, composition (different alloys), and nature (different metallic systems) Three types of dissimilar metallic joints: dissimilar thickness (Kubit et al. 2018); dissimilar alloys – Al 5XXX/Al 6XXX (Li et al. 2017), Al 6XXX/Al 7XXX (Shen, Ding, et al. 2018), etc.; dissimilar alloying system low melting point/low melting point – Al/Mg (Suhuddin, Fischer, and dos Santos 2013b), (Suhuddin, Fischer, and dos Santos 2013a), Al/Cu (Shen, Suhuddin, et al. 2014), (Cardillo et al. 2018), etc.; low melting point/high melting point – Al/Ti, Mg/Ti, Al/Steel, Mg/Steel, and low melting point/Coated High melting point – Al/(Zn) Steel, Al(AlSi) Steel, Mg/(Zn) Steel
Keyhole closure	Repairing of damages through holes: broken tools, drilled defects, internal cracks or volumetric defects, external and fatigue cracks (Fox 2010), keyholes left by broken mechanical fastenings (bolts, rivets) (Reimann et al. 2016) Closure of termination Keyhole in any friction stir based technology: Friction Stir Welding (FSW), Bobbin Tool FSW (BT-FSW), Stationary Shoulder FSW (SSFSW), Stationary Shoulder Bobbin Tool FSW (SSBT-FSW), etc., with special attention to double side technologies and through holes, in which friction stir keyhole closure process can't be applied (Reimann et al. 2017) Ability of refill through holes and enhanced manufacturing properties when compared to friction plug welding (Reimann et al. 2017)
Dissimilar Welding of Metal Foils	Uceu Suhuddin is currently studying the feasibility of welding multiple foils by Refill-FSSW, in a project together with the automotive industry, for manufacturing batteries for future generation electric cars

[1] Natalia Manente is a PhD student in HZG, currently finishing her Doctoral thesis

[2] Dr. Uceu is currently working in HZG as head of the Refill Friction Stir Spot Welding division

2.4.4 Process Parameters and Welding Cycle

Like any other welding technique, the joint resistance and microstructure is influenced by many environment variables, but hopefully more significantly by the set of welding parameters. Depending of the specific process and system, each parameter assumes a particular relative importance. For Refill-FSSW, the most important welding parameters are according to its nature, classified as (Suhuddin et al. 2013), (Mishra, De, and Kumar 2014):

Geometric Parameters (already explored in section 2.4.2)

- Characteristic dimensions;
- Component Shape and special design features.

Process Parameters

- Clamping Force (CF);
- Surface Dwell time (before plunging and/or before withdrawing stage);
- Sleeve Rotation Speed (Sleeve RS) and Probe Rotation Speed (Probe RS) or simply Rotation Speed (RS) in case of conventional rotation (equal angular velocity for both);
- Plunge Depth (PD) or depth of penetration *;
- Dwell Time (DT) or hold time*;
- Plunge Time (PT) or physically equivalent average Plunge Rate (PR) *;
- Retract Time (RT) or physically equivalent average Retract Rate (RR) *;

Regarding the process parameters, it can be easily observed that the probe and sleeve are the two most active elements in the tool set. The clamping ring has only associated to it the clamping force. The parameters signed with (*) always refer to the plunged component, independently of the variant used. Since the dominant variant is the sleeve plunge cycle and for sake of simplicity, the reference to the plunged component is usually omitted, and sleeve parameters are assumed. It will be also omitted when detailing the results in chapter 4. The only exception is the dwell time that is always equal to both probe and sleeve, independently the variant used. The surface dwell time is often of less importance for the majority of the authors, but some authors (Shen, Chen, et al. 2018) also controlled it. With the exception of RS, all process parameters of the sleeve and probe are related by the stroke factor or areas ratio, which must ensure equal swept volumes by each component. The majority of the dedicated Refill-FSSW machines compute automatically the related probe parameters from the input given for the sleeve parameters, or vice-versa. The travel displacement and travel rate of the probe, during the plunging or refilling stage, whether in sleeve or probe variant, is manually calculated by the stroke factor as shown in equation (1). Figure 35 shows a typical evolution of the travelling position and the rotation speed of both probe and sleeve in conventional rotation Refill-FSSW cycle, in sleeve plunge mode. In this specific case, the travelling times were controlled instead of the travelling rates. In subchapter 3.2.5, some advantages of controlling the PT and RT instead of the travelling rates are detailed.

$$\begin{cases} Travel\ distance_{\ Probe} = Travel\ distance_{\ Sleeve} \cdot \dfrac{\varphi^2_{sleeve} - \varphi^2_{probe}}{\varphi^2_{probe}} \\ Travel\ Rate_{\ probe} = Travel\ Rate_{\ Sleeve} \cdot \dfrac{Travel\ distance_{\ Probe}}{PD} \end{cases} \quad (1)$$

One other process parameter, not commonly mentioned and frequently not considered as one, is the basic position, Figure 36 a) - d) (Lacki, Derlatka, and Gałaczyński 2017). In standard Refill-FSSW, both sleeve and probe start at the zero level, referenced by the clamping ring position. The lack of alignment between the three components is usually considered as an error of the operator. To measure the alignment level of the three concentric tools a "zero weld" is done. It's a standard routine that consists on the first two steps described in Page 38. After running the short welding routine, the maximum

* Variable referred to the plunged component (probe in probe plunge variant, and sleeve in sleeve plunge variant)

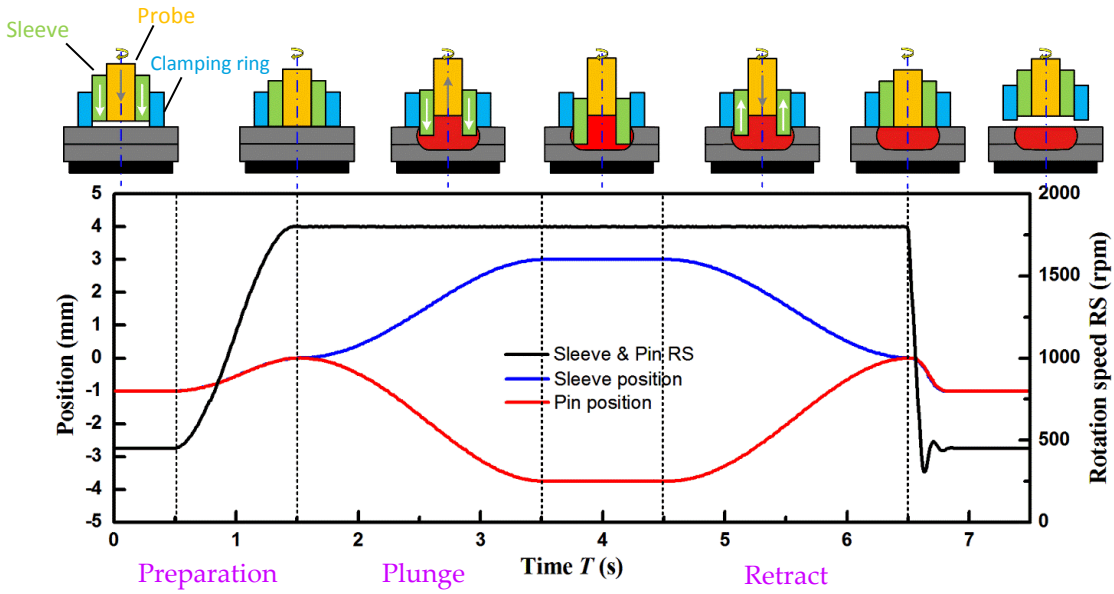

Figure 35- Typical conventional rotation Refill-FSSW cycle, performed with the following parameters: RS = 1800 rpm, PD = 3 mm, PT = 2 s, DT = 1 s and RT = 2 s. The vertical referential has its origin in the clamping ring position and is positive in the plunging movement.

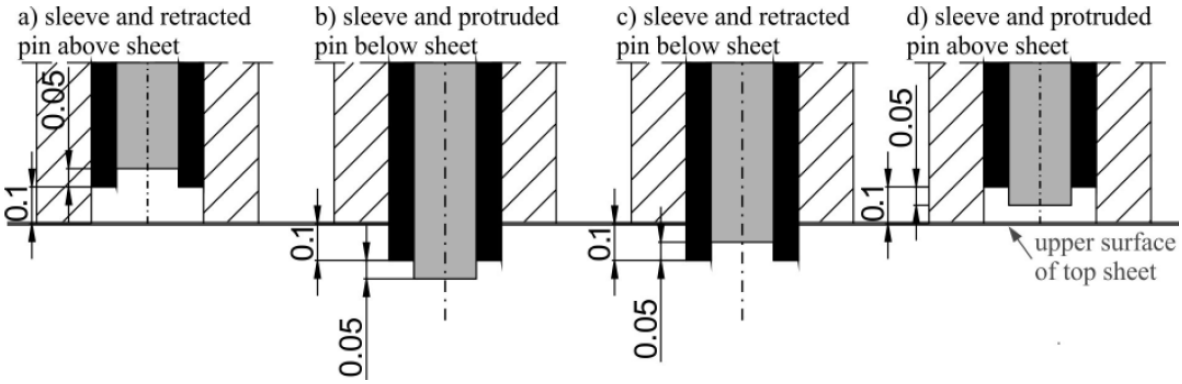

Figure 36- Illustration of the basic position concept (Lacki, Derlatka, and Gałaczyński 2017).

surface height variation is measured with a dial indicator. However, (Lacki, Derlatka, and Gałaczyński 2017) study the influence of the relative initial position of both probe and sleeve in the microstructure and strength of the joint. The arrangement in which the sleeve and probe are below the clamping ring surface, and the probe protrudes the sleeve, produced joints with higher strength. Other process parameter also usually considered more as an influence variable in the literature, is the initial tool temperature. (Shen, Hou, et al. 2016) studied the evolution of the joint strength with the initial temperature of the tool. For this, successive welds with 10 s interval were performed. The critical temperature, for which the joint strength stops to increase and starts to decrease, is around 350 ºC for the dissimilar welding of Al 6022-T4 to DP600 steel.

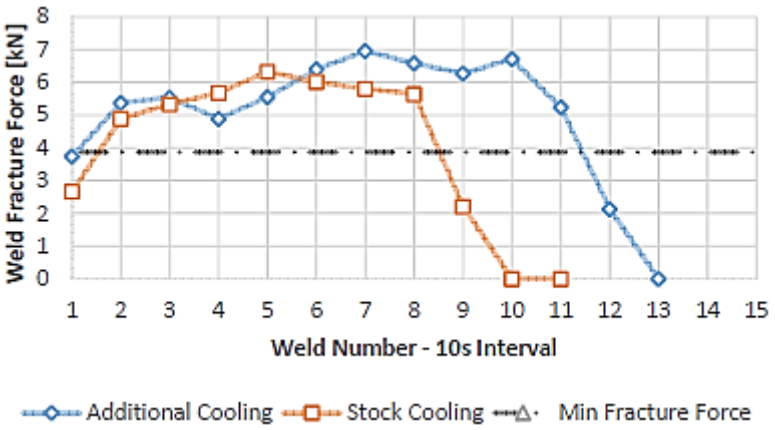

Figure 37- Evolution of the joint strength with the initial tool temperature, and the influence of an additional cooling system in the initial temperature and joint strength.

According to (Rosendo et al. 2011) and (Shen, Yang, et al. 2014), the process parameters control the heat input, material flow behaviour and material intermixing during welding. The increase in plunge depth, rotation speed and total welding time (PT+DT+RT) increase the amount of heat input, responsible for material flow behaviour and intermixing, microstructural changes, diffusion and metallurgical reactions such as the formation of solid solution, IMC's, partial film liquation, eutectics, etc. (Chen et al. 2015), (Tier et al. 2008). Plunge depth individually, increases the mechanical interlocking (Chen et al. 2015), (Pieta et al. 2014), (Tier et al. 2013), (Cao et al. 2016). In a different perspective, instead of PT and RT, the displacement rate can be controlled. However, the effect of plunge rate and retract rate is not always obvious even though it was already studied by several authors (Tier et al. 2008), (Santana et al. 2017). On their turns, the combination of - material flow behaviour, heat input, and mechanical interlocking and intermixing - result in different metallurgical perspectives of analyse:

- Microstructure evolution and texture variation (grain structure, grain size and refinement, microstructure transition, hardness, etc.) (Cao et al. 2017), (Shen, Yang, et al. 2014), (Suhuddin et al. 2014), (Cao et al. 2017), ;
- Macro and microstructural features of the weld region (hook, bonding ligament, partial bonding, mechanical interlocking, etc.);
- The presence, their number, and the dimension of metallurgical defects (voids, cracks, etc.).
- Interface reactions typical of dissimilar welding of soft materials with hard materials (e.g. Al/steel, Al/Ti, etc.) (Dong et al. 2016), (Ding, Shen, and Gerlich 2017),(Shen, Chen, et al. 2018), (Shen, Hou, et al. 2016), (Verastegui et al. 2014), etc.;

The joint strength and other mechanical properties will be influenced individually or simultaneously, by the aforementioned metallurgical outputs, depending essentially on the specific metal sheet combination. When running the process outside its process window, defects such as voids and cracks start to appear. In addition, the size and number of these defects play an important role in determining the fracture mechanism and thus the weld mechanical properties (Shen et al. 2013), (Cao et al. 2017). The strategy adopted by the majority of authors published until now, focus on finding a process window almost free of defects, and then study some of the topics and evaluate the one(s) that better correlate with the joint strength.

The magnitude of the effect (significant and not significant), and even the direction of the effect (increase or decrease the strength) of the major welding parameters don't have a unique correlation, applicable for all welding scenarios, Figure 38. For most relevant parameters - the alloy used or the alloys in case of dissimilar welding, the stack-up sequence of the material sheets (Peer and Rindler 2015), the surface preparation of both the lower sheet (coating acts as interlayer) and even the upper sheet, and finally the tool design (Shen, Ding, et al. 2018) - influence the strength evolution with the welding parameters. For example, the correlation of joining time for similar welding of 6061-T6 is unobvious, increase the welding time could either improve the joint quality by eliminating pores. or weaken the weld by creating a steeper hook profile (Cao et al. 2017).

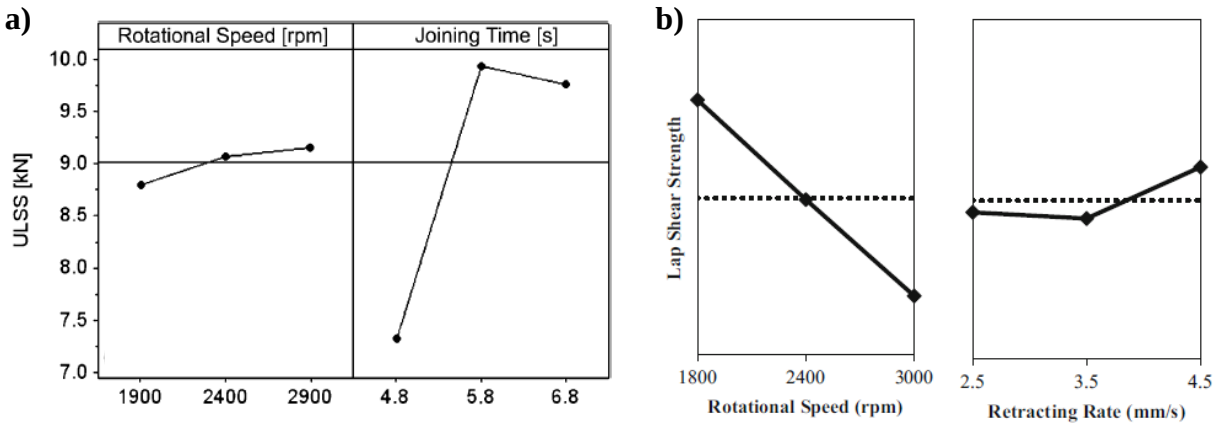

Figure 38- Illustration of different effects of the same welding parameters in a) 2024-T3 Al alloy (Amancio-Filho, Camillo, et al. 2011), and b) Al-Mg-Si wrought Al alloy (6XXX series) (Santana et al. 2017).

2.4.5 Typical Weld Macrostructure, Microstructure, Features and Defects

A typical cross-section of a Refill-FSSWed joint is illustrated in Figure 39. Analyzing the joint from the centerline of the spot to the periphery, it can be classified into four regions in terms of microstructural characteristics:

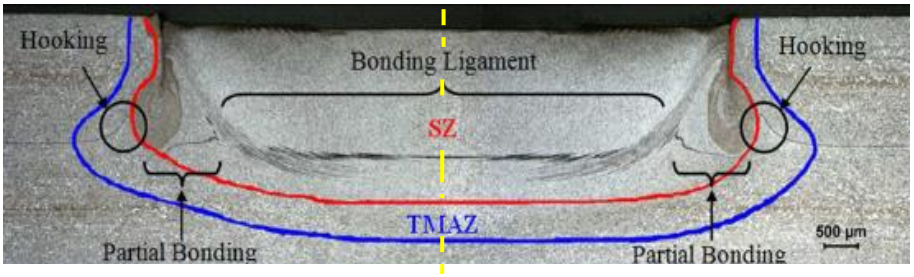

Figure 39- Highlight of typical regions of a Refill-FSSWed joint, along with the major metallurgical features. Macrograph of Refill-FSSW joint of 6181-T4 Al alloy, etched with Flick solution, adapted from (Rosendo et al. 2015).

- Stir Zone (SZ) or Nugget Zone (NZ) – is a dynamically recrystallized zone, with refined equiaxed grains due to heavily plastically deformed material due to higher temperatures and shear rates (Rosendo 2009), (Shen et al. 2013), (Amancio-Filho, Camillo, et al. 2011). The center of the SZ has usually higher grain size (lower refinement by recrystallization) than the rest of the SZ (Chen et al. 2015), Figure 41 b). It results from two tool actions: stirring movement that creates a peripheral velocity distribution, with a maximum in the outer surface of the sleeve, and a stagnation point in the spot center; and vertical complex travel movement of both probe and sleeve. Roughly, the SZ corresponds to the location delimitated by the outer diameter of the sleeve during welding. (Shen et al. 2013), (Shen, Yang, et al. 2014);
- Thermo-mechanically Affected Zone (TMAZ) – in contrast to the SZ, usually only partial recrystallization (Amancio-Filho, Camillo, et al. 2011), or no recrystallization at all occurs (Shen et al. 2013). Typical microstructure comprises deformed and elongated grains, which were less affected by plastic strain (produced by mechanical stirring of the tool at the vicinity of the SZ), and temperature exposure (Santana et al. 2017). However, it still has a recognizable microstructure when comparing to the parent material. This region is located between the SZ and HAZ, in a narrow zone around the periphery of the sleeve, with an average thickness range less than 2 mm (Rosendo et al. 2011);
- Heat Affected Zone (HAZ) – is subjected to a thermal cycle but it isn't deformed during welding, which leads to larger grains and coarsening of the grains and precipitates (Shen, Ding, et al. 2018). The softening in this region may also happens in thermally unstable microstructures, due to overageing of the parent alloy by dissolution of the precipitates (Cao et al. 2017). The HAZ is frequently not visible by optical microscopy, every so often even with etching, being most of the times only detected by micro-indentation hardness scanning;
- Base Material (BM) or Parent Material (PM) – is the surrounding region of the spot and remaining component, that doesn't suffer any structural changes after welding.

The different microstructural regions can affect the joint strength through grain size and orientation transitions, and/or hardness distribution. Sharp transition between the very fine grain structure of the SZ and the partially recrystallized grains of the TMAZ, and bonding strength between the two zones, are two main features affecting the joint strength (Shen et al. 2013), (Cao et al. 2017). The fracture usually initiates in the sites with less hardness. Thus, micro-indentation hardness scanning and mapping (several horizontal and vertical lines) are often part of the microstructural evaluation and correlation works, Figure 41 a) - b). Frequently the base material shows higher hardness levels, Figure 40 a). However, in Refill-FSSW of heat-treatable alloys, the hardness levels in the SZ can exceed the original base material (function of the welding parameters). This owes to the combination of solution-treatment, reprecipitation hardening - which leads to post-weld natural ageing of the material, and intensive grain refinement by recrystallization, Figure 40 b). The minimum hardness point is normally located in the HAZ and TMAZ boundary, or in the HAZ, as a result of the thermal cycle in the microstructure.

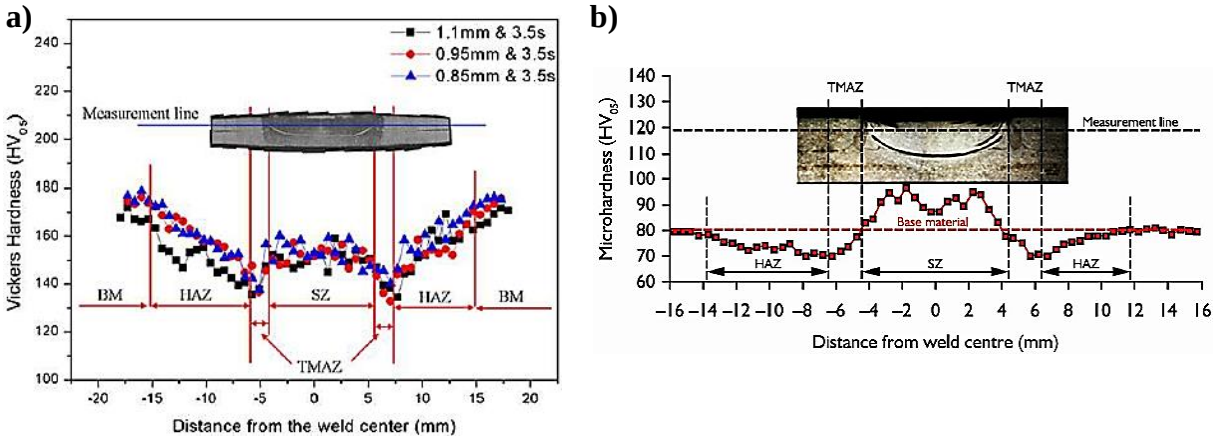

Figure 40- a) Horizontal micro-hardness profiles, in the mid thickness of the AA7075-T6 upper sheet for several Refill-FSSWed joints, produced with different welding parameters (Shen et al. 2015). b) Horizontal micro-hardness profile, in the mid thickness of the age hardening AA 6181-T4 upper sheet (Parra et al. 2011).

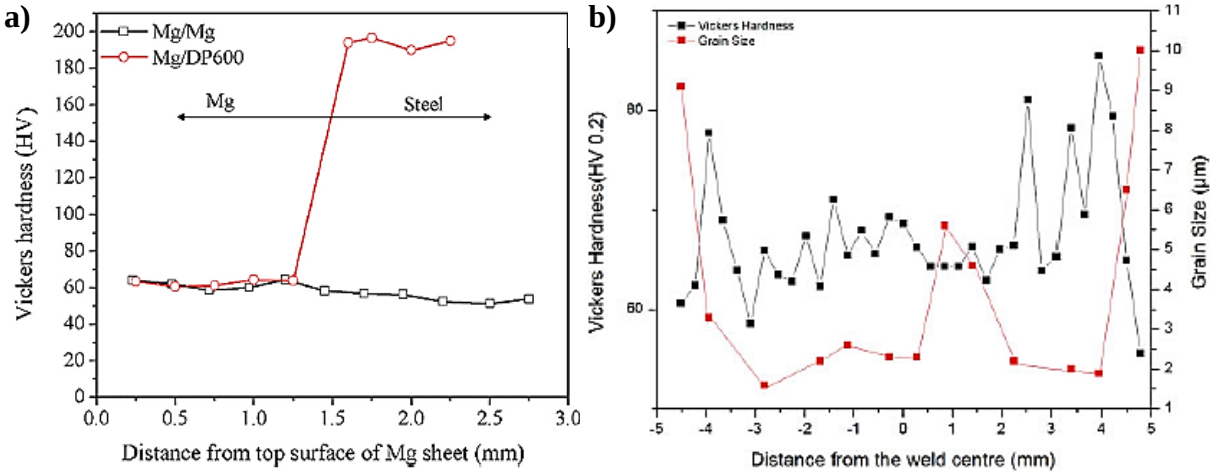

Figure 41- a) Vertical micro-indentation hardness profile along the centreline of the nugget, produced with RS=1800 rpm and WT=3.5 s (Shen, Ding, et al. 2016). b) Horizontal micro-indentation hardness profile across Mg SZ in ZEK100/DP600 joint, produced with RS=1800 rpm and WT=3.5 s (Chen et al. 2015).

Refill-FSSW Metallurgical Features:

In Refill-FSSW of some alloys, the elimination of particular flow patterns is impossible, and they result in several macro and microstructural features. Some authors (Cao et al. 2017), consider them as metallurgical defect, but the author agrees with the scientific stream that considers the following metallurgical formations as typical metallurgical features rather than metallurgical defects:

- Hook or hooking – is defined as a partially metallurgical bonded region, and consists in a transitional region between the fully or completely metallurgical bonded region and the unbonded interface separating the overlapped plates, Figure 42 c) and Figure 43 a). This deviation of the non-welded interface line is formed probably because of the upward bending of the sheet interface due to sleeve action (particularly retraction stage). This geometric feature (characterized by a height, sharpness, location, etc.) acts as a stress concentrator and provides a potential path for crack initiation and propagation (Santana et al. 2017), (Campanelli et al. 2013). The correlation between process parameters, hook geometry and ultimately mechanical properties of the joint were studied in detail by (Cao et al. 2016), Figure 42 a) - b) and d) - e), and Figure 43 b). Crack nucleation usually happens in the upper sheet when the hook tip becomes too sharp, Figure 44 b) (Shen, Yang, et al. 2014);

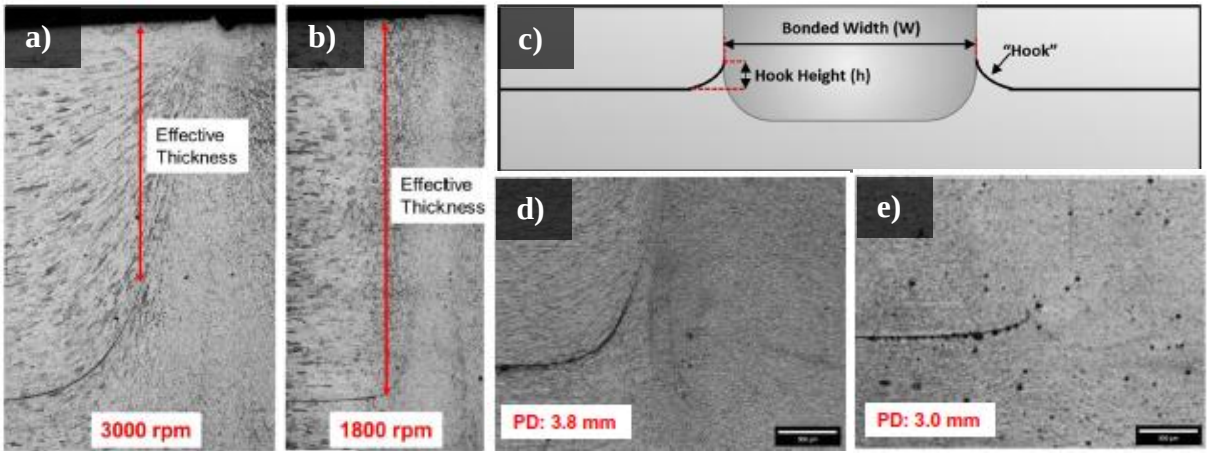

Figure 42- Detail of left side Hook feature for a) high RS, b) low RS, d) high PD, e) low PD (Santana et al. 2017). c) Schematic representation of the hook feature (Santana et al. 2017).

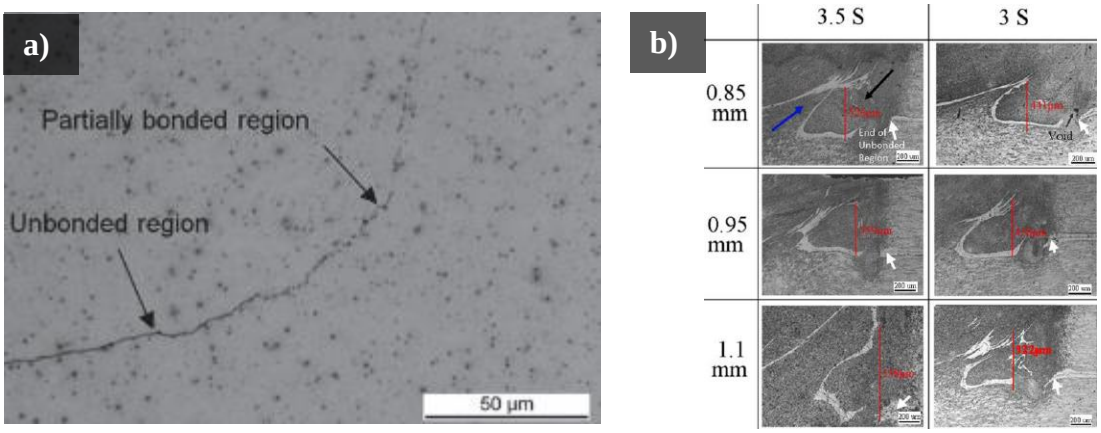

Figure 43- a) Higher magnification of the left side hook region in similar AZ31/AZ31 Refill-FSSW joints (Suhuddin et al. 2013). b) Influence of some welding parameters in the geometric characteristics of the hook in the right side of the joint, with the edge of the unbonded region marked by white arrows (Shen et al. 2015).

- Partial bonding or kiss bonding – is a transition region, located between the hook and bonding ligament features, in which the bonding between upper and lower sheet is not so strong. It is usually characterized by a short uneven linear geometry (Rosendo et al. 2011), Figure 44 b). According to several authors (Ding, Shen, and Gerlich 2017), (Rosendo et al. 2011) it can be a preferable crack nucleation site depending on its geometry, Figure 44 a) - b);

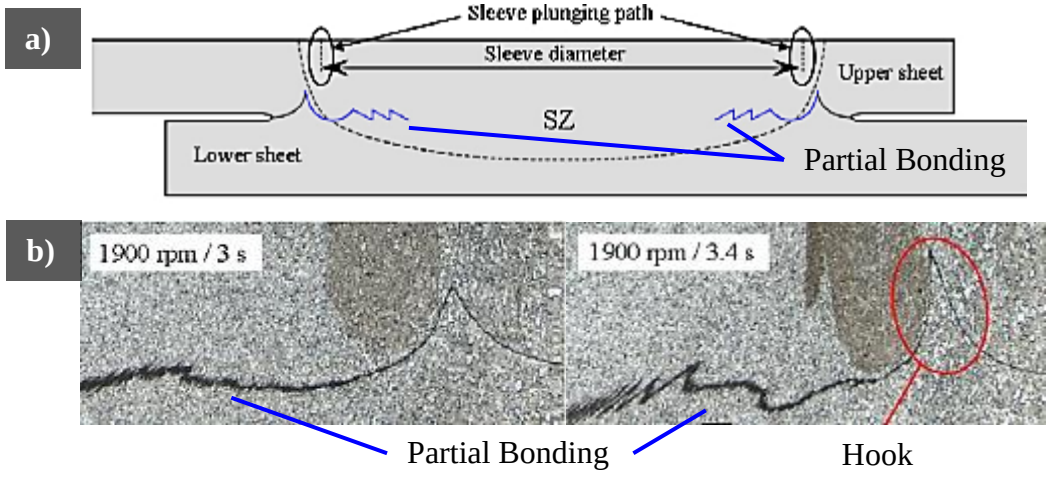

Figure 44- a) Schematic drawing highlighting the partial bonding region under stress (Rosendo et al. 2011). b) Influence of welding time in the geometry of the hook and partial bonding features (Rosendo et al. 2011).

- Bonding ligament – is a region of good adhesion between upper and lower sheets and a strong bonding between the two is expected. It results from metallurgical traces such as the oxide layer between the two sheets, coatings that act as interlayers, or not fully intermixed regions between dissimilar metals. The continuity of the bonding ligament is ensured by the material flow, defining also its characteristic shape (Shen, Lage, et al. 2018). This moving region is displaced upwards during plunging and pushed back to its original position during refilling stage (Rosendo et al. 2011), (Shen, Lage, et al. 2018). Similar to hook and partial bonding, the geometric characteristics of the bonding ligament are also influenced by the welding parameters (frequently in a lesser extent), Figure 45. Particularly for annular cracks, bonding ligament may also be a place for fracture propagation (Shen et al. 2015).

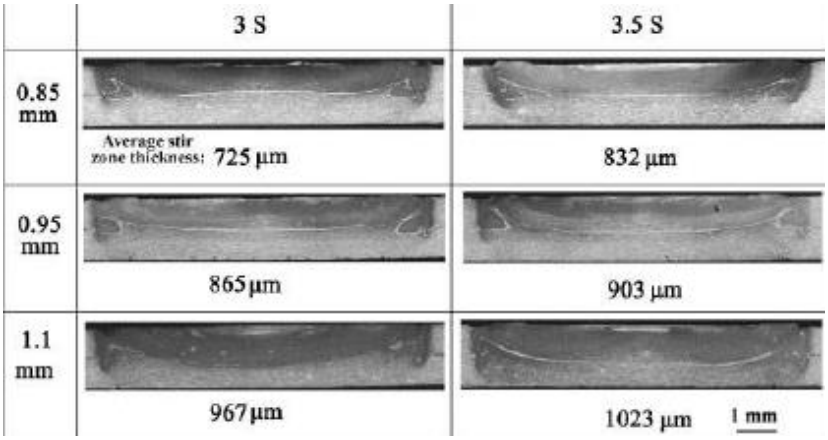

Figure 45- Evolution of the bonding ligament and overall macro and microstructure with PD and WT for similar Refill-FSSWed joints of 7075-T6 Al alloy (Shen et al. 2015).

The remnant metallurgical features previously referred and detailed in Figure 46, probably have a common root, which is related to a dissimilar region that wasn't destroyed or randomly distributed due to material flow imposed by the tool movement (Suhuddin et al. 2013).

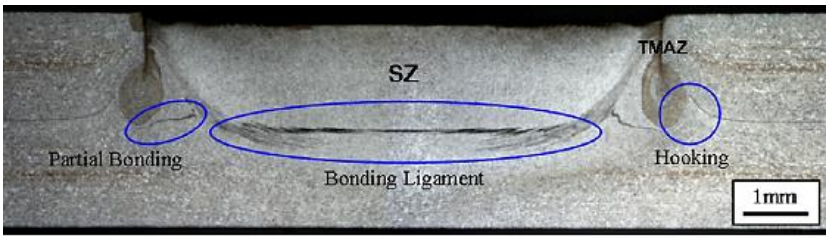

Figure 46- Representative macrograph taken by low magnification OM, of similar 6181 Al alloy (Rosendo et al. 2011).

Interfacial Bonding

Interfacial bonding phenomena such as the formation of solid solutions or metallurgical reactions to form IMC's are of extreme importance in dissimilar welding of different alloying systems. Several metal combinations were studied and published in the literature. Regarding the complete dissimilar welding spectrum, due to its importance for the automotive industry it is possible to highlight: Al/Ti - (Plaine et al. 2015), (Plaine, Gonzalez, et al. 2016), (Plaine, Suhuddin, Afonso, et al. 2016), (Plaine, Suhuddin, Alcântara, et al. 2016), (Vacchi et al. 2017); Al/Cu - (Shen, Suhuddin, et al. 2014); Al/steel - (Verastegui et al. 2014), (Fukada et al. 2014), (Qiao et al. 2016), (Dong et al. 2016), (Ding, Shen, and Gerlich 2017), (Ding, Shen, and Gerlich 2017), (Shen, Chen, et al. 2018); Al/Mg - (Suhuddin et al. 2014), (Suhuddin, Fischer, and dos Santos 2013a), (Liu, Ren, and Liu 2014); and Mg/steel - (Chen et al. 2015), (Shen, Ding, et al. 2016). Figure 47 shows the lap joint strength achieved for a wide spectrum of metal combinations, studied in HZG or from data published in the literature.

The feasibility of joining Mg to steel by Refill-FSSW was first studied by (Chen et al. 2015), using ZEK100 Mg alloy, Table 16. It was reported that the metallurgical bonding between the ZEK100 Mg matrix and DP600 steel matrix was accommodate by discontinuous particles of Fe-Al IMC's. Partial

bonding and brazing effect due to Zn reaction and partial liquation contributed to the weld strength. The fatigue behavior of ZEK100/ZEK100 similar joints and ZEK100/DP600 dissimilar joints was studied by (Shen, Ding, et al. 2016). Promising results were achieved, unlike typical dissimilar Refill-FSSW, the fatigue life of the ZEK100/DP600 dissimilar joints was significantly higher than the similar combination.

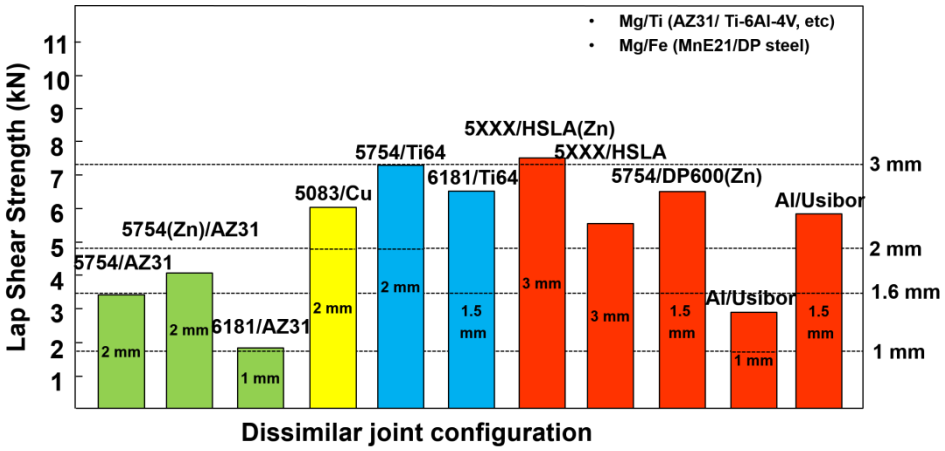

Figure 47- Lap shear results for different metal dissimilar joints. Internal results achieved in several works of WMP and published lierature.

Table 16- Main element composition for AZ31 (Banglong Fu) and ZEK100 (Shen, Ding, et al. 2016).

Reference	Alloy / Comp. (wt.%)	Al	Zn	Zr	Nb (RE)	Mn
Current Report	AM50	4.9	0.2	---	----	0.45
Banglong Fu work	AZ31	3.1	0.8	----	----	0.44
(Shen, Ding, et al. 2016)	ZEK100	---	1.3	0.25	0.2	0.01

Metallurgical Defects

Since there are no standard classifications for defects present in Refill-FSSWed joints, work currently being conducted in HZG facilities, the author created a possible self-designated classification, in which the defects are group in - Volume defects, Surface defects and Lack of Bonding. Combinations of welding parameters outside the process window, which result in improper heat input (lack or excessive), along with abnormal material flow behavior (insufficient or violent), are responsible for the formation of these defects.

- Surface Defects, Figure 48 – can be further classified in under fill or undercut, excessive flash (distinct from indentation marks), and poor surface finish. Poor surface finish is usually related to inadequate process parameters, but for under fill and flash defect, severe tool wear can be an additional factor;
- Volume Defects, Figure 49 – can be further classified in voids and wormholes, cracks, and lack of refill or incomplete refill. They are usually located: in the sleeve plunge path; near the major metallurgical features (hook, partial bonding, etc.); or near the interface, when the lower sheet is neither plunged nor its material intermixed (Mg-steel, Al-steel). Often associated to poor material flowability or inadequate heat input, the natural loss of material (even slight) can also contribute to the occurrence of volume defects (Zhao et al. 2014). These often upper sheet defects, depending on their number and dimensions can be preferable nucleation sites (Rosendo et al. 2011);
- Lack of bonding or Lack of Mixing, Figure 50 – are characterized by cracks or very weak bonding in the interface between the SZ and TMAZ (Shen et al. 2013), it is usually associated with plug type fracture on the upper sheet (nugget stays in the lower sheet). It is formed probably formed due to lack of stirred material or poor material plastic flow;

- Generic Defects – similar to any manufacturing process, common welding defects such as miss alignment between the two sheets, and other operation errors can occur (but they are progressively reduced by the increase in the automation level). When welding very thin non-conductive metal sheets or composite sheets (e.g. less than 1 mm), small thermal distortions and mechanical bending can occur if the clamping system wasn't properly designed.

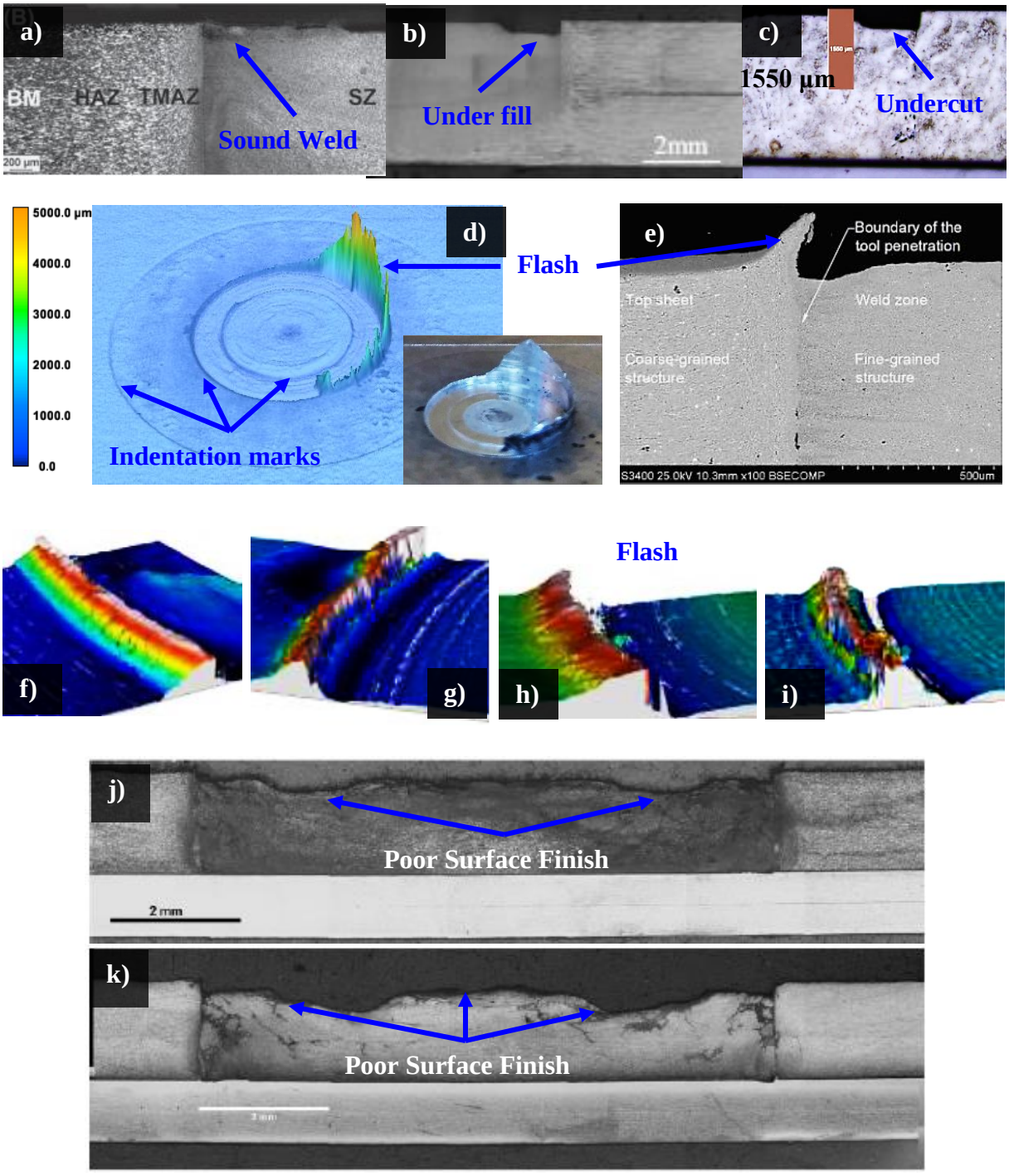

Figure 48- a) Sound weld with no surface defects (Amancio-Filho, Camillo, et al. 2011). b) Under fill in similar welding of 2 mm thick 2198-T8 Al alloy sheet, produced with PD=2.4 mm (Yue et al. 2017). c) Severe undercut produced by inadequate heat input in dissimilar welding of 3 mm thick AM50 to steel, produced with: PD=2.8 mm, RS=1500 rpm, PT=1 s, DT=0 s, RT=1 s. d) 3D laser mapping and photography of flash defect in dissimilar welding of 3 mm thick AM50 to bare steel, produced with PD=2.9 mm, RS=1800 rpm, PT= 1.5 s, DT=0 s, RT=1s. e) Detail of small flash formed in dissimilar welding in thickness, of 7075-T6 Al alloy (Kluz, Kubit, and Wydrzyński 2017). Evolution of flash with tool wear in similar welding of 6082-T6 after: f) 250, g) 814, h) 1080, i) 1303 spots (Montag et al. 2014). Effect of RS in the surface finish of the SZ in dissimilar welding of ZEK100 Mg alloy to DP600 steel, produced with: j) RS=1800 rpm and WT=3 s; and k) RS=3000 rpm and WT=3 s (Chen et al. 2015).

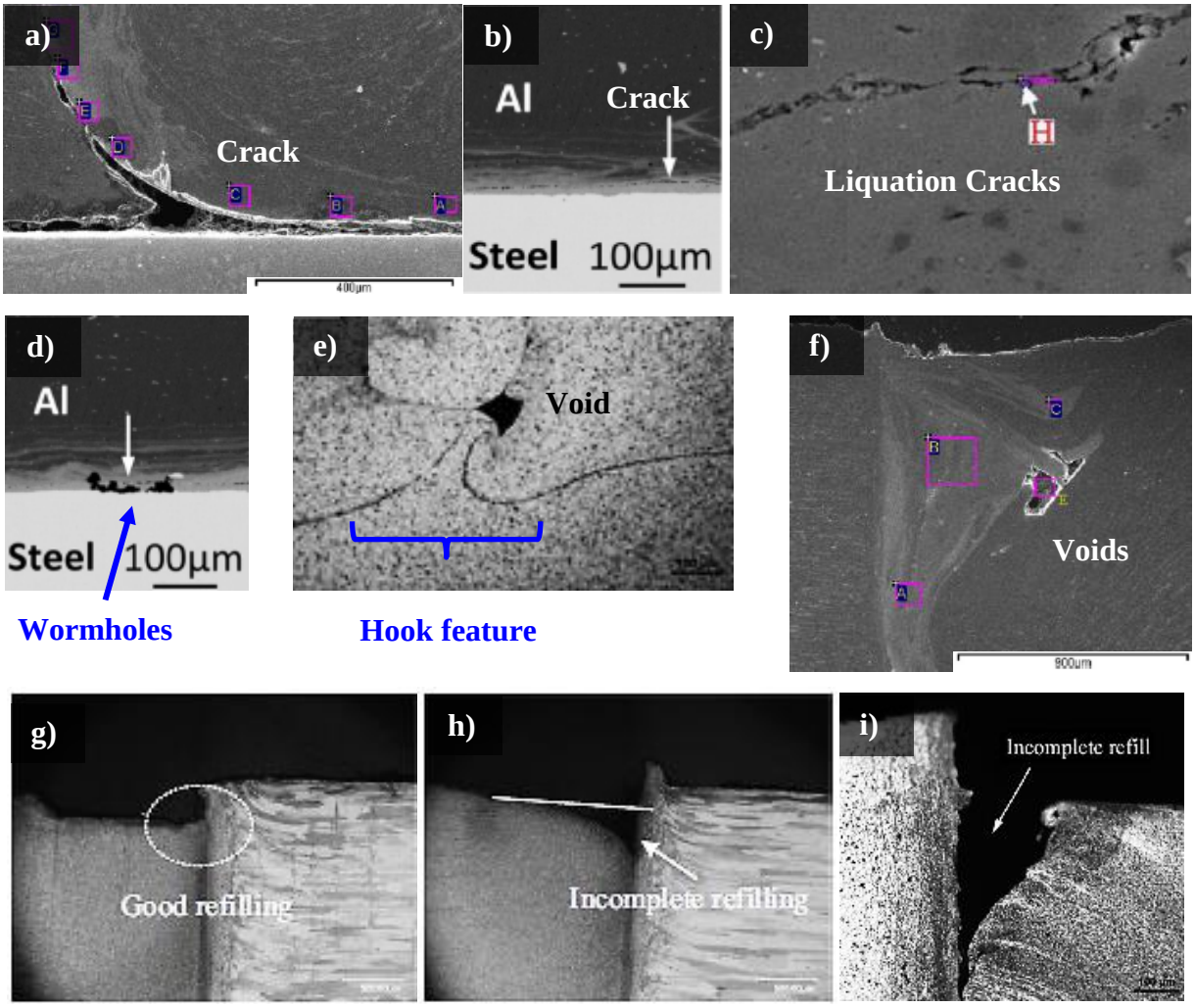

Figure 49- a) Crack at the interface near the sleeve path, in dissimilar welding of Mg-steel (Shen, Ding, et al. 2016). b) Crack near the interface in dissimilar welding of Al-steel (Dong et al. 2016). c) Liquation cracks in similar welding of 7075-T6 Al alloy (Shen et al. 2015). d) Wormholes in dissimilar welding of Al-steel (Dong et al. 2016). e) Void near hook feature (Shen, Yang, et al. 2014). f) Voids in dissimilar welding of Mg-steel in the SZ near the sleeve plunge path. g) Example of good joint refilling (Yue et al. 2017). Detail of incomplete refill for h) 2198-T8 Al alloy (Yue et al. 2017) and i) 7075-T6 Al alloy (Shen et al. 2013).

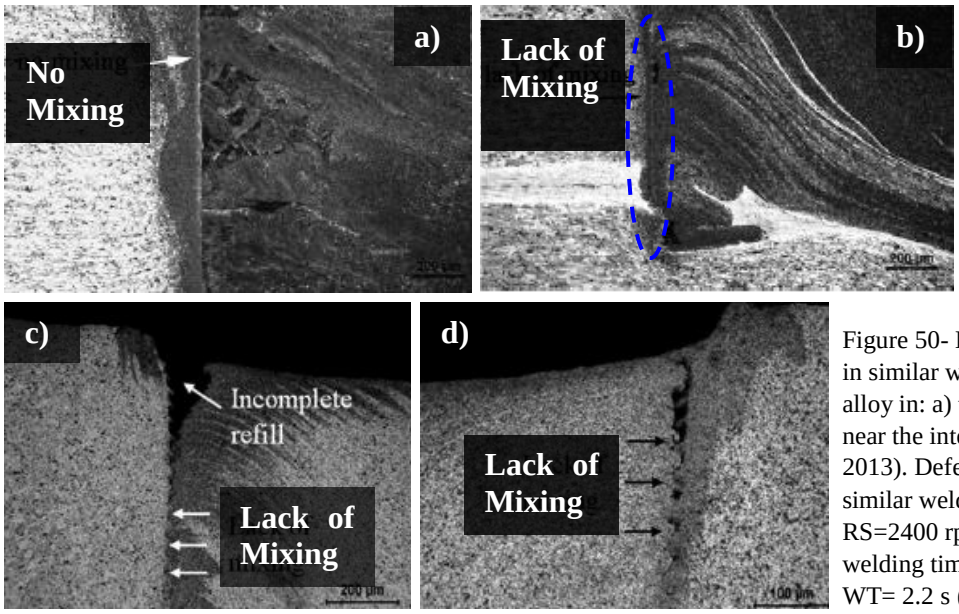

Figure 50- Detail of lack of mixing in similar welding of 7075-T6 Al alloy in: a) the upper sheet and b) near the interface (Shen et al. 2013). Defects found in 6181-T4 similar welds, produced with RS=2400 rpm and short total welding times: c) WT=2 s and d) WT= 2.2 s (Rosendo et al. 2015)

2.4.6 Bonding Mechanisms and Fracture Mechanisms under Static Loading

The bonding in Refill-FSSWed joints is a combination of several mechanisms: metallurgical bonding, mechanical intermixing, mechanical interlocking (Chen and Nakata 2010), and possible brazing/soldering additional effects (Shen, Ding, et al. 2016). Usually in dissimilar welding of soft-hard metals, mechanical intermixing doesn't occur. However, partial mechanical interlocking by partial deformation of the lower sheet, bending upwards into the upper sheet, can also play a significant role in the joint strength (Chen 2015).

Currently, there are no standards for classifying the fracture modes of Refill-FSSWed joints, under lap shear test. Thus, similar to what was done in section 2.4.5 for the metallurgical defects; the author organized the data collected from the literature in a possible self-designated classification. The fracture mechanisms are ultimately determined by the combination or individual action, of the different features detailed in section 2.4.5. The final failure mode results from the evolution of two different crack propagation mechanisms (Shen et al. 2015): annular cracks – that propagate along a plane parallel to the sheet surface, and are often associated with tearing of the region near the partial bonding and bonding ligament; and circumferential cracks - that propagate along a plane perpendicular to the sheet surface, and may nucleate in the upper, lower, or in both sheets (Rosendo et al. 2015). Combinations of different fracture modes are often associated to higher fracture loads and energy absorption (Shen, Yang, et al. 2014). The virtual combinations of fracture modes are illustrated in Figure 51, and some examples given in Figure 52 d), e) and h). Starting from the modes frequently associated to higher energy absorption capacity and mechanical strength, they can be classified in:

- Base Material (BM) or Plug fracture Sheet failure mode – occurs when the plastic limit of the cross section of the weaker metal sheet is reached. The fracture commonly propagates near the weld nugget due to stress concentration imposed by the spot, Figure 52 a) - b). The fracture surface usually evidences ductile failure behavior by tensile fracture of the parent sheet;
- Pullout Failure (PF), Through thickness, or Shear-plug mode – is essentially brought out by the circumferential crack mechanism (nugget rotation) (Shen et al. 2013), (Shen, Yang, et al. 2014), and the weld nugget is completely pulled out from at least one of the metal sheets. Depending in which sheet the plug hole is left, Figure 52 c), the failure type can be further classified in plug on upper sheet - fracture mode significantly more frequent, that can result from cracks initiated in the Hook, in the SZ/TMAZ interface, etc.; and plug on lower sheet - preferential mode that is related to better metallurgical bonding between the different welding zones (Shen et al. 2013). The total failure mode is characterized by the complete detachment of the nugget from both surfaces, and is explored in detail by (Rosendo 2009);
- Through Weld, Partial through thickness, Shear fracture, or Nugget debonding mode – the annular cracks propagate through the weld nugget region, or along the region of the weaker remnant faying surfaces (brittle cleavage fracture), Figure 52 e) - f) (Shen, Yang, et al. 2014);
- Interfacial Failure (IF) mode – the term interfacial failure was reserved to fracture through the interface for dissimilar welding between soft and hard metals, in which there wasn't penetration into the lower sheet, Figure 52 g) - h).

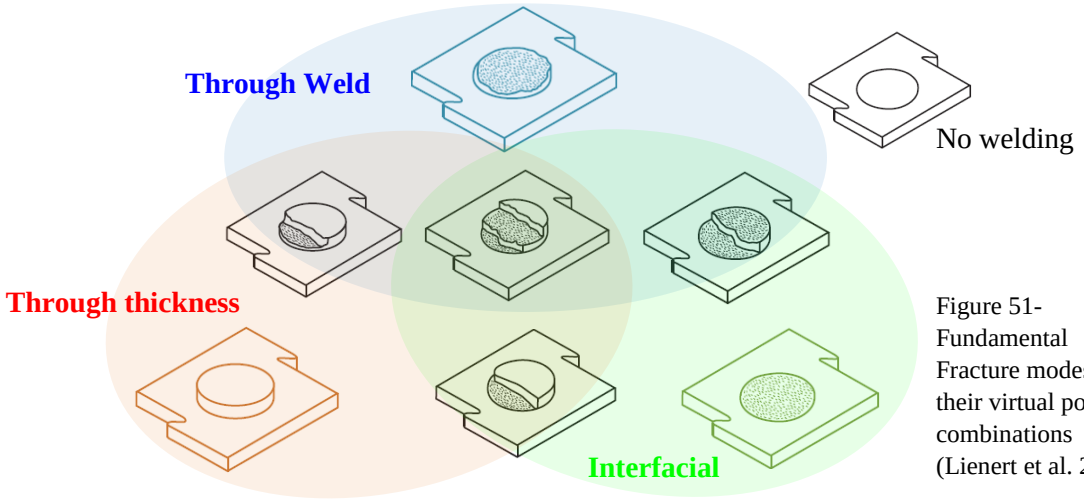

Figure 51- Fundamental Fracture modes and their virtual possible combinations (Lienert et al. 2011).

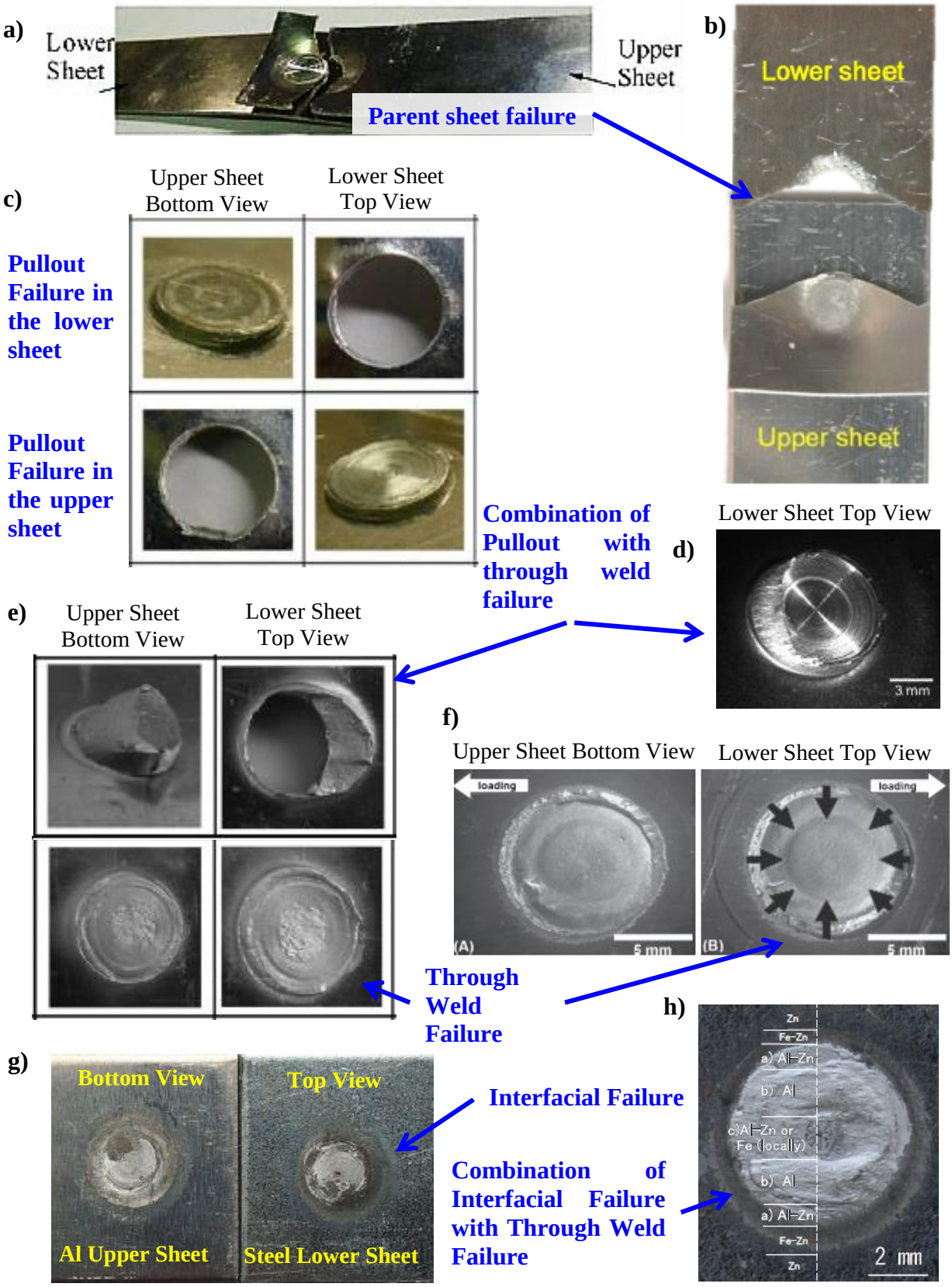

Figure 52- a) Fracture mode of 7075-T6 Al alloy (Shen et al. 2015). b) Fracture mode of 1.6/0.8 mm thick sheets of 7075-T6 Al alloy produced with RS=2400 rpm, PD=1.5, WT=3.5 s (Kubit et al. 2018). c) Pullout failures in 7075-T6 Al alloy (Shen et al. 2015). d) Fracture mode of 1.5 mm thick sheets of 5052-O Al alloy produced with RS=900 rpm, PD=1.55 mm (Tier et al. 2017). e) Fracture modes in 6061-T4 Al alloy (Shen, Yang, et al. 2014). f) Fracture mode of 3 mm thick sheet of 2024-T3 Al alloy, produced with RS= 2900 rpm, WT=5.8 s, PD=2.5 mm (Amancio-Filho, Camillo, et al. 2011). g) Interfacial fracture surface of Al-steel dissimilar welding (Shen, Chen, et al. 2018). h) Fracture surface of dissimilar welding of 6061 Al alloy to steel (Fukada et al. 2014).

2.5 Design of Experiments – Basic Generic Concepts

Design of Experiments (DoE) is a structured scientific methodology used to study any given system in which is possible to rigorously control the independent (also called input) variables or predictors. and record with an adequate measurement system the values of the dependent (also called output or response) variables (Mathews 2005). In other words, it resorts to active experiments. Active experiments are experiments in which the research controls the factors (input variable) values and records the response, whereas in passive experiments both the inputs and outputs are simply recorded (Montgomery 2017). This type of experiments is resource costly and time consuming, but it is used when the process can't be disturbed. Figure 53 illustrates the concept of a typical system whereupon DoE is applied. Other distinguishing feature of DoE is the possibility of recording in a random order all observations. Using this procedure is expected that the noise of random variables, not investigated nor controlled, gets cancelled out. Thus, the change in the response is essentially the result of the investigated factors.

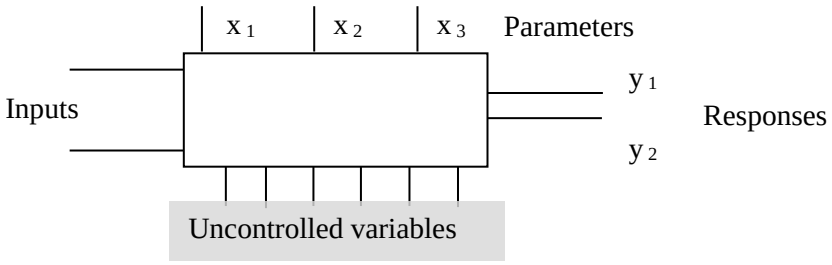

Figure 53- Schematic model of a generic system.

This technique is more powerful, robust, and most of the times more efficient than the traditional One Factor At Time (OFAT) or One Variable At Time (OVAT) technique. OFAT scientific method is used since the 19th century in empirical studies. It consists in a trial and error procedure where only one variable is changed at time (the best value is kept), in the pursuit of the best combination of parameters (Mathews 2005). It has some advantages and several drawbacks as enumerated below:

- First scientific method for experimentation and well rooted in the scientific community;
- For simple processes/systems can lead to less runs;
- Only adequate for main-effects systems – systems in which the response geometry is a multi-dimension plane (linear relations in all dimensions), Figure 54 a). Each factor has the same effect independently of the value of the other factors;

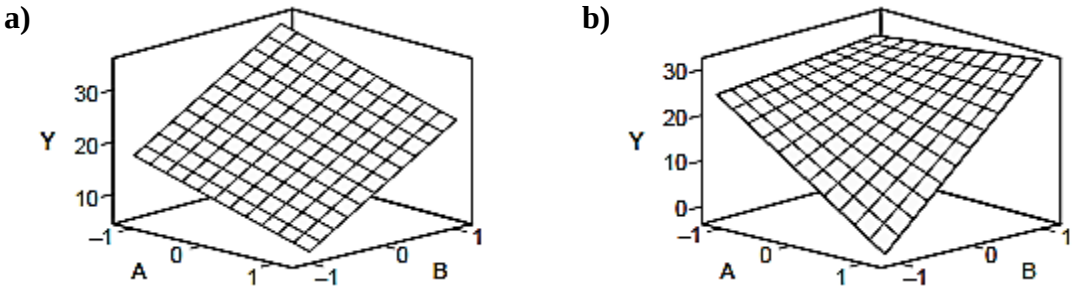

Figure 54- Graphic representation highlighting the difference between: a) first order model with only main factor terms, accuratly model by OFAT; and b) model with interactions terms, didn't modeled bt OFAT (Mathews 2005).

- Cannot identify nor quantify factor interactions. Figure 54 b) illustrates the surface response of a linear 2-factor model with interactions;
- Doesn't allow full randomization;
- Cannot perform optimization analysis.

(Mathews 2005), (Ryan 2007)

DoE is particularly interesting for multivariable systems, with simple or complex interactions between factors. Each design consists in a routine for the experiment. It specifies the levels (discrete values that the factors can assume) in each treatment/trial (combination of factor levels). After recording the output for each treatment, a multi-way Analysis of Variance (ANOVA) along with multivariable regression technique is used to fit a particular model to the data collected (Montgomery 2017), (Mathews 2005). The software used for this purpose was Minitab®, however there is a wide number of commercial and free software's available. In Figure 55, the mathematical definitions used to describe a generic model equation are illustrated.

$$y_1 + y_2 = \beta_0 \quad \beta_1 x_1 + \beta_2 x_2 + \ldots \quad \beta_{12}\, x_1 \cdot x_2 + \beta_{23}\, x_2 \cdot x_3 + \ldots \quad \beta_{123}\, x_1 \cdot x_2 \cdot x_3 + \ldots \quad \beta_{11}\, x_1^{\,2} + \ldots$$

Responses	Mean	Main Factors	Two-factor interaction Terms	Three-factor interaction Terms	Quadratic terms

Figure 55- Illustration of typical nomenclature used in DoE technical literature (Mathews 2005).

Even though the two-factor or higher-factor interaction terms are higher order terms, they cannot model curvature in the hyper-geometric surface response. Only models that have quadratic or higher order polynomial terms can in fact account for curvature. These types of models are used in design optimization of systems with high curvature in at least one factor or interaction. The surface twist should not be confused with model curvature, if one factor is fixed, the contour remains a straight line; the difference between the two is illustrated in Figure 56 a) - b) (Montgomery 2017).

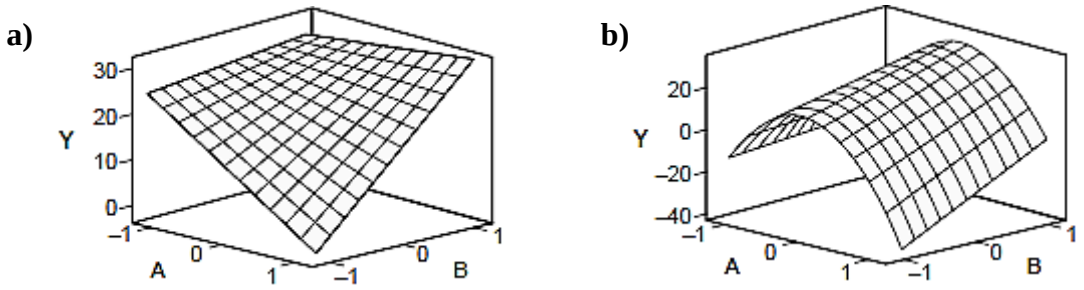

Figure 56- Surface response for a) two factor complete model; and b) model with true curvature (Mathews 2005).

The initial step of planning any experiment is to define the basis of the design i.e. the number of factors to take in account, the number of levels of each factor, and the extreme/corner values for each level (construction of the inference space). Only then it is possible to start to select the type of design (RSM, factorial, etc.), the standard design (Box-Behnken, Central composite Design, etc.), and finally the design features (Nº of center points and replicas, blocking, randomization, etc.). The only way to fill this knowledge gaps is to perform a preliminary study or test. Its success is critical to decrease the risks of unnecessary large designs. A preliminary test without the formality of the DoE usually takes the form of small sets of runs to investigate one or two variables at a time. It is usually conducted on basis of the previous experience of the researcher, and data collected from the literature. This pilot test should not be neglected, among other topics, it can (Montgomery 2017):

- Bring experience with new experimental variables for the researcher- check for unidentified variables (even if they are random variables) and check if each variable were identified and classified correctly (experimental, fixed, uncontrolled measurable and non-measurable);
- Roughly investigate the presence of curvature – corroborate the literature data or give a small suspicion of curvature. In the positive case, an intermediate level or center point is added to quantify or detect curvature in the output;
- Assess the consistency of materials and machines in the experiment – run the process a few times with the same set of parameters to obtain preliminary estimates of variation. or standard error;
- Identify the safe upper and lower bounds for the different experimental combinations of the factor levels, which can be run safely – safe parameter settings, are combinations of parameters that ensure no loss of data due to process instability.

After finishing the preliminary evaluation, the natural sequence is to run a screening design. This type of design gives the main effects and the statistically significant interactions. This allows eliminating some non-significant initially considered factors, and refines the model with only the most significant ones. For systems of very high complexity, more than one screening designs may be conducted, using for example hybrid steps of full and fractional factorial designs. The last step of an experiment sequence is to optimize the settings of the system with a Response Surface Method (RSM). The optimal search requires second or higher order polynomial terms, achieved usually with a minimum of three levels.

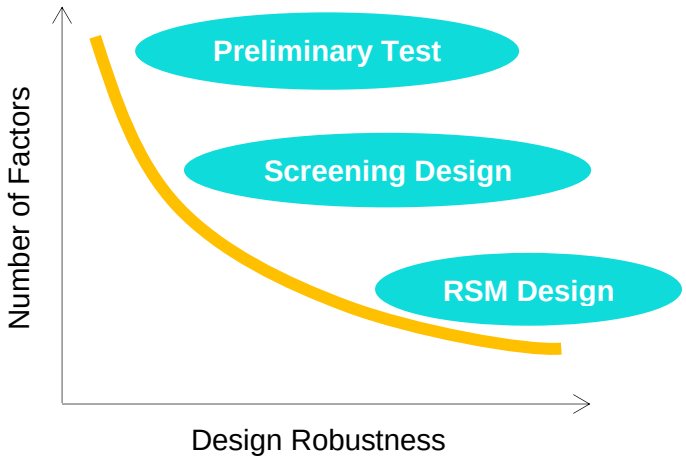

Figure 57- Natural path in the development of a generic experiment for study a given system.

Usually designs are classified according to their construction principle (full/fractional and number of levels) and principle usages. Table 17 suggests a possible classification of designs by their construction features and also gives examples of some designs. Different concepts and properties of experiment designs are summarized in Table 18.

Table 17- Classification of Design according to the output refinement and its main goal (Mathews 2005), (Montgomery 2010).

Partial/Fractional Factorial	Do not test all possible combination, allowing to reduce the total number of necessary runs Evaluates the statistical significance of each factor Study the relations and interactions between factors Used in screening design of experiments Designs: 2^{k-p}, Plackett-Burman's, 2^k Taguchi, etc…
Full Factorial	Study all possible factor combination The most common used are 2^k full factorial design. This type of design only considers first order linear relations between parameters and doesn't take in account response curvature. Used in screening designs for small factor systems or after a fractional factorial design was used Designs: 2^k, 3^k (quadratic design), m^k (null practical usage for higher levels)
Optimization DoE/ Response Surface Methodology (RSM)	Search for the optimal factor setting Designs: 2^k Centered (cofounded terms only allow to identify the presence of curvature), 3^k Design, Box-Behnken (BB), Central Composite Design (CCD), Taguchi 3^k

After choosing the design of the experiment, other topics like full randomization or randomization within blocks, number of blocks, number of runs, center points, etc. ought to be considered, subchapter 3.2.5.

Table 18- Different features and properties of experiment designs (Mathews 2005), (Montgomery 2010), (Cavazzuti 2012).

Classification Criteria		Description
Constraints	Factorial Design	No constraints are added to the domain of each factor
	Mixture Design	The independent factors are proportions of different components of a blend/mixture/composition Commonly used in chemical and metallurgical fields • Standard Mixture - The sum of each factor must be equal to 100% (e.g. optimization of alloy composition for its mechanical behavior) Designs: Simplex-Lattice, Simplex-Centroid Designs, etc… • Constrained Mixture - In addition to the sum=100% constraint, others constraints like maximum and/or minimum are added to the experiment factors. Designs: Simplex Centroid, Simplex lattice, Extreme Vertices designs, etc.
Replicas	Unreplicated	Only one observation for each corner point
	Replicated	Multiple observations for each corner point treatment Allow to compute signal to noise ratio
Factor Levels	Balanced	Each factor has the same nº of treatments for each of its levels
	Unbalanced	E.g.: Box-Behnken Design, Central Composite Design, etc.
Model Organization	Hierarchical	All possible lower-order terms that can appear in the model are present before higher order terms are introduced
	Non-hierarchical	Can be useful in model reduction in same cases Example: $y = x_1+x_2+x_3+x_1x_2+x_1x_3+x_1x_2x_3$; ~~x_2x_3~~
Number of Outputs	Single Output	Typical maximization, minimization or on-target problem
	Multiple Outputs	A desirability function is used to transform the response scale to the zero-to-one desirability scale. Its shape and distribution is defined by the weight ascribed to each output
Orthogonality	Orthogonal	Each factor is evaluated independently of all the other factors
	Non-orthogonal	Can lead to biased or incorrect conclusions
Number of runs – dimension of the model	Unsaturated	Nº runs is higher than the DF consumed by the model
	Saturated	Degrees of freedom available are null
	Supersaturated	Nº runs is lower than the number of terms of the model (severe limitation on the nº runs available for screening)
Rotatability	Rotatable	Variance of the predicted response at any point is only a function of the distance from the central point (not direction)
	Non-rotatable	After rotating the design points about the centre point the moments of the distribution of the design change

[blank page]

3 Experimental Procedure and Preliminary Considerations

3.1 Base Material and Specimen Geometry

3.1.1 AM50A - Magnesium Alloy

To produce the dissimilar joints, 100 x 25.4 x 3 mm^3 specimens of AM50A cast Magnesium alloy were used. From the plate geometry, only the 3 mm thickness was imposed. The remaining dimensions are defined as internal standard within the WMP department. As mentioned in the state of art subchapter 2.1, cast Mg alloys are essentially casted by die casting process (Moscovitch, Eliezer, and Aghion 2005), reaching 98% of the total cast Mg (Gándara 2011). However, the AM50A Mg alloy used throughout the entire experimental study was casted by a modified permanent molding process.

This permanent molding process is different from the conventional permanent molding processes. The microstructure and mechanical properties achieved by this process are comparable with those achieved with a common die casting process, enabling to produce final results easily transferable to the automotive industry. It is a laboratory scale optimized chill permanent mold casting technology, illustrated in Figure 58 a) - b). It assures ingots with a very homogeneous composition, microstructure uniformity and distribution, without porosity nor cracks or inclusions. With the set of parameters shown in Annex G, no macro segregation patterns were observed. The Mg coupons used were machined directly from the Ingot state. Mg can't be machined by water jet, since it easily oxidizes in contact with water. Thus, saw cutting and posterior milling were employed. In order to reduce the fire hazard (by reducing heat generation and by creating heavy chips and turnings), high speeds, heavy feeds and heavy depths-of-cut were used. However, some plates were discarded due the presence of surface burns. To avoid large solidification structures near the ingot walls, the plates were prepared has indicated in Annex G. In addition to inevitable metal solidification features, the heat transfer during the process is not uniform. Thus, a margin of at least 25 mm in the ingot upper part, and 15 mm in the lower part, were given to ensure structure and composition homogeneity, as illustrated in Figure 59. The cutting direction of the Mg plates schematized in Figure 59, only concerns material usage efficiency and technological aspects during machining operation. One of the reasons why a conventional die casting process wasn't used is because HZG (particularly MagIC division) doesn't have the necessary machinery. It would be necessary to buy the Magnesium ingots to the supply industry. However, that would imply buying a typical industrial batch, what would be completely excessive for the project material demands. On the other hand, since the modified permanent molding process was created by HZG, all the equipment needed was available and the delivering time shorter.

Chemical Composition and Metallographic Analysis

The chemical composition analysis was carried out by a HZG internal procedure. Material samples were cut from the casted ingots, in order to ascertain the real average chemical composition. In Table 19, industrial composition limits for the AM50A Mg alloy, as well the chemical analysis are presented (GrantaDesign 2017). A good agreement between the chemical analysis results and the industrial established values was obtained. The only exception was the Be and Ni content. The Be content is almost residual and without negative effect, but elements such as Ni, Cu and Fe are considered impurities and have a detrimental effect in the corrosion properties of the alloy. In order to control Ni and Cu content, careful control of the composition of the constituent alloys is necessary. At the moment there are no established methods to control these two impurity elements (Friedrich and Mordike 2006). Even though the Ni content exceeded slightly the interval, the Cu content is within the acceptable limits.

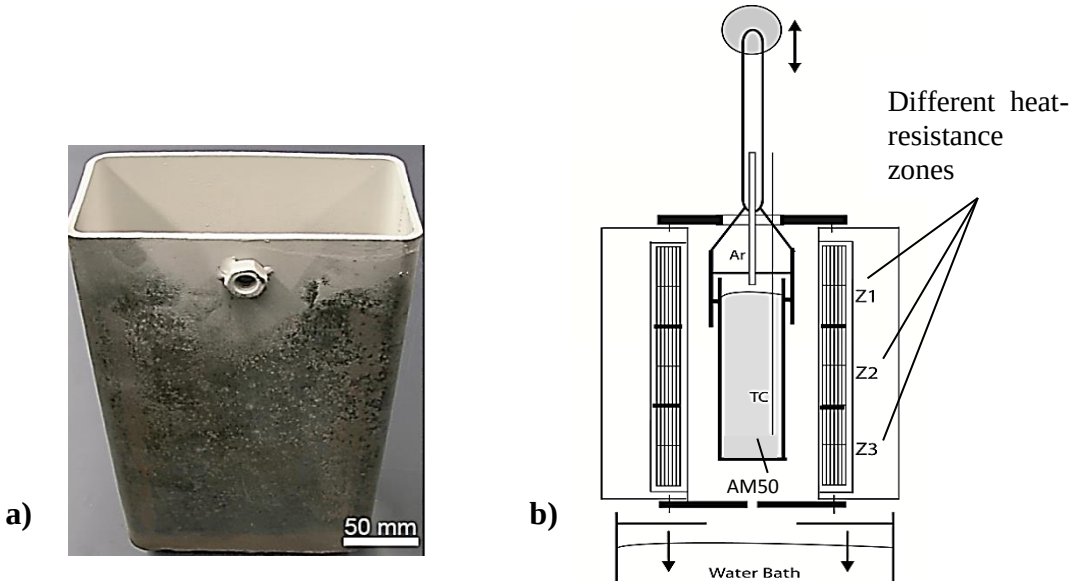

Figure 58- a) Stainless steel permanent mold, coated in the inner surface with a boron nitride thin layer, used to produce the ingots. b) Schematic illustration of the modified permanent molding process used, Annex G. (Elsayed et al. 2011).

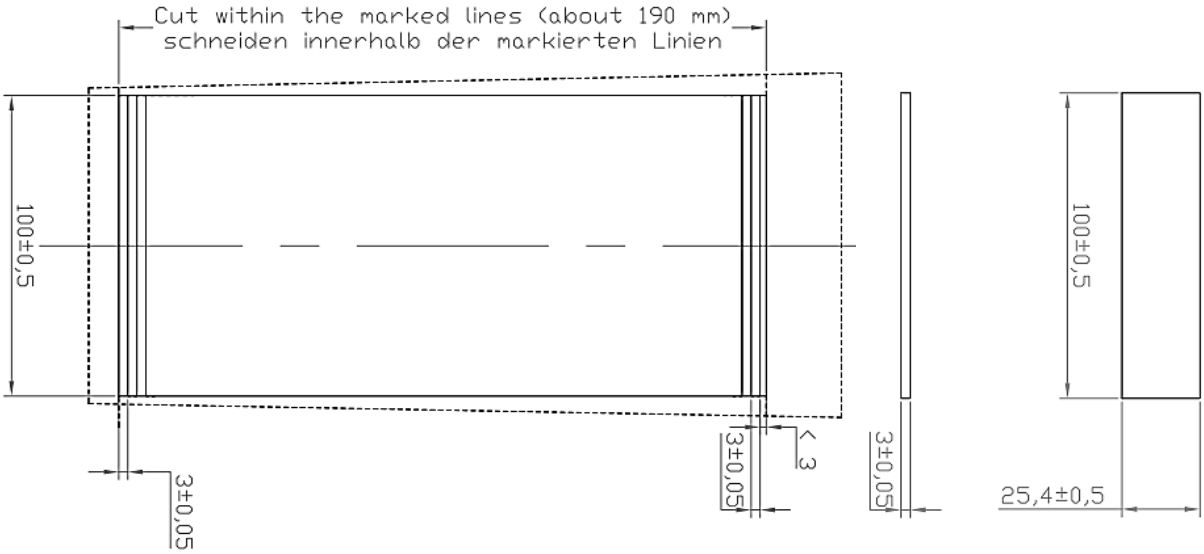

Figure 59- Technical drawing of the plate production from the Mg ingots, illustrating the safety margin left to ensure good macrostructural homogeneity.

Table 19- Measured chemical composition, and typical industrial values admitted for the casting AM50A Magnesium alloy (GrantaDesign 2017).

Chemical Element	Typical Chemical Composition (average % mass)	Measured Chemical Composition (average % mass)
Mg	[93.7 ; 95.3]	Balance
Al	[4.4 ; 5.4]	4.9
Mn	[0.26 ; 0.6]	0.45
Be	---	0.001
Cu	[0 ; 0.01]	< 0.008
Ni	[0 ; 0.002]	< 0.01
Si	[0 ; 0.1]	< 0.05
Zn	[0 ; 0.22]	0.2

In an ingot condition, as stated by (Kiełbus, Rzychoń, and Cibis 2006), AM50A is a heterogeneous alloy, consisting essentially of one primary solid solution, an intermediate eutectic, and minor secondary phases due to third alloying elements. In a simple way, is characterized by (Kiełbus, Rzychoń, and Cibis 2006), (Campbell 2008):

- Terminal solid solution α-Mg – globular primary equiaxed dendritic phase, consisting mainly of Mg lattice with substitution Al atoms. The grains of the α-Mg HCP matrix show a wide range of morphologies;
- Partially divorced eutectic α-Mg + $Mg_{17}Al_{12}$ – this metastable structure consists of a near-stoichiometric intermetallic γ-phase (also called β phase (Monas et al. 2015)) or compound (simple cubic structure), and α-Mg. The eutectic can show a widely range of morphologies, but tend to appear as partially or fully divorced eutectic. These microstructures distribute in the matrix rather homogeneously, nucleating both in the interdendritic regions and on the grain boundaries. Fully divorced eutectic structures are characterized by particles of γ-phase eutectic that are surrounded by interdendritic α-Mg eutectic phase. In the case of partially divorced eutectic, the γ-phase eutectic particles have small "islands" of α-Mg eutectic phase (Dahle et al. 2001);
- Precipitates of Mn_5Al_8 – typically exhibit polygonal or irregular morphologies such as spines, and have a heterogeneous distribution in the matrix, precipitating both inside and on the grain boundaries.

Microstructural features of the Mg base material are shown in Figure 60. Figure 60 a) shows by Optical Microscopy (OM), the grain morphology in an etched sample observed with polarized light; and Figure 60 c) details the Mg-Al partially divorced eutectic and the Al-Mn precipitates. SEM Figure 60 b), details the Mg-Al partially divorced eutectic structure and the multiple morphologies that Al-Mn precipitates can present. Figure 60 d) points out the segregation of the Al element into the grain boundaries. There are some differences regarding the permanent molding process used and the more often used die casting process, which are summarized in Table 20.

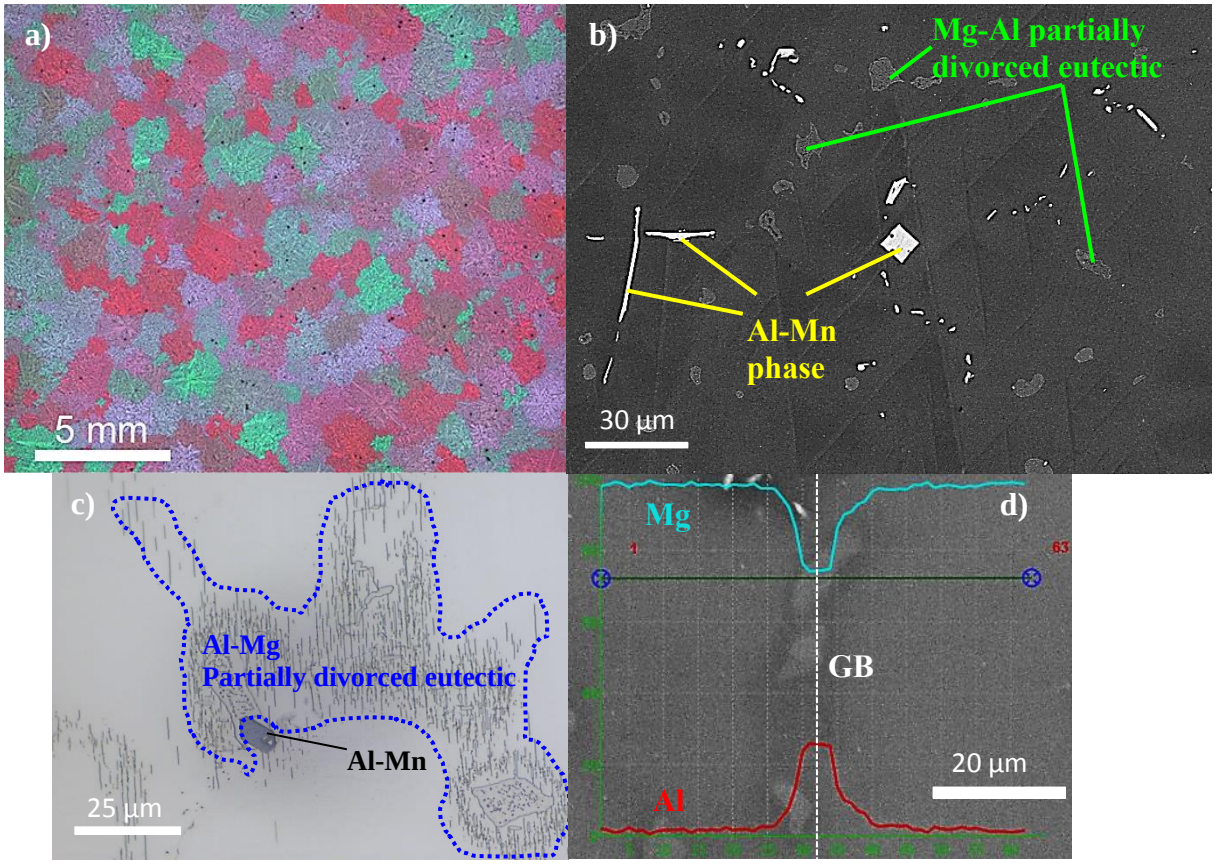

Figure 60- a) Equiaxed dendritic α-Mg growth, with an average grain size of 1.76 mm. Detail of the partial divorced eutectic structure and the Mn-Al precipitates b) - c). d) Al micro-segregation into the grain boundaries.

Table 20- Summary of the main microstructural differences between the die casting and permanent molding processes.

Permanent mold casting	**Die casting**
Coarse grain size (1.76 mm)	Finely (~100 μm) distributed structure
Partially divorced eutectic	Fully divorced eutectic
Solid Solution α-Mg structure	
Eutectic structure has interdendritic nucleation and is located inside or on the grain boundaries [1]	Lamellar γ-structure [2] Homogenously distribute in the matrix [2] γ-structure located on the grain boundaries [1]
Mn_5Al_8 precipitates both inside and on the grain boundaries [1] Polygonal or irregular morphology (spines) [1]	Mn_5Al_8 distribute more heterogeneously [2] Polygonal morphology [2] Mn_5Al_8 precipitates both inside and on the grain boundaries [1]
[1] (Kiełbus, Rzychoń, and Cibis 2006)	Hot chamber die casting machine + Permanent Molding
[2] (Wang, Eliezer, and Gutman 2003)	Cold chamber die casting machine

The Magnesium alloy plates were welded in bare condition. Neither surface treatments nor coatings were applied before welding. It is well known that Magnesium alloys generically have high corrosion susceptibility, which have greatly limited their larger scale use (Hu et al. 2012). Organic coatings (Hu et al. 2012), Chemical Conversion (Shashikala et al. 2008), Anodizing treatment (Blawert et al. 2006), and Metallic Platting (Bestetti and Da Forno 2011), are some of the most used protective coatings. Bare condition was imposed by the initial partner of the project. Corrosion protection will be given by post weld painting with organic coating. No further details, if a typical organic multi-layer painting or different advanced coatings (Upadhyay et al. 2017) would be applied, were given by the partner.

Mechanical Properties

Some deviation from the literature values was expected, The lab scale permanent mold casting process used was only recently developed in partnership with HZG (Elsayed et al. 2011). In addition, the data stored in the material databases is essentially industrial deep-rooted information based. In order to evaluate the tensile properties (Young modulus, yield strength, ultimate strength and elongation) of the base material, four tensile specimens were manufactured by the HZG workshop. The geometrical features of the tensile specimens are presented in the technical drawing sheet found in Annex H. The mechanical properties weren't evaluated by the author but rather downloaded directly from the material list provided by WMP. A fairly good agreement between the established and measured property values was found, Table 21. The only exceptions were: the elongation after rupture and hardness, which revealed significant higher values than the requirements (but without motives for concern); and the yield strength that was below the recommended values.

Table 21- Mechanical properties of the AM50 Mg alloy (GrantaDesign 2017).

Mechanical Properties	**Typical Properties**	**Measured Properties***
Young Modulus [GPa]	40 – 45	41
Yield Strength [MPa]	120 – 130	122
Ultimate Tensile Strength [MPa]	195 – 200	175
Elongation [%]	6.5 – 7.5	10
Hardness [$HV_{0.1}$]	36 – 39	50

* Average values

3.1.2 DP600 – Steel Alloy

To produce the dissimilar welds, 100 x 25.4 x 1.5 mm^3 HDG Zinc coated DP600 Dual Phase steel plates were used. Metal sheets of the desired material with thickness of 1.5 mm were already available in stock. The remaining dimensions are defined as internal standard within the WMP department. Usually referred by its most common commercial name DP 600, it is a dual phase AHSS (Advanced High Strength Steel). Depending on the thermomechanical treatment that the DP steel underwent, cold rolling or hot rolling, its designation according to the European Standards is HCT 600X or HDT 580X respectively (GrantaDesign 2017). The manufacturing route wasn't specified in the project requirements, being the author's responsibility to determine which type of DP to use. The justification to use cold or hot rolled DP600 was considered as part of the experimental procedure, reason why it wasn't detailed in the literature review. In the automotive industry, both processing methods are used. Hot rolled steel is commonly used for structural components and other applications where incredibly precise shapes, dimension precision, and surface finish (scaly aspect), have less importance. Typical applications include metal sheets for off-screen components, heavier frames and some beams. Cold rolled is usually produced with lower thickness and has better strength as a result of strain hardening. These properties make cold-rolled steel most suitable for steel auto body and when aesthetics and visual appeal are a priority (Kumar et al. 2014). Since there weren't specifications regarding the production process, and commercially available cold rolled steel sheet was available in stock, lap joints were produced by cold rolled DP 600 plates. The longitudinal direction of the coupon is transversal to the rolling direction as depicted in Figure 61. In order to study the influence of the Zn coating in the welding mechanism, similar plates of the same material and geometry were machined. The manufacturing process was the same, with the only exception that no Zinc coating was applied in the final stage after rolling the metal sheet.

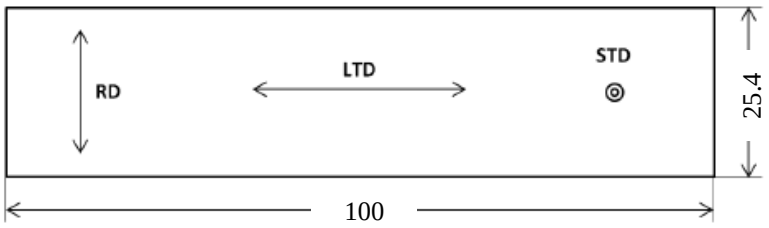

RD Rolling Direction LTD Longitudinal direction STD Short Transverse Direction

Figure 61- Schematic representation of the cutting direction of the steel plates regarding the rolling direction.

Chemical Composition and Metallographic Analysis

As defined by (Silva, Alves, and Marques 2013), steel is considered to be alloyed to a certain element, when at least one of the industrially accepted limits of Table 22 is exceeded. The chemical composition results are shown in Table 23; typical industrial values were also added.

Table 22- Element maximum mass %, in order to not be considered impurity (Silva, Alves, and Marques 2013).

Chemical Element in wt.%									
Al	Co	Cr	Cu	Mo	Ni	P+S	Ti	W	V
0.10	0.30	0.25	0.35	0.10	0.50	0.12	0.05	0.30	0.05

Regarding the steel matrix microstructure, typical refine grains can be observed in Figure 62 a). AHSS Zn coated coupons were manufactured with an average 10 μm zinc coating layer. The coating process was Zinc Hot-Dip Galvanizing (HDG), commonly used in the automotive and other industries. Several Zinc and other different coating processes, with more or less application, are also used in the auto industry. Several common types of zinc coating process are summarized in Annex D. A significant uniform Zn coating was observed, with a 9.7 ± 3.9 μm thickness range in the measured zones. It is also worth notice the presence of an ultra- thin Fe-Al IMC's layer, between the pure Zinc layer and the steel

matrix, Figure 62 b). This layer with an average thickness below 1 µm, was probably formed during the Hot-dip Galvanizing (HDG) process, and was mainly composed of $Fe_2 Al_5$ intermetallic compounds. The Al present in the IMC's was probably captured during the hot bath. According to (Shibli, Meena, and Remya 2015), Al is added in order to supress the formation of Fe-Zn brittle IMC's layer.

Table 23- Measured chemical composition and typical industrial values for DP600 steel (GrantaDesign 2017).

Chemical Element	Typical Chemical Composition (% mass)	Measured Chemical Composition (% mass)
C	[0.06 ; 0.17]	0.10
Al	[1.2 ; 2.2]	0.8
Mn	[0.4 ; 2.5]	1.70
Si	[0.18 ; 1.4]	0.25
V	[0 ; 0.2]	0.002
P	[0 ; 0.08]	0.02
S	[0 ; 0.015]	0.005
Cr+Mo	[0 ; 2]	0.5
Ti+Nb	[0 ; 0.30]	0.02
B	[0 ; 0.005]	0.003

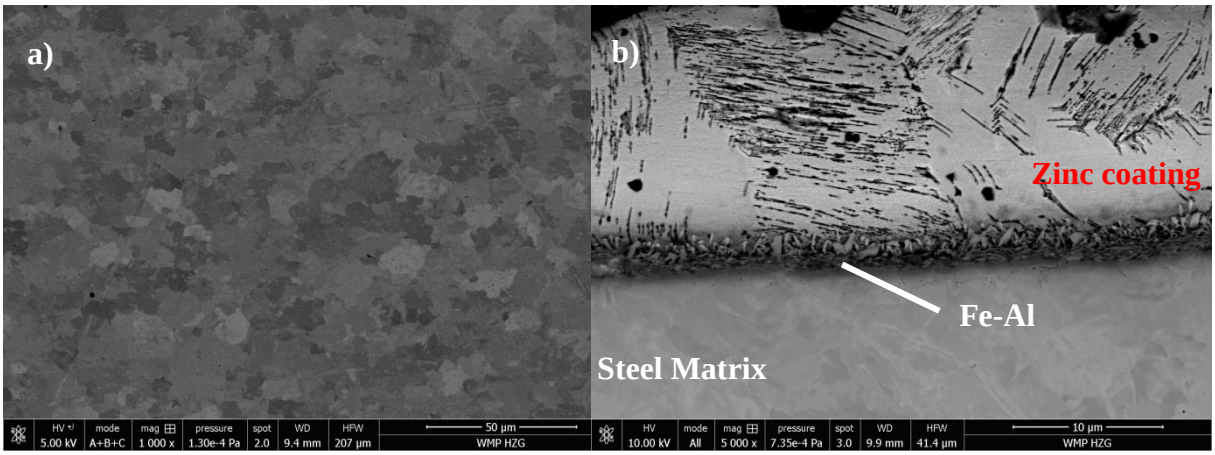

Figure 62- a) Metallographic analysis of the steel base material in transverse direction. b) Detail of the Zinc coating composition and morphology.

Mechanical Properties

The steel sheet used evinced typical mechanical properties of Dual phase steels, a good trade-off between high strength and ductility. An overall good accordance between the measured and established values was obtained, as detailed in Table 24. The bare steel used exhibits the same mechanical properties.

Table 24- Mechanical properties of the steel base material (GrantaDesign 2017).

Mechanical Properties	Typical Properties Range	Measured Properties
Young Modulus [GPa]	200 – 221	213
Yield Strength [MPa]	330 – 450	379
Ultimate Tensile Strength [MPa]	600 – 700	624
Elongation [%]	16 – 30	22
Hardness [$HV_{0.1}$]	181 – 205	201

3.2 Welding Procedure

3.2.1 Experimental Procedure

Figure 63 outlines the experimental work proposed to follow during this project. First the base materials were proper characterized and a small literature review of each was done. After that, some welding trials will be performed to conduct a preliminary study to check the feasibility of the dissimilar welding and to decide which parameters and their extreme levels to study in the DoE. With the study window defined the first part of the DoE followed, in which the lap shear tests would be conducted and all the statistical analysis performed. Finally, the metallurgical study of the relevant parameters will be conducted. This part of the experiment is scientifically more compelling since it explains the physical and chemical processes that occur during welding, and unveils the bonding mechanism.

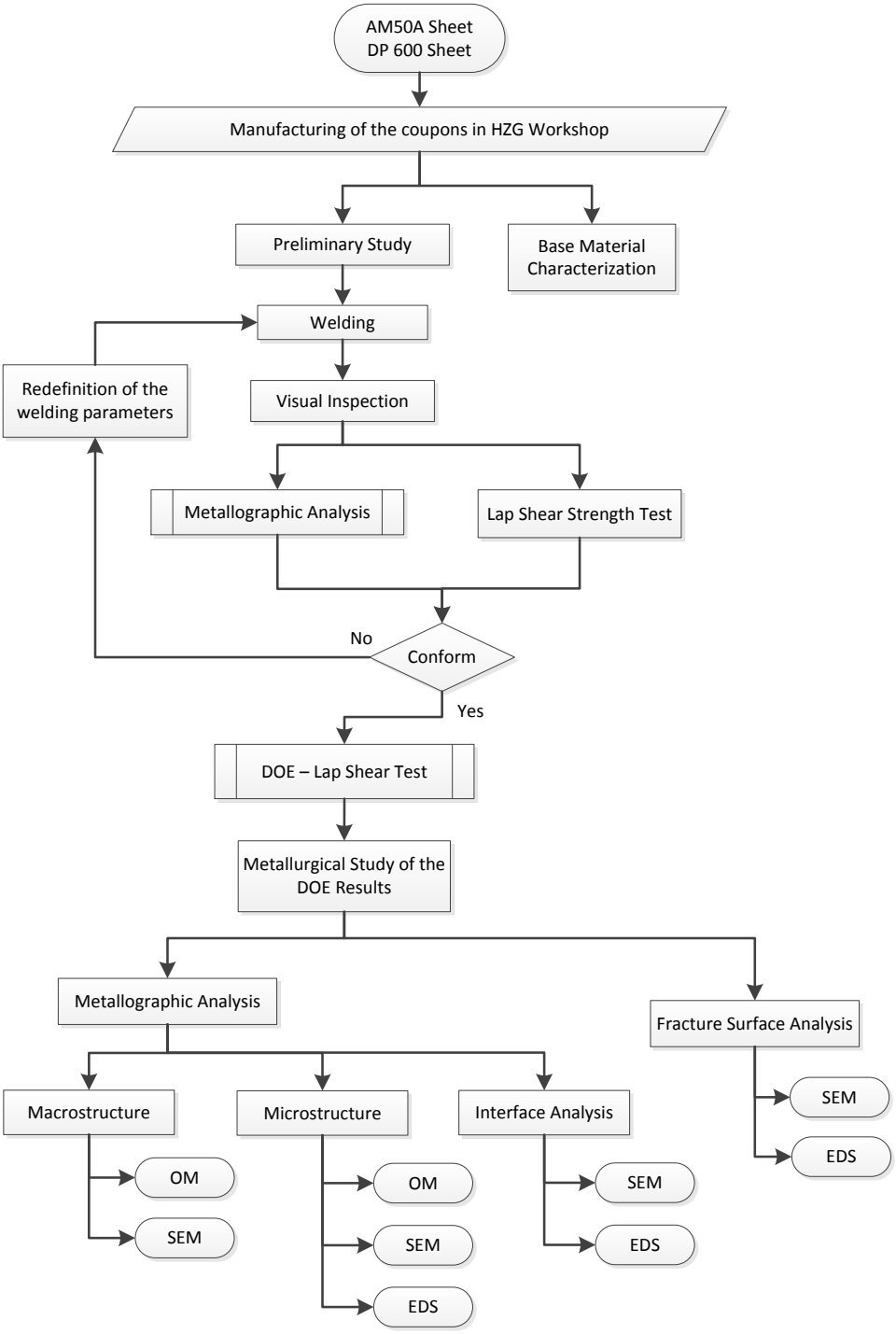

Figure 63- Workflow of the experimental work.

3.2.2 Welding Machine and Welding Technique

All welds studied during this report were performed in RPS200 Refill-FSSW machine at HZG facilities, Germany. This piece of equipment isn't commercially available, but rather a single series order. RPS200 was developed by Harms & Wende, according to the specifications and with the support of WMP department, Figure 64 a). The welding machine wasn't design to support industrial work rates; it is dedicated to small to medium-size specimen production with structural testing purposes, being able to weld high strength materials such as steel and Ti. HZG has other commercially available Refill-FSSW machines (e.g. RPS100), but RPS200 was used since it is the only machine that allows to perform Differential Rotation (DR). Table 25 summarizes the main characteristics of the welding machine used. As a technological highlight of the equipment used regarding the DR capability, only the direction of the probe rotation could be changed. Even though the actuators of either probe or sleeve can invert their rotation direction, the sleeve torque is transferred by an assembling mechanism that is thread based. Thus, it can get loosed if the rotation is inverted. In contrast, the torque is transfer to the probe by a hexagonal head, as illustrated in Figure 69. The machine is equipped with a series of transducers. Torque and axial force from both sleeve and probe were recorded during the welding. A pneumatic spring offsets the machine head weight. The quantitative torque precision can be affected from an average friction force of more or less 250 N. Angular velocities and travelling positions were also recorded. Temperature measurements were performed using the external apparatus illustrated in Figure 68 a) - c), since the machine transducer was only capable of measure the tool temperature. The positioning system and clamping system for the lap joint are clamped to the backing support depicted in Figure 64 b), which in its turn was fixed to the working table by two different clamping devices, Figure 64 c) - d).

A different welding technique from the one commonly used for soft similar and dissimilar materials (e.g. Figure 29), was employed during the experiment described in this report. This technique is similar to typical Refill-FSSW but with the particularity of only plunging into the upper soft Mg material sheet. The joint configuration is always with the softer material (Mg, Al, etc.) as the upper plate, and the harder material (steel, Ti, etc.) as the lower plate. The process is illustrated in Figure 65 and the main advantage is to be able to use lower cost tools based on tool steel. The bonding process is essentially pure metallurgical bonding, and it has been successfully already employed for Refill-FSSW of Al-steel (Suhuddin et al. 2017), Al-Ti (Plaine et al. 2015), and wrought Mg-steel (Chen et al. 2015).

Table 25- Main features of the Harms & Wende RPS200 welding machine used to perform the Refill-FSSWed joints.

Hardware	Welding Force	35 kN
	Clamping Force	40 kN
	Max Torque	60 Nm (90 Nm for 15 s)
	Bi-rotational Speed for probe and sleeve (independently)	3300 rpm
	Max Travelling Velocity for sleeve *apply area factor for probe velocity	6 mm/s
	Stroke of Welding Tools	10 mm
	Stroke of Welding Head	300 mm
	Welding Table	1000 mm x 500 mm
	Weight	4,7 t
	Voltage Supply	400 V / 50 Hz
	Pneumatic Supply	6 bar
Sensors	Travel displacement	Probe, Sleeve and Clamp
	Intrusion Force / Clamp Force	Probe and Sleeve / Clamp
	Torque	Probe and Sleeve
Control	Position / Displacement control	Precision of 0.05 mm

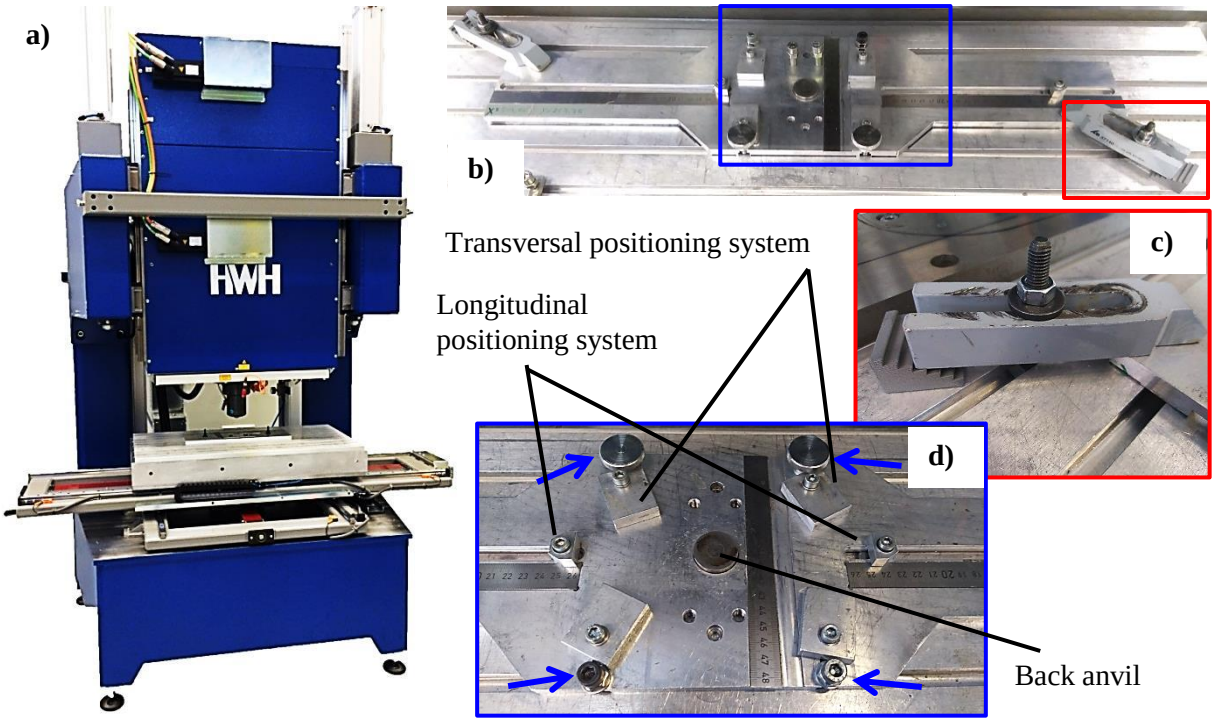

Figure 64- a) Refill-FSSW machine RPS200. b) Backing support device and details of the two clamping systems used to fix it to the workholding table c) - d). In d) is also possible to observe the clamping system for the lap joint.

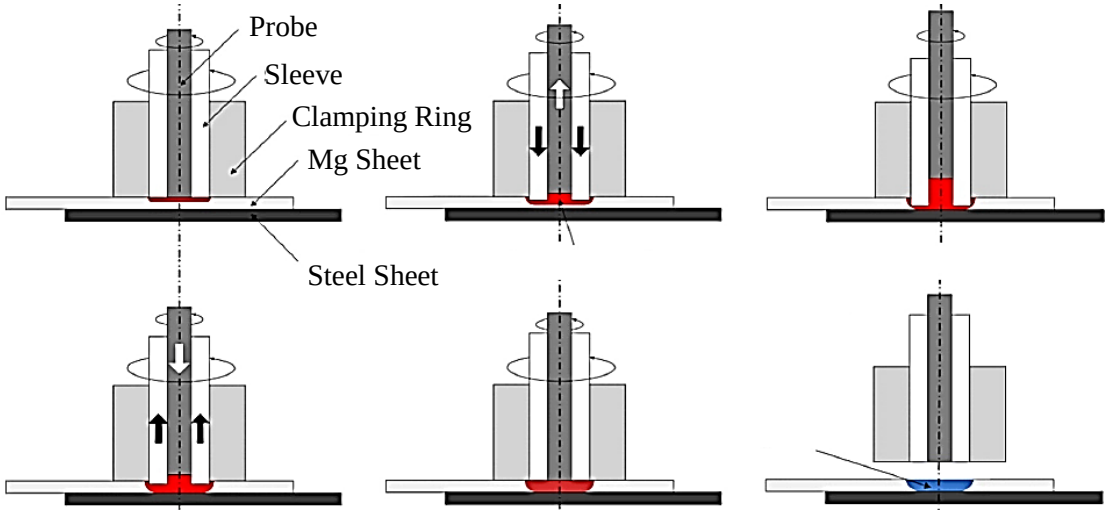

Figure 65- Illustration of the Refill-FSSW technique used to produce dissimilar joints of a soft material and a hard material. The detail of only plunging the upper sheet is highlighted (Dong et al. 2016).

3.2.3 Lap Joint Preparation, different Lap Joint Configurations, and Temperature Measurement Apparatus

For the AM50 Mg alloy the specimens used for the lap shear joint consisted of a 100 x 25.4 x 3 mm^3 plate, Figure 66 a). The faying surface were manually ground with a complete circumferential pattern of -45º/0º/45º/90º immediately before welding. For this procedure, a Starcke® alumina abrasive cloth was used. It consists of microgrit ISO 6344/FEPA P400 flexible cloth with average particle diameter of 35 µm. With this step, it was intended to remove the Mg-O oxide superficial layer, allowing a better experimental control. Before and after grinding, both surfaces were manually cleaned with ethanol. Neither chemical grinding nor ultrasonic bath was performed.

The DP600 steel specimen consisted of a 100 x 25.4 x 1.5 mm^3 plate, Figure 66 a). The coupon surface was in as-delivered condition, and no surface treatment was conducted to avoid damaging the

Zinc coating layer. During cold rolling, lubricants are purposely introduced in order to: reduce friction coefficient and friction heat generated between strips and roll surfaces, remove contamination, and reduce corrosion during storage. Thus, steel specimens were only manually cleaned with ethanol to remove the contamination layer. For the case of bare steel, the joint surface preparation was equal to the procedure adopted for the Mg plates faying surface. Since there is no Zn coating to protect the steel, it is necessary to remove the Fe-O oxides layer that naturally forms with atmospheric exposure over time. Neither chemical grinding nor ultrasonic bath was performed.

For the lap shear test, the specimens were clamped in the configuration illustrated in Figure 66 b). The Mg plate was maintained on the upper position during the complete experiment. The overlap length of 25.4 mm is defined internally as standard, Figure 66 a). All the specimens were welded in the center of the overlapped area. To ensure the alignment of the plates and the correct overlap distance, two spacers of the same material were used. A 40 mm diameter back anvil detailed in Figure 64 d) and assembled in the backing support of Figure 64 b) supported the axial loads, granting stiffness in the overlap region.

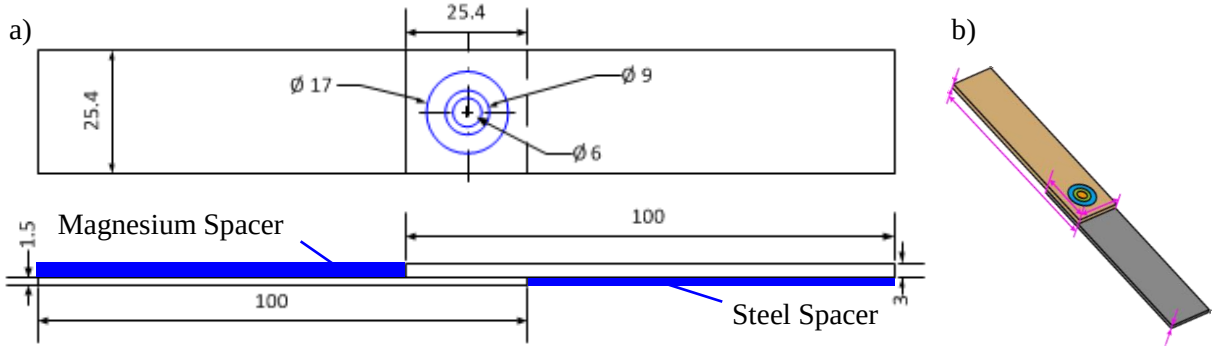

Figure 66- a) 2D schematic drawing; and b) 3D model of the overlap configuration.

As can be seen in Figure 64 d), the lap joint can be adjusted in the xy plane perpendicular to welding movement. Two mechanical end stops adjust the longitudinal position, and other four adjust the transversal position avoiding rotation in the z axis, Figure 67 a). First the back anvil is aligned with the center of the clamping ring by manually controlling the worktable position. Then the specimens in the correct lap joint configuration are manually aligned so that the center of the overlap area is aligned with the center of the back anvil; then the end stops are fixed. This step is a trial and error process until achieving the proper overlap positioning references. Before welding, the fixing device illustrated in Figure 67 b) is assembled and only half of the previous positioning system removed (to avoid losing the positioning references). This allows the joint to deform freely, as a result of thermal expansion and volumetric elastic straining imposed by tool action. Full overlapping shown in Figure 67 c) was used in metallographic samples and samples for temperature measurements.

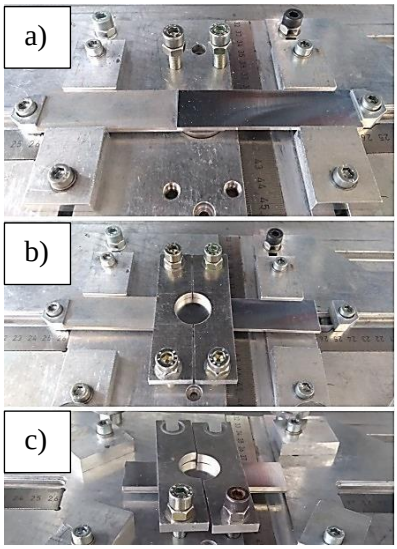

Figure 67- Detail of the clamping system used: a) to set the welding position; b) during welding. c) Full overlapping apparatus.

The configuration previously detailed was only used to produce lap shear test specimens. Concerning the spot welding of joints for metallographic samples and temperature recoding, the configuration adopted was the two plates in full overlap. In the full overlapped plates, three spots were produced as illustrated in see Figure 68 a). It allowed increasing material usage efficiency, important to manage the experiment with the material in stock. The positioning system of Figure 64 d) didn't allow controlling the position of each spot in the total overlap configuration. Thus, the three spots were distributed more or less evenly based on the machine operator skill.

There are several methods that can be used to measure the temperature during welding process (Nandan, DebRoy, and Bhadeshia 2008), e.g. thermal camera that measures the surface temperature is being widely used for friction surfacing process. However, a system based in an embedded thermocouple

in the lower sheet was preferred. It is one of the most common and rather simple temperature measurements systems in FSW, and in particular Refill-FSSW, that is capable of recording the temperature near the interface of the two plates, Figure 68 a) - c). Initially the temperature of the Mg-steel interface in the center of the spot and in the mid-thickness of the clamping ring was intended to be measured. However, some difficulties were experienced in correctly assembling both thermocouples, and guarantee that both tips were in contact with the bottom of the blind holes. The data shown in this report only concerns the temperature recorded in the center of the spot, the temperature in the mid-thickness of the clamping ring was also recorded but not in due time. In order to ensure that the thermocouples were aligned with the center of the tool, guidance marks in the upper surface of the Mg plate were traced with a height scriber, Figure 68 a). These marks circumscribed the clamping ring, helping to manually align both plates with the welding tool. To measure the temperature, type K thermocouples (+Ni Cr / -Ni Al) with 0.5 mm diameter were used. This type of thermocouples is one of the most common type because of it is cost effective, accurate, reliable, and has a significant wide temperature range. LabView 2010® software operated with a National Instruments™ data acquisition module, capable of measuring with a 100 Hz fixed rate, was used, Figure 68 b). The holes in the steel plate were manufactured in an Alzmetall® Alztronic 6 bench drill with 1300 rpm, 3 manual penetration steps and a Bungard® hard carbide metal drill with 0.6 mm diameter.

a)

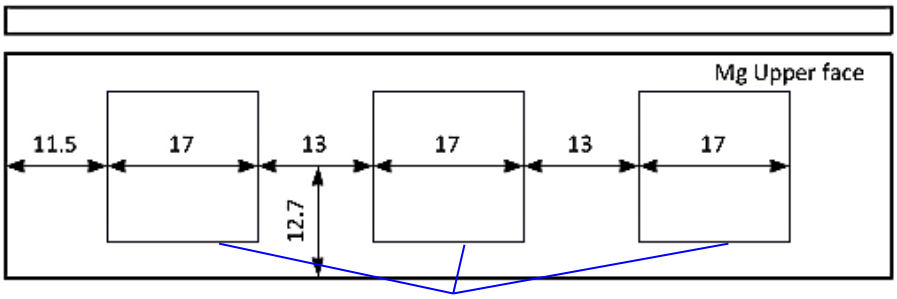

Guidance Marks traced in the Mg upper surface to align the center of the tool and the

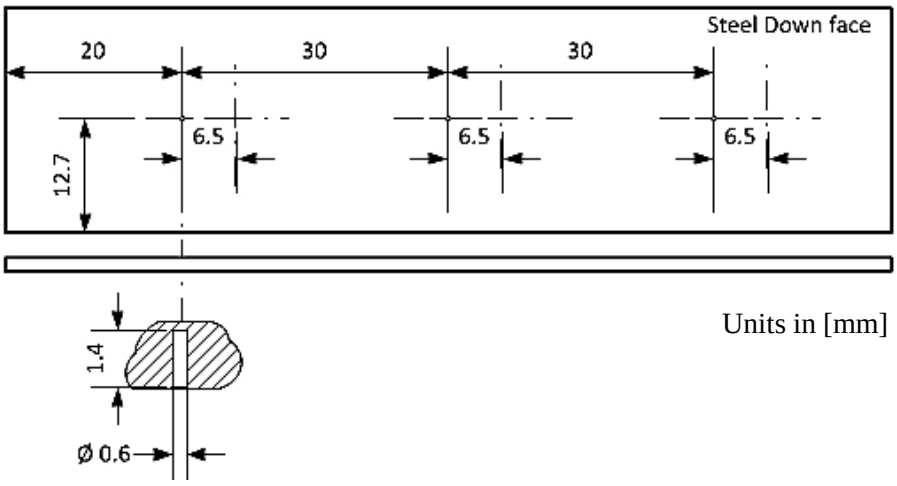

Units in [mm]

b)

Texas Instruments™ module for data acquisition.

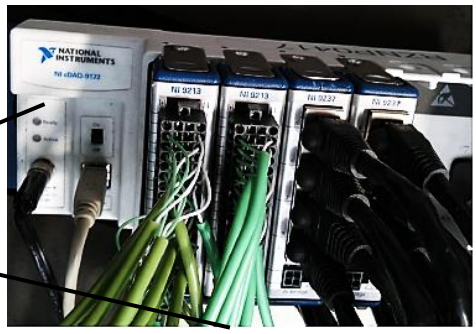

Thermocouples connection

c)

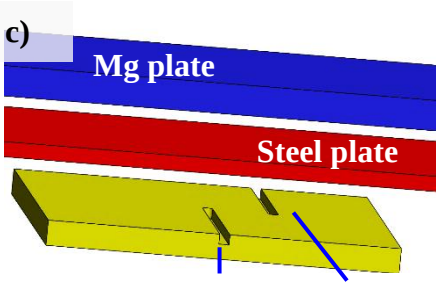

Channels to guide and accommodate the tips of the thermocouples

Figure 68- a) Schematic drawing of the specimen used for temperature measurement. b) Module used to acquire the temperature data. c) Scheme of the spatial configuration of the system used to assemble the thermocouples.

3.2.4 Refill-FSSW Tool

In order to perform the Refill-FSSWed joints, a tool made of UDDEHOLM HOTVAR® hot-work tool steel alloyed to molybdenum-vanadium was used. It is an AISI H13 equivalent hot working steel and its basic mechanical properties are given in Table 26. The tool is shown in Figure 69 and its main geometric features can be found in Table 27. Due to a cylindricity tolerance between probe and sleeve of 0.2 mm, special cautions during tool assembling were taken. In order to ensure consistency, weld quality, and reproducibility during the experiment, two complementary methods were used to keep the toolset cleaned.

- In between welds, a manual cleaning cycle was performed to minimize the build-up of material during trials. It consisted in moving the probe (10 rpm) and sleeve (20 rpm) throughout their maximum travelling course with different rotation speed. After some welds, these cleaning cycles were insufficient to remove the deeply accrued Magnesium;
- Periodically, after no more than 25 welds, the three pieces were disassembled from the machine and left in a cleaning solution. It consisted of 20 ml of commercially available vinegar (25% acetic acid by volume) diluted in 80 ml of distilled water. They were left until all the Magnesium was consumed by the chemical reaction (when the bubbling stops), depending on the amount of accumulated material, up to 15 min were needed it.

After bathing in the acid solution, they were generously cleaned in the following order: with ethanol (to remove the acid solution), distilled water (to remove the compounds hypothetically formed) and finally with ethanol again (to remove the water) and dried with compressed air to avoid the formation of rust.

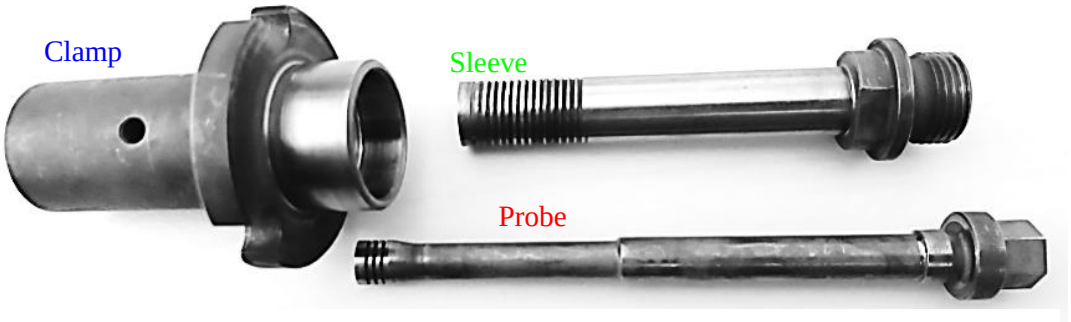

Figure 69- Appearance of the three-piece tool system used to perform the Refill-FSSWed lap joints.

Table 26- Mechanical properties of the tool steel used to produce the Refill-FSSW tool, (Uddeholm 2011).

Mechanical Properties	
Hardness	56 HRC
Yield Strength	1820 MPa
Ultimate Tensile Strength	2200 MPa

Table 27- Summary of the characteristic dimensions of each component of the welding tool.

Component	Inner Diameter [mm]	Outer Diameter [mm]	Tip surface	Features
Probe	---	6	Plane	Outer wall-grooved
Sleeve	6	9	Plane	Outer wall-threaded Inner wall-smooth
Clamping	9	17	Plane	Outer wall-plane Inner wall-grooved

3.3 Experiment Design – Conventional Rotation Refill-FSSW

The procedure used to define the final design for the experiment in CR Refill-FSSW, is detailed in Figure 70. All steps and assumptions behind the selection process are detail in this subchapter.

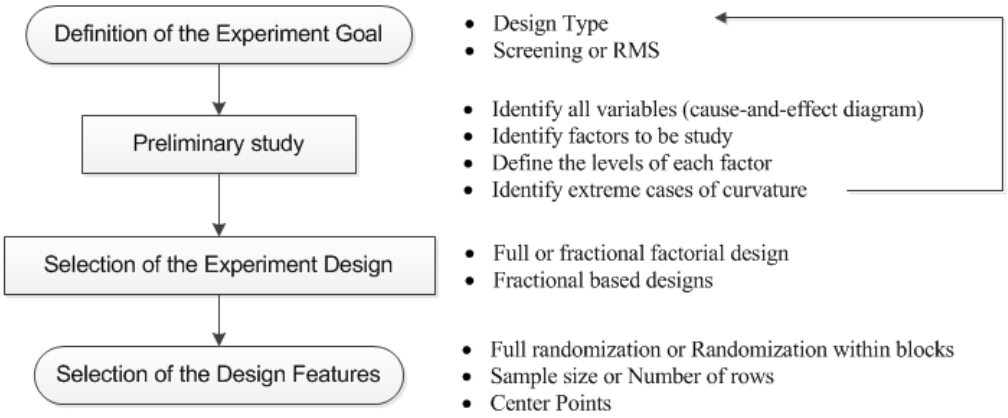

Figure 70- Methodology used in the design of the experiment.

Depending on the experiment goals and context, a specific type of design is more adequate than others. Response Surface Methodologies (RSM) are designs more often used in industrial environments. From the scientific point of view, it is more interesting to explain from the physical and metallurgical perspective the main effects from main factors and their interactions; a task adequately done by screening designs. When high suspicions of response curvature (non-linearity of the effects) for a specific parameter are raised during the preliminary study, a quadratic design should then be considered. However, that wasn't the case for the study detailed in section 4.1.2. Thus, the DoE will be based on a screening design. In order to perform a screening design, usually only 2 levels are necessary for each factor. Three levels or more are often used for parameters optimization in RSM. Other designs could have also been considered. For instance, a short reference to Taguchi designs will be made in page 79.

The response metric considered to be the most significant for the experiment purposes, was the maximum LSS, i.e. peak load of the joints in a lap shear test. One of the specifications of the industrial partner in the beginning of the project was precisely the parameters optimization for LSS. It is worth noticing that the lap shear strength is not always used as the parameter to be optimized. Other physical and mechanical parameters such as welding temperature, residual stresses, electric resistance, etc., can be important for example in battery manufacturing. Using desirability functions, even two or more outputs can be optimized by assigning for each a weight or desire level (Montgomery 2017).

The preliminary study from section 4.1.2, in conjunction with the experience of the workgroup, allowed to: identify all variables that possibly influence the response of the system; choose the relevant factors to be considered in the experiment; and define the extreme valid levels for each factor.

As any other real physical system, there are a lot of variables that influence the desired joint outputs. It is common procedure to identify and document the many input variables and responses of the system to be studied. The identified possible effects and outputs are summarized in the modified cause-and-effect diagram, Figure 71. This type of document is important even though contains numerous variables that aren't controlled nor measured. It allows tracing possible errors/randomness during the experiments, consider more or less variables to control in similar future experiments, and to communicate with team members of different fields.

In the present report, only some main welding parameters were selected for formal scrutiny with DoE techniques, namely Rotation Speed (RS), Plunge Depth (PD), Plunge Time (PT), Dwell Time (DT) and Retract Time (RT). A small note will be made in the next page regarding the selection of travelling times instead of travelling rates variables for the plunged element. The Clamp Force (CF) will be kept constant and equal to 10 kN and the tool geometry is fixed and defined in section 0. These results are based on the previous experience and dissertation work of the supervisor of this project in HZG.

The process window was established based on different considerations: machine limitations,

welding feasibility, joint strength, and a total welding time compatible with typical industrial requirements. The factors studied, and the high/low levels for each factor are given in Table 28. However, since the data used to define the process window was considered as a result, the justifications and procedures that were in the basis of Table 28 are only detailed later in section 4.1.2 (all work's results are detailed in Chapter 4).

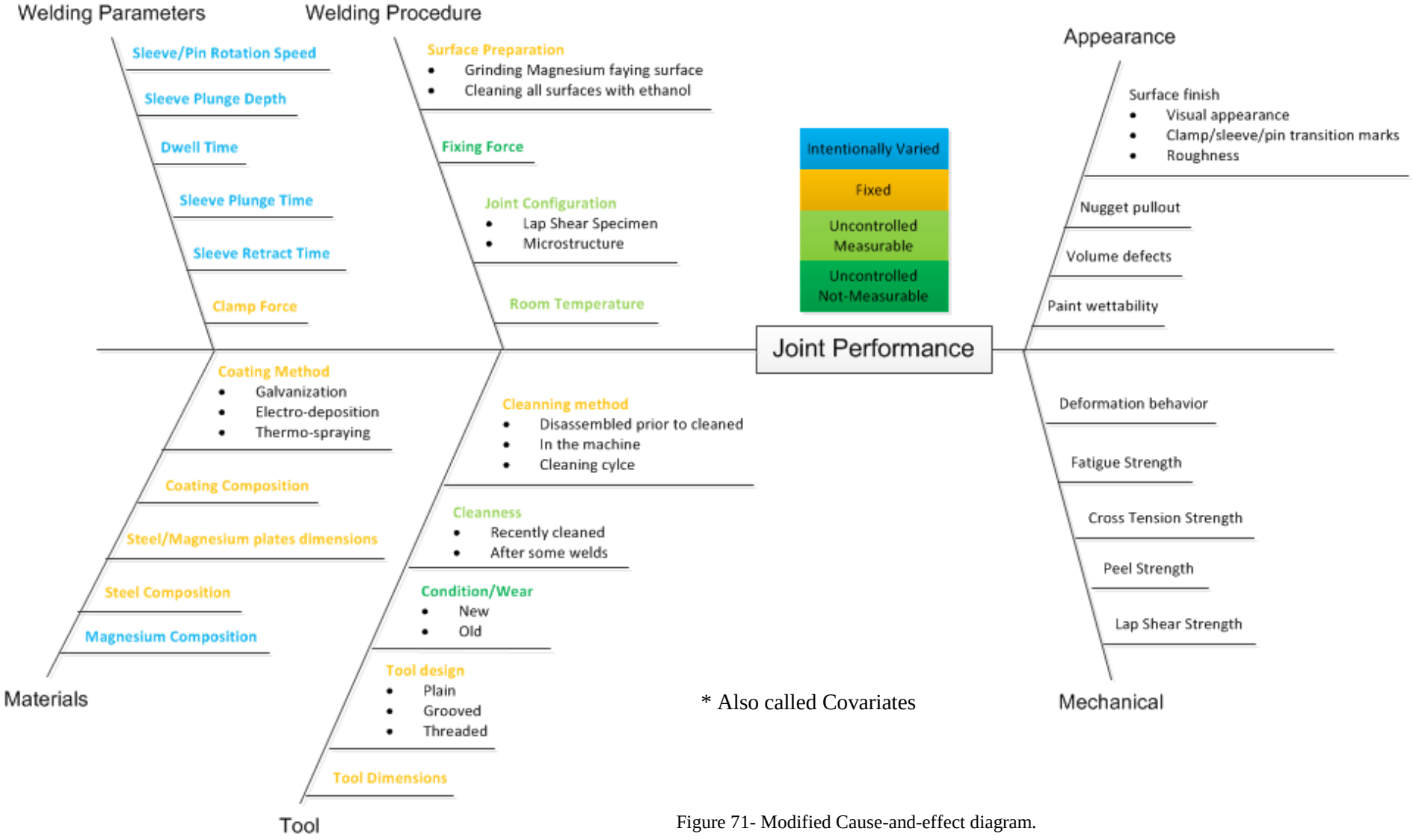

Figure 71- Modified Cause-and-effect diagram.

Table 28- Modified variables matrix of the experiment design, defining the factor's levels and the center point.

Factor	Coded Level	Uncoded Level	Center Point
RS [rpm]	-1	1500	1800
	+1	2100	
PD [mm]	-1	2.2	2.5
	+1	2.8	
PT [s]	-1	1.5	2
	+1	2.5	
DT [s]	-1	0	0.5
	+1	1	
RT [s]	-1	1	1.5
	+1	2	

There isn't a consensus in the technical literature or even within the Refill-FSSW group of HZG, about which variable to control, travelling times or travelling rates (velocity). By the basic physical mean velocity relation, either the linear traveling velocity or the travel time can be used in conjunction with the PD. However, there are some advantages and aspects in favor of considering the time, as variable to be controlled:

- Lower associated error – most of the dedicated Refill-FSSW machines (including the one used) have a position feedback control, the axial velocity and force will be given by the material flow behavior for each welding parameter;
- Easier programing, less truncation errors and linear domain variation – the machine input is usually (including the one used) the traveling times and not the travelling rates. Thus, the use of velocity besides involving additional calculation, may sometimes force to truncate the time obtained from the specified velocity. In addition, the variation of the velocity will be different from the variation of the time. A linear progression for the velocity levels yields a hyperbolic progression for the time input, as indicated in equations (2) and (3):

$$v = C_0 + \alpha x \quad (2)$$

$$t = PD / (C_0 + \alpha x) \quad (3)$$

- Non-constant velocity profile – the machine used has position control and constantly tries to impose a sinusoidal travelling profile, Figure 72 a). The specific sinusoidal profile tries to avoid high impact during plunging and/or retracting. The average velocity from Figure 72 b), will be equal to the indirectly specified average velocity (by the travelling times and PD);

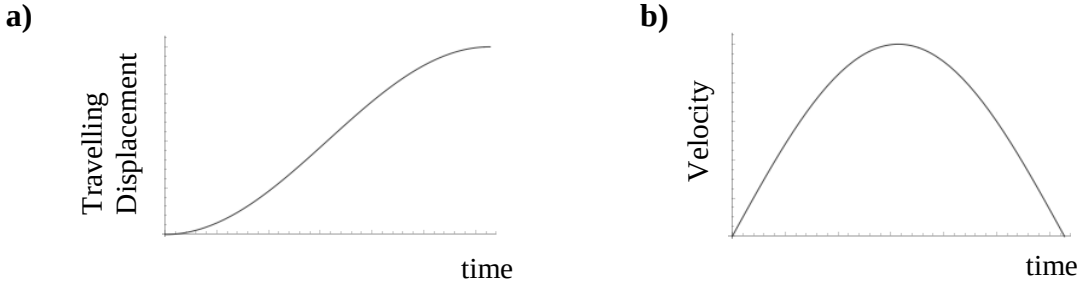

Figure 72- Illustration of the a) travelling displacement and b) velocity profile followed during plunging stage.

- Units and variables homogeneity – if the dwell time is considered as an intentionally changed variable, it will always be a time variable, during the DoE analysis is more coherent to have interactions between times than between time and velocity.

After the experimental variables are selected and their high and low levels are defined, the experiment can be designed. Concerning a screening design, first it is necessary to decide whether to run a full-factorial or a fractional-factorial based DoE. And if a fractional-factorial is chosen, which standard design is more adequate. The concepts upon which these decisions were based weren't explored in the literature review chapter. The author feared that these concepts would be decontextualized if presented as simple literature review, since these are rather specific regarding the design choice.

(Ryan, Joiner, and Cryer 2012) and (Montgomery 2010) propose a rule of thumbs for whether to choose a full factorial or a fractional factorial:

- If there are less than 5 factors, a 2^k full-factorial is the best option – for modeling all 2-factor interactions it is only necessary 4 runs (for 2 factors), 8 runs (for 3 factors) or 16 runs (for 4 factors);
- If the number of factors is 5 or more, a fractional factorial design is probably the best choice – if the time and resources allow it, a design with resolution V (Table 29) or higher is preferable. In addition to reduce the number of runs (as any fractional-factorial), they have two main advantages: allow modeling correctly all two-factor interactions, and to expand the original model to fit a quadratic model (e.g. Center Composite Design).

In Table 29, the concept of resolution for two-level fractional-factorial design is detailed. Factorial designs have a specific nomenclature. They are usually designated by the number of levels and factors that the standard design has. Table 30 gives some insights regarding typical nomenclature of two-level factional and full factorial designs, particularly the one used throughout this report.

Table 29- Description of each resolution level for fractional factorial designs (Montgomery 2010). (Montgomery 2017).

Resolution	**Main factors Confound w/**	**Two-factor Interactions Confounded w/**	**Three-factor Interactions Confounded w/**	**Four-factor Interactions Confounded w/**
I	*	---	---	---
II	Main factors	---	---	---
III	Two-factor Interactions	---	---	---
IV	Three-factor interactions	Two-factor interactions	---	---
V	Four-factor interactions	Three-fator interactions	Three-factor interactions	---
VI	Five-factor interactions	Four factor interactions	Four-factor interactions	Four-factor interactions

* Special resolution case (not useful!), it consists of one Run experiment with only one factor and one level

Table 30- Nomenclature used in two-level Full Factorial and Fractional-Factorial designs (Montgomery 2017).

Designation	**Nomenclature**
Number of Factors	k
Number of levels (for two levels)	L^k (2^k)
Number of Treatments in the Full Factorial	2^k
Number of Treatments in the Fractional-Factorial	2^{k-p}
Fraction of Reduction	$1 / 2^p$
Half Fraction Factorial	p=1
Quarter Fraction Factorial	p=2

Considering that the number of studied factors is 5, a fractional-factorial design was chosen to run the DoE. However, it is still necessary to choose which standard fractional-factorial design. Table 31 summarizes the main advantages of two-level five-factor fractional factorial designs and of the full factorial design.

Table 31- Summary of some features regarding screening designs of 2-level 5-factor experiments (Antony 2014), (Mead 1990), (Montgomery 2010), (Montgomery 2017).

	Standard Parameters			
Design	**Nº Runs**	**Resolution**	**Advantages**	**Disadvantages**
Full Factorial 2^5 (2^k)	32	Full	No aliased factors	Higher number of runs
Half Factorial 2^{5-1}	16	V	Smaller number of runs	Can't estimate three-factor interactions correctly
Quarter Factorial 2^{5-2}	8	III	Useful for experiments with 7 or more factors	Can't identify interactions
Plackett-Burman	8	III		Main factors confounded with two-factors interactions

The stock of materials allowed performing a resolution V fractional-factorial design, and typical physical systems have insignificant three or higher-order interaction terms. Thus, a half fraction factorial design was chosen. Table 32 defines the design matrix used, and in Page 81 further explanations will be given regarding the no. of center points chosen (3 center points). The design matrices from the remaining designs suggested in Table 31 are also given in Table 33, simply as mere additional information. Even though these won't be used, Table 33 illustrates to the reader different but also valid approaches. Considering that the selection of a particular design is sometimes a subjective process, with the inclusion of this table, the author intended to save time and ease the understanding of prospective readers.

Table 32- Standard half fraction factorial design matrix, with additional 3x replicated center point (Montgomery 2017).

Standard Order	**RS [rpm]**	**PD [mm]**	**DT [s]**	**PT [s]**	**RT [s]**
1	-	-	-	-	+
2	+	-	-	-	-
3	-	+	-	-	-
4	+	+	-	-	+
5	-	-	+	-	-
6	+	-	+	-	+
7	-	+	+	-	+
8	+	+	+	-	-
9	-	-	-	+	-
10	+	-	-	+	+
11	-	+	-	+	+
12	+	+	-	+	-
13	-	-	+	+	+
14	+	-	+	+	-
15	-	+	+	+	-
16	+	+	+	+	+
17	**0**	**0**	**0**	**0**	**0**
18	**0**	**0**	**0**	**0**	**0**
19	**0**	**0**	**0**	**0**	**0**

Table 33- Design matrix for different screening five factors-two levels designs (Montgomery 2017), (Montgomery 2010), (Mathews 2005), (Antony 2014).

Design	**Standard Order**	x_1	x_2	x_3	x_4	x_5
Plackett-Burman	1	+	-	-	+	-
	2	+	+	-	-	+
	3	+	+	+	-	-
	4	-	+	+	+	-
	5	+	-	+	+	+
	6	-	+	-	+	+
	7	-	-	+	-	+
	8	-	-	-	-	-
Quarter Factorial 2^{5-2}	1	-	-	-	+	+
	2	+	-	-	-	-
	3	-	+	-	-	+
	4	+	+	-	+	-
	5	-	-	+	+	-
	6	+	-	+	-	+
	7	-	+	+	-	-
	8	+	+	+	+	+
Full Factorial 2^5	1	-	-	-	-	-
	2	+	-	-	-	-
	3	-	+	-	-	-
	4	+	+	-	-	-
	5	-	-	+	-	-
	6	+	-	+	-	-
	7	-	+	+	-	-
	8	+	+	+	-	-
	9	-	-	-	+	-
	10	+	-	-	+	-
	11	-	+	-	+	-
	12	+	+	-	+	-
	13	-	-	+	+	-
	14	+	-	+	+	-
	15	-	+	+	+	-
	16	+	+	+	+	-
	17	-	-	-	-	+
	18	+	-	-	-	+
	19	-	+	-	-	+
	20	+	+	-	-	+
	21	-	-	+	-	+
	22	+	-	+	-	+
	23	-	+	+	-	+
	24	+	+	+	-	+
	25	-	-	-	+	+
	26	+	-	-	+	+
	27	-	+	-	+	+
	28	+	+	-	+	+
	29	-	-	+	+	+
	30	+	-	+	+	+
	31	-	+	+	+	+
	32	+	+	+	+	+

Since Taguchi's orthogonal method was also considered in the preliminary phase, and this type of DoE is often used in Refill-FSSW research (Effertz, Quintino, and Infante 2017), (Campanelli et al. 2012), (Mesquita, Suhuddin, and dos Santos 2012), some reflections will also be made regarding this design. It provides an alternative to standard factorial designs, enabling to set a process that functions more consistently, regardless of the operating environment in which it is used. Taguchi designs try to identify controllable factors that minimize the effect of the noise factors (or simply noise), by maximizing signal to noise ratio. For that, usually require at least three replicates for each run. In addition to require replicating the entire design, it is more suitable for industrial applications since its main goal is to control the process reproducibility. Taguchi designs tend to be used to optimize process robustness, rather than product properties (de Souza et al. 2013). Thus, it wasn't considered in this analysis. Before a Taguchi design is selected to compose the DoE runs, in addition to the selection of the factors and the number of levels for each factor, it is also necessary to select the interactions between the controlled factors. Main factors and interactions are assigned to the array columns via linear graphs to simplify or 'shortcut' the DoE. An overall background explanation with practical examples is given by (de Souza et al. 2013), (Xin 2013).

All two-level standard factorial (full or fractional) models are saturated, i.e. the degrees of freedom (DF) of the full model are exactly the same as the total DF (zero DF available). The 2^5 full factorial design deserves a closer look, since the fractional factorial design used is based on it and it is useful to derive the alias structure. Its full model in an expanded version is detailed in Table 34. Aliasing is the process of estimating an effect by including the influence of one or more other effects (usually high order interactions). For example, in a 2-level half fraction factorial design with four factors, the effect of the main factor A is in fact the estimate of the combination of A+ ABC. This is the bases of fractional factorial designs, and isn't a major error source for the majority of the practical systems. Usually, higher order interaction terms are either non-existent or insignificant when compared to main and second order interaction terms. From Table 34, it can be inferred that in the half fraction factorial design used, the left side terms will be the dominant terms in the alias structure (modeled with reasonable accuracy). Precisely 16 degrees of freedom are consumed with high-order interactions: three, four and five-factor interaction terms (all right-side terms will be aliased).

Table 34- Distribution of DF for each factor type of the model in a 2^5 full factorial design.

Classification	**DF**	**Term**	**Classification**	**DF**	**Term**	**Balance**
Constant	1	Constant	3-factor Interaction term	10	$PD \cdot RS \cdot PT$	DF Total 31
Main Factor term	5	PD			$PD \cdot RS \cdot DT$	
		RS			$PD \cdot RS \cdot RT$	
		PT			$PD \cdot PT \cdot DT$	
		DT			$PD \cdot PT \cdot RT$	
		RT			$PD \cdot DT \cdot RT$	
2-factor Interaction term	10	$PD \cdot RS$			$RS \cdot PT \cdot DT$	DF Model 31
		$PD \cdot PT$			$RS \cdot PT \cdot RT$	
		$PD \cdot DT$			$RS \cdot DT \cdot RT$	
		$PD \cdot RT$			$PT \cdot DT \cdot RT$	
		$RS \cdot PT$	4-factor Interaction term	5	$PD \cdot RS \cdot PT \cdot DT$	DF Available 0
		$RS \cdot DT$			$PD \cdot RS \cdot PT \cdot RT$	
		$RS \cdot RT$			$PD \cdot RS \cdot DT \cdot RT$	
		$PT \cdot DT$			$PD \cdot PT \cdot DT \cdot RT$	
		$PT \cdot RT$			$RS \cdot PT \cdot DT \cdot RT$	
		$DT \cdot RT$	5-factor interaction term	1	$PD \cdot RS \cdot PT \cdot DT \cdot RT$	

Hard-to-change factors are factors that because of some practical or technological reason, their resetting is extremely costly or time consuming when compared with the remaining factors. The setup time of changing from one machine to another, the cost of clean a production system to change the chemical composition of an industrial bath, are some examples of typical real constraints. When this type of situation is faced, approaches like split-plots are employed (not confuse with blocking techniques). For detailed practical information on blocking concept and its uses see (Mathews 2005). Regarding split-plot designs see (Federer and King 2007). Since none of the studied parameters is considered hard-to-change, no special split-plot design was considered.

Blocking is a technique for arranging experimental runs in groups (blocks), within which a common blocking variable is kept the same. A variable can be considered as a blocking variable if it isn't of primary interest to the researcher, and is a source of variability for the experiment. Blocking allows reducing the variability associated with a defined and regular source of noise that introduces randomness in the experiment. According to the cause-and-effect diagram in Figure 71, there are no nuisance variables capable of blocking. Even the room temperature, due to schedule limitations of the machine and work timetable can't be blocked.

Finally, since there are no hard-to-change factors neither the possibility (nor necessity) of blocking, the standard runs of the design were fully randomized by an internal function from Minitab® software (check the difference between run order and standard order in Table 49, Page 99). This prevents mixing the estimated effect of a factor with the effect of one or more untested and not controlled lurking variables. Full randomization tries to cancel out all the factors not being investigated in the experiment, limiting the change in the output only due to investigated factors.

To check for the necessity of replicating the chosen design, sample-size calculators are available with the majority of statistical software. The calculation of sample-size requires the same inputs as for calculating signal to noise ratio. For factorial designs, the actual computations can, in practice, only be done by dedicated statistical software. It is necessary to iteratively solve the transcendental equations (4) and (5), or iteratively calculate F statistics with tables or software. For information on how to manually calculate the sample size for generic 2^k (fractional) factorial designs see (Mathews 2005).

$$solve\ [\ Power = 1 - CDF(f_a, 1, v, \lambda)\ ] \tag{4}$$

$$solve\ [\ a = 1 - f(F \leq f_a\ ;\ 1, v)\ ] \tag{5}$$

$$v = N_{runs} \cdot n + N_{CtPoint} - 1 + N_{Reuced} \tag{6}$$

$$\lambda = \frac{n \cdot N \cdot \delta^2}{4 \cdot \sigma^2} \tag{7}$$

CDF	Cumulative density function of F statistics
n	Number of replicas
N_{runs}	Number of runs of the standard design
$N_{CtPoint}$	Number of center points
$N_{Reduced}$	Number of terms omitted from the model
δ	Desired detectable effect
σ	Estimated standard deviation

Sample-size calculators solve iteratively equation (4) for any of the missing variables, as indicated in Table 35. In this case, either the number of replicas or the number of center points could be selected as the unknown variable. A counterintuitive approach was followed. Instead of determining the number of replicas, the number of replicas was fixed and the number of center points was selected as the unknown variable due to the following reasons: 1) one center point must be used - at least one center point must be added if it's desired to perform the curvature test; 2) replicating the entire design dramatically increases the size of the experiment, so is advantageous to first test if it is possible to avoid replicas, by adding an adequate number of center points. Thus, a first attempt to compute the required

number of center points was made, fixing the number of replicas in one (minimum required), and the number of center points for curvature in one. The input values for the remaining parameters are given in Table 35. The output from the sample-size calculator was two center points, that adding to the one used for curvature testing, gives precisely the three center points already detailed in Table 32. If the number of center points required to obey the inputs from Table 35 had been too large, the procedure would be to increase the number of replicas, and recalculate the number of center points in a trial-and-error process (always assuring this way, that the minimum number of replicas is used).

There are a lot of possible reasons for introducing center points. Three center points were introduced in the original standard half fraction factorial design because (Ryan, Joiner, and Cryer 2012), (Mathews 2005):

- Increase design power – the power of a design is the probability of revealing an active effect i.e. the other side of power concept is the risk of not detecting a significant effect (type II error). It is the complementary of the type I error assessed by ANOVA;
- Increase the number of degrees of freedom available – available DF can be used to compute other features of the model such as the lack of fit error and/or pure error;
- Increasing the number of center points is a competitive technique when compared to replicate, to what concerns power and available degrees of freedom – center points can be easily "replicated" whereas the replicate of the entire design increases drastically the number of runs. However, whereas center points and replicates have the same effect in the number of DF available, the effect of center points in the design power decreases drastically with the increase in the nº of center points;
- Test for curvature (test the assumption of linearity) – all 2^k (full or fractional) factorial designs assume that the effects of the factors on the response are reasonably linear (can be modeled adequately with a straight line) within the inference space;
- Future fitting of a quadratic model – useful for Central Composite Designs that can include data from previous factorial experiments (sequential experimentation);

While factorial designs can detect curvature if centre points are used, is necessary a RSM to model the curvature (build a quadratic equation). The center points were added without changing the process window evaluated in the preliminary tests. This gives a security level in the safety of the response values. In order to check for trends during the experiment, the center points were not fully randomized in the run matrix. Instead, they were randomly fitted within three regions: start, middle and in the end of the run sequence (see final section 4.2.1).

Table 35- Input parameters of the sample-size calculator tool of Minitab®. Intermediate parameters necessary to estimate the number of terms omitted from the model are also presented.

Nº Factors	**Nº Corner Points**	**Effect***	**Power Values**	**Standard Deviation****
5	16	2.83	0.8	1
Nº Runs	**DF available**	**DF model**	**Nº terms omitted**	**Nº Center Points*****
16	15	5+10=15	0	1
Nº Blocks	**Nº Replicates**		**Nº Center Points per block**	
1	1			

Input Values
Unknown

* Effect size, not a real effect in units of response – number of times the real effect is higher than the standard deviation

** When =1 is inputted, no real estimated standard deviation is assumed – the effect parameter change is meaning to effect size

*** Number of center points dedicated for curvature testing only, additional center points will be added to ensure the power required

The real effect is internally computed by Minitab® by the equation (8). Typical power values lay between the 80-95 % range, and the effect size was estimated based on previous works of Banglong Fu.

$$Effect = Effect^{*} \cdot StDev \quad (8)$$

3.4 Mechanical Tests – Lap Shear Test

There are several tests and configurations to evaluate the static strength of a spot overlap joint; lap shear, cross-tension and peeling test are the most used in Refill-FSSW. (Kluz, Kubit, and Wydrzyński 2017) studied the mechanical behavior of similar Al joints by lap shear and peeling tests. (Shen, Yang, et al. 2014), and (Ji et al. 2017) in 2024 Al alloys, and (da Silva et al. 2007) in 6061 Al series compared the strength of similar Al joints achieved by lap shear and cross-tension tests. Before describing the adopted testing procedure, some considerations regarding the test select and the joint configuration will be made.

Overlap spot joints obtained by spot welding have poor mechanical performance in mode I loading (Kluz, Kubit, and Wydrzyński 2017). Thus, automobile chassis or any other structures containing spot welds are designed so that their lap joints are essentially loaded in shear (mode II). Consequently, shear based mechanical tests are preferred to: 1) evaluate generic design information, as the majority of structural loads should in fact be in plane shearing, the primary design criterion is the shear strength; and 2) compare research works between different process and/or materials, as the majority of the published work resorts on lap shear tests. On the other hand, pulling tests such as coach-peeling, cross-tension, KSII, etc. are very important to evaluate mode I behavior and are normally used: 1) when designing a specific structure - in which peeling or tension forces are known to be present, or simply to assess the behavior of the joint when non-design loading is applied; and 2) for weld quality evaluation, since the load is applied directly in the metallurgical interface. The main goal of the project is to study the feasibility of welding casting Mg to steel; with no specific component geometry in mind. Besides, it was even only required by the initial partner to test for shearing properties. Thus, the static mechanical properties of the joint were only evaluated by quasi static and monotonic lap shear test.

Overlap shear test, or (single) lap shear test, is commonly used for assess lap joint shear properties. Usually classified as shear test, it is in fact a mixed-mode I/II test. The bending moment introduced by plate deflection near the spot, causes additional tension stresses, Figure 121. A double lap specimen could also be used; its geometry results in less bending moment in the spot region, and is naturally aligned. However, is more complicated to assemble, perform and maintain uniformity during the welds and tests. The doubling of joint strength could also imply to use thicker material on the single plate side, which is restrained by imposed project specifications. In addition, it consumes more material and, since it is a lot less used, it is rather difficult to compare with the published literature data. For the reasons previously mentioned, the most commonly used single lap shear test was adopted.

The lap shear strength was evaluated with a Zwick/Roell® servo-controlled universal testing machine operated in displacement control, Figure 73 a). No external gauge transducer was used; the displacement measurement resorted in the internal position signal (naturally affected by the overall structural stiffness of the machine). A summary of the principle features of the machine used is given in Table 36. The test parameters were kept constant for the entire lap shear tests conducted and are organized in Table 37. The grip used allows defining the offset about the centerline, i.e. each jaw (left and right) of each grip (upper and lower) can be moved independently. It has two operation modes: simultaneous and independent movement of the left and right jaws. Before assembling the test specimens, is necessary to align the two jaws in the center. This procedure is done by moving them to the widest position in independent mode, after which the mode is changed to simultaneous movement, and the jaws moved to the closest position. Then one contrary jaw of each grip (upper and lower) is open to be able to fix the lap joint. In order to ensure centerline alignment by increasing the stiffness of each jaw, the final gripping is done in simultaneous mode. This clamping system increases the precision of the center lap alignment and reproducibility of the test, since there is no need to assemble tabs or adhesively bonded spacers.

The alignment of the specimen (in the loading plane) and the correct grip length were ensured by trace marks. Surface marks were performed with a scriber height gage equipped with a 0.05 mm precision Vernier scale. The center line and the grip length line were traced in the surfaces of the same side of each coupon. It should be notice that the surface groove introduced when tracing, are irrelevant to the joint resistance (even more when considering static tests), the failure always occurred at the interface of the joint. Since the steel is a harder material, it is more difficult to properly clamp it. Thus, higher grip length was used to ensure good clamping without significant slippage. The lap shear specimen is made of dissimilar coupons with different thicknesses and materials. Thus, in order to keep

the loading conditions constant, the joint configuration should be fixed throughout the experimental study, particularly during the DoE. For example, the reference position should be the Mg plate always fixed in the upper grip on the left of the center line. The majority of tensile machine constructions are based on one moving head, and one static side. In the particular case of the machine used, the upper frame is fixed. Since the Mg plate is softer, it is easily fixed. Even though the loading is quasi-static, in fact it starts to be applied in the lower grip and then the loading is transferred upwards. Thus, the easier clamped material should be in the moving grip. By the pervious said, the Magnesium plate was kept in the lower grip, in the position illustrated in Figure 73 b), during the whole experiment.

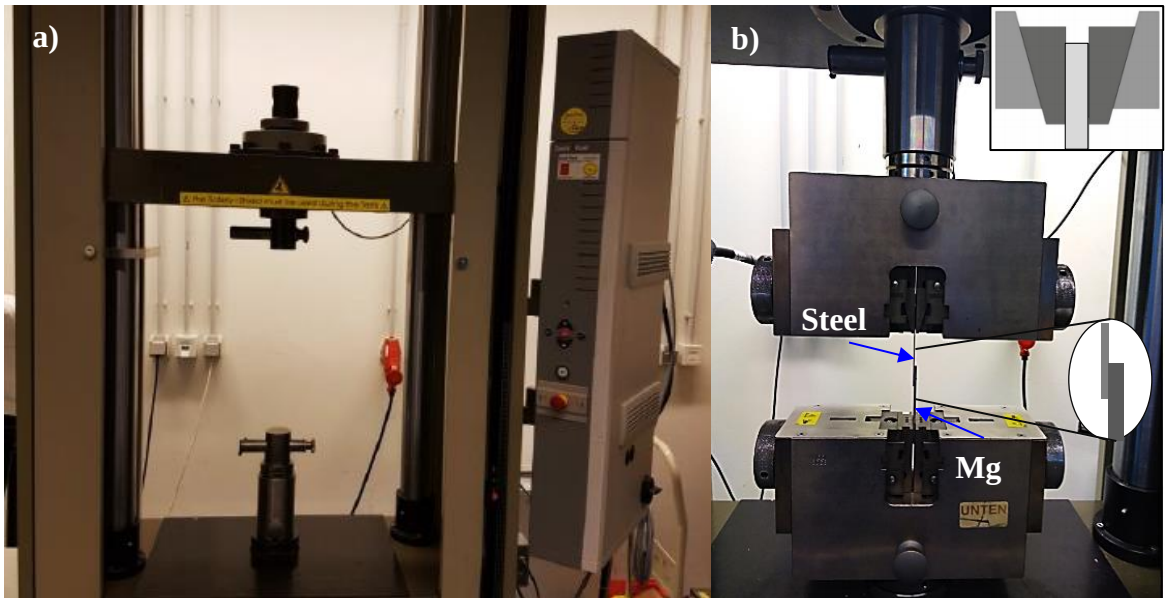

Figure 73- a) Universal testing machine used to perform the lap shear tests. b) Detail of the mechanical wedge grip system used, highlighting: the offset capacity, the joint configuration, and the testing position.

Table 36- Summary of the main characteristics of the Zwick/Roell® Z100TN universal tensile machine.

Hardware	Transmission	Screw driven machine
	Stroke of Crosshead	1275 mm
	Crosshead speed	0.005 - 300 mm/min
	Max. Load Capacity	100 kN
	Weight	530 kg
	Voltage Supply	230 VAC / 50-60 Hz
Sensor	Force measurement	grade 0.5 / 1 DIN EN ISO 7500-1, ASTM E4
	Positioning accuracy	± 2 µm
	External gauge	Additional feature

Table 37- Parameters used in the lap shear tensile tests.

Head travelling Speed	1 mm/min
Pre-load	50 N
Type of Grip	Wedge-screw
Grip length	25.4 mm for AM50 plate 30 mm for DP600 plate
Temperature	20 ± 3 ºC (individual lab)
Atmospheric conditions	Not pressure nor composition control

3.5 Metallographic Microscopy

Metallographic analysis (or more generically materialography) was performed to observe the structural modifications that occurred during welding: understand the different weld zones, check for defects or cracks in the welds, evidence the grain size morphology and different new phases, and structures formed during welding; and reveal the welding mechanisms: to observe the possible metal interlocking between the two plates, and to evidence the different mechanisms of metallurgical bonding at the interface.

Macrostructure and microstructure observations (at least part of it) were conducted by a Leica Microsystems™ DM IRM optical microscope, Figure 74 a). Macrographs of the cross-sections were taken using a 50x total magnification by a combination of 5x10 zoom lenses. Micrographs of both base material and cross-section of the joint were taken using up to 500x total magnification.

The Quanta™ 650 FEG SEM Microscope used is illustrated in Figure 74 b) and its main properties are summarized in Annex J Table 1. SEM analyses were conducted to study both the macrostructure and microstructure of the spot joints. SEM inspections of different features such as eutectic and new phase's distribution, presence of defects, the Mg-steel interface, and also the fracture surface unveiled from lap shear strength test were performed. In order to understand some results and conclusions regarding SEM data, some basic concepts need to be worked on first. Essentially two observation modes were used: backscattered electrons (A+B) – mode sensitive to the atomic mass of the nuclei from which the electrons of the original or primary beam scattered, it consists in collecting the electrons that underwent backscattering in the way that they rebound from the sample surface (heavier elements backscatter more efficiently so they appear brighter than lighter elements that appear darker); and secondary electrons (SE) – more surface sensitive mode that consists in collecting the electrons that are emitted by atoms near the surface of the sample when their electrons (excited) have sufficient energy to escape, creating an image that displays the topography and morphology of the surface (lighter colour means higher regions and darker colours deeper locations). The elements present in the studied joint can be ordered by their atomic number in: Zn (brighter in A+B mode) – steel/Fe – Al – Mg – O (darker in A+B mode). Electron Dispersive X-ray Spectroscopy (EDS or EDX) feature was used to obtain chemical compositional information. Whenever a secondary electron escapes from its energetic well defined shell, a higher energetic state electron (further away from the nucleus) fill in the gap releasing characteristic (from each element) X-ray wave signals (Committee 2004). This is a semi-quantitative analysis that gives a good indication of the local composition. In order to be studied using SEM technology, the samples were first left during 24 hours in a vacuum chamber for decontamination (removal of organic compounds and water) and to reduce oxidation of the prepared surface. The experimental procedure will not be further detailed since it was not carried out by the author. Only authorized researches with specific training could prepare the samples and operate the equipment on account of its high costs and fragility.

a) **b)**

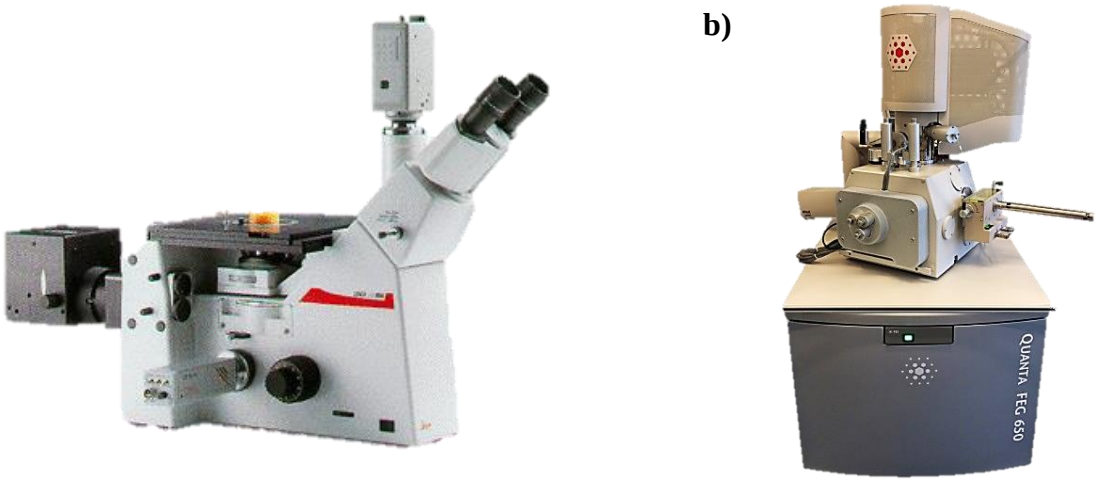

Figure 74- a) Leica® DM IRM optical microscope. b) Quanta™ 650 FEG scanning electron microscope without additional attachments and anti-magnetic barrier.

3.6 Sample preparation

3.6.1 Fractured Samples and Samples with SZ Pull-out Defect

There were three particular types of metallographic spot joints that didn't have a direct cross-sectioning procedure. These are schematically illustrated in Figure 75 a), and can be summarized as: (i) samples with nugget pull-out defect; (ii) fractured samples after lap shear test; and (iii) the combination of both cases. The additional cares necessary to conduct metallographic observation of these types of joints is worth by several reasons. Firstly, it is interesting to observe the cross-section of samples that have the pull-out defect, since it enables to correlate the welding parameters with metallurgical features. And secondly, observing the cross-section of spot welded joints after lap shear test along with prior fracture surface analysis by SEM, gives an idea of possible behaviors of particular microstructures during loading and fracture.

The metallographic preparation in these cases requires an additional bonding step then the standard cross-sectioned samples detailed in the next section. Individual cutting of each metal piece is also practiced by some researchers. However, several technological and clamping difficulties during cutting and mounting arise, leading to inaccurate center cross-sectioning. Thus, a procedure that firstly makes the two pieces rigidly joined, allowing cutting them on the original diameter and configuration of the spot weld was adopted. Independently of the case, the two metal pieces were first joined using a low viscosity mounting resin. The process is illustrated in Figure 75 b), showing three lap shear specimens after failure among which two had previous nugget pull-out defect after welding. The resin was applied abundantly in the interface of the two substrates, in the fillet region and in the nugget interface (when applicable). A Buehler Epoxi Cure2™ epoxy resin, based on both hardener and resin in the liquid state, was used to fix the two plates and/or the pulled nugget. The curing time was a lot higher than the resin normally used for sample mounting. However, its low viscosity and high fluidibility allowed better fulfilling and wetting of the cavities left after fracture. The resin features and its curing parameters are given in Table 38. The application of nonstructural glue is also found in the literature. However empirical experience has proven that this procedure left too many voids during the subsequent curing process in mounting (probable volatilization due to exothermic reaction). After the two pieces were fitted in, fixed, and cross-sectioned along the loading direction and through the weld center, a standard metallographic procedure was conducted as detailed in the next section.

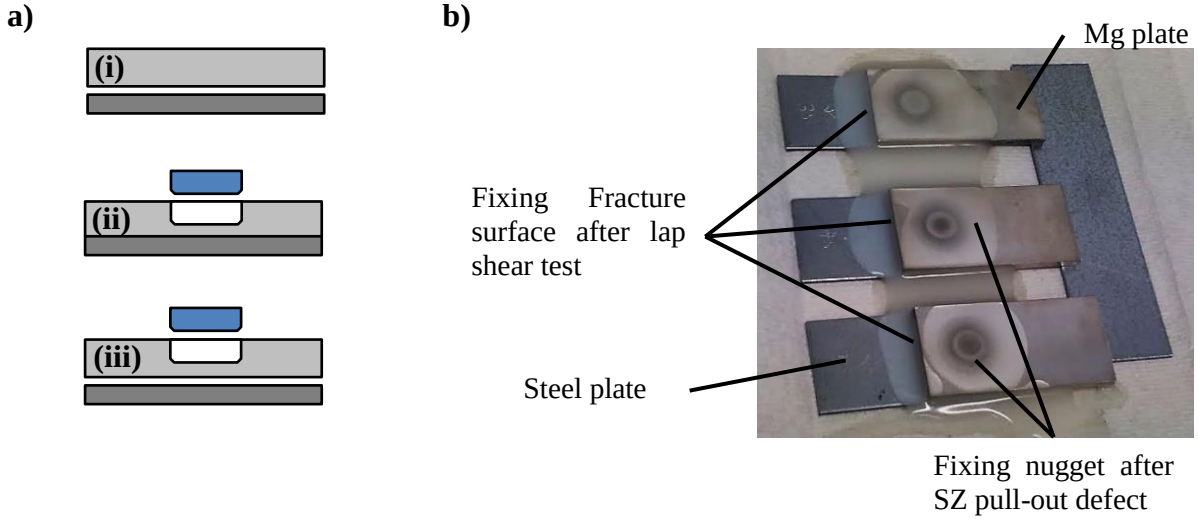

Figure 75- a) Illustration of the particular cases of sample preparation. b) Intermediate mounting process to fix the metal parts during cutting.

Table 38- Curing parameters of the Epoxi Cure 2® resin used for fixing the fractured joints or the nugget in SZ pull-out defect.

Resin	Resin: Hardener Ratio	Pressure [Bar]	Time [h]	Temperature [ºC]
Epoxi Cure2	5:1	Atmospheric	48	Room Temperature

3.6.2 Standard Metallographic Samples

In order to study the macro and microstructure of the Refill-FSSW cross-sections, some selected samples from the preliminary study and from the DoE were prepared according to standard procedures. The welds to be evaluated were cross-sectioned slightly off-center so that after mounting, grinding and polishing, the exact section of the centerline plane was available for examination. The cutting marks were traced with a scriber height gage. First the spot region was isolated from the whole lap joint, and then a cross section was longitudinally cut slightly off on the diameter of the spot weld. The cut was made by abrasive wet direct cutting process using a Struers® Secotom-50 automatic machine, Figure 76 a). Direct cut is usually preferred in normal circumstances since the contact area is constantly changing, improving cooling efficiency, as illustrated in Figure 76 b). An alumina Bakelite resin based Struers® EN 12413 50A20, 200 mm diameter cut-off disk was used (> HV 500 and ISO 8486 grit 20). Usually, alumina based cut-off-wheels are appropriate for slicing ferrous materials, whereas SiC based disks are used for non-ferrous soft materials. The sample was comprised of Magnesium alloy (soft material) and dual phase AHSS (hard material). In order to get a good cut surface, without introducing too many microstructural changes, an alumina cut-off disk (compatible with steel) was used in combination with an increased rotation speed of the cut-off wheel (enhancing the cutting of the Magnesium plate). The main concern during this process was to minimize thermal damage or burning of the specimen surface and ensure that the cut-off wheel endures minimal wear (controlled abrasive release) – allowing to obtain a smooth and uniform surface with homogeneous scratches. The cutting parameters used are summarized in Table 39. The cooling used was automatic dispensed tap water that also has flushing and lubricant functions. (Struers 2015), (ASTM International Standards 2011)

Table 39- Summary of the cutting parameters used for all samples.

Cutting Speed [rpm]	Feeding Speed [mm/s]	Cooling fluid
2200	0.075	Water

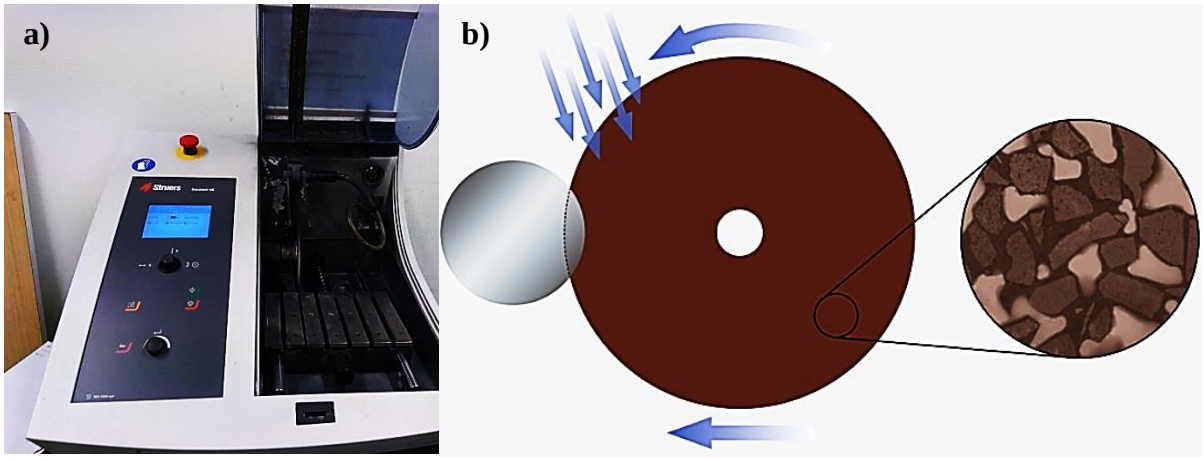

Figure 76- a) Secotom50® cutting machine. b) Illustration of the direct cutting process used (Struers 2015).

The specimens were cleaned prior to mounting in a BANDELIN® Sonorex RK 52 ultrasonic bath. This removes intricate contaminants and improves adhesion between the sample and the mounting medium. The samples were left for 60 s, in a non-heating, 35 kHz ultrasonic bath. Acetone was used as cleaning solvent. After cleaned, the samples were blow-dried and mounted using a standard cold mounting process. The mounting process protects fragile samples, making it easier to handle, and with its uniform sizes it's possible to use holders for automatic grinding and polishing. This type of mounting has a higher curing time but features a series of advantages comparing to hot mounting process: optimized accuracy and repeatability; does not affect the microstructure, segregation compounds and precipitation second phases; and is suitable for heat sensitive materials. Cold mounting epoxy resins have a higher curing time and are usually applied when vacuum impregnation is required e.g. porous materials, such as ceramics or sprayed coatings. So instead of epoxy, an acrylic based resin was used.

Two resins were alternately used according to their stock availability: Demotec® DEMOTEC® 20 (first choice) or Struers® ClaroCite®. Their mixtures and curing process parameters are detailed in Table 40. Pressure was kept uniform with a pressure curing pot from Leone America®. In a mixing cup both powders were weighted, poured and mixed with a disposable wooden stirrer. The liquid mixture was then poured in a 30 mm diameter mounting cup. Its size must be selected carefully, a cup bigger than necessary increase material consumption and can induce thermal modifications during the curing process. To avoid material consumption, and given the samples geometry, no fixation clip was needed. However, a two-side adhesive tape was applied in the bottom of the cup to ensure that the sample didn't move during pouring the pasty resin.

Table 40- Curing process parameters for each type of resin used.

Parameter	**ClaroCite®**	**DEMOTEC 20®**
Powder: liquid ratio [g/g]	10:6	2:1
Pressure [bar]	2	2.5
Time [min]	40	
Temperature [ºC]	Room Temperature	

After embedded, the samples were ground, diamond polished (mechanical) and oxide polished (combined mechanical and chemical action) in an automatic Struers® set: TegraPol-31 machine + TegraDoser-5 automatic dispenser. The procedure adopted is summarized in Table 42. Soft and ductile materials usually require a final polish using oxide polishing. OP-S and OP-U are commercially available by HZG supplier as 9.8 pH alkaline final polishing solutions. OP-S is suitable for a wide range of materials, particularly very ductile materials. Whereas OP-U is slightly less aggressive, so is more applicable to heterogeneous non-ferrous materials and composites. Thus, the final oxide polishing was performed with 0.2 µm water free OP-S. After polishing and prior to etching, the samples were observed in SEM, its analysis requires mirror-like surfaces but without etching.

Chemical etching was used, with no need for more sophisticated process such as electrochemical, electrolytic, thermal, Magnetic or Plasma etching. The etching process lasted usually no more than 8 s in an acid picric solution defined in Table 41. The sample surface was immersed in the etching solution until a thin red film formed above the Mg surface. It should be notice that only the Mg part was etched by the solution. Different solutions for dual phase steels such as 2% Nital (Medina et al. 2017), sequential etching (Lawson, Matlock, and Krauss 1980), etc. are stated and regularly used in the literature. The etching process for steel promotes severe corrosion of the Mg surface. Thus, if steel etching is also intended, the mg surface should be etched and analyzed prior to steel. Then, the two data can be merged with any image editing software. Since the steel plate wasn't penetrated, and previous studies in Al-steel welding (Shen, Hou, et al. 2016) indicated that the temperatures reached in the welding process aren't enough to produce microstructural changes in the steel sheet, no particular procedures for etching the steel were taken. For security reasons, the whole procedure was performed in a HoHenloher® hotte by the supervisor of this thesis, Figure 77. Past incidents with former master students during etching dictated to do so.

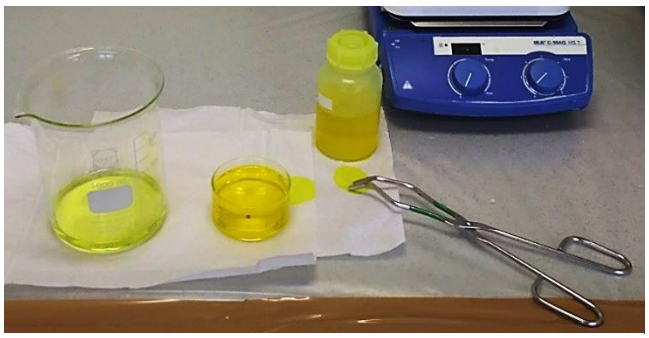

Figure 77- Illustration of the etching process.

Table 41- Composition of the etching solution used in the dissimilar Magnesium-steel samples.

Etching Solution			
Picric Acid	Acetic Acid	Ethanol	Distilled Water
4 g	7 ml	150 ml	40 ml

Table 42- Grinding and polishing (diamond and oxide) procedure adopted for metallography analysis.

Step	Mode	Disc / Cloth	Abrasive	Lubricant	Time [s]	Rotation Speed [rpm]
Grinding	Manual	FEPA P320	Grinding Foil SiC (46 μm)	Water	25 [1)]	150
	Automatic	FEPA P800	Grinding Foil SiC (22 μm)	Water	180 [1) / 2)]	150
Diamond Polishing	Automatic	PLAN [3)]	DiaPro Diamond Susp. (9 μm)	DP-Lubricant Blue Alcohol based	360 [2)]	150
	Automatic	MOL/FLOC [3)]	DiaPro Diamond Susp. (3 μm)	DP-Lubricant Blue Alcohol based	360 [2)]	150
	Automatic	NAP [3)]	DiaPro Diamond Susp. (1 μm)	DP-Lubricant Blue Alcohol based	600 [2)]	150
Oxide Polishing	Manual	CHEM [3)]	Colloidal Silica (0.2 μm) Alkaline solution (pH 9.8)	[5)]	360-480 [4) / 6)]	120
	Manual	CHEM [3)]	Colloidal Silica (0.2 μm) Alkaline solution (pH 9.8)	OP-S	300 [7) / 8) / 9)]	80

1) This step is applied in both sample surfaces
2) Visual inspection each 30 s for the ground sample surface (when applicable)
3) Designation of Struers®
4) The sample direction was rotated 90º each 30 s
5) Mixture of OP-S colloidal silica-0.2 μm (50 ml), Blue lubricant (30 ml), distilled water (20 ml)
6) This step is finish when there are no eye visible scratches. The process should finish with the cross-section aligned with the horizontal direction
7) Polishing only perpendicular to the direction with more scratches. It should be with the cross-section aligned with the vertical direction.
8) Steel plate in the inner part: 25 s; Mg plate in the inner part: 45 s
9) This step is repeated until no scratches are visible in the optical microscope (dark field)

4 Results and Discussion

4.1 Preliminary Analysis

4.1.1 Project Conditions

Previously to the pilot study launch, some of the project conditions were thoroughly revaluated. In order to try to understand and justify some project specifications, in this section, requirements like tool material, thickness of the Mg plate, and surface conditions of both Mg and steel plates were tackled.

The tool used is made of hot working steel, meaning it is technologically impossible to penetrate into the steel plate. In the event of steel plunging, extremely severe tool wear, with high possibility of tool breakage by welding it to the steel plate would be a reality. In order to be able to penetrate into the steel plate, a tool from Tungsten Carbide (WC) or any other ceramic based similar wear resistant material is necessary, section 2.4.2. In friction stir spot welding, (Liyanage et al. 2014) with a W-25 Re Tungsten alloy tool, plunged 0.4 mm into the DP600 steel plate. They reported improved mechanical properties by Mg-steel interlocking. Thus, three main reasons are advanced for not using this type of tool in this study, and generally in mass production. According to the researcher Eng.er Luciano Bergmann, also responsible for stock and material/equipment purchases of WMP, ceramic based tools:

- Have higher cost – average of 4 to 5 times higher, reaching 5000€ depending on the supplier;
- Require specialized equipment – the tool manufactures only supply for one specific manufacturer of welding machines, absence of true open market;
- There are only a small number of manufactures cable of supplying tools with the required quality – several difficulties in manufacturing ceramic based tools with complex geometry.

A 3 mm thickness Magnesium plate was imposed in the initial phase of the project arrangements, and by matter of congruence was kept throughout the complete project. According to data already published (Chen et al. 2015), (Shen, Ding, et al. 2016) and not yet published (Refill- FSSWed AZ31 Mg alloy to DP600 high strength steel), the welding mechanism will be essentially interfacial by metallurgical bonding for Refill-FSSW without steel plunging. Thus, it is necessary to generate and provide the right amount of heat in that specific region. Theoretically, the thickness of the steel plate has little effect in the welding, since the heat is generated in the Magnesium upper plate. The steel plate thickness wasn't specified by VW group, 1.5 mm steel sheet was used because enough material plates already prepared were available. However, the thickness of the Magnesium plate may have a quiet influence in heat transfer history during welding. The Magnesium acts like a heat sink, with high specific heat capacity and thermal conductivity as illustrated in Figure 78. In theory, lower thicknesses should be easier to weld and would require shorter welding cycles. However, casting products usually have minimum thickness requirements. Even if high pressure die casting Magnesium products can be produced with small wall thickness [1 - 1.5 mm] (Luo 2013), stiffness issues may require variable thickness walls or introduction of localized ribs. As indicated by Figure 79, Mg alloys have comparable specific strength with steel and Al alloys, however its specific stiffness is significantly lower. Some trials with Magnesium plate of different thicknesses were aimed, with the intention of recording the welding time and temperature. However, schedule incompatibilities of the workshop didn't allow it.

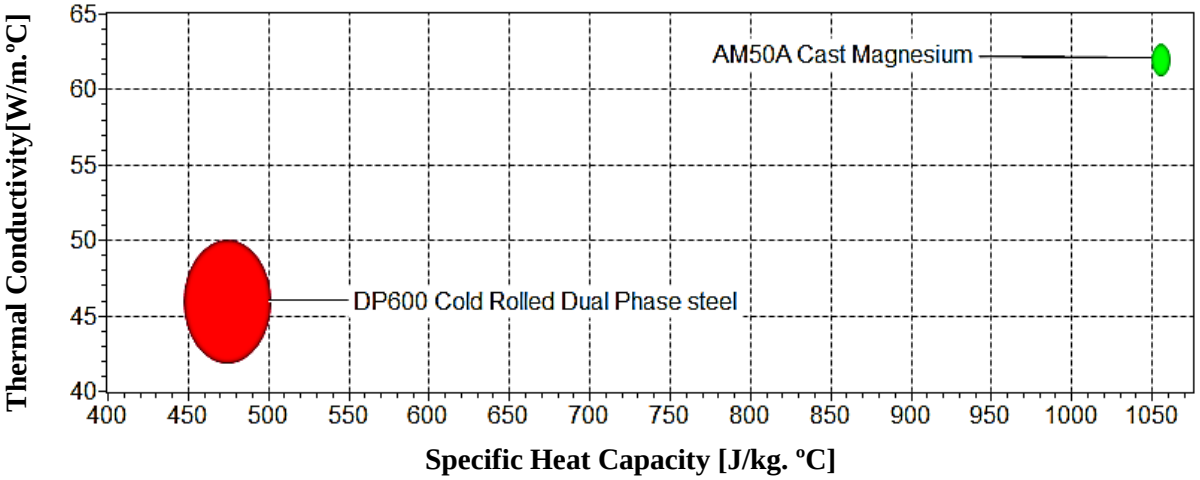

Figure 78- Thermal properties of AM50 magnesium alloy and DP600 steel (GrantaDesign 2017).

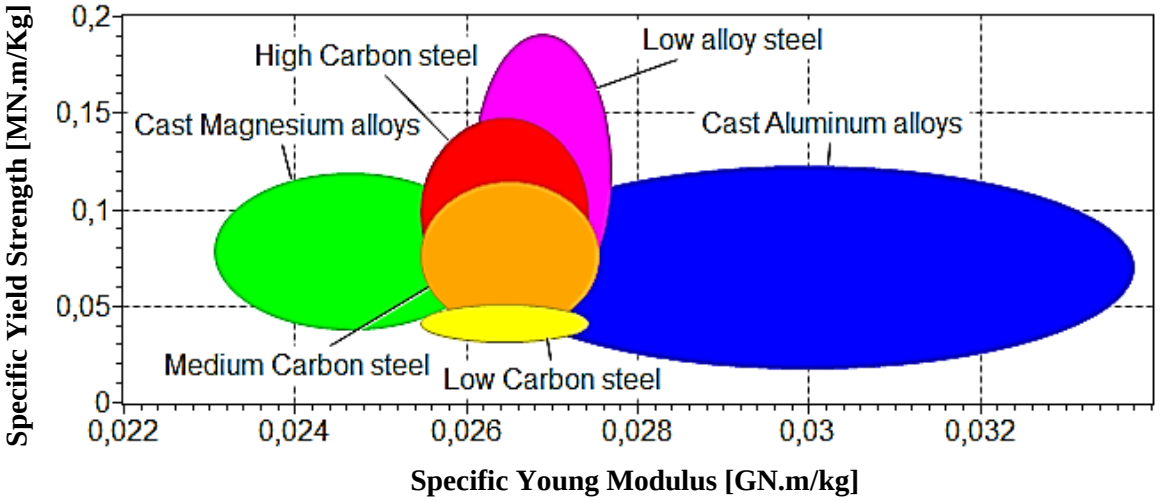

Figure 79- Specific properties for casting Mg and Al alloys, and common steel alloys (GrantaDesign 2017).

The surface condition of Mg was already explored in section 3.1.1. According to (Louda 2007), different types of functional corrosion resistant coatings are used in the automotive industry, namely Zinc and Zinc alloys (Zn-Fe, Zn-Al, Zn-Mg-Al, Zn-Al-Si, etc.)(de Rincón et al. 2009), (Arizmendi et al. 2003), Conversion Coatings, Aluminizing (Dosdat et al. 2011), and Sealers. (Akafuah et al. 2016) stated that the most common corrosion protection systems for steels in car body/chassis manufacturing, particularly for AHSS are Zinc coatings. Concerning the coating of steel, this protection is achieved by two methods: barrier protection – the zinc coating isolates the steel from the corrosion environment, so the coating will be first corroded before the steel; and galvanic protection – zinc is a less noble metal or anodic than Iron at room temperature, so will be used as a sacrifice material. In case of some of the steel is exposed to the corrosive atmosphere (by cut edges, local peeling or scratches) the surrounding coating corrodes to protect the steel substrate (Marder 2000). Zinc Hot-Dip Galvanized (HDG) steel sheets were used in this study. These pre-coated metal sheets are cost-effective technologies that provide corrosion protection during storage, increased product durability, improve lubrication in forming operations, and avoid the usage of other costly corrosion protection measures (Smith and Goodwin 2010). Different zinc coating process are also used in the auto industry (El Rehim et al. 1996), (Shibli, Meena, and Remya 2015), a brief outline is made in Annex D. The zinc coatings produced by Hot Dipping (HD) galvanization can be classified according to their Al content in: Galvanized (< 1 wt.% Al), MicroZinc D4 (>3 wt.% Al), Galfan/Zinkopal/Supergalva (5 wt.% Al-Zn), Galvalume (55 wt.% Al-Zn) (Marder 2000). The Aluminum is added in order to avoid the formation of Fe-Zn brittle compounds in the intermediate layer. The VW group confirmed, during the initial project arrangements, that bared steel was rarely used.

4.1.2 Preliminary Study

Visual inspection and laser scanning microscopy were used to ensure acceptable appearance. The operation of the laser microscope required a special training, due to time limitation and since it was only a one-time usage, the author didn't receive it. Thus, the operation of the equipment was responsibility of this work's supervisor. The author outlined the concept of quantifying the surface quality (by laser microscopy), and processed the output data. In Figure 80, two different outputs are shown – a roughness profile of the mid region was traced, and a 2D map overlaid in the upper surface photography of a typical spot. Fully refilled welds were produced with a particularly shiny surface, and overall good surface finish. Annular indent marks near the transition of tool components - original surface/clamp, clamp/sleeve, and sleeve/probe - can be detected by touch or by visual inspection. The height variation across the spot was below 0.25 mm. Faint marks in keyholes upper surface were also reported by (Buffa, Fratini, and Piacentini 2008) and (Chen et al. 2015). The roughness profile indicates steep height transitions near the original surface/clamp transition and clamp/sleeve boundary, which may indicate some wear from the clamping ring.

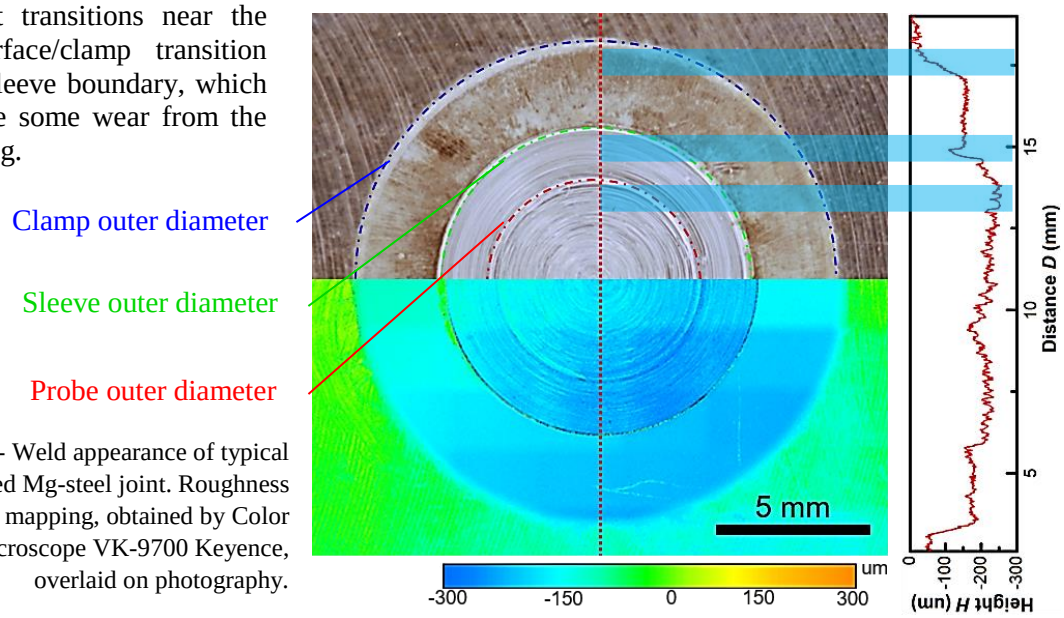

Figure 80- Weld appearance of typical Refill-FSSWed Mg-steel joint. Roughness profile and 2D mapping, obtained by Color 3D laser microscope VK-9700 Keyence, overlaid on photography.

Surface preparation of the Mg plates assures reproducibility during the study. However, this procedure is time consuming and usually avoided in any low-cost and high-volume production industry, such as the automobile industry. Thus, the feasibility of welding Mg plates with their natural oxide coating in the faying surface was briefly examined. The specimen surfaces were only cleaned with ethanol, and no grinding or chemical treatment was applied. Before welding, the Mg plates had a shiny mirrored surface from the Mg-O layer. Sound welds were achieved for low and high heat input parameters, as summarized in Table 43. The effect on the mechanical properties wasn't investigated in this report, but a similar study was conducted by (Chen 2015) in Refill-FSSW of ZEK100-steel. In his work, no obvious correlation between the joint strength and the Mg surface condition was observed.

Table 43- Feasibility of welding Mg to Zn coated steel without any particular surface treatment.

Surface Treatment	No Mechanical or Chemical treat.		**Surface Cleaning**	Ethanol
PD [mm]	**RS [rpm]**	**PT [s]**	**DT [s]**	**RT [s]**	**Outcome**
2.2	1500	1.5	0	1	Welded
2.8	2100	2.5	1	2	Welded

Before using DoE statistical techniques to model the welding process, a pilot study was conducted. The first goal was to set forth, in a preliminary way, the feasibility of welding AM50 Mg alloy to Zn coated DP600 steel. The second and main goal was to screen for relevant factors, and establish the low and high levels for each selected factor. The final results of this study were already summarized in the variables matrix in Table 28, from section 3.3. In the following pages, the rationale used behind the selection of the extreme levels for each factor (detailed previously in Table 28) is now finally given.

Rotation Speed:

- The feasible higher level for the RS was 2100 rpm. For RS higher than 2100, the nugget pull-out defect occurred, Figure 81 a). Table 44 sets out the boundary for the defect presence.

Table 44- Fraction of welding experiment worksheet, highlighting the maximum threshold for rotation speed.

RS [rpm]	PD [mm]	PT [s]	DT [s]	RT [s]	LSS [kN]	Pull-out Defect
2100	2.5	2.5	1	2	7.202	No
2100	2.8	1.5	1	1	---	No
2300	2.5	1.5	1	1.5	4.79	Yes
2300	2.8	1.5	1	1	---	Yes

- The min. RS that ensured defect free welds, for a wide range of parameters, was 1500 rpm. Nevertheless, for RS=1500 rpm, combined with low heat input parameters (low PD or low travelling times), some defects began to appear, Figure 81 c). This limit was also based on previous results from welding AZ31 Mg alloy to steel, Figure 81 b).

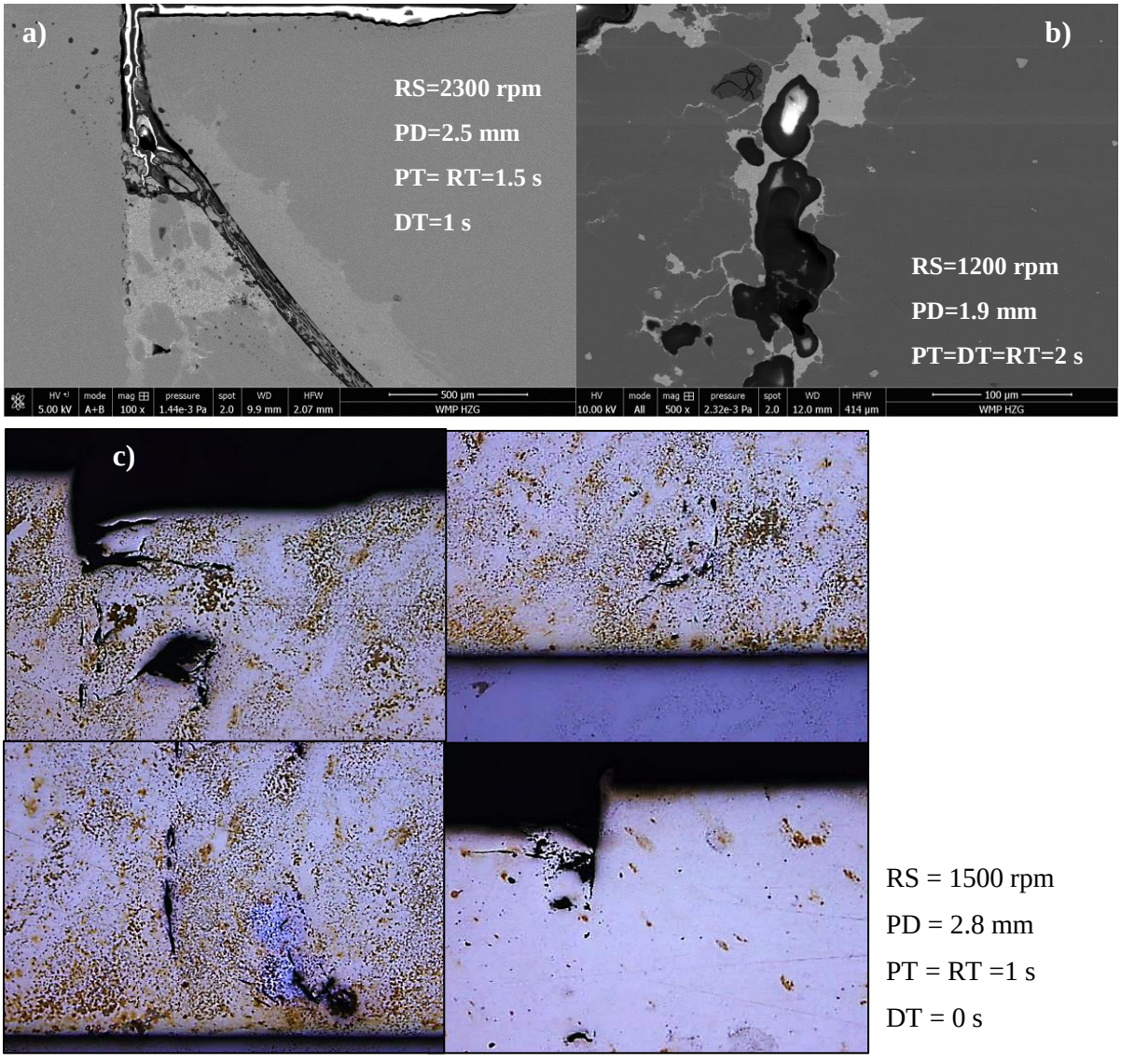

Figure 81- a) SEM micrograph of AM50-Steel sample with nugget pull-out defect. Sample produced with high RS and intermediate PD. b) SEM micrograph of defects observed in sample of AZ31-steel joint with RS=1200 rpm. c) Merge of multiple micrographs from weld defects of weld produced with inadequate heat input.

Plunge Depth:

- Since the tool was made of hot working steel, plunging into the steel plate wasn't an option. Thus, the higher value for the plunge depth was firstly limited by the thickness of the Magnesium plate, 3 mm. However, the plunge depth was even further limited. Aiming to offset possible errors, particularly from the machine head position measurement and fluctuations of the steel plate thickness (the thickness of the Mg plate didn't influence since the reference position wasn't the upper sheet). The safe upper value was then fixed in 2.9 mm by this work's supervisor, simply as a caution measure. However, the sleeve plunge depth of 2.9 mm caused nugget pull-out defect. Figure 82 illustrates this defect, and section 4.1.3 explores in detail this type of defect;

PD = 2.9 mm
RS = 1500 rpm
PT = 2.5 s
DT = 1 s
RT = 2 s

Figure 82- Cross-sectional macrostructure of SZ pull-out defect.

It was observed that reducing the maximum PD to 2.8 mm could avoid the detachment of the stir zone, as delimitated by the threshold line present in Table 45. Thus, a PD of 2.8 mm was defined as the final upper bond for the DoE;

Table 45- Fraction of welding experiment worksheet, highlighting the maximum threshold for PD.

PD [mm]	RS [rpm]	PT [s]	DT [s]	RT [s]	LSS [kN]	Pull-out Defect
2.8	1500	1	0	1	---	No
2.8	1500	2.5	1	2	6.008	No
2.8	1800	1.5	1	1	---	No
2.8	2100	2	1	2	---	No
2.9	1500	1.5	0	1.5	---	Yes
2.9	1800	1.5	1	1.5	5.445	Yes
2.9	2100	1.5	1	1.5	5.196	Yes

- Penetrations lower than 2.2 mm didn't ensure welds with enough strength* for the majority of combinations of welding parameters. A strong positive relation between the plunge depth and the LSS was observed, as indicated in Figure 89. In other words, it seems that the LSS decreases with the decrease in PD. In Table 46, the strength threshold (highlighted in bold), according to the AWS D17.2 standard, allowed to define the limit for the PD lower bond.

Table 46- Fraction of welding experiment worksheet, highlighting the relation between PD and LSS.

PD [mm]	RS [rpm]	PT [s]	DT [s]	RT [s]	Pull-out Defect	LSS [kN]
2.2	1500	2.5	1	2	No	**4.727**
2.5	1500	1.5	0	1	No	6.001
2.8	1500	2.5	1	2	No	6.632

* Assessed by comparing with AWS D17.2 resistance welding standard aviation, further details and the reasons for using this standard are given in section 4.2.1. For this combination of materials, the strength requirements stated in the standard are: **min. 4560 N** and min. avg. 5715 N.

Plunge Time and Retract Time:

- The total Welding Time (WT) must be competitive with other techniques used in the automotive industry, WT = PT + DT + RT. It shouldn't take no more than 6 s to complete the welding cycle;
- The Plunge Time (PT) should be higher than or at least equal to the Retract Time (RT) – During the plunging step, the material has a lower level of plasticization when compared with the retract step. Thus, in the beginning of the process is necessary higher heat input to enhance material flow (for the same heat flux, higher time means higher transferred energy);
- The higher level for the travelling times were defined based on the total welding time condition and the condition that PT should be higher than RT;
- The minimum value for the Plunge and Retract time were imposed by machine limitations, metallurgical aspects and tool wear conditions. The maximum sleeve travel speed is 6 mm/s, i.e. PT or RT lower than 0.5 s is technological impossible for a plunge depth of 3 mm. Lower travelling times, equivalent to higher travelling velocities, led to refilling problems and poor surface finish, since the machine couldn't reproduce a smooth penetration. Also, to reduce tool wear, higher travelling velocities were avoided.

Dwell Time:

- Preliminary results indicated that the dwell had a small effect in the LSS response, Table 47, and shorter dwell times are positive for any industry. Thus, based on previous results from AZ31-DP600 welds, 1 s was chosen as maximum dwell time The lower limit is automatically defined by the condition of not existing dwell time;

Table 47- Fraction of welding experiment worksheet, highlighting the influence of DT in the LSS.

PD [mm]	RS [rpm]	PT [s]	DT [s]	RT [s]	LSS [kN]
2.9	2100	1.5	0	1.5	5.176
2.9	2100	1.5	1	1.5	5.196

Figure 83 illustrates typical curves for the lap shear tests of Mg-steel Refill-FSSW. Even though the data from all lap shear tests was collected, the energy absorption capacity of the joint won't be studied (future work). The main conclusions from the preliminary study are summarized below:

- Sound welds between Casting Mg and Zn coated steel can be obtained;
- Defect free welds are achievable if the welding parameters are kept within the proposed process window. Good surface finish and refilling capacity from the Casting AM50 Mg alloy;
- Welds with acceptable strength according to the AWS D17.2 standard (see detailed exploration of this topic in section 4.2.1);
- The steel plate doesn't suffer structural changes by mechanical stirring or thermal action.

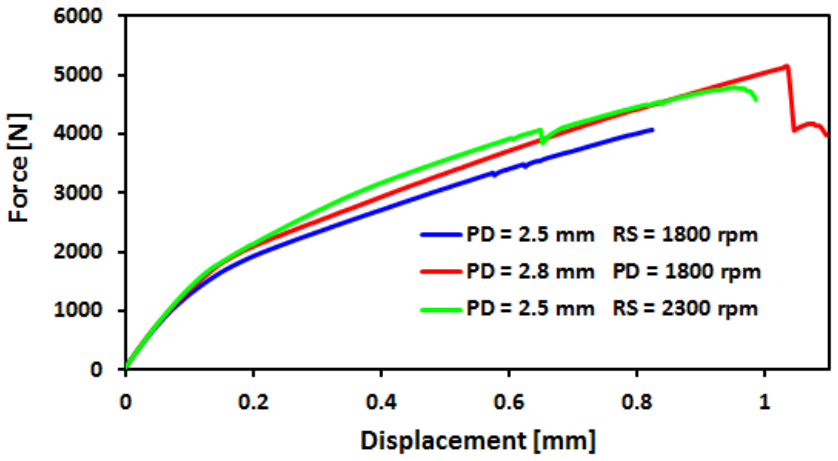

Figure 83- Typical force-displacement curve for the lap shear test.

4.1.3 Nugget/SZ Pull-out Defect

Nugget pull-out or Stir Zone (SZ) pull-out is a defect characterized by a hole left in the SZ, which is partially pulled-out when the tool retracts after welding. The upper surface of the SZ is bonded to the tool by an IMC's layer that forms after stirring. It generally occurs in welds with high heat input and is mainly dependent on the PD. For a PD equal to 2.9 mm it appears for a wide range of different welding parameters. The relation between the PD and the occurrence of this type of defect is explored later in section 4.3.1 and 4.3.2. In Figure 84, a 3D map of the upper surface of the defect and the bottom of the pulled material is shown.

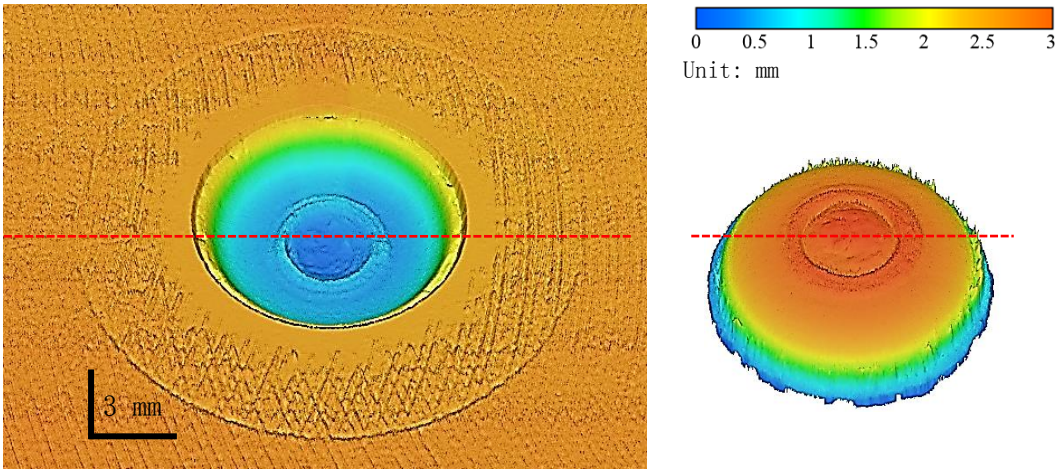

Figure 84- Surface height 3D map from the hole left in the surface, and the nugget bottom. Surface mapped by laser scanning microscopy.

Whether or not the defect occurs, depends on the strength balance between two bonding regions: interface between the tool and the upper section of the SZ, region (I), and the Mg-Zn rich characteristic region, region (II), that was firstly assumed to be eutectic structure. When the tool is removed, the nugget sticks to the tool, and if the possible Mg-Zn eutectic is already partially consolidated and waistbands the pull, the refill is successful. These two main regions, illustrated in Figure 85, are formed by:

- Region (I) – the reaction between the Al in the Mg alloy (5 wt.%) and the Fe (92 wt.%) from the tool (Hot Working Steel), led to the formation of a thin Al-Fe IMC's layer. To corroborate this assumption, a comparison to published data was made, (Chen 2015). The tool used was similar to the one used in this study, hot working tool steel. (Chen 2015) in Refill-FSSW of ZEK100 Mg alloy (without Al), reported that the adhesion of the Mg alloy to the steel tooling wasn't an issue, whereas during this complete experiment, severe Mg built-up in the steel tool;
- Region (II) – Mg-Zn eutectic is distributed as illustrated in Figure 85, and formed probably by diffusion of Zn from the Zn coating. The recorded temperatures in section 4.4.2 were above the melting point of Mg-Zn eutectic (~340 ºC). During material consolidation, this low melting point eutectic structure weakens the metallurgical bonding in this region.

Strength balance can be leaned towards one or other region by heat input conditions and material flow behavior. In the end of this section, two approaches to change region I are explored, and one last approach affecting region II. An approach to change the Mg-Zn eutectic distribution (region II) is given further in subchapter 4.4, using differential rotation Refill-FSSW. Thus, first is necessary to further study each region. Figure 85 illustrates in a schematic version the regions typical formed during Refill-FSSW of Mg-steel. In order to simplify the understanding and for the sake of visual cleanness, features like TMAZ (Thermomechanical Affected Zone) or HAZ (Heat affected Zone) weren't detailed. Also, the Mg-Zn rich region was exploded and isolated. Solid state welding joints are typically achieved with low temperatures (Shen, Hou, et al. 2016). According to the Fe-Al phase diagram, Figure 2 b) from Annex I, Al_3Fe is formed at the lowest temperature. (Wan and Huang 2017) reported the solid-state formation of Al_3Fe IMC's layer in FSW of Al to steel in lap joint configuration. Also in FSWed joints, (Kimapong and Watanabe 2005) detected the presence of Fe-Al IMC's, particularly Al_3Fe, formed at solid state temperatures. They were mainly located in the Al-rich region of the phase diagram, as a result

of its low melting point. The presence of a similar IMC's were also reported for Refill-FSSWed joints of Al to steel by (Shen, Chen, et al. 2018). The presence of Al_3Fe in the region (I), wasn't confirmed by chemical analysis. However, it will be assumed that the Fe-Al is composed mainly of Al_3Fe. This compound will be used as reference to compare with the Ti_3Fe IMC in approach #3 detailed in the last page of this section 4.1.3.

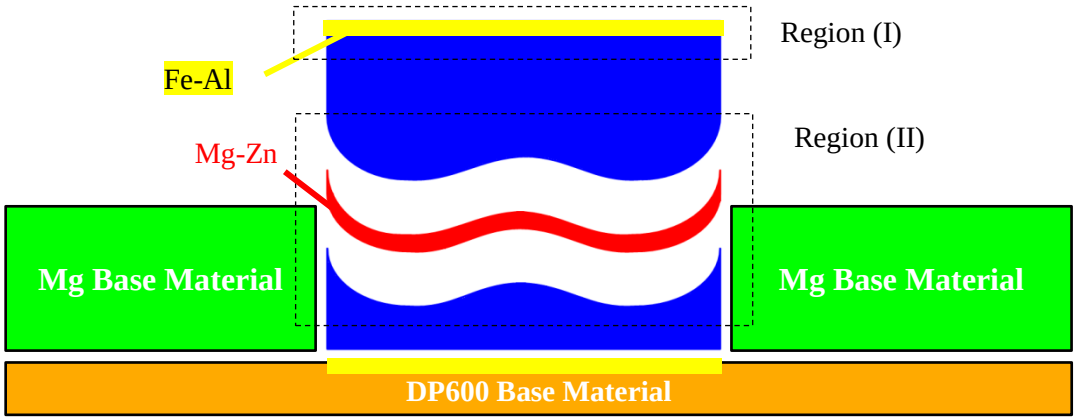

Figure 85- Cross-section schematic illustration of the multiple regions that characterize the pull-out defect.

Based on the previous statements, SEM and EDS analysis of defected spot welds were conducted. The metallographic samples were prepared according to the procedure detailed in section 3.6.1. The macrograph in Figure 86, points that the crack propagated along the Mg-Zn region. The crack highlighted in red color, is surrounded by Mg-Zn eutectic structure (blue color).

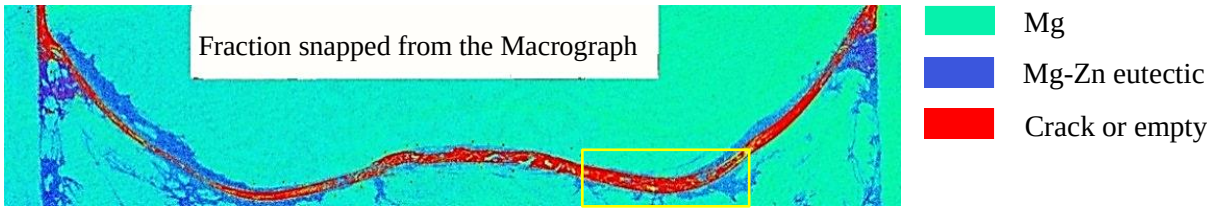

Figure 86- Macrograph of cross-section from weld with SZ pull-out defect, capture with SEM. Weld produced with the following parameters: PD=2.5 mm, RS=2300 rpm, PT= 1.5 s, DT=1 s, RT= 1.5 s.

Higher magnification micrographs of the crack surrounding area were taken with SEM; Figure 87 a) is the magnification of the yellow rectangular region in Figure 86. Figure 87 b) corresponds to a 25x magnification of the area delimited by the red square in Figure 87 a). The eutectic like structure of Figure 87 b) corroborates the previous assumptions.

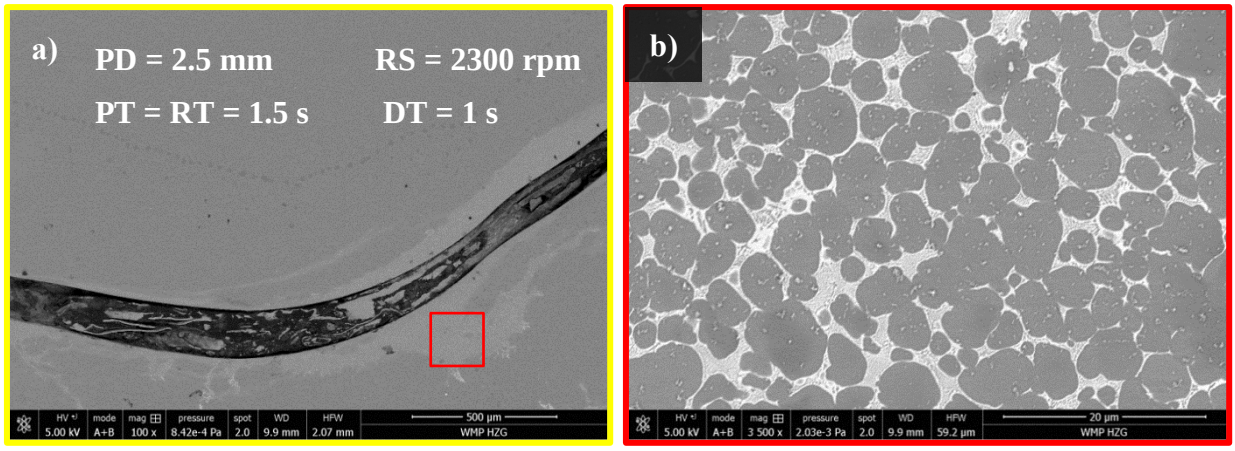

Figure 87- SEM micrograph from Refill-FSSWed spot with SZ pull-out defect. High heat input weld.

The Mg-Zn eutectic distribution illustrated in Figure 85 and analyzed in detail in Figure 86, occurred not only when the SZ pull-out defect was present. For sound refilled welds this distribution

was also observed, Figure 88 a) - c). However, for lower heat input the bonding in the eutectic region was stronger than the braked transient bonding between the tool and the SZ. Lower heat input probably induced less eutectic liquation[4], and allowed it to be in a more consolidated state during tool removal. The formation of Mg-Zn eutectic is inevitable, occurring in different locations and with different extents.

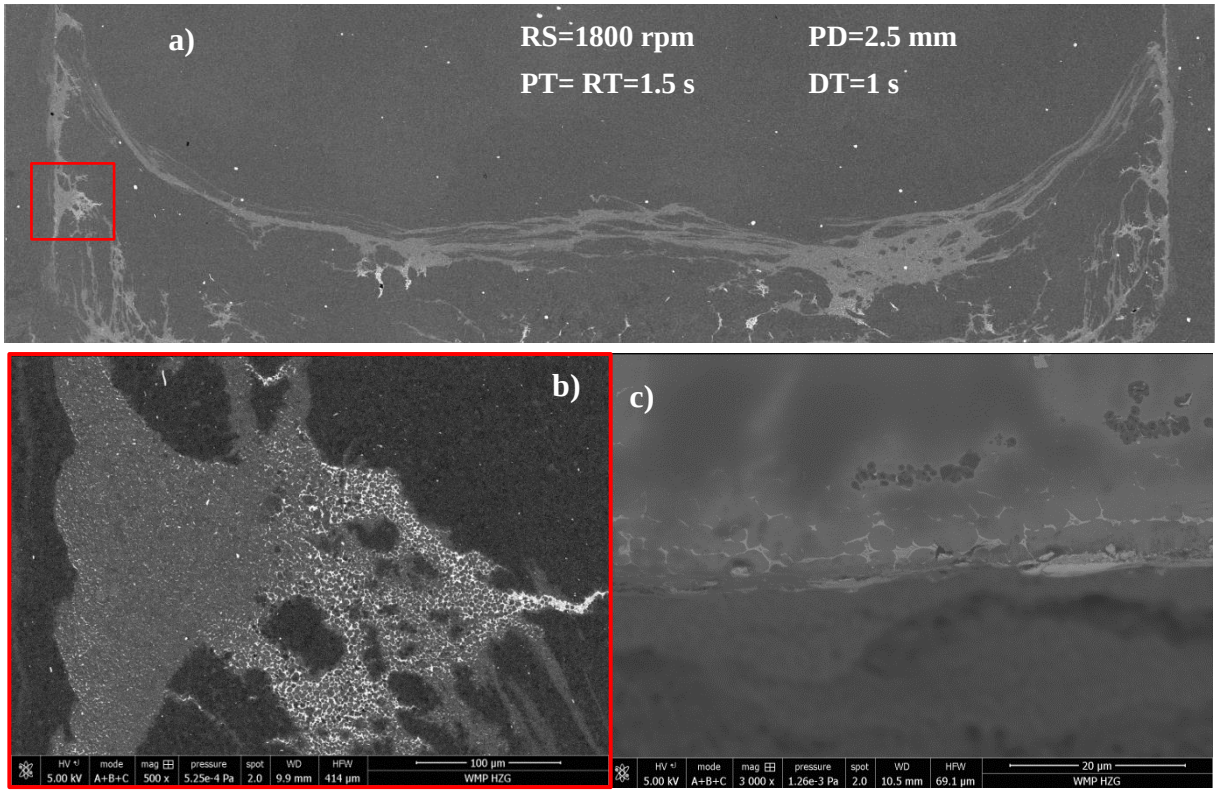

Figure 88- a) SEM macrograph of defect free spot weld, with intermediate parameters. b) Magnification of a). c) Micrograph of joint produced with the same parameters, but after lap shear test.

During the first trials, a consistent trend in the evolution of LSS with plunge depth was observed. Without considering interactions between factors, the LSS increased continuously with the increasing in plunge depth, Figure 89.

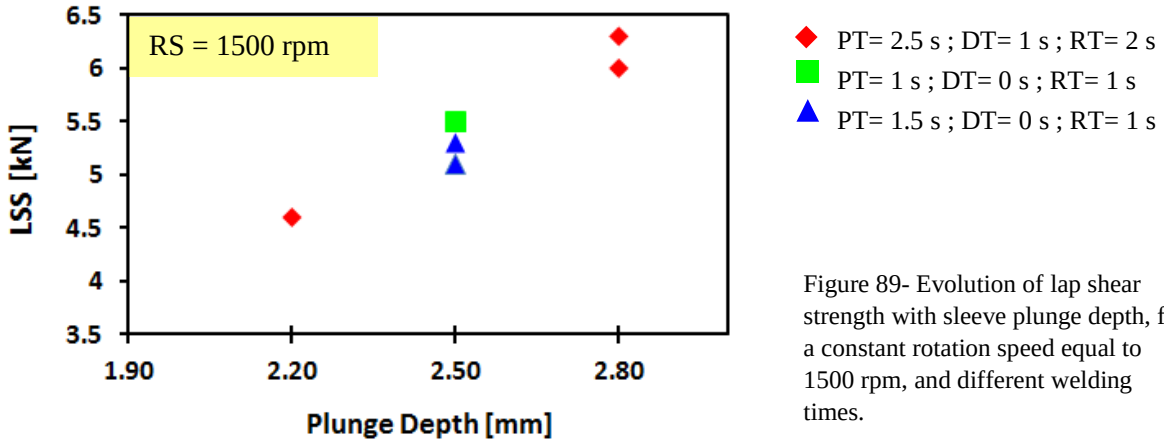

Figure 89- Evolution of lap shear strength with sleeve plunge depth, for a constant rotation speed equal to 1500 rpm, and different welding times.

Thus, a simple and direct way to enhance LSS would be to increase PD. However, as it was already concluded, for PD higher than 2.8 mm the nugget pull-out defect occurred after tool removing. This was one of the reasons why so much attention was given to this particular defect. In addition, this type of defect also lacks proper study according to the published literature. Hence, the three following (unsuccessful) approaches were tested to avoid this type of defect for PD higher than 2.8 mm.

[4] Partial melting of one constituent of an alloy system, without melting the remaining constituents.

Approach #1: A Cu foil made of 99% of copper metal was attached to the probe's bottom surface. The Cu foil was cut as illustrated in Figure 90 a). To ensure minimal accuracy, a hole punch tool with a 6 mm nominal diameter (equal to the probe nominal diameter) was used. The commercially available Cu tape consisted in a typical pressure-sensitive adhesive coated onto the back of the foil. No additional adhesives were used to produce the chemical bonding between the probe's bottom surface and the foil. Unsatisfactory refilling results, with intermixing of the Cu foil and Mg in the SZ are reported in Figure 90 b) and c). No lap shear tests were further conducted due to the unacceptable weld appearance.

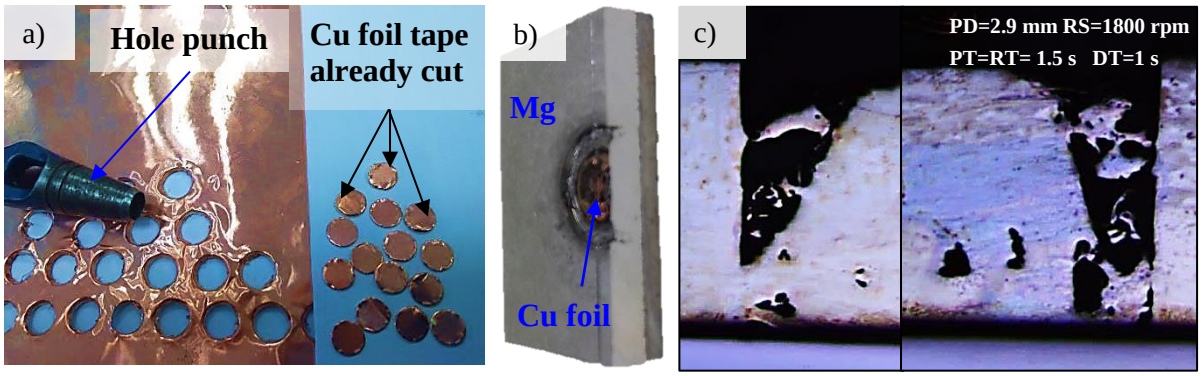

Figure 90- a) Illustration of the procedure used to prepare the Cu foil with the right geometry to attach it to the probe's bottom. b) Illustration of the Cu layer that was left after welding. c) Cross-section of Refill-FSSW trial with Cu foil attached to the probe surface.

Approach #2: This approach consisted in the replacement of the hot working steel probe by a titanium one. Due to human errors in the internal workshop from HZG, the probe wasn't manufactured with the specified dimensions. Its geometry was incompatible with the probe support dimensions. So, the practical feasibility was not check. Nevertheless, a few theoretical considerations were made, considering the possible outcome of this approach. Two phenomena were taken in account:

- Interface reaction potential [5] - To evaluate the potential for IMC's in the interface between the stirred material and the tool surface (region I), the enthalpy of formation for IMC's of Fe-Al and Ti-Al was compared. The reaction enthalpy of Al and Ti at 300 K is similar to Al_3Fe, Table 48. Thus, Al_3Ti compounds between the probe surface and stirred material would probably have also formed, and resulted in similar defect;
- Interface reaction activation temperature - Ti exhibits poorer heat transfer properties than Fe. The heat conductivity of Ti is 1/5 of Fe, and its heat capacity is also significantly higher. In consequence, the interface temperature between probe bottom and Mg plasticized material should have been higher, and this might had resulted in the increased bonding between probe and SZ.

Table 48- Thermal properties of Iron and Titanium pure metals, exported from CES Edupack®; and enthalpies of formation for the lower temperature IMC's, data extracted from (Bozzolo, Noebe, and Abel 2007) for Al_3Fe, and (Xu et al. 2006) for the Al_3Ti.

Element	Thermal Conductivity [W/m.ºC]	Specific Heat [J/kg.ºC]	IMC	Reaction Enthalpy Δh [kJ/mol of atoms]
Ti	16-18	539 - 541	Al_3Ti	-37
Fe	70-81	444 - 456	Al_3Fe	-28

Approach #3: The last approach consisted in programming an additional step in, the welding machine routine, before the withdrawing stage. After the refilling stage, the tool was held for a few seconds in the zero-level position. It was expected that the simultaneous pressing force of all tool components improved the consolidation process of the Mg-Zn rich characteristic region. However, no successful results were achieved and the SZ pull-out defect still appeared for higher plunge depths.

[5] For similar reasons described for the Fe-Al IMC's, $Ti\,Al_3$ will be used for comparison. By the Ti-Al phase diagram, Figure 2 a) from Annex I, $Ti\,Al_3$ is the IMC with the lowest melting point.

4.2 Conventional Rotation Refill FSSW – DoE Statistical Analysis

4.2.1 Lap Shear Results and Preliminary Analysis

Currently for Refill-FSSW, there are no standards at all (concerning the automotive or aviation industry) that allow to assess weld strength and quality by comparing the results from lap shear tests. However, an effort to create a specific standard for Refill-FSSW is being made by WMP department. As an alternative, all Refill-FSSWelds results were compared with the AWS D17.2 resistance welding aviation standard (covering both spot and seam welding). The RSW process was used as reference due to its similarity with Refill-FSSW, and because RSW is the main competitor with Refill-FSSW for most of the applications, particularly in the automotive industry. However, there are still some rather questionable topics regarding this decision, which cannot be ignored:

- This standard was elaborated specifically for aviation applications – The joint strength requirements highly vary with the project in hands, i.e. with the field of application, e.g. aeronautics, automotive industry, battery manufacturing, home appliance industry, etc.;
- The RSW process produces nuggets, whose dimensions are highly dependent of the welding parameters (voltage, current, etc.) – It is difficult to compare the real bonding diameters, since the bonding diameter produced by Refill-FSSW depends almost entirely from the sleeve diameter, instead of the welding parameters.

In spite of the previously mentioned cautions about using the referred standard, this procedure was (and continuous to be) defined as internal practice by the Refill-FSSW metal group from WMP, HZG. Two reasons can be advanced for not using a specific standard from the automotive field. Firstly, there aren't specific standards for the automotive industry regarding RSW of Mg alloys, only the AWS

Table 49- Experimenter version of the design matrix (ordered by runs), along with the response results.

Run Order	Standard Order	RS [rpm]	PD [mm]	DT [s]	PT [s]	RT [s]	LSS [kN]
1	10	2100	2.2	0.0	2.5	2.0	4.410
2	11	1500	2.8	0.0	2.5	2.0	6.058
3	13	1500	2.2	1.0	2.5	2.0	4.727
4	12	2100	2.8	0.0	2.5	1.0	5.656
5	4	2100	2.8	0.0	1.5	2.0	6.013
6	17	**1800**	**2.5**	**0.5**	**2.0**	**1.5**	**5.504**
7	14	2100	2.2	1.0	2.5	1.0	4.979
8	3	1500	2.8	0.0	1.5	1.0	5.818
9	18	**1800**	**2.5**	**0.5**	**2.0**	**1.5**	**5.367**
10	7	1500	2.8	1.0	1.5	2.0	6.073
11	6	2100	2.2	1.0	1.5	2.0	4.652
12	1	1500	2.2	0.0	1.5	2.0	5.174
13	16	2100	2.8	1.0	2.5	2.0	5.671
14	15	1500	2.8	1.0	2.5	1.0	5.589
15	9	1500	2.2	0.0	2.5	1.0	5.337
16	8	2100	2.8	1.0	1.5	1.0	6.042
17	5	1500	2.2	1.0	1.5	1.0	5.451
18	19	**1800**	**2.5**	**0.5**	**2.0**	**1.5**	**5.784**
19	2	2100	2.2	0.0	1.5	1.0	4.995

*LSS (Lap Shear Strength) **Center Point**

D8.1M for steels, and AWS D8.2M for Al alloys (Lienert et al. 2011). And secondly, aeronautics and aerospace are highly demanding fields, requiring high levels of security in the weld quality assessment. Thus, if the lap joints designed for automotive structural applications fulfill the aviation requirements, this gives automatically to the designer a natural safety factor (the results are slightly underrated). The aviation standard AMS-W-6858B, (SAE 2007), was used throughout the literature in the past as reference, however was superseded by the AWS equivalent.

In Table 49, the outcome of the lap shear tests performed for the DoE are presented with the corresponding welding parameters; the center point replicas are also highlighted in bold. During the static strength evaluation, all fractures occurred in the interface between the Mg alloy and Zinc coated steel, section 4.3.3. This failure mode in dissimilar welds between AHSS is commonly observed in the literature, owing to the high strength and hardness of the base material (Shen, Hou, et al. 2016), (Dong et al. 2016), (Khan et al. 2007). Particularly for Refill-FSSW of Magnesium alloy to AHSS steel without steel plunging, (Chen et al. 2015) also reported interface failure for all welds.

As it's possible to verify in Figure 91, the majority of the weld runs fulfilled the AWS D17.2 standard. Thus, the DoE corroborates the weld feasibility advanced in the preliminary study, and also the capacity of Refill-FSSW to achieve high strength joints between casting Mg and steel. The data used to compute the minimum, and minimum average load from the standard, is given in Table 50. As strength of reference, the material with the minimum load capacity was considered. The best set of parameters was estimated using the optimization tool of Minitab® - response optimizer. These are given in Table 51 and were used to perform three welds. The final LSS for the estimated best set of parameters was obtained by averaging the loads of the three individual samples. Both lap shear strength of each test, their average and the joint efficiency are showed in Figure 92 b). Joint efficiency was calculated by comparing the average maximum load of the joint, when stressed in lap shear tensile testing test, with the maximum load carrying capacity of the weaker parent material sheet section (based on ultimate tensile strength). The data and mathematical formula used to compute the joint efficiency are given in Table 52 and equation (9) respectively.

Min. – Minimum lap shear strength that any individual joint must withstand

Min. avg. – Minimum value for the average obtained using the lap shear strength data from the individual joints, in a test with multiple specimens

Figure 91- Lap shear results for all runs of the DoE organize in a column plot along with D17.2 standard requirements.

Table 50- Adapted from AWS D17.2 aviation standard for resistance spot welding.

	Material sheet	**AM50**	**DP600**
	Ultimate Tensile Strength [1)]	198	650
Standard Input	Ultimate Tensile Strength Interval [2)] [MPa]	135-239.9	620 – 1033.9
	Thickness [mm]	3	1.5
Standard Output	Minimum Load Capacity [N] / spot	4560	8630
	Minimum Average Load Capacity [N] / spot	5715	10633

[1)] Typical average values [2)] Parent Material

Table 51- Best possible estimation of optimal set of parameters.

RS [rpm]	PD [mm]	PT [s]	DT [s]	RT [s]
1500	2.8	1.5	0	2.0

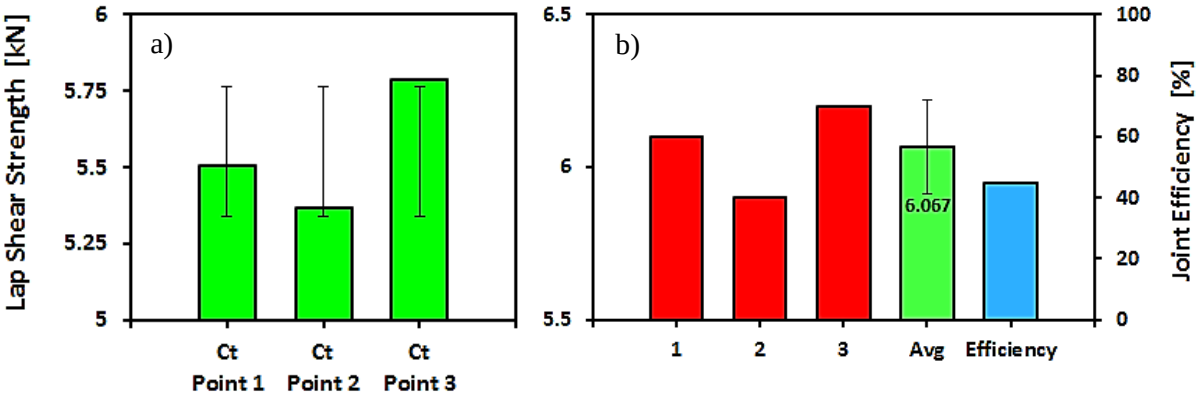

Figure 92- a) Column plot of the centre points, sorted by their run order, with the respective standard deviation. b) Column plot for the results regarding the estimated best set of parameters.

Table 52- Data used for the determination of the weaker parent material sheet.

Properties / Material sheet	AM50	DP600
Ultimate Tensile Strength [MPa]	175	650
Cross section Area [mm^2]	76.2	38.1
Load carrying capacity [N]	13335*	24765

$$\eta_{joint}\,[\%] = \frac{LSS_{joint}}{LC_{weak\ sheet}} \cdot 100 \tag{9}$$

LSS – Lap Shear Strength
LC – Load Capacity

When plotting the variation of the data with the real sequence of the experiment, scatterplot from Figure 93, no particular trend can be observed. The aforementioned indicates a stable experimental environment during the DoE. If center points aren't fully randomized (which was the case), they can be used, as a first approach, to look for trends (similar to residual analysis), subchapter 3.2.5. From the plot shown in Figure 92 a), or red data points from Figure 93, the data is stable with small variance and no trend or particular pattern, only the natural randomness of any physical system is observed.

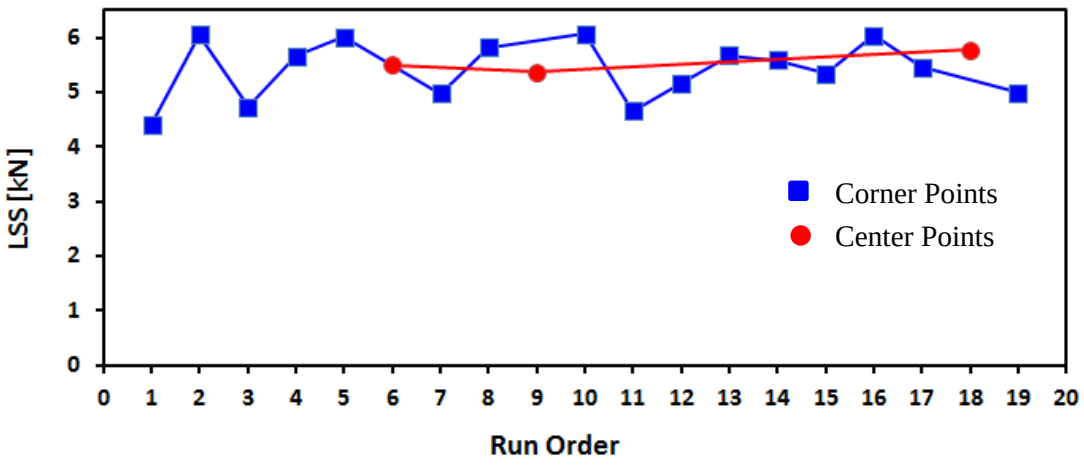

Figure 93- Scatterplot of lap shear strength vs. Run order.

A first superficial comparison of the lap shear results, achieved with this DoE, with other Mg-steel joints welded by different process was done in Figure 94. Refill-FSSW can be stated as a competitive technique for welding Mg to steel, achieving a superior mechanical performance than others solid-state and fusion processes. The majority of solid-state processes, particularly the friction-based process, achieved higher strengths than advanced fusion welding processes. The only exception was the combination of RSW and adhesive bonding. However, it was reported that the strength was mainly due to the adhesive. Regarding other solid-state processes, the Refill-FSSWed joints achieved higher strengths than USW and was just slightly lower than USWB (combination of adhesive bonding). Even though the strength achieved with Refill-FSSW was lower than FSSW, FSSW has the major drawback of leaving a keyhole.

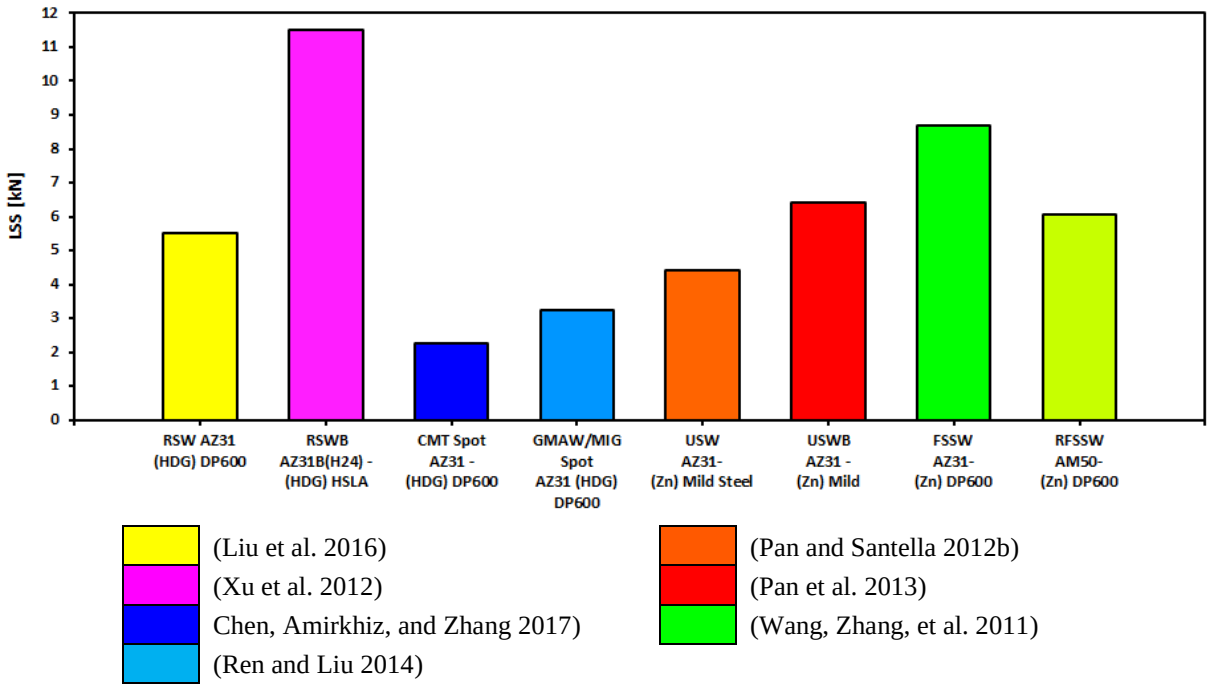

Figure 94- Lap shear strength achieved by different spot joining process for Mg-Steel and some similar joints. Data extracted from the literature.

In Figure 95, Refill-FSSWed joints of different Mg-steel material combinations with the respective similar joint are compared. For this, literature data and internal results from HZG were used. It has three main goals, namely: 1) evaluate the relative strength between the similar and dissimilar joints; 2) compare the LSS achieved in this experiment, with results from other experimental works; and 3) compare the welding times for different Mg alloys in Mg-steel joints (the three bars depicted in Figure 95 where the total welding time is shown inside them). The two data points highlighted by a rose shadow were collected from a different work and don't have a relation with the ZEK100 base material similar joint - these were plotted with a different purpose, to highlight the influence of the Zn coating in the LSS. A significant increase in the LSS due to the Zinc coating can be observed. Even though (Shen, Ding, et al. 2016) and (Chen et al. 2015) studied the same material combination, different plunge depths were used, hence the different LSS.

To evaluate the relative strength difference between the dissimilar joint and the similar base material welding resistance, Mg-Mg similar joints were used. No similar or dissimilar Refill-FSSWeld joints between steels are reported in the open literature. In addition, Magnesium is the weaker base material when compared to AHSS. The results for Refill-FSSWed AM50 Mg-Mg joints were extracted from part of the doctoral thesis of this work's supervisor, Banglong Fu[6]. When comparing AM50 Magnesium Refill-FSSWed similar with dissimilar joints, a decrease higher than 7% in the LSS was observed. The optimal LSS for similar AM50/AM50 joints of 6.5 kN was obtained with the following parameters: RS = 2900 rpm, PD = 4.5 mm, PT = 2 s, DT =1 s, RT = 2 s. In the literature, the difference

[6] Its publication and defense didn't occur yet

between similar and dissimilar joints follows exactly the opposite trend. (Shen, Ding, et al. 2016) studied the Refill-FSSW of ZEK100-ZEK100 and ZEK100-DP600 similar and dissimilar joints respectively. An increase almost of 44% of the dissimilar welding when compared with the Magnesium similar welding was observed. In AZ31-DP600 dissimilar joints Banglong Fu achieved an increase of more than 58%, when compared with the AZ31-AZ31 similar joints studied by (Campanelli et al. 2012). No reasonable explanation can be advanced for the distinct relation between similar/dissimilar joints when it comes to the results produced in this DoE and the data given in the literature/internal.

A completely different Magnesium alloy was studied by (Shen, Ding, et al. 2016). By its ASTM classification (see subchapter 2.1), ZEK100 is mainly alloyed to Zinc (1 wt.%), Rare Earth Elements (<1 wt.%) and Zirconium (<1 w.%). The exact chemical composition of the alloy studied is given in Table 16. The main differences are the absence of Aluminum, and the higher Zn content in the Magnesium alloy. In contrast with AZ31, the welding times of these two material combinations are very similar. However, poor strength was achieved, almost half of AM50-Steel load bearing capacity. This can be attributed to the presence of cracks in the Mg-steel interface. In addition, the absence of Al in the Mg alloy should also be considered. (Shen, Ding, et al. 2016) reported the presence of a discontinuous layer of Fe-Al_2 IMC's, which accommodated the bonding between the two insoluble matrixes. The source of Al was ascribed to Zinc coated steel. Aluminum is added in small quantities (<1 wt.%), during the Hot-Dip bath to: reduce coating embrittlement by suppressing Fe-Zn phases, and promote better adhesion, as described by (Marder 2000). The inability to form a continuous IMC's may be the reason behind the significant lower strength. Within the project in which this thesis is written in, the influence of the Al content of the AM50 Mg alloy will be further studied. With the optimized parameters determined in this chapter, lap joints of DP600 steel and different Magnesium sheets will be welded. AM50 equivalent chemical composition sheets will used, only Al element will be changed. Ingots with 3, 9 and null Al wt.% instead of the standard 5 Al wt.% were already casted at MagIC. Even though the manufacturing plan was ordered by the author, the plates weren't available for study in due time.

According to the ASTM designation, AZ31 is a wrought Magnesium alloy constituted mainly by Aluminum (3 wt.% avg.) and Zinc (1 wt.% avg.). The exact chemical composition of the alloy studied is given in Table 16. When comparing Refill-FSSW of AZ31-DP600 with AM50-DP600 dissimilar welding, some differences are worth notice. Welding AM50 to steel requires significant less welding time to achieve comparable high strength, about 2.8 times lower. This is due to the intrinsic liquation tendency of the AM50 that aids the formation of Al-Fe IMC (responsible for the metallurgical bonding). Its higher liquation tendency is justified by higher Al content and larger amount of Al-Mg eutectic structure.

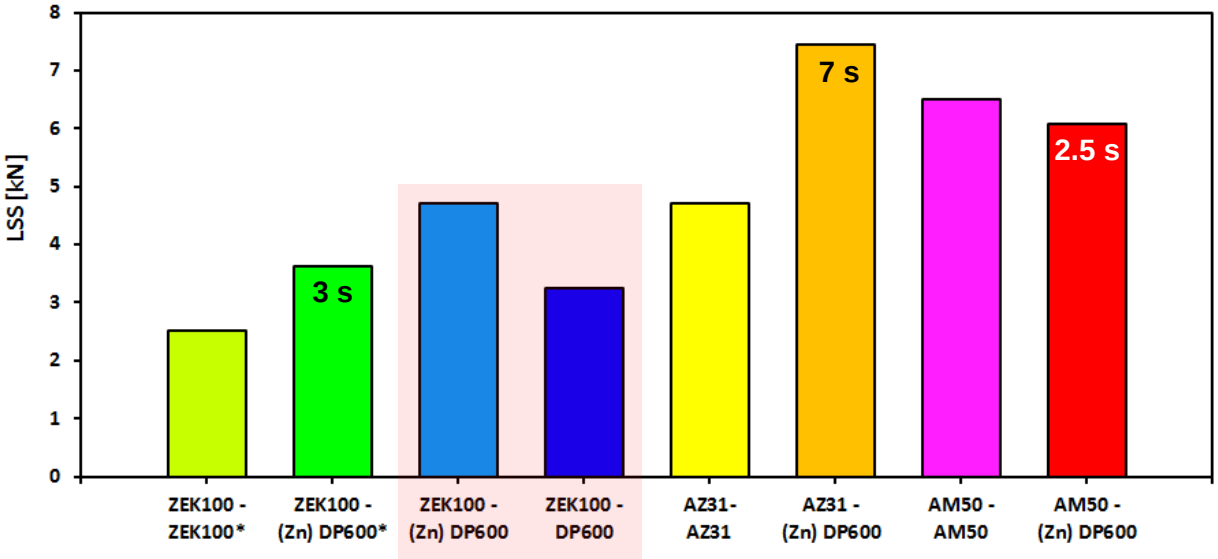

ZEK100 - ZEK100	(Shen, Ding, et al. 2016)	AZ31 – AZ31	(Campanelli et al. 2012)
ZEK100 – (Zn) DP600		AZ31 – (Zn) DP600	Banglong Fu PhD thesis
ZEK100 – (Zn) DP600	(Chen et al. 2015)	AM50 – AM50	
ZEK100 – DP600	(Chen 2015)	AM50 – (Zn) DP600	Present Work

Figure 95- Lap shear strength achieved by Refill-FSSW for different similar and dissimilar material combinations.

4.2.2 Practical Significance – Main Factors and Interactions

The analysis of effect estimates allows computing the practical influence of each term in the output of the response. The unstandardized effect, also called impact or delta, quantifies the magnitude and the importance of each term, and was computed by equation (10). The magnitude, direction (sign) and algorithm calculation of the effects can be checked in Table 53, and can also be visualized by the mean LSS plots in Figure 96.

$$Impact_i = \left| \frac{1}{N_{i+}} \sum_{j \neq i} LSS_{j+} - \frac{1}{N_{i-}} \sum_{j \neq i} LSS_{j-} \right| \quad (10)$$

j Represents each factor: RS, PD, DT, PT, RT, PD*RS, RS*DT, PD*RT

+- Level of each factor. When interaction terms are considered, it refers to the algebraic value resulting from the product of the level of each factor: $++$ or $--=+$ and $+-$or $-+=-$

N Number of replicas given for a *i* term with a specific level

Table 53- Summary of the results for the unstandardized effects and their process of determination.

Term	Mean LSS for - level	Mean LSS for 0 Center Point	Mean LSS for + level	Unstandardized Effect or Impact	Rank
RS	5.5284	5.552	5.3023	-0.2261	3
PD	4.9656		5.8650	0.8994	1
DT	5.4326		5.3980	-0.0346	8
PT	5.5273		5.3034	-0.2239	4
RT	5.4834		5.3473	-0.1361	6
RS*PD	5.3218		5.5089	0.1871	5
RS*DT	5.3643		5.4664	0.1021	7
PD*RT	5.2585		5.5721	0.3136	2

Examining the size of the effect of each term is a good way to assess the practical significance of the effect that the different factors have on lap shear strength of the lap joint. The effect of each term can be mathematically translated in the difference between the (mean) system response when the term is tuned in the upper level, and the (mean) system response when it is tuned in the lower level. The statistical significance of the difference between the means of the two created populations (treatments tuned in the upper value and lower value of a given factor) is determined by a t-test. Table 54 relies on parameters computed by ANOVA, so it isn't truly analysis of effects in terms of practical significance. Table 54 and Table 56 are two different perspectives of computing the same statistical significance. These are often the default outputs from many commercially available statistical software (e.g. Minitab®), reason why both tables are presented.

Table 54- Coefficients table for Analyze Factorial Designs.

Parameter	(Unstandardized) Effect	Coef.	Coef. SE	T-value	P-value
RS	-0.2261	-0.1131	0.0379	-2.986	0.01533
PD	0.8994	0.4497		11.871	0.00000
DT	-0.0346	-0.0173		-0.457	0.65849
PT	-0.2239	-0.1119		-2.954	0.01609
RT	-0.1361	-0.0681		-1.798	0.10594
RS*PD	0.1871	0.0936		2.471	0.03558
RS*DT	0.1021	0.0511		1.349	0.21062
PD*RT	0.3136	0.1568		4.139	0.00252

* Only the statistically significant factors were detailed

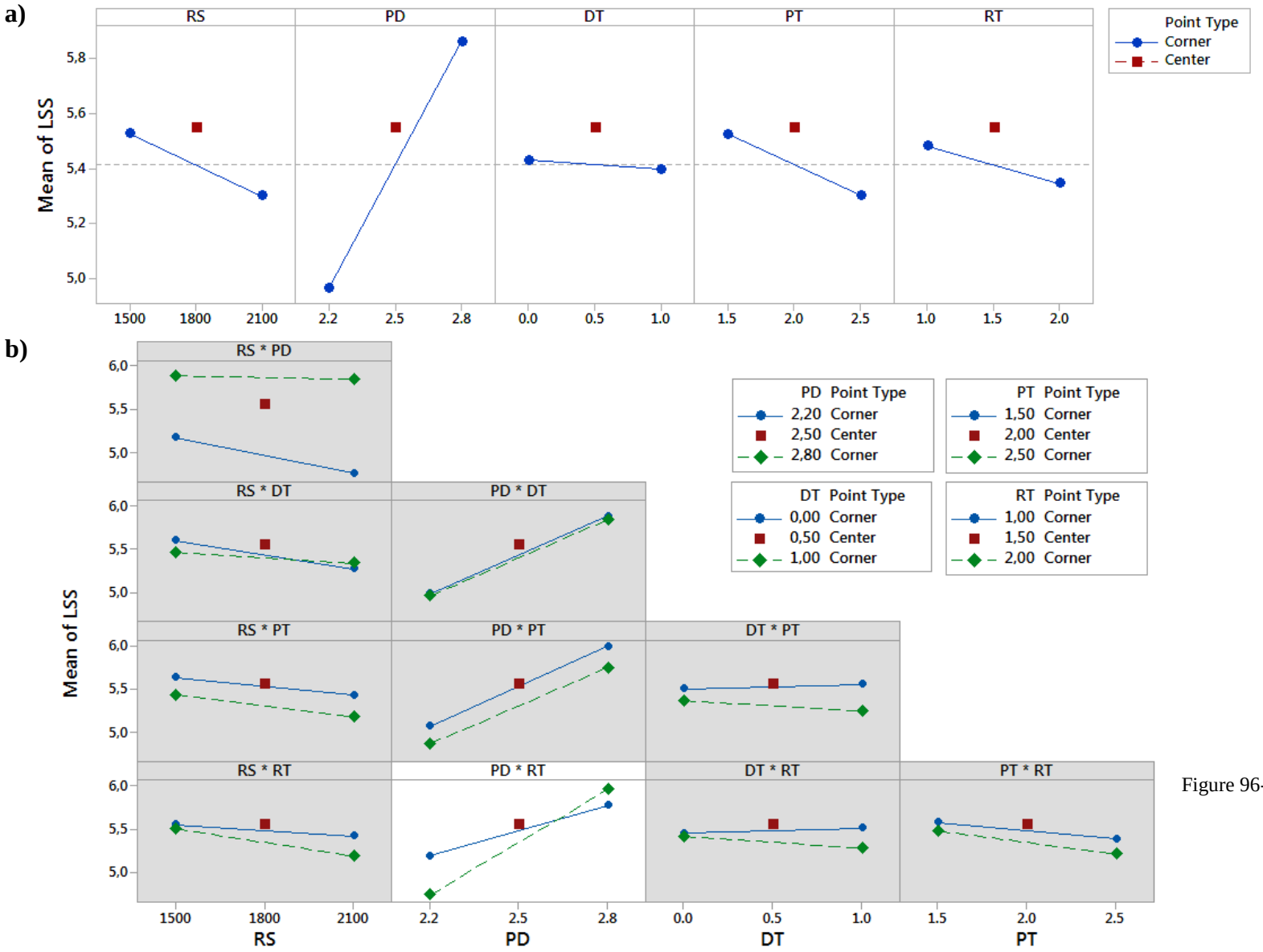

Figure 96- a) Mean response plot of all main factors

b) Interaction plots for the two-interaction factors.

The P-value is the probability of getting a result at least as extreme as the one that was actually observed, given that the null hypothesis is true. In this case, the null hypothesis is defined as: the means of the output are not different (between the upper and lower level) or the coefficient is statistically equal to zero. In practice, the P-value determines which terms have statistically significant effect on the Lap Shear Strength of the lap joint, by defining a significance threshold independent of the degrees of freedom. Their practical meaning is detailed in Table 55.

Table 55- Interpretation of the P value used in hypothesis tests.

P ∞ α	**CI of the sample**	**Statistically Significance**
P < α	Doesn't include the null hypothesis	Yes
P > α	Includes the null hypothesis	No

A typical confidence level (CL) of 95% or 0.95 was used for the t-test. The significance level (α) is the probability of rejecting the null hypothesis when it is true, i.e. defines the threshold for statistical significance, and was simply calculated by equation (11). Equations (12-15) detail the procedure to compute each entry of Table 54.

$$\alpha = 1\text{-}CL = 1\text{-}0.95 = 0.05 \tag{11}$$

$$P_{value} = 1 - CDF\ (T \leq T\_value)\ ;\ \begin{cases} DF = DF_{Error} = 9 \\ Tail = Two\ Tailed \end{cases} \tag{12}$$

* In some statistical software, the last two inputs can also appear collapsed into $Quantile = (1 - \alpha/2)$

$$T_{value} = Standardized\ Effect = \frac{Coef_{\ i}}{Coef\ SE} \tag{13}$$

$$Coef_{\ i} = \frac{Unstandardized\ Effect}{2} \tag{14}$$

$$Coef\ SE = \sqrt{\frac{Adj\ \ MS_{Error}\ ^{*}}{2^{5-1} \cdot replicas}} \tag{15}$$

* Parameter calculated in section 4.2.3 using ANOVA, but basically defines the variance within each group

The importance of each factor was determined by the mean effect concept and plotted as usual in a Pareto chart, Figure 97. The bars that cross the reference line (blue dashed line) are statistically significant. The standardized effects are t-statistics as indicated by equation (13). Pareto chart displays the absolute value of the effects (or standardize effects when the adjusted sum of squares of the error is computed), so you cannot determine which effects increase or decrease the response, only which factors have the largest effect.

Finally, from the first analysis of effects, it is possible to conclude that:

- The main effect was given by **Plunge Depth (PD)** with almost triple the effect of the, the second most significant factor **PD*PT**;
- Standardize effects and T-values are based on ANOVA data, thus the P-values associated with them are identical to P-values associated with F-values. The analysis of the coefficient table leads to similar conclusions achieved by ANOVA method.

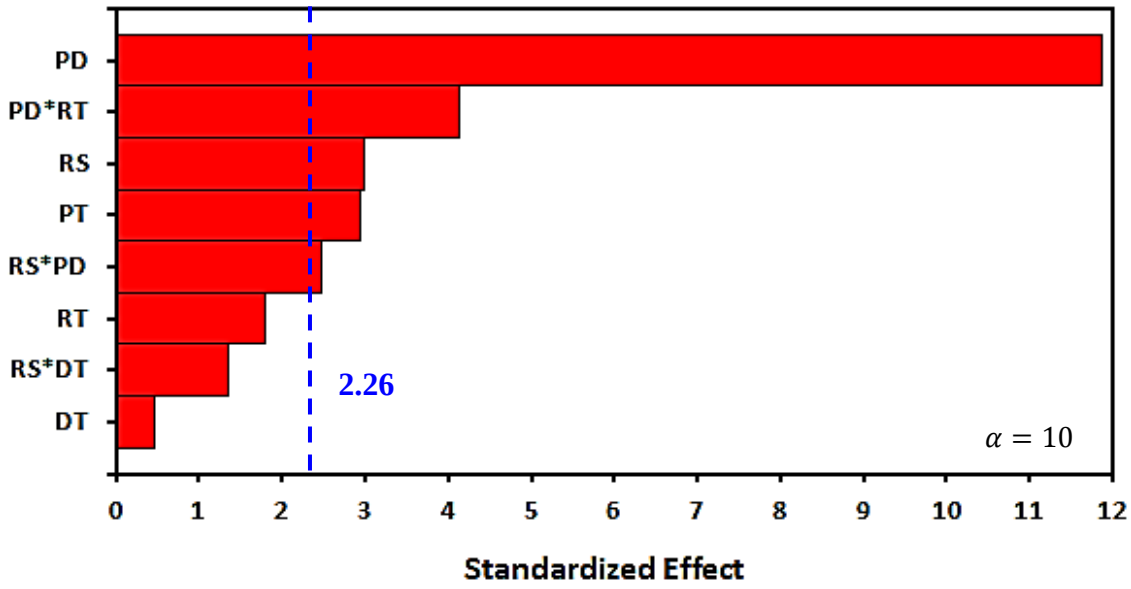

Figure 97- Modified Pareto chart for the main effects and interactions terms, the absolute value of the standardized effects is displayed.

4.2.3 Statistical Significance – Analysis of Variance (ANOVA)

This chapter aims to justify how certain intermediate parameters, previously shown in section 4.2.2, were obtained using the Analysis of Variance (ANOVA). ANOVA is a library of statistical models (and their associated estimation procedures) used to analyze the differences among group means in a sample. ANOVA's principle is the partitioning of the variance into components attributable to different sources of variation - variation within and between groups; being associated to factors, error and curvature. In its simplest form, ANOVA generalizes the F-test to more than two groups. It provides a statistical test of whether the population means of several groups are equal by actually analyzing their variance. Analysis of variance can be viewed as a special case of multi-variable regression modeling. (Ryan 2007)

The interpretation of the ANOVA can be resumed to the P-value for the F-statistics (last column of ANOVA Table 56 for convenience). In this case, the null hypothesis is that the model does not explain any of the variation in the response, i.e. the variance between groups is the same as the variance within groups. P-value is the probability of getting a ratio of variance between groups/ variance within groups at least as extreme as the one that was actually observed, given that the null hypothesis is true. The remaining data, usually showed by common formalism, consists of intermediate parameters that quantify and decompose the variance. They are the base of ANOVA, and are necessary to compute the final P-value, and other parameters related to model fitting (see section 4.2.4). Table 56 summarizes the ANOVA output. Table 57 summarizes the main equations used throughout this subchapter. Before starting analyzing its results, is necessary to state some considerations regarding the true meaning that P-value takes on particular cases. For detail information about the distribution of the Degrees of Freedom please see section 4.2.4.

It is important to notice that the outcome of the lack-of-fit (LoF) test is the inverse of what is usually intended. Here the null hypothesis assumes that model describe the relation between the output and the factors. The P-value for it should be higher than the significance level, and favorably closer to the unity (the test does not detect any model lack-of-fit). LoF can occur if important terms from the model such as interactions or higher-order terms (particularly quadratic terms) are not included. It is usually associated to large residuals resulting from fitting the model. Pure error (PE) on the other hand, is the error due to natural randomness of every real physical process. When the PE is significantly lower than the LoF, it may indicate that the model used is not adequate for the system. In this scenario, rewriting the entire model is advisable. It may be necessary to add higher-order interaction terms or change the design for a RSM capable of modeling quadratic terms.

Table 56- ANOVA table from the DoE, generated by Minitab® software.

		Factor	DF	Adj SS	Adj MS	F-value	P-value
Model	Main Effects	RS	1	0.20453	0.20453	8.91	0.015
		PD	1	3.23550	3.23550	140.92	0.000
		DT	1	0.00480	0.00480	0.21	0.658
		PT	1	0.20048	0.20048	8.73	0.016
		RT	1	0.07412	0.07412	3.23	0.106
	2-factor interactions	RS*PD	1	0.14006	0.14006	6.10	0.036
		RS*DT	1	0.04172	0.04172	1.82	0.211
		PD*RT	1	0.39344	0.39344	17.14	0.003
	Curvature		1	0.04697	0.04697	2.05	0.186
Error	Lack-of-fit		7	0.11629	0.01661	0.37	0.866
	Pure Error		2	0.09035	0.04518		
Total			18	4.54826			

Statistically Significant

Curvature can't be modeled in factorial designs, full or fractional. However, it can be statistically tested to check if it is necessary to upgrade the current design to a RSM. The curvature test outcome is also the inverse of what is usually intended. In this case, the null hypothesis is that the model has no curvature, i.e. all the relationships between the factors and the response are linear. The P-value is the probability of getting a difference between the fitted mean of the response at the center points relative to the expected mean (if the relationships between the model terms and the response are linear) at least as extreme as the one that was actually observed, given that the null hypothesis is true. Thus, the higher the P-value, the more evidences in favor of the null hypothesis, the model has no curvature.

The contribution is a rough but effective guide to the relative importance of each term of the model. Figure 98 complements the information given by the effect analysis, giving a visual representation of the plunge depth importance in the LSS variance.

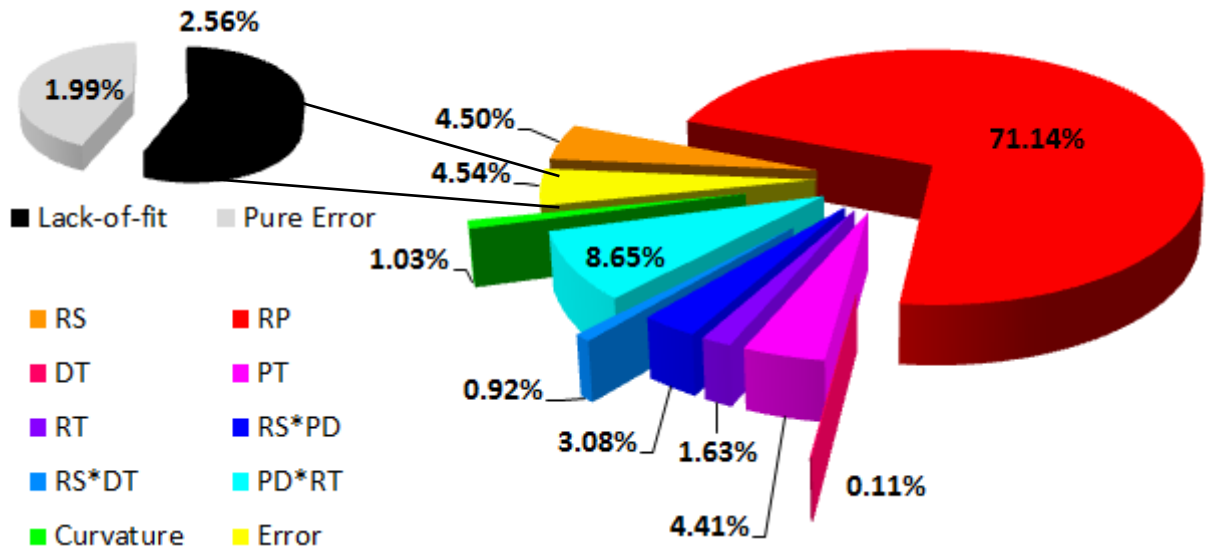

Figure 98- Contribution percentage of each term of the model.

Probability computed from the Cumulative Distribution Function (CDF) of F-distribution. Determine whether the term is associated with the response

$$P_{value} = 1 - CDF\ (F \leq F_{value})\ ;\ \begin{cases} DF_{Numerator} = DF_{F/C} = 1 \\ DF_{Denominator} = DF_{E} = 9 \\ Two - tailed \end{cases} \quad (16)$$

$$P_{value} = 1 - CDF\ (F \leq F_{value})\ ;\ \begin{cases} DF_{Numerator} = DF_{LOF} = 7 \\ DF_{Denominator} = DF_{PE} = 2 \\ Two - Tailed \end{cases} \quad (17)$$

$$F_{\ k/C} = \frac{Adj\ MS_{\ k/C}}{Adj\ MS_{\ error}} \quad and \quad F_{\ LOF} = \frac{Adj\ MS_{LOF}}{Adj\ MS_{Pure\ Error}} \quad (18)$$

i	Identifies the high level
j	Identifies Low level
m	Identifies the run order
k	identifies each factor of the model
E	Total or Residual Error
PE	Pure Error
LoF	Lack-of-fit
C	Curvature

Main conclusions and considerations:

- Statistically significant factors are highlighted in Table 56 and also given in Pareto Chart Figure 97 – PD, PD*RT, RS, PT, RS*PD;
- The complete dominance of the plunge depth effect over the remaining statistically significant factors may indicate that only the influence of plunge depth is worth studying (Dong et al. 2016);
- By looking at the Adjusted MS of the pure error and lack-of-fit (independent of the number of Degrees of freedom), pure error has higher MS than lack-of-fit. This indicates that the model captures the relation between the output and factors, and no higher-order interaction terms should be added;
- In addition, no lack-of-fit was reported in the ANOVA table;
- Even though the hypothesis for curvature of any factor wasn't rejected, its lower P-value may indicate a presence of slight curvature;
- The center points were left in the model, even though curvature wasn't statistically different. They were left to increase the predictability of the model. The disadvantage is that Minitab assumes that the model contains curvature that the factorial design cannot fit. As a direct consequence, Contour Plot, Surface Plot, and Overlaid Contour Plot weren't available.

Table 57- Summary of the statistical equations used to construct the ANOVA table.

Parameter	Designation	Statistics Description		
SS	Sum of Squares of Factors	Variation between groups	$SS_k = \frac{(2^{5-1} \cdot replicas \cdot Effect_k)^2}{4}$	(19)
SS	Total Sum of Squares	Total variation in the model	$SS_{total} = \sum_m (y_m - \bar{y})^2$	(20)
SS	Sum of Squares of total Error	Sum of the squared residuals or Variation within treatments	$SS_{error} = SS_{Total} - \sum_m SS_{Factor} - SS_{Curvature}$	(21)
SS	Sum of Squares of Lack-of-Fit	Total effect of all estimable interaction terms omitted from the model. Variance around the fitted values	$SS_{Lack-of-fit} = SS_{error} - SS_{Pure\ Error}$	(22)
SS	Sum of Squares of Pure Error	Distance between each data point and its group (set of replicates) mean	$SS_{Pure\ Error} = \sum_{i,j} (y_{ijm} - \bar{y}_{ij})^2$	(23)
SS	Sum of Squares of Curvature	Reduction in the sum of squares of the residual error you obtain when you add the centre point term to the model.	$SS_{Curvature} = N_{Cent\ P}(\bar{y}_{Cent} - \bar{y})^2 + N_{Corner\ P}(\bar{y}_{Corn} - \bar{y})^2$	(24)
Adj SS	Adjusted sum of squares	Variation of different components of the model	$Adj\ SS = SS$, for orthogonal designs	(25)
Adj MS	Adjusted Mean Squares	Considers the degrees of freedom	$Adj\ MS_k = \frac{Adj\ SS_k}{DF_k}$	(26)
---	Contribution		$Contribution = \frac{Adj\ SS_k}{Adj\ SS_{Total}}$	(27)

4.2.4 Model Construction, Fitting and Validation

To model the system characterized by the spot welding of a lap joint, a fractional factorial design was considered. Since only half all possible combinations of factor levels were tested, it is necessary to alias half of the factors present in the full factorial model. Table 58 shows the aliases structure on the left and the final aliases structure on the right after model reduction.

Table 58- Alias structure of the standard half fraction factorial design (on the left) and of the reduced model after ANOVA (on the right).

Saturated Model			**Reduced Model**	
Type	**Terms**	**Aliases**	**Terms**	**Aliases**
Constant	I (Identity)	$PD \cdot RS \cdot PT \cdot DT \cdot RT$	I (Identity)	$PD \cdot RS \cdot PT \cdot DT \cdot RT$
Main Factors DF=5	PD	$RS \cdot PT \cdot DT \cdot RT$	PD	$PD \cdot RS \cdot PT \cdot DT \cdot RT$
	RS	$PD \cdot PT \cdot DT \cdot RT$	RS	$PD \cdot RS \cdot PT \cdot DT \cdot RT$
	PT	$PD \cdot RS \cdot DT \cdot RT$	PT	$PD \cdot RS \cdot PT \cdot DT \cdot RT$
	DT	$PD \cdot RS \cdot PT \cdot RT$	DT	$PD \cdot RS \cdot PT \cdot RT$
	RT	$PD \cdot RS \cdot PT \cdot DT$	RT	$PD \cdot RS \cdot PT \cdot DT$
Two-factor Interactions DF=15	$PD \cdot RS$	$PT \cdot DT \cdot RT$	$PD \cdot RS$	$PT \cdot DT \cdot RT$
	$PD \cdot PT$	$RS \cdot DT \cdot RT$	$PD \cdot RT$	$RS \cdot PT \cdot DT$
	$PD \cdot DT$	$RS \cdot PT \cdot RT$	$RS \cdot DT$	$PD \cdot PT \cdot RT$
	$PD \cdot RT$	$RS \cdot PT \cdot DT$		
	$RS \cdot PT$	$PD \cdot DT \cdot RT$		
	$RS \cdot DT$	$PD \cdot PT \cdot RT$		
	$RS \cdot RT$	$PD \cdot PT \cdot DT$		
	$PT \cdot DT$	$PD \cdot RS \cdot RT$		
	$PT \cdot RT$	$PD \cdot RS \cdot DT$		
	$DT \cdot RT$	$PD \cdot RS \cdot PT$		

* I from Identity

Replicas or center points aren't the only solutions available to increase power and the number of DF available. Model refinement or model reduction - the elimination of one or more higher-factor interaction terms from the model - can also increase power and the number of DF available. This is usually done after a first ANOVA study has been run, considering the full model. After that, non-significant terms (interactions or even main terms) can be eliminated. A particular case of model reduction occurs when all terms containing one given factor are eliminated. It is statistical equivalent to replicate one time the entire design, e.g. 2 level 3 factor full factorial design where the terms ABC, AC, BC, C were removed from the model because they didn't have statistical significance. Cautions are needed to keep the model hierarchical. The elimination of the terms should be conducted so that the more complex terms are evaluated and eliminated first. For example, eliminate all non-significant 3-factor interactions before evaluating 2-factor interactions. The process used to refine the model will be detailed later in this section.

The amount of information in the collected data is characterized by the total Degrees of Freedom (DF) of the design. There are two perspectives to evaluate the degrees of freedom: the total available DF - determined by the number of observations (runs) of the design; and the consumed DF – each term uses a portion of the total information to estimate the unknown parameters. The distribution of the total DF of the design is given by the following equations.

$$DF_{Total} = Number\ of\ Runs - 1 \tag{28}$$

$$DF_{Model} = Nº\ terms - 1 \tag{29}$$

$$DF_{Available} = DF_{total} - DF_{model} \tag{30}$$

When the design is not saturated, and there are available DF, several parameters can be estimated. However, the DF can't be allocated arbitrarily. Table 59 specifies the possible sources for the degrees of freedom available to estimate Pure Error, Lack-of-fit and the presence of Curvature. They can be calculated by the following equations, (31) - (33). It should be noticed that there are some common sources, so the number specified (e.g. number of replicas or center points) is in fact the earmarked number for each one (Montgomery 2017), (Antony 2014). Regarding the refined model that was used, the distribution of available DF is given in Table 60.

Table 59- Possible sources for the Degrees of Freedom used to estimate different errors and test for curvature.

Sources of DF	**Lack-of-fit**	**Pure Error**	**Curvature**
Center points	X	X	X
Replicas	X	X	
Replicas*	X	X	
Model Reduction	X		

* If all terms containing one given factor are eliminated,

$$DF_{Curvature} = N_{Center\ \ Points} \tag{31}$$

$$DF_{Pure\ \ Error} = N_{Corner\ Points} \cdot \left(N_{Replicas} - 1\right) + \left(N_{Center\ Points} - 1\right) \tag{32}$$

$$DF_{lack\ of\ fit} = DF_{Available} - DF_{Pure\ Error} - DF_{Curvature} \tag{33}$$

Table 60- Specification of where the Degrees of Freedom were used.

DF_{Total}	18	$DF_{Standard\ Design}$	15	$DF_{Reduced\ Model}$	8	DF_{Model}	8
				$DF_{Reduction}$	7	$DF_{Lack\ of\ fit}$	7
		$DF_{Center\ Points}$	3	$DF_{Curvature}$	1		
				$DF_{Pure\ Error}$	2		

The Multiple regression model equation in uncoded (original) units is given by equation (34). The coefficients of Table 54 are de coded version of the coefficients of each term in the regression equation. Transformation from coded units to uncoded units is easily done by changing variables with equation (35) (Montgomery 2017). However, when the model is hierarchical, the majority of statistics software (including Minitab®) gives the regression equation in uncoded units.

$$\begin{aligned} LSS = {} & 11.92 - 0.00315\ RS - 1.940\ PD - 0.647\ DT - 0.2239\ PT - 2.750\ RT \\ & + 0.001040\ RS \cdot PD + 0.000340\ RS \cdot DT + 1.045\ PD \cdot RT \\ & + 0.1364\ Ct\ Pt \end{aligned} \tag{34}$$

$$Ct\ Pt = \begin{cases} 0, & Corner\ Points \\ 1, & Center\ Points \end{cases}$$

$$C_i = \frac{X_i - \bar{X}_i}{\Delta X_i / 2} \tag{35}$$

C_i	Predictor *i* in coded Units [-1,+1]	$\bar{X}_i$	Intermediate value for the *i* factor/predictor
X_i	Predictor *i* in uncoded Units	ΔX_i	Upper bond - Lower bond

To access how well the model fits the sampled data and its prediction capability, different statistics are summarized in Table 61. In order to get the most information about it, a few statements about each one ought to be made.

Table 61- Summary of the goodness-of-fit statistics.

S (I)	**R^2 (**II)	**R^2 (adjusted) (**III)	**R^2 (predicted) (**IV)
0.1515	95.46 %	90.91 %	82.17%

I	Standard deviation in response units [kN]
II	Increase with the model size
III	Independent of the number of factors used
IV	Prediction capacity

The S value measures how far the data values fall from the fitted values (in the original units of the response), i.e. is the standard deviation of the fitting error. It should only be used to compare models. It is calculated by the following equation (Montgomery 2017):

$$S = \sqrt{MS_{Error}} = \sqrt{\frac{Adj\ SS_{Pure\ Error} + Adj\ SS_{Lack-of-fit}}{DF_{Error}}} \tag{36}$$

R^2 is the percentage of total variation in the system output that is explained by the model. R^2 increases with the increase of the number of terms of the model (even when there is no real improvement of the model). Thus, this statistics should be used carefully and only to compare models with the same size (Montgomery 2010). It is calculated by the following equation:

$$R^2 = 1 - \frac{Adj\ SS_{Error}}{Adj\ SS_{Total}} \tag{37}$$

Adjusted R^2 is the percentage of total variation in the system output that is explained by the model, adjusted for the number of terms in the model relative to the number of runs. Whereas R^2 increases as the number of terms of the model increase, adjusted R^2 incorporates the number of terms in order to be insensitive to that. Thus, it allows comparing models with different numbers of predictors (Montgomery 2010). It is calculated by the following equation:

$${R_{Adj}}^2 = 1 - \frac{Adj\ MS_{Error}}{Adj\ MS_{Total}} = 1 - \frac{Adj\ MS_{Error}}{Adj\ SS_{Error}\ /\ DF_{Total}} \tag{38}$$

Predicted R^2 is a metric of the model predictability capability. It is calculated by a more complex process detailed in (Montgomery 2010). However, it is equivalent to systematically remove one observation, estimate the regression equation, predict the removed observation and determine the error associated to it. Important cautions are needed to not over-fit the model. It occurs when no important terms are added just to increase the goodness-of-fit metrics, tailoring the model to the sample data. When the predicted R^2 is significantly lower than R^2 , it may be an indicator that the model is over-fitted (Montgomery 2010).

Throughout the analysis of Table 61 it i s possible to highlight: a low S value, order of magnitude of 150 kN; a satisfactory adjusted R^2, similar to R^2 which discards the use of irrelevant terms in the model; and finally a predicted R^2 close to R^2, corroborating the absence of model over-fitting (Montgomery 2017).

Different statistical software programs have different methods to perform the reduction of the model. Minitab® has four methods in its tool library:

- Manual/None – the user must decide which factor to eliminate;
- Stepwise – Iterative process that starts with an empty model (or includes specified terms by the user) and adds or remove only for each step. The stopping criterion is all terms not included in

the model have equal or higher P-values than the minimum specified and all terms included in the model have P-values equal or lower than the maximum specified.

- Forward selection – Iterative process that starts with an empty model (or includes specified terms by the user) and adds the most significant term for each step. The stopping criterion is all terms not included in the model have P-values higher than the minimum specified;
- Backward Elimination – Iterative process that starts with all terms in the model (or only with the specified potential terms) and removes the least significant term for each step. The stopping criterion is all terms in the model have P-values equal or lower than the maximum specified.

A basic recommendation that was followed was to not extrapolate beyond the inference space. All predicted data was within the design space determined in subchapter 3.2.5. In order to evaluate the prediction capacity of the model, in addition to the data collected during the DoE, data points of not yet tested combinations of the full factorial design were sampled. A more refined sampling near the optimized conditions was conducted with 3 samples. All data is organized in Figure 99. The plot of Figure 99 indicates a fairly good prediction capacity, where almost all the predicted values lay down in the confidence interval of 95% confidence level. The Prediction Intervals (PI) is naturally always wider than the corresponding Confidence Intervals (CI) of the prediction, due to the added uncertainty involved in predicting a single response versus the mean response.

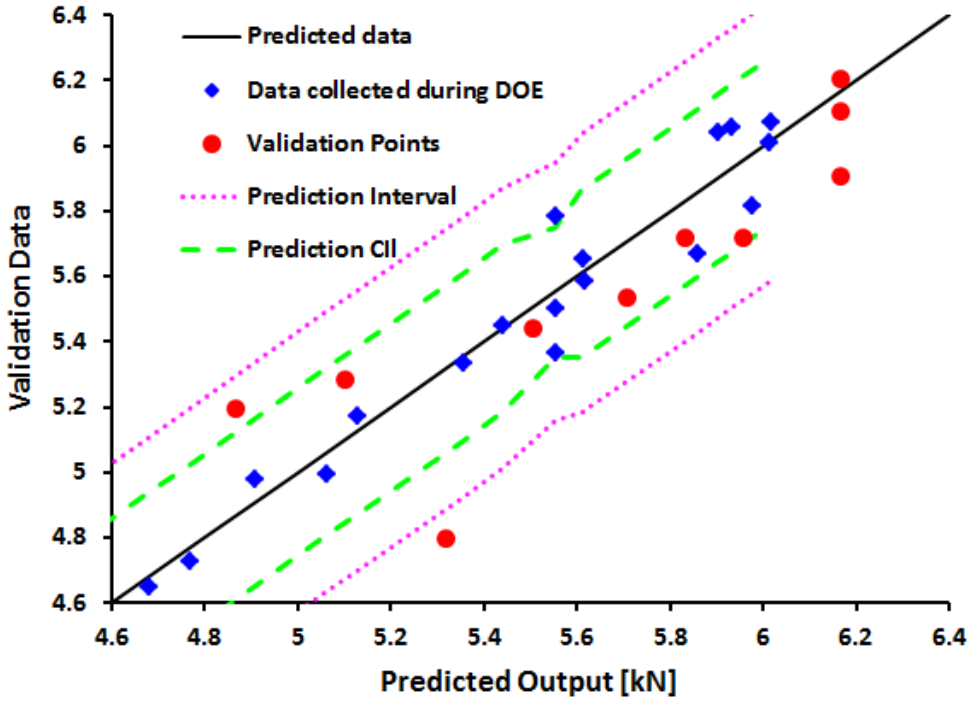

Figure 99- Comparison of Prediction values with data collected during the DoE and validation points.

4.2.5 Residual Analysis

The analysis of the residuals consists in a series of diagnostic tests. It is important to assess the fulfillment of the model assumptions and identify outliers (by definition have high residuals). Any design of experiments is based on ANOVA analysis, its statistic tests and confidence interval, and multiple regression of ANOVA model (least square assumptions). The design must meet their base tool assumptions. Consequently, to construct the previous model (see section 4.2.4), the residuals have to obey a few hypotheses, namely:

- Mean equal to zero – by construction of the statistical estimators this condition is imposed;
- Follow a normal distribution;
- Have reasonably equal variance and random distribution;
- Must be independent of each other.

Residuals are the "error" component that isn't explained by the regression line. They are simply calculated by:

$$Residual = y - \hat{y} \tag{39}$$

$$Standard\ deviation\ (StDev) = \sqrt{\frac{\sum(residuals^{\,2})}{Number_{Runs} - 1}} \tag{40}$$

$$Standardize\ Residual = Residual\ /\ StDev \tag{41}$$

A histogram simply plots the absolute frequency of the residuals that lay in a given interval of a given size. A rule of thumbs to know whether or not is advisable to consider the information of a histogram, is to ensure that 20 or more data points are collected. For short sample designs (small data points for each bar), the estimation of skewness and the identification of outliers can be misleading. In addition, the size of the groups used to plot the histogram (coarser or more refined intervals) influence its appearance. In summary, no conclusions about normality should be made, being only helpful in the identification of skewness or possible outliers. No disturbing left or right skewness is observed in Figure 100, and not outstanding outliers can be guessed at first sight (Montgomery 2010).

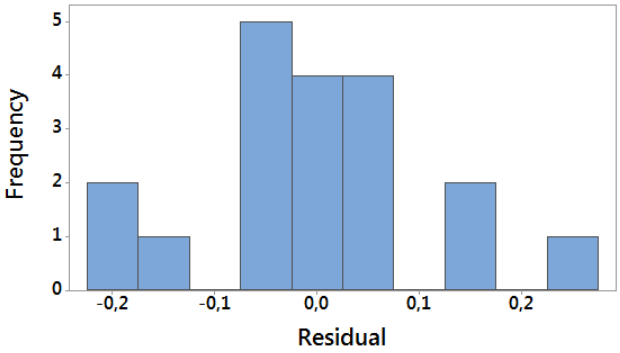

Figure 100- Histogram of the residuals, generated by Minitab®.

A normal probability plot of the residuals is a graphical technique for assessing whether or not a data set (the residuals) is approximately normally distributed (John et al. 1983). The red straight line represents the normal cumulative distribution function (normal CDF) for the residuals range, of a normal distribution with zero mean and standard deviation given by equation (40). The residuals should closely scatter around it. Typical patterns and probable issues can be summarized as: s-curve (long tail distribution), invert s-curve (short tail distribution), downward curve (left skewed distribution), upward curve (right skewed distribution) and sort of curvature or up-and-down shape (bimodal distribution).

The normal plot of Figure 101 a) shows a distribution virtually normal with a small number of outliers but with no visible trend in both tails. The standardized residual (SR) plot is also shown, Figure 101 b). Minitab® flags the data points with SR outside the [-2; 2] interval. According to this criterion, no critical outliers were detected. If a non-normal pattern was observed, the other residual plots would point to other problems with the model. These problems could be due to missing terms (need of more variables or higher order terms), outliers or high leverage points (particularly by loss of data or doubtful data in the extremes points), or a time order effect (bad randomization).

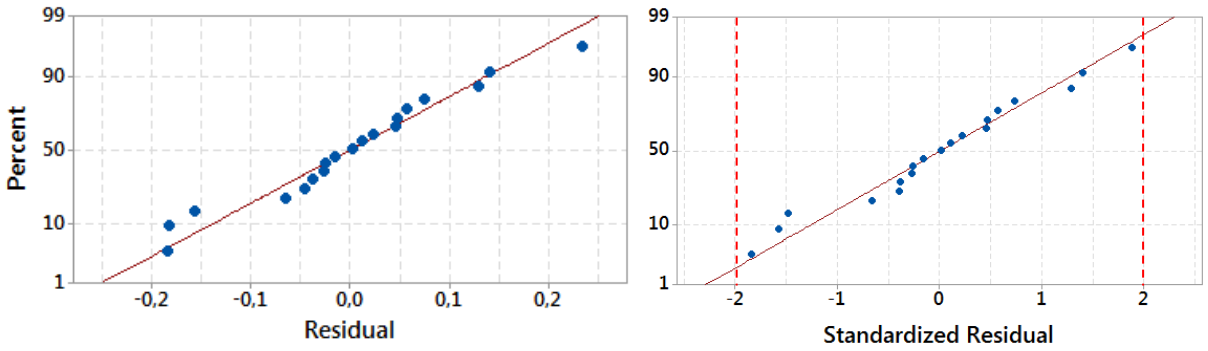

Figure 101- a) Normal probability plot of: a) the absolute residuals; b) standardize residuals. Generated by Minitab®.

The residuals-order plot allows verifying independency between factors. It simply plots the absolute value of the residuals against the time (characterized by the run or observation order). The residuals ideally should manifest no trends or patterns, falling randomly around the center line. Typical patterns can be classified in cyclic, ascending or descending, and with sudden shift with a steep transition region. The presence of these patterns may indicate that residuals are sequentially correlated, questioning its independency.

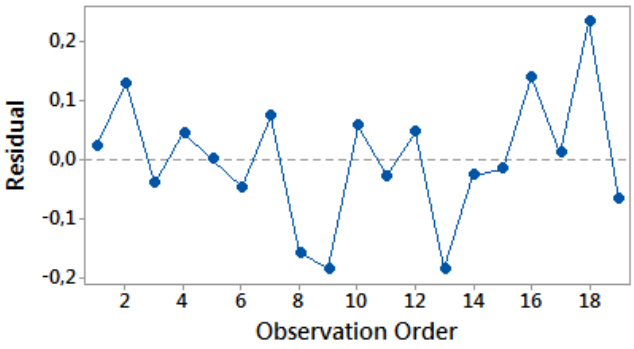

Figure 102- Residuals-observation order plot, generated by Minitab®.

As it is shown in Figure 102, the residuals fall fairly randomly around the center line. The residuals-fits plot allows ascertaining the randomness of the distribution and uniformity/constancy of variance of the residuals (homoscedasticity) (Vogt and Johnson 2015). It essentially plots the absolute value of the residuals against the fitted values (response data collected). The residuals ideally should fall randomly on both sides of the null line, manifesting no recognizable patterns or bias. Typical patterns and suggested solutions can be summarized as: outliers (correct data entry or measurement errors or remove one-time events), fanning of residuals in one direction or increasingly widen scatter of the residuals (variable transformation), y-axis unbalanced (variable transformation), x-axis unbalanced (variable transformation), large y-axis data points (one or more variables are missing), nonlinear or curvilinear (higher order term missing or one or more variables are missing).

From Figure 103 a small variance change (slightly no constant variance) can be identified by the uneven spreading of the residuals. However, further measures such as box-cox transformation (adaptive variable transformation tool of Minitab®) are not needed.

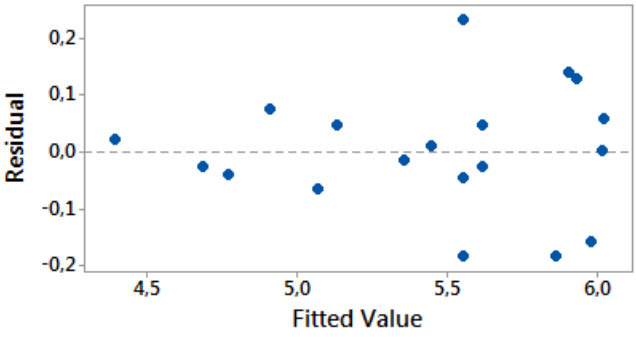

Figure 103- Plot of the residuals-fitted value, generated by Minitab®.

(Moore and Kirkland 2007), (Montgomery 2017), (Mead 1990), (Ryan, Joiner, and Cryer 2012), (Snow 2011)

4.2.6 Suggestions for RSM Optimization

The implementation of a Response Surface Methodology (RSM) after a screening design has more industrial than scientific interest, statement later justified. In order for this type of studies to be completely successful, it's necessary to ensure that all variables not studied are kept the same: machine, tool, clamp system, surface preparation, parts geometry, etc. Even though the main effects and relations keep the same, the value obtained usually suffers an offset. That's the main reason why this type of studies is usually either conducted by the process owner; or when specifically ordered by an industrial partner, only gives a good guess to find the true optimal point. As already mentioned, the project initially resulted from a partnership between HZG and an automobile enterprise group. In industrial applications, particularly the automotive sector, usually only the best set of parameters is desired. Thus, in this section, a suggestion for the optimization of the system parameters is given. The model was refined with reduction of the number of factors to be studied and a quadratic design capable of curvature handling is proposed. The study wasn't conduct in HZG; the idea is that it will be carried on in loco (in the industrial plant itself).

In order to optimize the welding parameters, a Box-Behnken (BB) design is suggested. Box-Behnken designs are incomplete three-level factorial designs that were introduced in order to limit the sample size as the number of parameters grows. Supported by the previous screening design results, only the following parameters should be optimized: Rotation Speed (RS), Plunge Depth (PD) and Plunge Time (PT), the remaining process parameters are fixed, and their values are given in Table 62.

Table 62- Suggested values for the welding parameters fixed in the experiment.

Clamping Force [kN]	Dwell Time [s]	Retract Time [s]
10	0	1

Other RSM could also be used; their disadvantages and possible advantages are summarized in Table 63. BB design was chosen mainly due to its superior cost/time effectiveness, relevant factors in an industrial environment. In addition, (Mathews 2005) states that the number of degrees of freedom left for error estimate should be within the 8 and 20. However, usually there are a few two-factor interaction terms that can be dropped after first ANOVA analysis, justifying the options of a BB design. Similar to the experiment conducted by (Santana et al. 2017) for Al alloys.

Table 63- Advantages and disadvantages of typical used RSM quadratic designs for 3 factors optimization (Montgomery 2017), (Antony 2014).

Design	Number of Runs	DF_{Total}	DF_{Model} *	$DF_{Available}$ *	Description
Full Factorial 3^k	27	26	9	17	Resources wasteful Excessive degrees of freedom for error estimative More sensitive to variable effects
Central Composite CC(2^3) *Based on a 2^3 factorial design	20	19	9	10	Some resource waste Possible practical difficulties in impose the star points (physical limitations) Rotatable and Orthogonal design Used when safe limits are not known
Box-Behnken Design BB(3) *With 3 factors	15	14	9	5	Some Rotability Safer than the 3^k design

* Only main terms, two-factor interactions and quadratic terms are considered worth modeling. The higher order interaction are aliased and the remaining degrees of freedom used for error estimative

To conduct the future experiment, the Box-Behnken design matrix is considered the best approach and is given in Table 64. The table is given in the coded version. A visual representation of the design space is also given in Figure 104. Other quadratic designs adequate for three factors optimization are also given in Table 65, and some variations of the Central Composite Design (CCD) proposed are also shown in Table 66.

Table 64- Box-Behnken design matrix factors settings BB(3), evidencing the three replicas for the center point (Montgomery 2017).

Standard Order	Replicas	RS [rpm]	PD [mm]	PT [s]
1	1	-1	-1	0
2	1	+1	-1	0
3	1	-1	+1	0
4	1	+1	+1	0
5	1	-1	0	-1
6	1	+1	0	-1
7	1	-1	0	+1
8	1	+1	0	+1
9	1	0	-1	-1
10	1	0	+1	-1
11	1	0	-1	+1
12	1	0	+1	+1
13	3	0	0	0
14		0	0	0
15		0	0	0

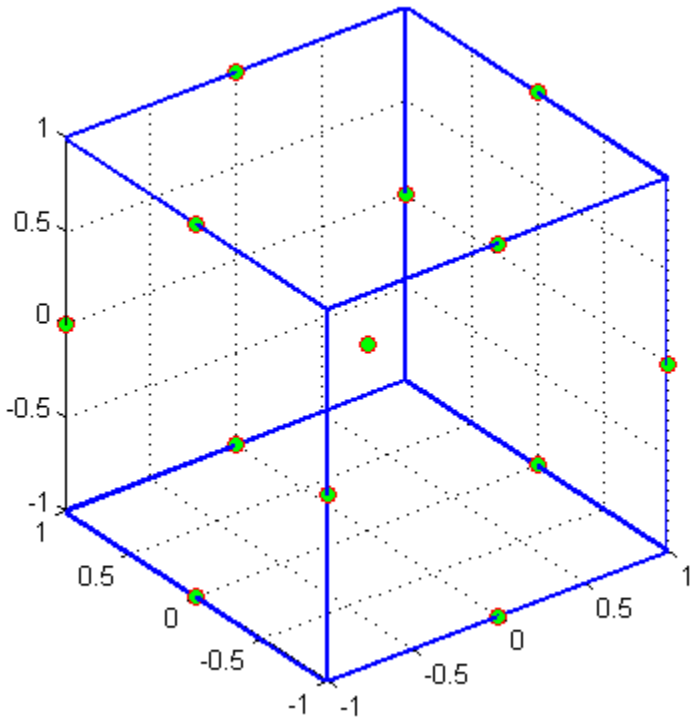

Figure 104- Illustration of the spatial location of the dada points collected when using a Box-Behnken design. Plot created with MATLAB©.

Table 65- Design matrix for different RMS three factors-three levels designs (Antony 2014).

Design	Standard Order	RS [rpm]	PD [mm]	PT [s]
Full Factorial	1	–	–	–
	2	–	–	0
	3	–	–	+
	4	–	0	–
	5	–	0	0
	6	–	0	+
	7	–	+	–
	8	–	+	0
	9	–	+	+
	10	0	–	–
	11	0	–	0
	12	0	–	+
	13	0	0	–
	14	0	0	0
	15	0	0	+
	16	0	+	–
	17	0	+	0
	18	0	+	+
	19	+	–	–
	20	+	–	0
	21	+	–	+
	22	+	0	–
	23	+	0	0
	24	+	0	+
	25	+	+	–
	26	+	+	0
	27	+	+	+
CCC(2^3) CCC designs provide high quality predictions over the entire design space (when compared with other Central Composite Designs) Require factor settings outside the range of the factors in the factorial part	1	–	–	–
	2	–	–	+
	3	–	+	–
	4	–	+	+
	5	+	–	–
	6	+	–	+
	7	+	+	–
	8	+	+	+
	9	0	0	0
	10	0	0	0
	11	0	0	0
	12	0	0	0
	13	0	0	0
	14	0	0	0
	15	–η	0	0
	16	η	0	0
	17	0	– η	0
	18	0	η	0
	19	0	0	– η
	20	0	0	η

H Star point, define the two levels added to the original three (+, 0, -) levels

Table 66- Alternative CCD with different features (Antony 2014), (Montgomery 2017).

Design	Standard Order	RS [rpm]	PD [mm]	PT [s]
	1	−	−	−
	2	−	−	+
	3	−	+	−
	4	−	+	+
CCI(2^3)	5	+	−	−
Central Composite Inscribed	6	+	−	+
	7	+	+	−
CCI design is a scaled down CCC design with each factor level of the CCC design divided by η	8	+	+	+
	9	0	0	0
	10	0	0	0
	11	0	0	0
Used in situations in which the limits specified for factor settings can't be exceeded	12	0	0	0
	13	0	0	0
	14	0	0	0
Lower quality prediction over the entire space compared to the CCC	15	−η	0	0
	16	η	0	0
	17	0	− η	0
	18	0	η	0
	19	0	0	− η
	20	0	0	η
	1	−	−	−
	2	+	−	
	3	−	+	−
CCF(2^3)	4	+	+	-
Central Composite Face-centered	5	-	−	+
	6	+	−	+
Relatively high-quality predictions over the entire design space (when compared with CCC designs)	7	-	+	+
	8	+	+	+
	9	-	0	0
	10	+	0	0
	11	0	-	0
D not require points outside the original factor window	12	0	+	0
	13	0	0	-
Not Rotatable	14	0	0	+
	15	0	0	0
Poor precision for estimating pure quadratic coefficients	16	0	0	0
	17	0	0	0
	18	0	0	0
	19	0	0	0
	20	0	0	0

The uncoded levels of the star points from CCC and the new extreme limits from CCI can be calculated as indicate by equations (42), (43) and (44) respectively.

$$\eta = \sqrt[4]{2^{k=3}} \tag{42}$$

$$L_{\eta} = L_0 \pm \eta \cdot \Delta / 2 \tag{43}$$

$$L_{\pm} = L_0 \pm \Delta / 2\eta \tag{44}$$

L Uncoded value of the factor level + - or 0

Δ Difference between the two extreme levels

4.3 Conventional Rotation Refill FSSW – Metallurgical Analysis

One of the major goals of the project was to better understand the welding mechanism between the Mg matrix and steel, and the role of the Zn present in the HDG coating. The fully understanding of the bonding mechanism draws in the capacity of explaining the correlation between the welding parameters and the joint resistance. The previous DoE results (from subchapter 4.2) weren't the project upshot, but simply a tool that allowed to taper the joint metallurgical analysis conducted in this subchapter 4.3. The current subchapter encompasses the most relevant results since it enabled to understand the physical (metallurgical) process behind the bonding mechanism. The role of Zn was studied in section 4.3.4, by comparing the joint resistance and fracture surface of different joints produced with AM50-Zn coated steel, and AM50-bare steel.

Subchapter 4.1, apart from enabling the definition of the DoE, it also detected the presence of the SZ pull-out defect, briefly characterizing it. This defect is related with part of this subchapter and subchapter 4.4. Part of this subchapter is dedicated to further enlighten this defect through macrostructural, microstructural and chemical analysis. Subchapter 4.4 has a similar layout to this subchapter, but a rather different goal. The main goal of this project wasn't to apply and study the novel technique[7] of Differential Rotation Refill-FSSW (DR Refill-FSSW) for Mg-steel dissimilar welding. The implementation of this technique should be exclusively seen as an approach to overcome the SZ pull-out defect.

The ANOVA statistical analysis indicated several statistically significant factors – PD, PD*RT, RS, PT, PD*RS. With the exception of the plunge depth, their significantly higher P value probably wouldn't allow detecting relevant metallurgical differences. Thus, due to the large difference between the plunge depth effect and the remaining factors (with statistical significance), it was opted to only study the metallurgical influence of the plunge depth.

Considering that only the influence of the plunge depth is going to be studied, the remaining parameters must be set in some particular value. Choosing the intermediate parameters or the best set of parameters are both common approaches in the literature. However, a different approach was followed. The parameters used as reference for metallographic analysis weren't the optimized ones:

- Welding Times – Regarding industrial concerns, minimum welding cycles are always preferred and their study has probably more practical impact. Since the difference in mechanical properties between the optimal point and the minimal welding cycle point was small, the last one was used as reference during this subchapter;
- Rotation Speed – Higher rotation speed usually means higher energy consumption and tool wear. However, it was preferred to use the mid-point rotation speed instead of the lower rotation speed level - indicated as optimal setting by the DoE (optimized parameters: RS = 1500 rpm). The mid-value of the rotation speed enabled joints less prone to defects, while keeping a good compromise with mechanical properties.

To summarize, the joint used as standard reference was produced with the following parameters: RS = 1800 rpm, PT = 1.5 s, DT = 0 s, RT = 1 s. The effect of plunge depth in the joint macrostructure, microstructure (until interface scale), and fracture surface will be further studied by analysing three discrete cases of plunge depth: 2.2 mm, 2.5 mm and 2.8 mm.

[7] The patent acquisition process and normative process of DR Refill-FSSW are still ongoing.

4.3.1 Macrostructure and Macroanalysis

Metallurgical defects like wormholes (or voids), cracks and tunnel defects (typical of FSW) are usually better identified prior to etching (Armstrong, Adams, and Arnold 2018). However, the main goal of macrostructural observation was to enhance the visualization of Mg-Zn rich region. Since all fractures during the complete experiment occurred in the interface, small metallurgical defects (hypothetically obscured by the etching process), outside the interface have little or none influence on the static behaviour of the joint (Chen et al. 2015).

Thus, macrostructures from Figure 105 to Figure 106 were taken with Optical Microscopy (OM), after chemical etching with a picric solution detailed in Table 41. Considering the information of the OM macrographs, defect free welds with no clear voids at the interface are observed. Moreover, both sheets appear to be in direct contact with a tight Mg-steel boundary. The darker area at the Mg-steel interface present in all macrographs was due to enhanced etching and not defects, statement confirmed further in the interface analysis.

In all macrostructures from Figure 105 to Figure 106 a) it is possible to observe in the SZ, a clearly pronounced distribution of a contrast region that is related to chemical composition differences. Also, it is interesting to see that the distribution of what was assume to be a Mg-Zn rich region, is similar to the bonding ligament feature, common in the Refill-FSSW of Al alloys (Suhuddin et al. 2013). Even though the plunge depth changes a total of 0.6 mm from Figure 105 a), b), to c), there are no detectable correlation between the plunge depth and the geometric distribution of the contrast region. This characteristic Mg-Zn layered structure divides the SZ in two parts, and is usually about 1 mm above the Mg-Steel interface.

The presence of small portions of Mg-Zn rich region in the SZ is more concentrated below the characteristic trace. No correlation between the presence of defects and the PD was found. The sequence of Figure 106 a), Figure 105 c), and Figure 106 b), tries to depict the effect of RS in the macrostructure. No visible correlation can be drawn, but it can be stated that for the extreme cases of RS, Figure 106, the presence of voids and cracks is enhanced. Regarding Figure 106 b), it should be notice that the presence of the SZ pull-out defect, for some boundary parameters, doesn't have much repeatability. Depending on the room temperature, and the heat transfer boundary conditions/joint shape - lap joint or macrostructure configuration, and in the case of complete overlap, the spot can be at the center or corner - the SZ pull-out defect may or not be present for 2.8 mm PD.

The contrast region distributed as evidenced in Figure 105 and Figure 106 a) is most probably formed due to the macroscopic material flow during welding. (Shen, Lage, et al. 2018) studied the texture development and material flow in similar welding of Al alloys by stop-action technique. It was found that in the SZ, the global straining state during all stages of welding was characterized as simple shear. The material flow model proposed assumed two main driven components for the material flow - the simple shear acting on the horizontal plane, and the extrusion acting on the vertical plane. In both stages, the material flow occurred layer by layer, with an unobvious vertical flow. This stable layered material flow behavior probably also occur in dissimilar welding of Mg to steel, since there was no steel plunging (to mix the dissimilar materials) and the dwell was short or null (Shen, Lage, et al. 2018). The contrast region was probably formed during penetrating stage, due to progressively reaction of the Zn (from the steel coating), with the Mg matrix under high pressure and heat imposed by the tool action. The global material flow could be described as a pilling up of layers along the whole welding SZ, similar to a stack where the first layer is pushed by the second without jumping, enabling the development of the continuous Mg-Zn region during the whole welding process.

Figure 107 consists in the same macrograph as Figure 105 a), but captured using Scanning Electron Microscope (SEM) in backscattered electron mode. What looks like voids and lack of mixture in OM, can be easily observed as complete integral and sound structures in Figure 107. The dark contrast region evidenced by OM, can be easily distinguished now with bright contrast, because exhibits higher Zn content. This is due to the large difference between the atomic number from Mg (that is smaller) and Zn (that is almost 3x bigger). Elements with higher atomic number tend to appear brighter in the backscattered mode.

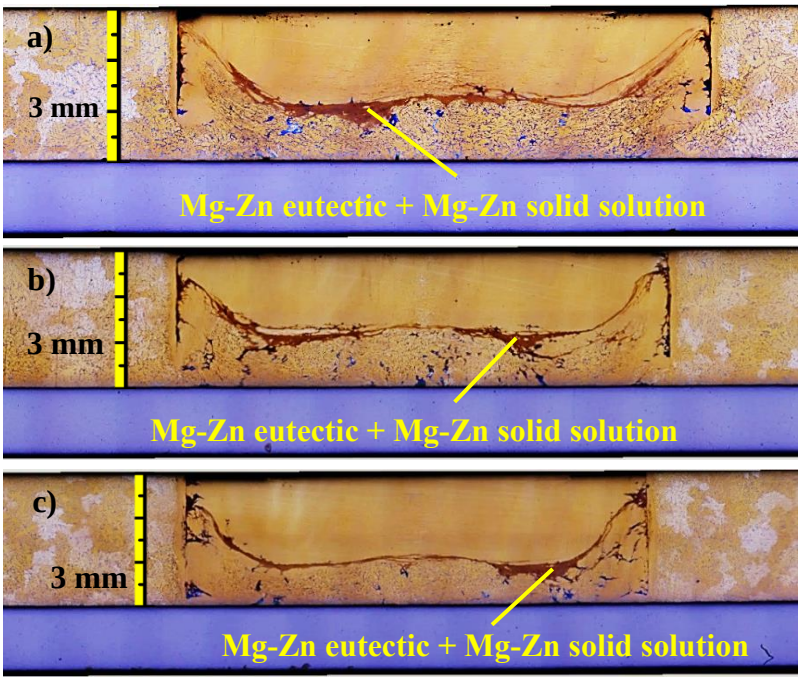

Figure 105- Macrographs captured by optical microscopy for different Plunge Depth: a) PD=2.2 mm; b) PD=2.5 mm; and c) PD=2.8 mm. The remaining parameters were kept the same.

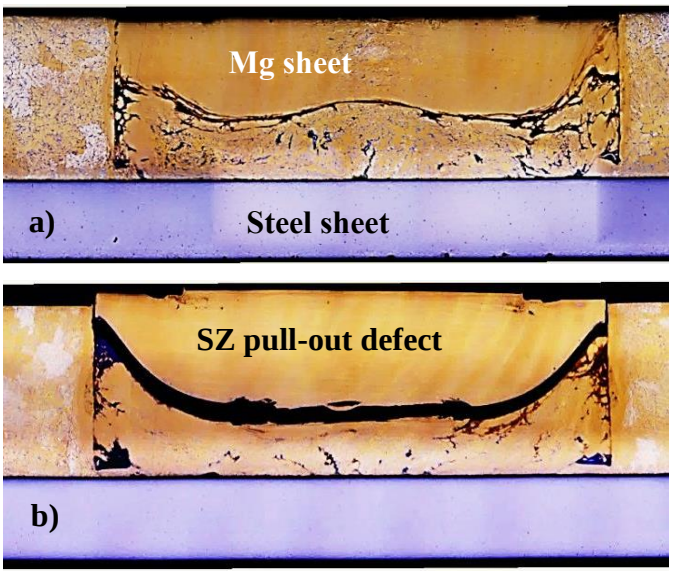

Figure 106- Macrostructures obtained by optical microscope for different Rotation Speeds: a) RS=1500 rpm; and b) RS=2100 rpm. The remaining parameters were kept the same: PD = 2.8 mm, PT= 1.5 s, DT= 0 s, RT= 1 s

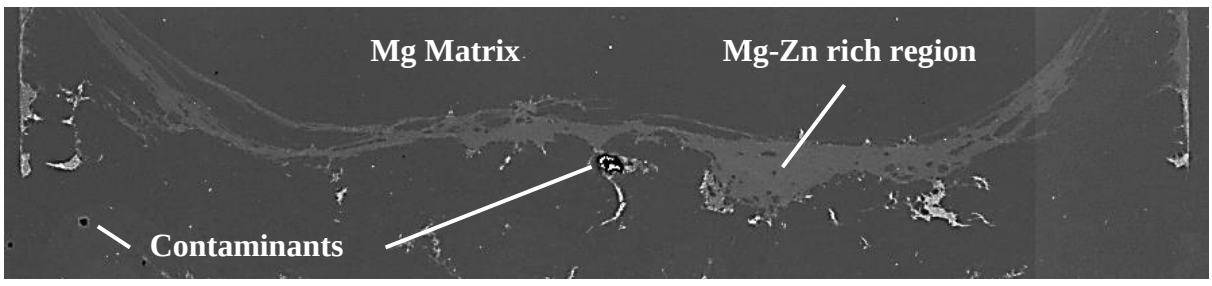

Figure 107- SEM macrograph of joint with low PD = 2.2 mm, RS= 1800 rpm, PT = 1.5 s, DT = 0 s, RT = 1 s.

4.3.2 Microstructure and Microanalysis

Several microstructure modifications were observed. The Stir Zone (SZ) experienced typical grain refinement by dynamic recrystallization (due to stirring action), Figure 108 b). The Thermomechanical Affect Zone (TMAZ) is easily identified near the SZ. However, to identify the Heat Affected Zone (HAZ) in common Refill-FSSWed joints, frequently micro-indentation hardness test must be performed. The large grains of the casting Mg base material increase even more the difficulty to observe the HAZ, Figure 108 a).

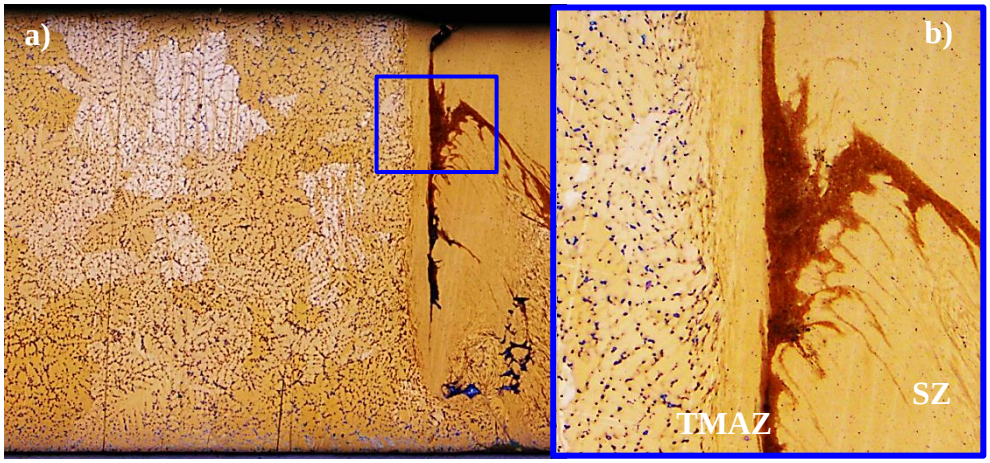

Figure 108- a) Partial macrograph of cross section from intermediate heat input weld. b) Detail of different grain size development, evidencing the ST and TMAZ.

In addition to the typical microstructural changes for Refill-FSSW joints, several particular features were observed after welding, Figure 109. The Mg-Al eutectic structure suffered a refinement with fine particles homogeneously distributed (the interdendritic network or interdendritic coarser particles was broken). In fact, the eutectic is metastable in the Mg-Al system, as discussed in section 2.1.3. Simple heat treatment can therefore result in a complete dissolution of the Mg_{17} Al_{12} intermetallic phase (Dahle et al. 2001). Thus after welding, the transformation of the partially divorced eutectic in fully divorced eutectic was observed. The Al-Mn precipitates didn't melt, they only fractured under the combined action of heat and severe deformation. The Al element segregation was also eliminated.

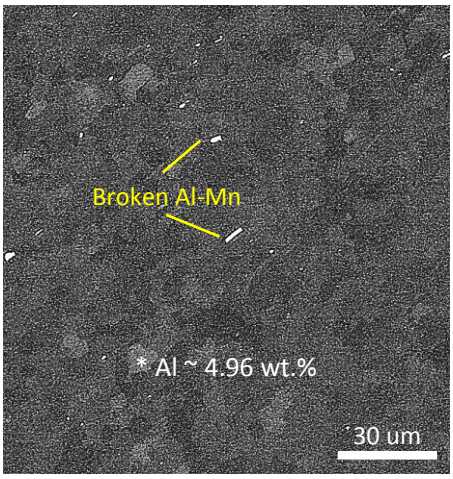

Figure 109- SEM micrograph of SZ, detailing microstructure modifications in the Mg matrix after welding.

SEM microstructures observation of the Mg-Zn contrast feature is shown with sequential magnification through Figure 110 a) - e). They indicate that the Mg-Zn characteristic region is in fact composed of Mg-Zn solid solution, Figure 110 d), and Mg-Zn eutectic, Figure 110 e). Even though the Mg-Zn rich region lies down mainly in the interior of the SZ (reaching its boundaries), some Zn rich regions located near the Mg-steel interface are depicted in Figure 110 f) and g). As indicated in Figure 110 a), their distribution isn't continuous through Mg-steel interface, but rather sparse within the lower part of the SZ. According to the Mg-Zn phase diagram of Figure 3 from Annex I, the eutectic transformation can be written as: $L \rightarrow \alpha\text{-Mg} + Mg_7 Zn_3$, and the α-Mg has a composition (at.%) within 2.4% Zn, and the eutectic structure around 28 % Zn (at.%). EDS local analysis of Mg-Zn region near the boundary of the sleeve plunge diameter are shown in Figure 111. It is possible to correlate the increase in Zn element and the brighter contrast colour in the SEM microstructure. The compositions are consistent with the microstructural features observed – lamellar structure typical of eutectic reactions

(Area 2 from Figure 111); and second brighter regions identified as Mg-Zn solid solution (region with the second higher Zn content in the SZ). The formations of Mg-Zn solid solution and Mg-Zn IMC's in the SZ suggest that during the welding process, Zn coating of the steel surface reacts with Mg and is transferred under the combined effects of heat (diffusion) and force (mechanical mass transfer).

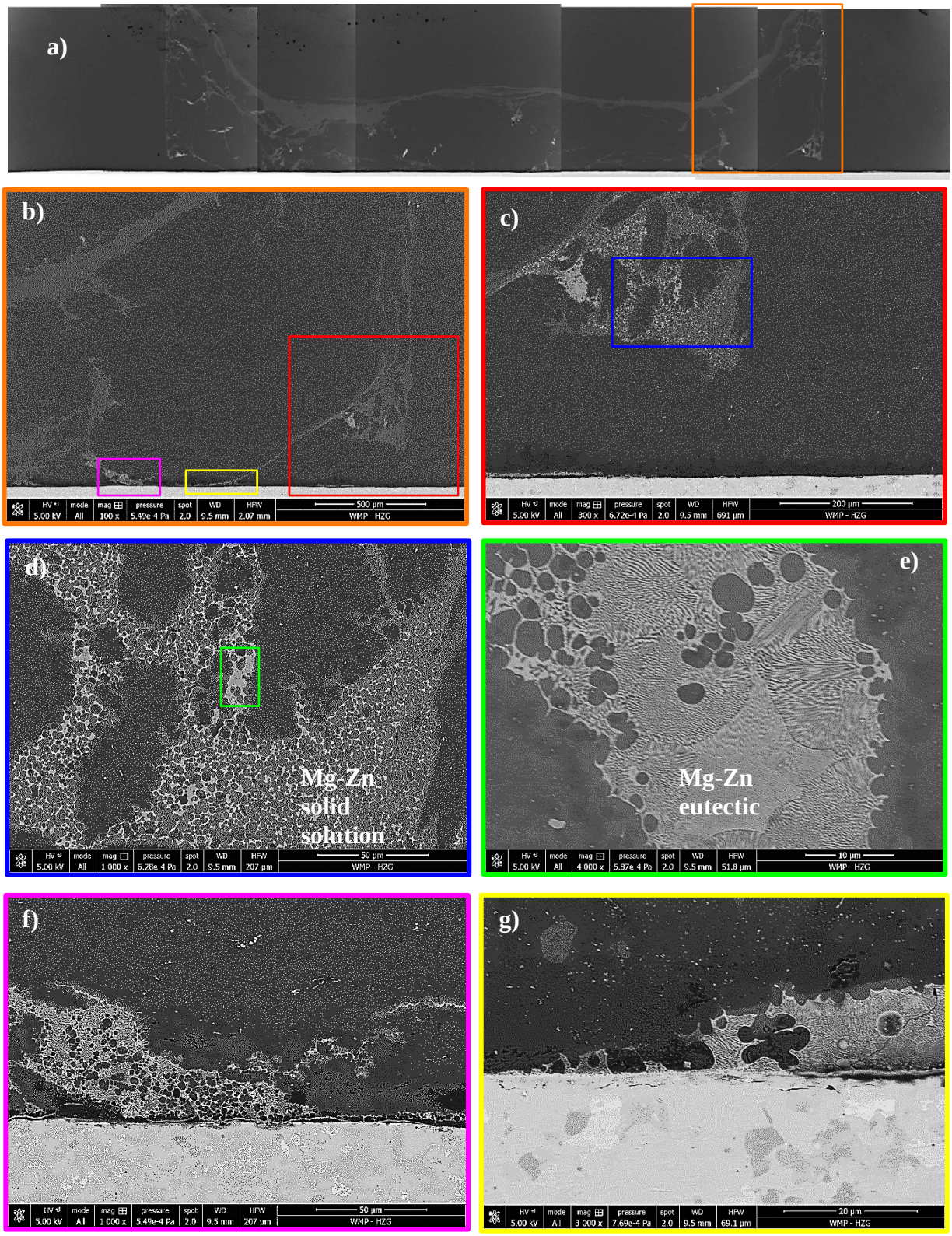

Figure 110- a) Macrostructure of high plunge depth cross-sectioned joint, produced with the following parameters: PD = 2.8 mm, RS = 1800 rpm, PT = 1.5 s, DT = 0 s, RT = 1 s. Figures b) to e) are several sequential magnifications of the Mg-Zn region from figure a). Figure f) and g) are high magnifications of the bright contrast region of Mg-Zn located near the interface and the center of the SZ.

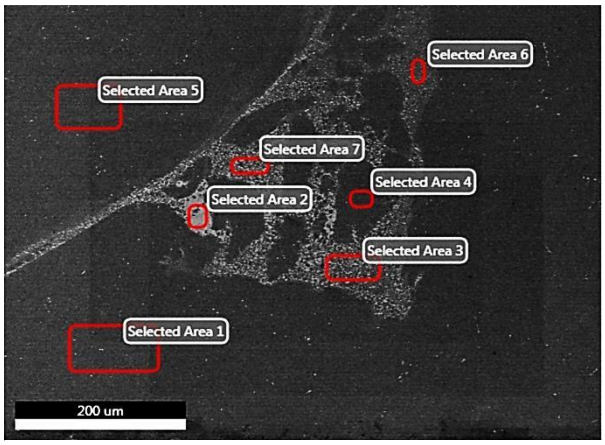

Area	Mg (at %)	Al (at %)	Zn (at %)
Area 1	95.40	4.60	-
Area 2	68.10	6.02	25.89
Area 3	87.96	3.19	8.86
Area 4	95.81	4.19	-
Area 5	95.17	4.83	-
Area 6	92.04	3.10	4.86
Area 7	87.92	4.18	7.90

Figure 111- SEM microstructure backed by EDS results for Mg-Zn contrast region.

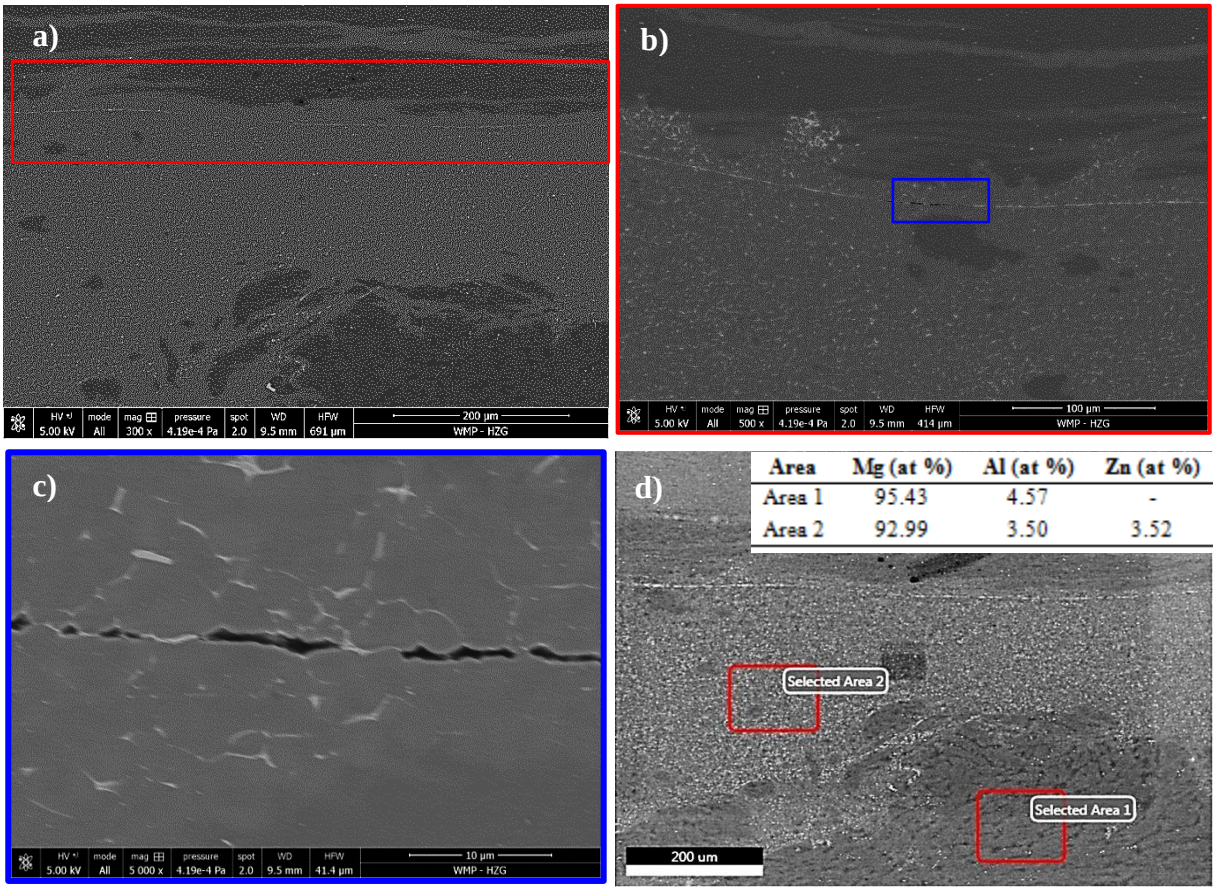

Figure 112- Sequential magnifications of Mg-Zn layered structure a) - c).d) EDS local analysis of a). Cross-sectioned joint produced with the following welding parameters: PD = 2.8 mm, RS = 1800 rpm, PT = 1.5 s, DT = 0 s, RT =1 s.

Further observations of the Mg-Zn layered traces in the SZ were conducted and shown in sequential magnification through Figure 112 a) - c). In the micrographs it is possible to observe thin but continuous cracks within the Mg-Zn region (continuously distributed), which were oriented along it. During tool removal after welding, the recent formed thin layer of Fe-Al IMC's, between the bottom surface of the tool and upper surface of the SZ, transfer the tensile load along the SZ. The small unbounded interface offers a path for crack propagation, resulting in the SZ pull-out defect. Even though the Mg-Zn characteristic region has similar distribution for high and low PD, the SZ pull-out defect only occurs for higher PD. This might be related to the total heat input, because for high RS (e.g. RS = 2900 rpm) the SZ pull-out defect was also reported. Probably, for higher PD and/or higher RS, the amount of Mg-Zn eutectic formed during welding enables longer continuous cracks, through which fracture propagates during tool removal, ultimately lidding to the SZ pull-out defect.

In Refill-FSSW of soft metals (dissimilar or not), even when the plunge is limited to the upper sheet or until the interface between the two sheets, a variable content of mechanical intermixing (function of the remaining parameters) between the material from the two sheets still occurs (Kubit et al. 2018). In the particular case of similar Refill-FSSW with sleeve plunge variant for Al alloys, (Shen, Lage, et al. 2018) stated that the SZ is usually slightly larger when compared to the sleeve diameter, and its depth is much larger than the nominal plunge depth of the sleeve. However, the heat input and torque necessary to stir the Mg are much lower than the required for steel stirring. Consequently, since there was no plunge into the steel lower sheet, i.e. the PD was always smaller than the Mg upper sheet thickness; the bonding phenomenon was essential interfacial. (Chen et al. 2015) and (Da Silva et al. 2010) proved that the microstructure of the soft metal upper sheet barely affects the weld strength in the presence of interfacial fracture. The relevant role of the interfacial reactions is evident considering that all failures during lap shear test occurred along the interface. Thus, a detailed study of the Mg/steel interface was conducted by Scanning Electronic Microscopy (SEM).

The macrostructure analysis from Figure 105, and Figure 106, and the SEM micrographs from Figure 113 suggest that the Mg-steel interface is rather uniform and the bonding between the two dissimilar metal sheets continuous. Perfect metallurgical continuity without cracks and voids in the interface was probably achieved due to the high pressure and temperature imposed by the tool stirring and plunging action. Since the tool didn't plunge the bottom steel sheet, no macro plastic deformation can be observed, i.e. mechanical interlocking doesn't occur (Dong et al. 2016). The SEM magnifications of Figure 113 are given in Figure 114, along with their respective EDS observations in Figure 115 and Figure 116. These suggested the occurrence of heterogeneous but continuous interfacial reactions; with four common regions identified at the Mg/steel interface. Interface I and II are located in the Clamping Ring (CR) region; interface III and IV are located in the peripheral boundary of the SZ and throughout the SZ development respectively. Starting from the interface away from the weld center, Figure 113 h), the different interfaces were named:

- Interface I – It is located away from the SZ, and a tight contact between the Mg and the galvanized steel is observed. The original Zn layer from the coating is preserved, with no traces of neither welding nor interfacial metallurgical reactions. A small partial mechanical interlocking between the Zn and the Mg matrix seems to be created by plastic deformation of the Zn coating, as a result of clamping ring fixing force. This non-reaction region is depicted in Figure 113 g) and with higher magnification in Figure 114 g) and h). The EDS results are given in Figure 116 c) - d);
- Interface II – It is composed by two non-discrete sub regions. Sub region 2.1 is located further away from the weld center, and is composed of Mg-Zn IMC's above preserved Zn coating in direct contact to the steel matrix. This double layer can be easily observed in Figure 113 e) and in higher magnification in Figure 114 e) and f). The EDS results are given in Figure 116 a) - b).

  Sub region 2.2 is located closer to the weld center (close to region III) and the original Zn coating gradually disappear and is replaced by Mg-Zn IMC's with different morphologies and chemical compositions, and Mg-Zn divorced eutectic, which offers a weld-brazing boding mechanism. The development of the eutectic divorced structure and Mg-Zn IMC's can be observed in Figure 113 c) and d) and in higher magnification in Figure 114 c) and d). The EDS results are given in Figure 115 a) - d);
- Interface III – It has an annular ring like geometry and is located in the peripheral region near the SZ exterior sleeve diameter. Is characterized by the absence of Zn coating and Mg-Zn eutectic, The Mg-Zn is squeezed as a result of the plunging movement to Interface II, and also extruded into the interior of the SZ. Figure 113 b) and with higher magnification Figure 114 b) depict interface III;
- Interface IV – Delimited exteriorly thereabout the sleeve plunge region, this interface features no Zn coating, Mg-Zn eutectic, nor Mg-Zn IMC's. The metallurgical bonding is ensured by the action of the original Fe-Al IMC's layer. The development of this interface in interaction with the others is shown in Figure 113 a) and with higher magnification in Figure 114 a).

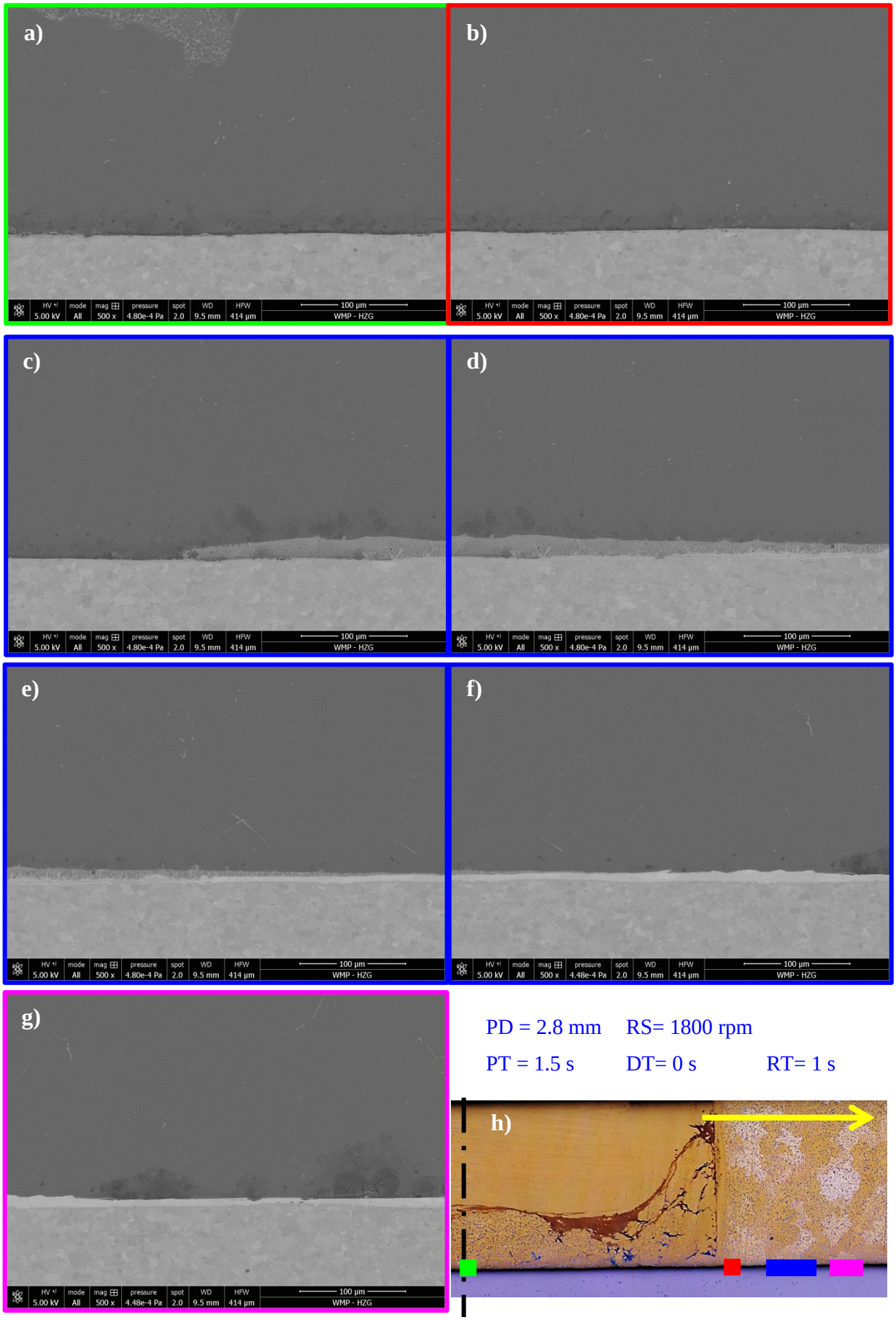

Figure 113- SEM micrographs from the Mg-steel interface with high PD. The analysis was conducted from the weld center in direction to the sleeve plunge region (continuously getting far away from the weld center) as indicated in h). Figure h) also codifies the color code used in the border of each picture to identify its location.

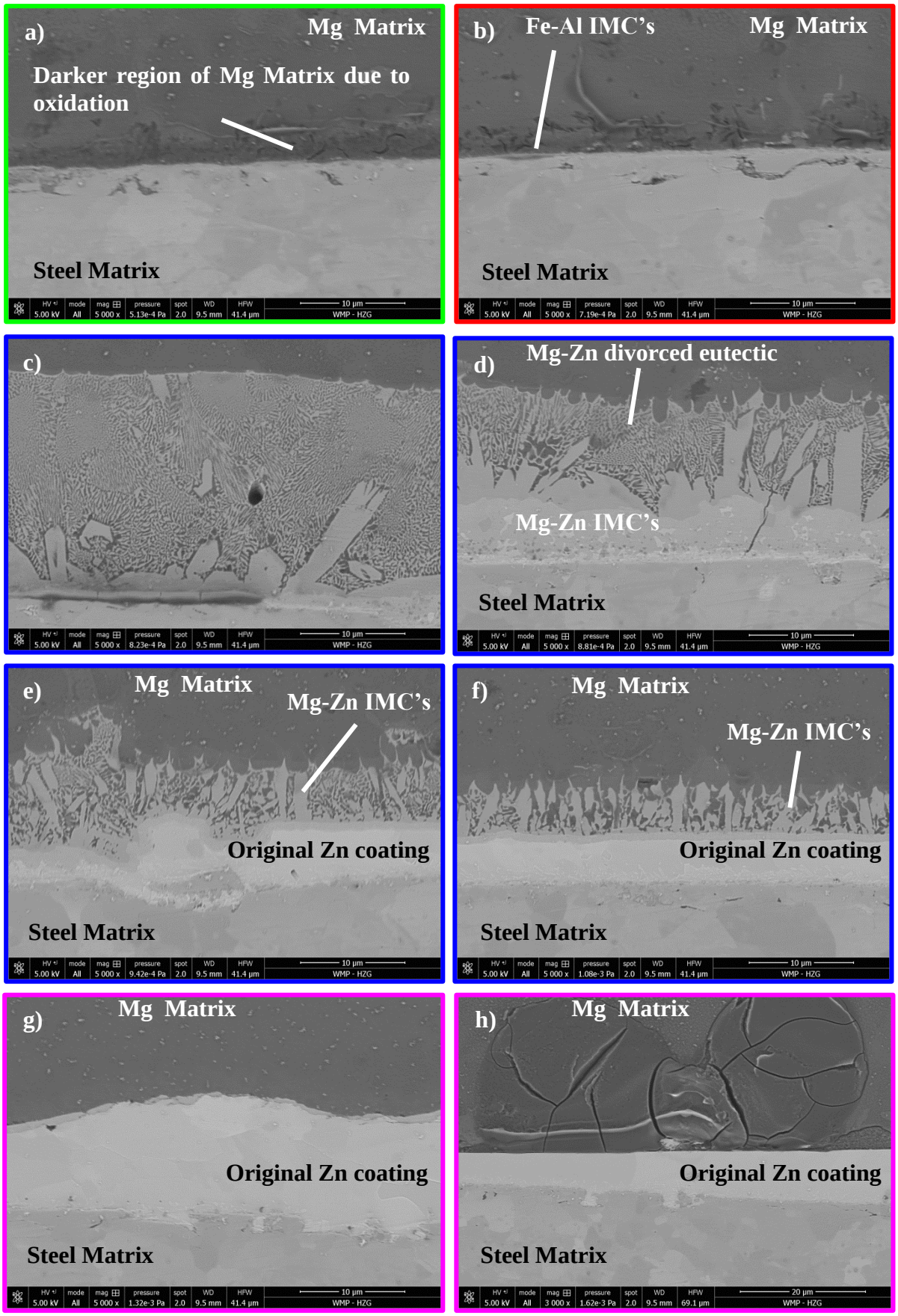

Figure 114- SEM higher magnifications of interfacial microstructures from Figure 113, with the same color code used in the borders of the pictures.

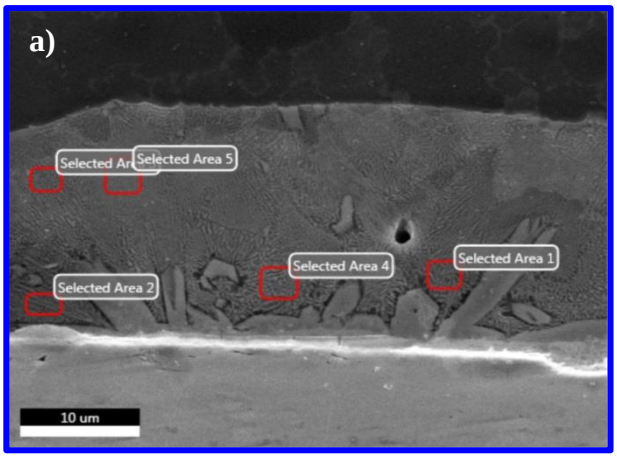

Area	Mg (at %)	Al (at %)	Zn (at %)
Area 1	68.53	5.72	25.74
Area 2	66.84	3.95	29.21
Area 3	72.79	3.89	23.32
Area 4	68.81	3.93	27.26

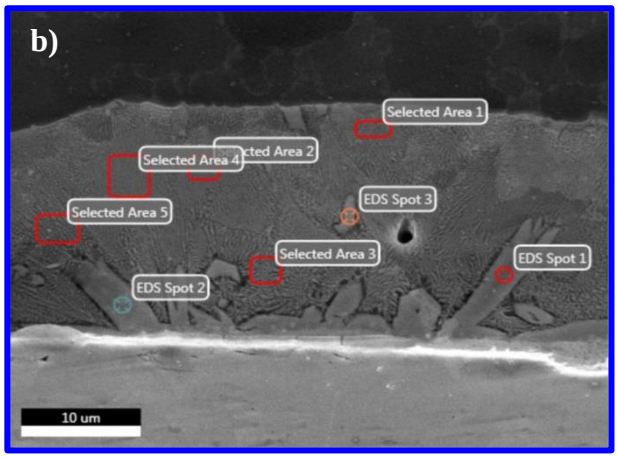

Area	Mg (at %)	Al (at %)	Zn (at %)
Area 1	64.59	3.03	32.38
Area 2	70.86	4.12	25.02
Area 3	71.04	3.63	25.33
Area 4	66.02	3.22	31.76
Area 5	70.25	4.11	25.63
Spot 1	60.57	4.80	34.63
Spot 2	47.60	4.26	48.13
Spot 3	62.73	4.48	32.79

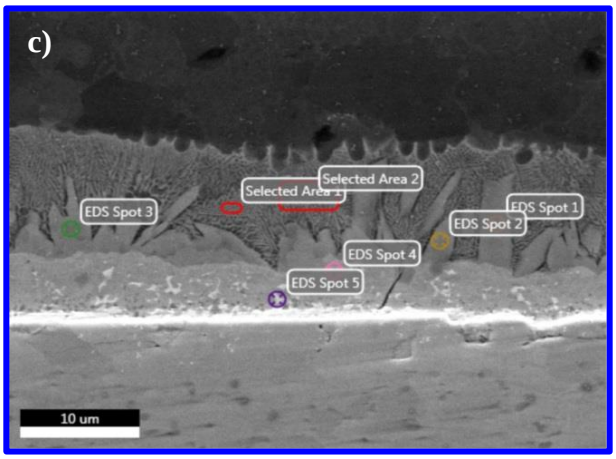

Spot	Mg (at %)	Al (at %)	Zn (at %)
Area 1	69.75	4.05	26.20
Area 2	64.61	3.30	32.10
Spot 1	56.68	5.25	38.07
Spot 2	55.04	5.27	39.69
Spot 3	53.02	5.27	41.71
Spot 4	40.36	-	59.64
Spot 5	21.50	-	78.50

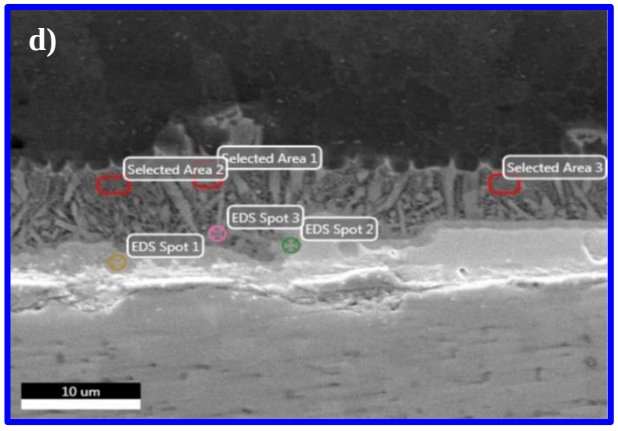

Spot	Mg (at %)	Al (at %)	Zn (at %)
Area 1	71.75	4.13	24.12
Area 2	75.35	3.65	20.99
Area 3	68.85	3.34	27.80
Spot 1	43.25	-	56.76
Spot 2	39.57	-	60.43
Spot 3	57.58	5.76	36.66

Figure 115- EDS local analysis of different regions from the interface II.

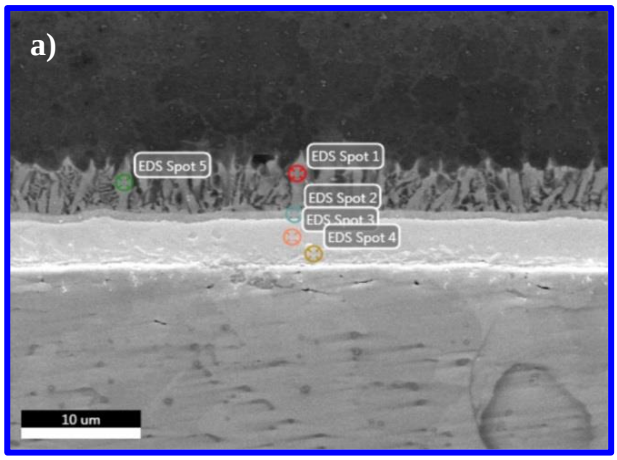

Spot	Mg (at %)	Al (at %)	Zn (at %)
Spot 1	50.75	5.37	43.88
Spot 2	32.84	2.62	64.53
Spot 3	-	-	100
Spot 4	100	100	100
Spot 5	56.94	5.14	37.91

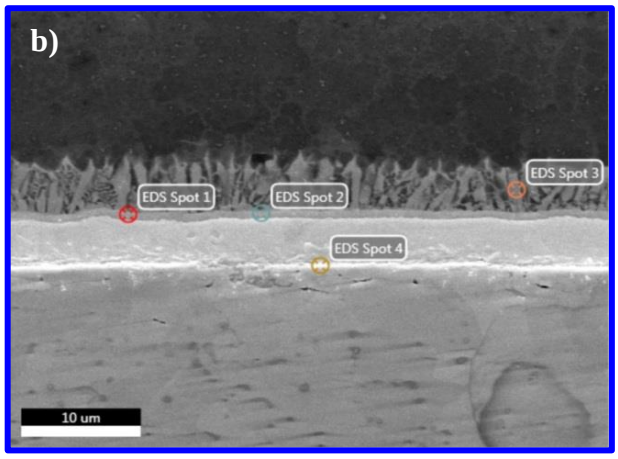

Spot	Mg (at %)	Al (at %)	Zn (at %)	Fe (at %)
Spot 1	41.18	4.09	54.73	-
Spot 2	39.19	3.96	56.85	-
Spot 3	58.96	4.80	36.24	-
Spot 4	12.46	7.13	20.75	59.66

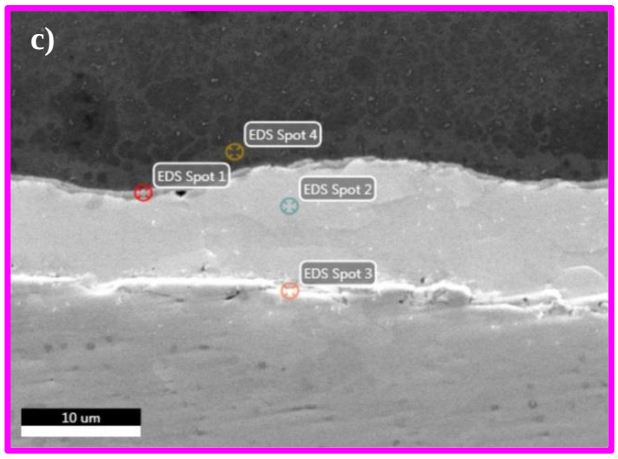

Spot	Mg (at %)	Al (at %)	Zn (at %)	Fe (at %)
Spot 1	55.21	-	44.79	-
Spot 2	-	-	100	-
Spot 3	7.89	18.07	50.53	23.51
Spot 4	94.81	3.18	2	-

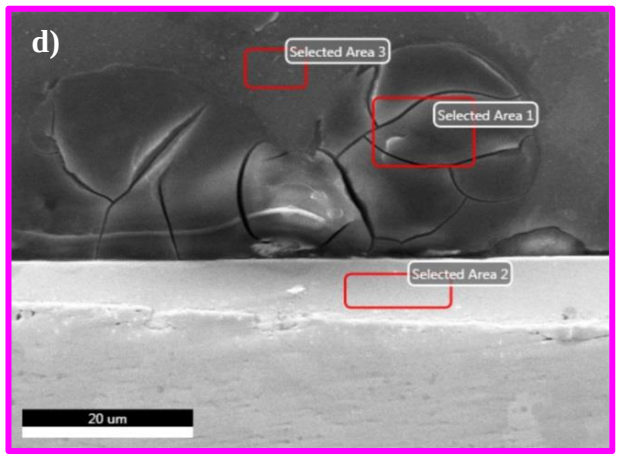

Area	Mg (at %)	Al (at %)	Zn (at %)	O (at %)
Area 1	55.95	-	-	44.05
Area 2	-	-	100	-
Area 3	96.37	3.63	-	-

Figure 116- EDS local analysis from interface II: a) and b); and interface I: c) and d).

Regarding interface I, in some regions of Mg side, the presence of small cracks near darker regions in the Mg matrix were observed, Figure 114 h). EDS analysis in Figure 116 d) shows that the region with cracks has higher oxygen content, which explains the surrounding darker region (O element has atomic number even lower than Mg). Mg is the most anodic metal in the galvanic series, in the other hand; Fe has much higher electronegativity or electrode potential. Thus, the formation of the cracks might be related to galvanic corrosion post welding. The corrosion process probably developed during polishing of the metallographic samples, since part of the steps use water as lubricant, and water base lubricants and solutions (efficient electrolyte). Even though in Figure 116 c) the brighter layer is almost preserved pure Zn coating (spot 2), EDS results in spot 1 and spot 4 indicate a small increase in Mg content. This may indicate that Mg diffuses into Zn during the welding process, beginning with the formation of Mg-Zn IMC's. Figure 115 a) - d) and Figure 116 a) - b) are localized EDS analysis of interface II (sub-region 2.1 and 2.2). They indicate that the average compositions of Mg-Zn eutectic structure, and different chemical compositions of Mg-Zn IMC's, are consistent with the interface features observed in Figure 114. The EDS line scans shown in Figure 117 a) and b), illustrate the gradual replacement of the original Zinc coating by Mg-Zn IMC's, when observing the Mg-steel interface from interface I to interface II (sub region 2.1).

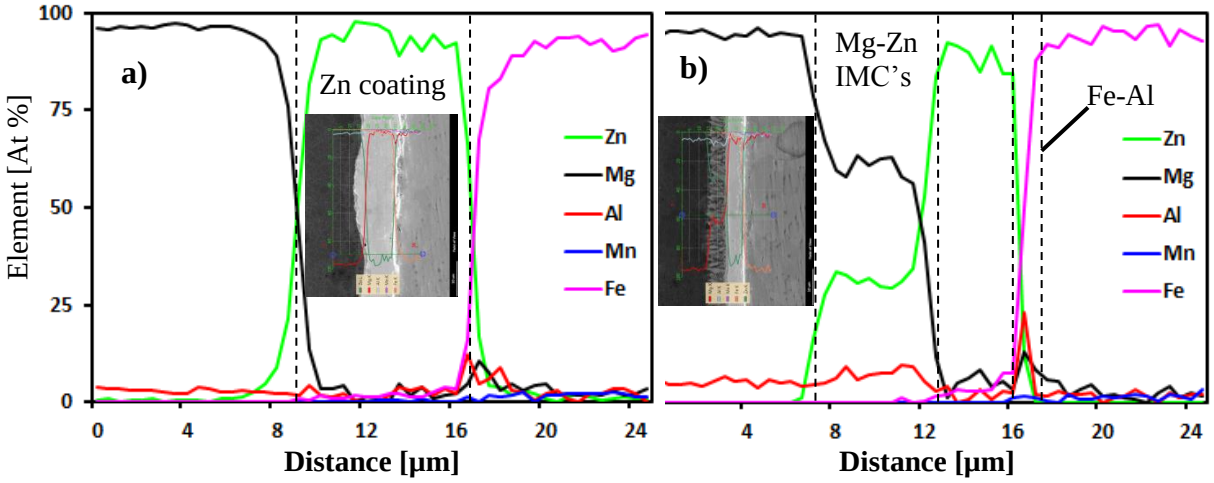

Figure 117- EDS line scan through a) interface I and b) interface II of the Mg-steel interface region.

The formation of interface III is consistent with the model of the material flow proposed in the literature, regarding Zn coating distribution in dissimilar welding of soft metals with Zn coated steel. Zn coating displacement during welding was studied by (Dong et al. 2016) using the ZnO oxide, formed by the reaction between the Zn coating and the natural passivation layer in the Al sheet, as a marker to trace the material flow. In sleeve plunge variant, during sleeve plunging, part of the superficial Zn coating is highly stirred and extruded towards the edge of spot weld, forming interface III. The remaining Zn is mixed in the center space, left by probe retraction. During refill stage, the products of Zn reaction with

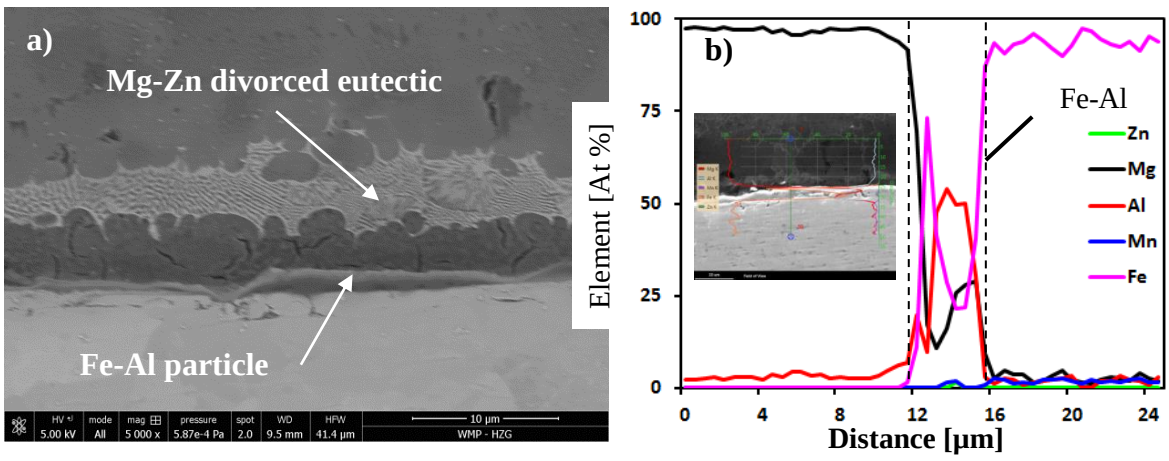

Figure 118- a) SEM micrograph and b) EDS line scan of the Mg-steel interface near the center of the SZ.

the Mg plasticized material are extruded back to the center of the SZ, as a result of the pressing action of the probe, creating the characteristic Mg-Zn rich region in the center and lower part of the SZ. The layered Mg-Zn doesn't break by the reasons pointed out in (Shen, Lage, et al. 2018).

Discontinuous portions of Fe-Al IMC's are the result of the diffusion behavior between Al and Fe. The metallurgical bonding between the insoluble Mg and steel matrix was precisely achieved by Al element, present in the Mg matrix and in the coating (lower pct.). The Fe-Al IMC's discontinuous layer accommodates the metallurgical bonding throughout interface IV, Figure 118 a). It is also possible to observe a Mg-Zn divorced eutectic region above the Fe-Al interlayer, usually located near the SZ boundaries. The EDS line scan in interface IV of a similar region but without Mg-Zn eutectic above was conducted and shown in Figure 118 b). A peak of Fe and Al elements indicate the presence of the Fe-Al layer. Thin and discontinuous IMC's Fe-Al layer was also reported in dissimilar Refill-FSSW of Al to steel and Mg to steel by (Shen, Chen, et al. 2018) and (Chen et al. 2015) respectively.

The DoE output results, detailed in 4.2, indicated a positive relation between PD and LSS; the LSS increased with the increased in the PD. Thus, the increase in PD must produce beneficial metallurgical modifications in the Mg-steel interface. The correlation between the strengthening mechanism and metallurgical modifications in the Mg-steel interface was studied. Table 67 indicates the relationship between the PD and the length of interface II and interface III. The increase in PD didn't change significantly the length of interface III. However, the length of the interface II increased with the increase of the PD. Figure 119 a) - b) illustrates the relative difference for the two extreme cases of PD. Since interface II offers the weld-brazing effect, the increase in the weld-brazing bonding area ultimately contributed to the increase in LSS, justifying the PD effect observed in the DoE.

Table 67- Length of interface II and III for different plunge depths.

PD [mm]	Interface II	Variation [%]	Interface III	Variation [%]
2.2	505 µm	-	407 µm	-
2.5	765 µm	51	495 µm	22
2.8	936 µm	85	530 µm	30

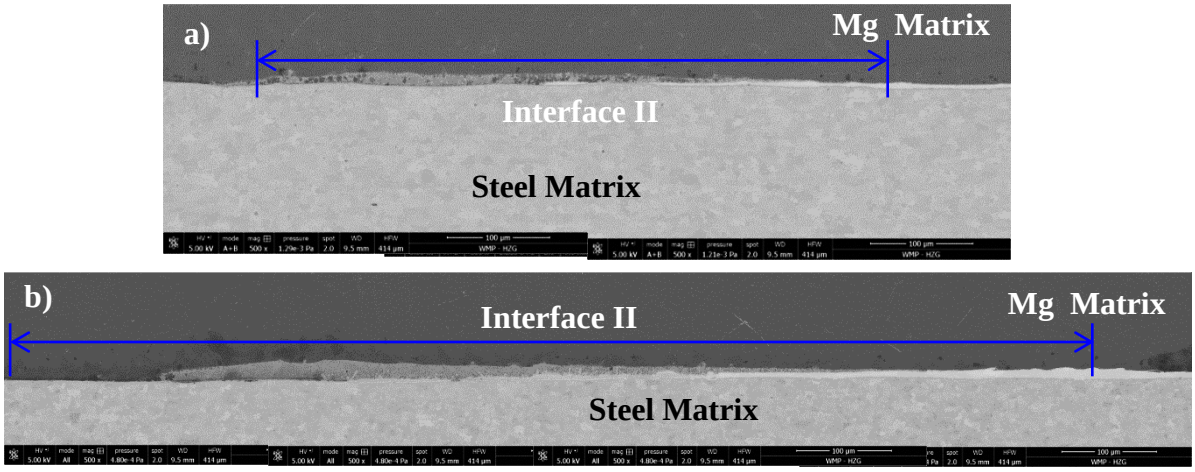

Figure 119- SEM micrographs detailing the interfaces II length for: a) PD = 2.2 mm; and b) PD = 2.8 mm.

The thickness or composition of the Fe-Al IMC's layer in the SZ interface (interface IV) was also aimed of study. Possible metallurgical changes in the SZ could further enhance the LSS, complementing the interface II wherefore. However, no significant changes in the Fe-Al layer at the SZ, with the variation of PD, were detected. The DoE suggested that in order to further increase the lap joint strength, the PD should be further increased. However, for higher PD (2.9 mm), the SZ pull-out defect appears for a wide spectrum of different welding parameters (conclusion detailed in the preliminary studied from section 4.1.3). In the next subchapter 4.4, DR Refill-FSSW will be applied precisely to allow increasing the sleeve PD, in order to further increase the strength of the joint without the presence of the SZ pull-out defect.

4.3.3 Fracture Surface and Surface Analysis

The typical fracture mechanisms that govern Refill-FSSWed joints aren't applicable in the dissimilar welding of soft-hard materials such as Mg-steel or Al-steel. The presence of hook features, bonding and partial bonding ligaments or voids, which are preferable sites for crack initiation and propagation near the TMAZ and HAZ (Rosendo et al. 2015), have little influence in the resistance of the studied joint. All fractures during the complete experience (preliminary study and DoE) occurred in interfacial fracture mode. Figure 120 depicts the appearance of a typical interfacial failure after lap shear test. It is possible to recognize on both sheets three main regions: the probe-refilled zone, sleeve-plunging zone and clamp action zone. It looks like the faying surfaces between the two metal sheets were almost sheared off. In the exposed fracture surface of both plates is possible to observe a whiter region, which probably results from the fracture of Mg matrix. The white arrow (considered a standard from now on) indicates the direction of the tensile loading applied during the lap shear test.

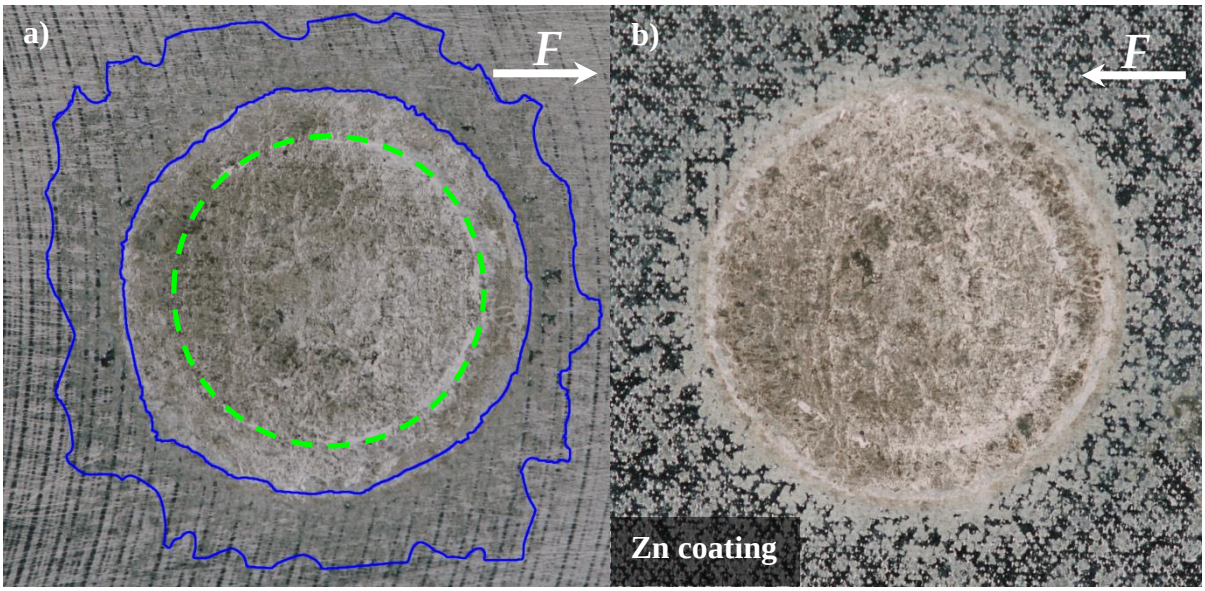

Figure 120- Photography of typical interfacial failure surface after lap shear test, in a joint produced with: RS= 1800 rpm, PD= 2.5 mm, PT= 1.5 s, DT=1 s and RT= 1.5 s. a) Failure surface of the Mg sheet bottom view. b) Failure surface of the steel top view.

As indicated in Figure 121, it is necessary to specify which side of the fracture surface is being observed, regarding the specimen loading. SEM macro and micrographs from Mg fracture surface, Figure 122 (right side) and Figure 123 (left side), indicate that the fracture propagation site is different depending on the side of the welded spot. As explained by (Rosendo et al. 2015), in the loading direction, the left side of the spot will be stressed to compression and the right side stressed to tension (upper sheet top view). Due to the stress distribution asymmetry, in order to ensure consistence in the analysis during this section and section 4.4.3, the right side always refers to the plate side in which the tensile force is applied during static test. For detailed analysis of the fracture surface, only the Mg bottom view surface will be used, and a sample with low plunge depth (PD = 2.2 mm) was chosen to be detailed. In order to assess the plunge depth strengthening mechanism in the fracture surface, a further comparison with fracture surfaces from samples with PD = 2.5 mm and PD = 2.8 mm is made in Figure 124.

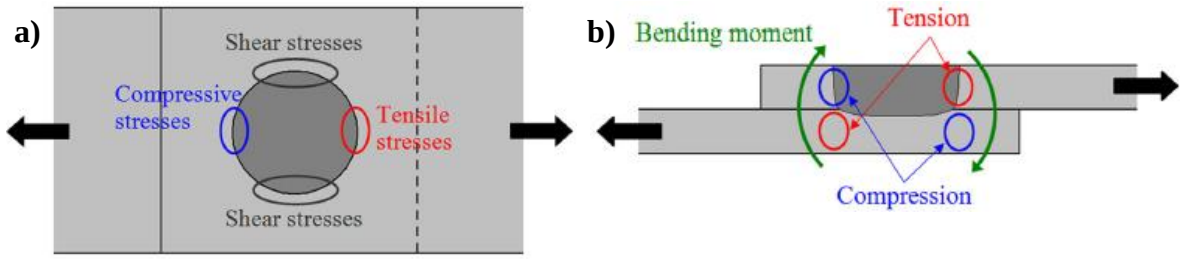

Figure 121- a) Schematic drawing of the stress distribution on a plane parallel to the sheet surface for a spot welded joint under shear tensile loading. b) Schematic drawing of the stress distribution on the longitudinal cross section of a spot welded joint under shear tensile loading (Rosendo et al. 2015).

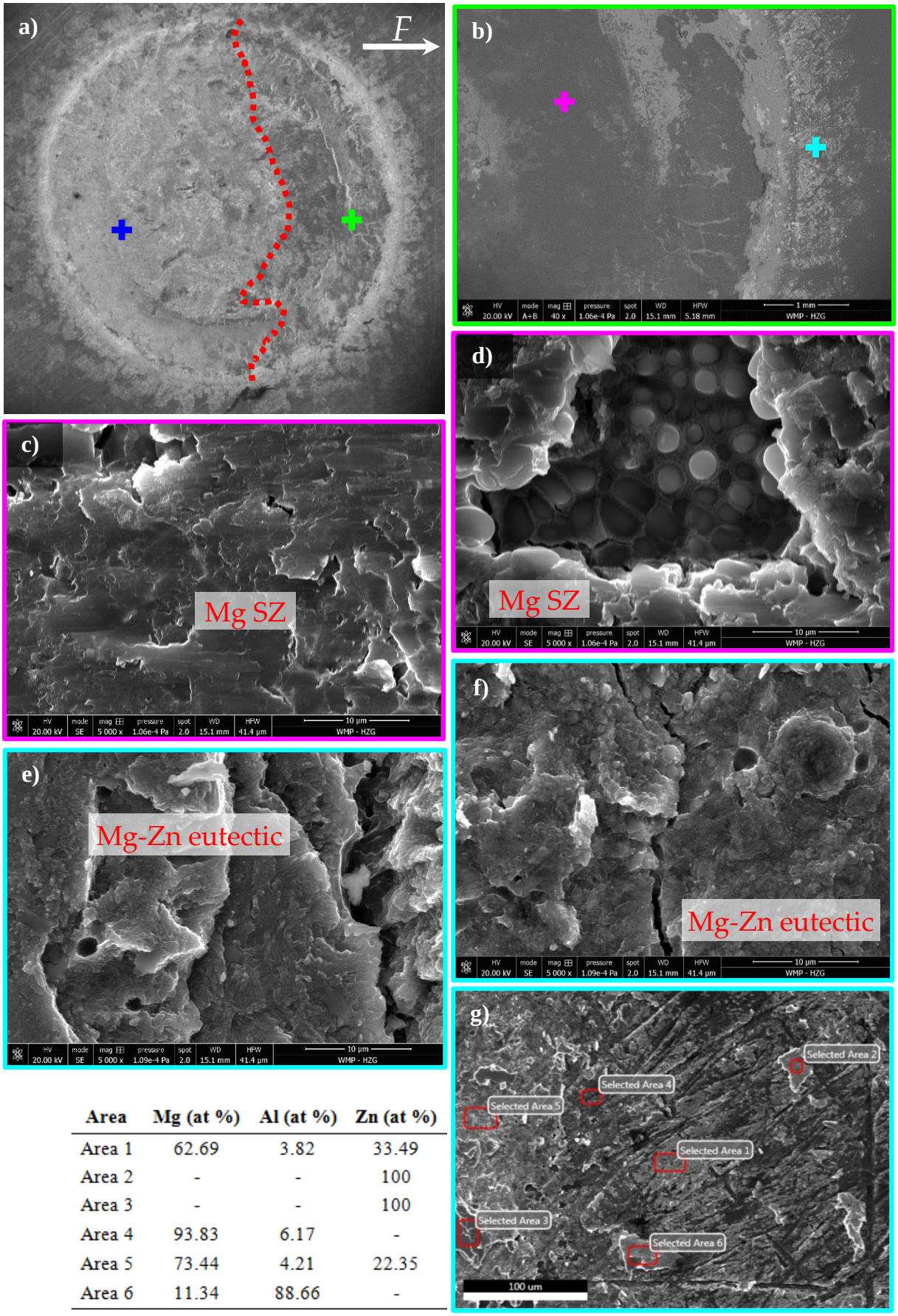

Area	Mg (at %)	Al (at %)	Zn (at %)
Area 1	62.69	3.82	33.49
Area 2	-	-	100
Area 3	-	-	100
Area 4	93.83	6.17	-
Area 5	73.44	4.21	22.35
Area 6	11.34	88.66	-

Figure 122- SEM fractographies of fracture surface from sample produced with low PD, backed with EDS analysis. a) Fracture surface overview of the Mg sheet bottom view. b) Detail of the right side of a). Higher magnifications of Mg SZ: c) and d); and Mg-Zn eutectic outer region: e) and f). g) EDS analysis of Mg-Zn eutectic.

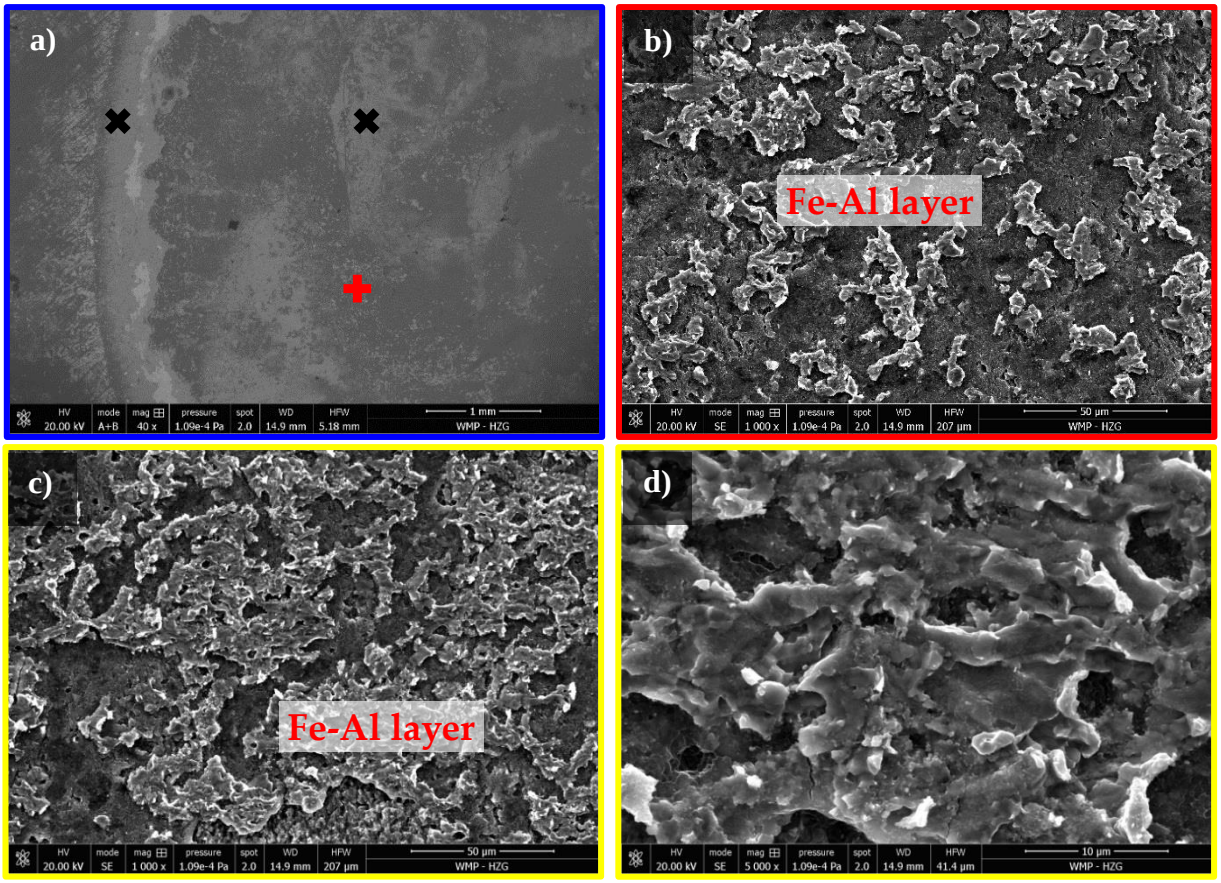

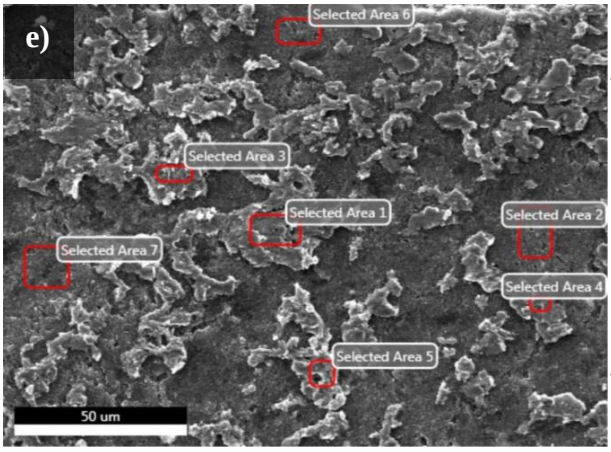

Area	Mg (at %)	Al (at %)	Zn (at %)	Fe (at %)	Mn (at%)
Area 1	27.89	17.52	2.36	52.23	-
Area 2	92.52	4.65	2.82	-	-
Area 3	17.90	18.75	16.47	43.09	3.80
Area 4	12.42	4.80	2.13	78.68	1.88
Area 5	22.90	16.08	7.60	51.96	1.46
Area 6	91.27	5.71	3.02	-	-
Area 7	92.11	5.24	2.66	-	-

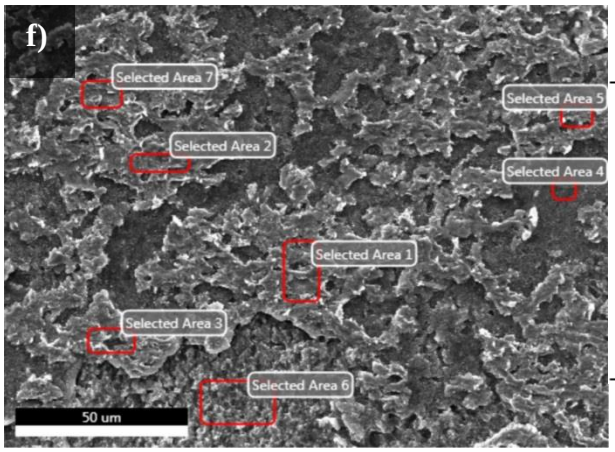

Area	Mg (at %)	Al (at %)	Zn (at %)	Fe (at %)	Mn (at%)
Area 1	24.58	15.22	3.22	55.19	1.78
Area 2	27.30	13.26	1.35	57.38	0.71
Area 3	31.67	12.33	2.59	52.14	1.26
Area 4	91.32	5.98	2.69	-	-
Area 5	34.54	19.68	3.33	41.30	1.16
Area 6	87.73	6.31	5.96	-	-
Area 7	19.22	11.24	1.99	66.16	1.39

Figure 123- SEM fractographies of fracture surface from sample produced with low PD, backed with EDS analysis. a) Detail of the left side of Mg fracture surface overview. Higher magnifications of Fe-Al IMC's layer: c) and d). EDS analysis of Fe-Al IMC's in different points e) and f).

From SEM overview of the fracture surface in Figure 122 a), it is possible to easily observe the difference in contrast between the right side in Figure 122 b) and left side in Figure 123 a). In the right side of the spot, the fracture is mainly along the Mg SZ, Figure 122 c). It is characterized by overall shear brittle fracture, with shallow cleavage steps and intergranular crack propagation path. No macro-deformation and very little micro-deformation were produced. However, a few small dimples or micro-voids can be observed in localized regions, as depicted in Figure 122 d). In some regions, the crack also extended along the Mg-Zn eutectic, showing traces of liquation, Figure 122 e) and f). In Figure 122 g), on which EDS analysis were conducted to check for Mg-Zn eutectic near compositions, it is also possible to observe small portions of Zn coating that was ripped off after fracture (area 2 and 3). In addition, the original grinding marks are easily seen, showing that no plastic deformation occurred in the interface. This can be justified by the fact that the observation area is in the outer periphery of the SZ.

On the other hand, in the left side of the spot, the fracture was mainly along the Mg-Zn eutectic and through the Fe-Al IMC's layer, Figure 123 b) - d). This brittle fracture surface in terms of strain to fracture may be associated with the presence of the IMCs at the interface. In Figure 123 e) and f), EDS analysis were conducted to check for Fe-Al IMC's close match compositions. The high peaks of Fe and Al elements in the Mg sheet bottom view fracture surface corroborate the assumption of formation of a Fe-Al IMC's interlayer, which accommodates the metallurgical bonding. No traces or peaks of O together with Zn element were found, which might have indicated the formation of ZnO - Oxide compound that when present, is usually found in both Mg and steel surfaces, and is often associated as the weakest structure, producing fractures similar to cohesive failure (Dong et al. 2016).

The increase in the LSS, as a consequence of the increase in PD, has a direct and detectable correlation with the fracture surface. Figure 124 a) and b) show the fracture surface overview of samples with intermediate (PD = 2.5 mm) and high (PD = 2.8 mm) plunge depth, in which a red line delimitates the fracture area across the SZ. With the increase in PD from 2.2 mm Figure 122 a), to 2.5 mm Figure 124 a), and finally to 2.8 mm Figure 124 b), the area of fracture along the Mg SZ (delimitated by a red line) increases, increasing the LSS.

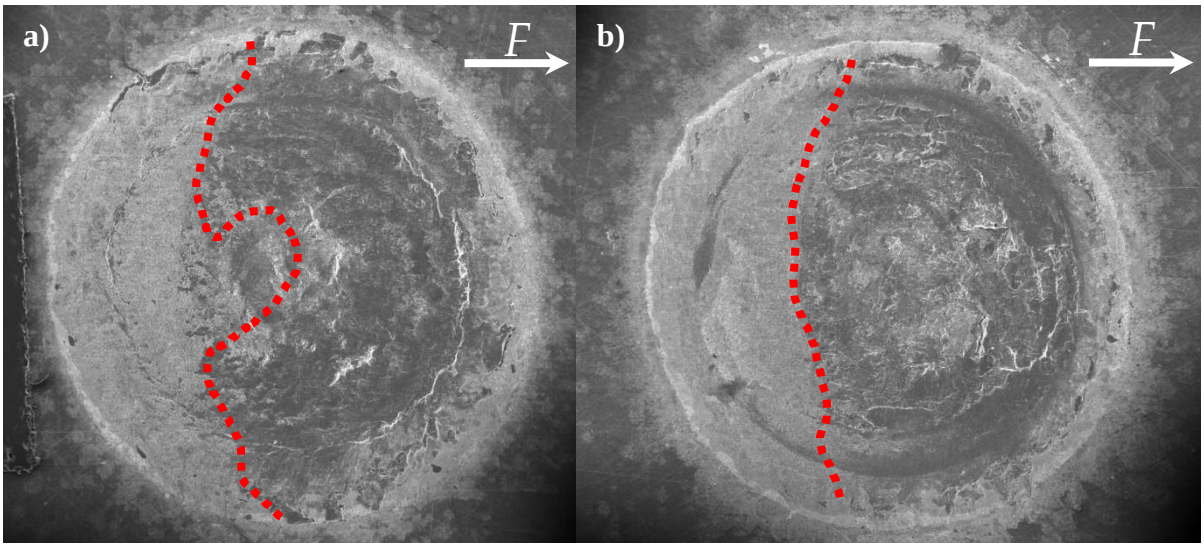

Figure 124- SEM fracture surface overview for welds produced with the reference welding parameters, and plunge depths equal to: a) 2.5 mm; and b) 2.8 mm.

4.3.4 Effect of Zn coating

In order to study the influence of the Zn coating in the bonding mechanism and consequently in the joint strength, the fracture surface of Mg and bare steel dissimilar welding was studied. The feasibility of welding without grinding the steel plate was also investigated, but not its influence in the mechanical performance of the joint. A joint produced with the reference parameters used for Zn coating steel was successfully welded by grinding only the Mg faying surface, Table 68, pointing out the robustness of the process. The influence of the Zn coating in the SZ pull-out defect and LSS was also checked. Since no Zn was present as interlayer before welding, the Mg-Zn characteristic contrast region (through which the SZ pull-out appears) shouldn't form. The assumption was correct and the results are given in Table 68. A substantial PD influence on the joint strength was observed.

Table 68- Effect of Zn coating in the presence of SZ pull-out defect and joint strength.

PD [mm]	RS [rpm]	PT [s]	DT [s]	RT [s]	Output	LSS [kN]
2.8					Successfully welded without steel grinding	
2.8	1800	1.5	0	1	No SZ pull-out defect	3.042
2.9					No SZ pull-out defect	3.965

Without the Zn interlayer, the main bonding mechanisms available are: partial mechanical interlocking (deformation of Mg into the steel micro-cavities produced by grinding); metallurgical bonding in the hypothetical case of some diffusion of Fe into the Mg matrix (always in small amounts); and metallurgical bonding by the formation of Fe-Al IMC's layer. No macro or micro-deformation occurred, evidenced by the grinding marks left in the fracture surface of both: Mg in Figure 125 b) - c), and bare steel in Figure 126 b). EDS analysis from Mg in Figure 125 c), and EDS mapping from bare steel in Figure 126 c) - e), show no traces of metallurgical bonding by diffusion whatsoever. In Figure 126 c) and d) Mg and Fe element can be only observed in the Mg peeled surface and in the fresh exposed bare steel surface respectively.

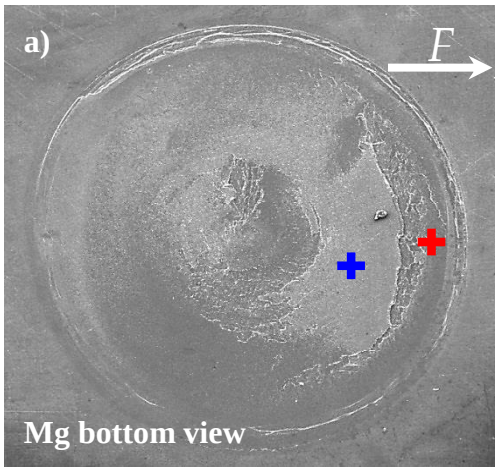

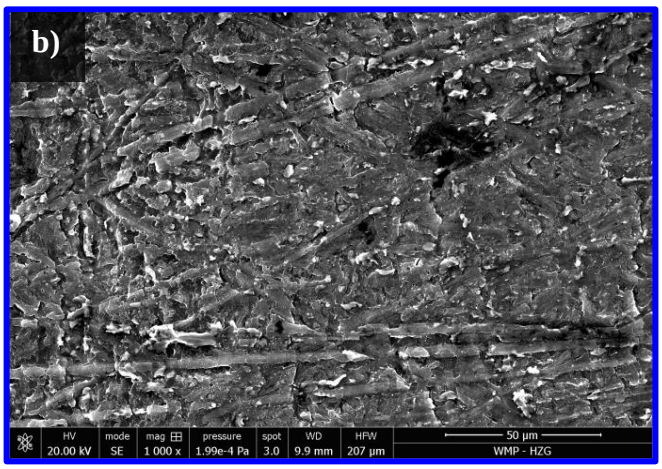

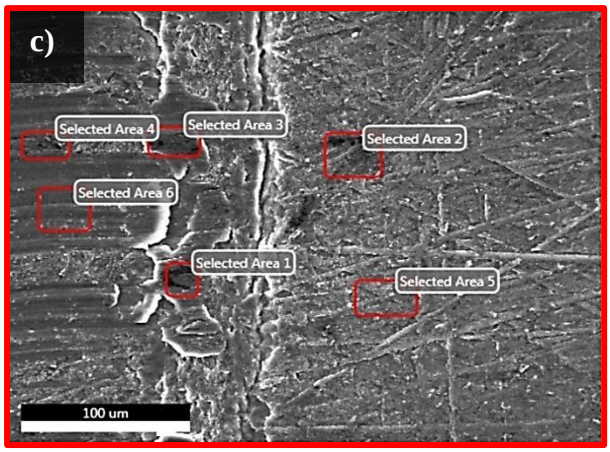

Area	Mg (at %)	Al (at %)	O (at %)
Area 1	92.89	3.97	3.13
Area 2	90.69	6.11	3.20
Area 3	95.25	4.75	-
Area 4	94.87	5.13	-
Area 5	93.64	6.36	-
Area 6	95.37	4.63	-

Figure 125- a) SEM macrograph of the Mg bottom view fracture surface overview. Higher magnification micrographs: b) near the centre; and c) in the periphery and backed with EDS local analysis.

The presence of O is identified in Figure 125 c) and Figure 126 f) in both steel and Mg sheets, probably originated from the insufficient grinding of the steel surface. In addition, as reported by (Nakata 2009) in FSW of Mg to Zn coated steel, the Zn coating had a cleaning effect of the joining interface, probably reason why no O was found in the fracture surface near the SZ for the Zn coated steel. Diffusion of Al, with reaction between Fe and Al, still occurs due to the high affinity between the couple. Nevertheless, this phenomenon was very limited, Figure 126 f). Closing up, the joining between Mg and steel probably resulted mainly due to adhesion bonding produced by the high pressure and temperature, justifying the fracture surface similar to a cohesive adhesive failure.

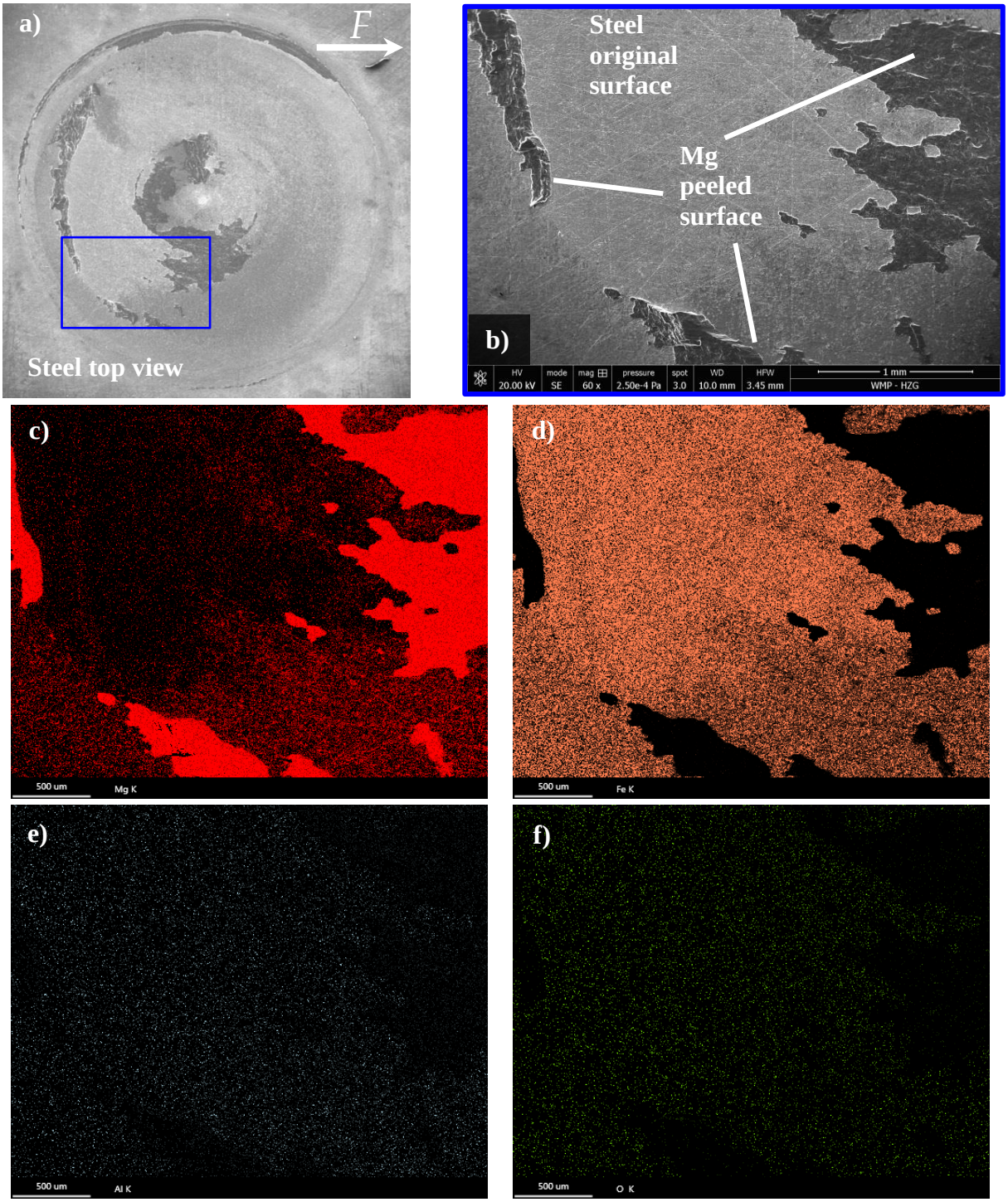

Figure 126- a) SEM macrograph with the bare steel top view fracture surface overview. b) Detail of the area analysed by EDS element mapping. EDS mapping results for several elements: c) Mg, d) Fe, e) Al and f) O.

4.4 Differential Rotation Refill FSSW – Metallurgical Analysis

The DoE of Conventional Rotation Refill-FSSW (CR Refill-FSSW) corroborated the assumption made in section 4.1.2, that Plunge Depth (PD) was the most significant factor in the variance of lap shear strength (LSS). In addition, it was the only main factor with a direct positive influence in LSS. Thus, a simple and direct way to enhance LSS would be to increase PD. However, as concluded in the preliminary study, for plunge depths higher than 2.8 mm (particularly for higher heat input parameters), the nugget pull-out defect often occurred after tool removal. Different approaches, detailed in the end of section 4.1.3, were tried in order to avoid this defect. Regardless, none of them was successful in removing the SZ pull-out defect.

Differential Rotation Refill Friction Stir Spot Welding (DR Refill-FSSW) was studied and applied in order to further complement the approaches previously and unsuccessfully tried, to avoid SZ pull-out defect for PD higher than 2.8 mm. As already detailed in the Refill-FSSW literature review, section 2.4.2, differential rotation refers to differences in angular velocity of sleeve/probe in either rotation direction, angular speed or a combination of both. The main idea was to test a modification of the initial process used to avoid the SZ pull-out defect, without changing too much the study line followed so far. So, the study of DR Refill-FSSW will continue to use the sleeve plunge mode performed until now. Regarding the differential rotation aspect, only the modulus of the angular velocity of the probe was varied, keeping the sleeve and probe rotating in the same direction. The complete welding technique adopted is summarized and illustrated in Figure 127 a) - b), and its selection justified in the next paragraph.

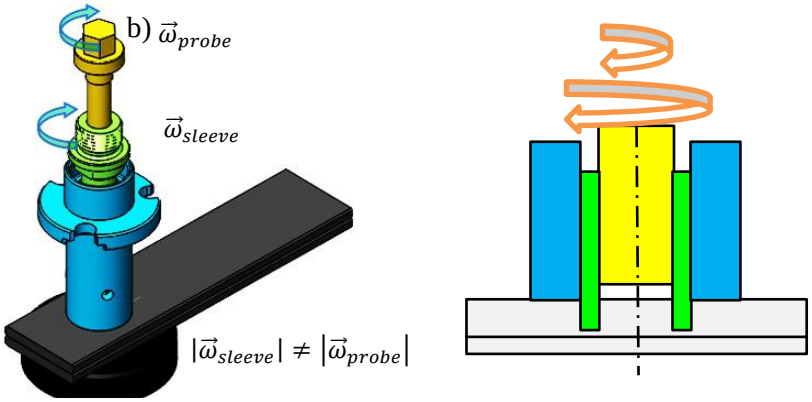

- Sleeve Plunge Variant;
- Probe and Sleeve with the same rotation direction;
- Probe with lower rotation speed than sleeve (different rotation speed);

Figure 127- a) 3D Illustration of the case of differential rotation technique used. b) 2D schematic representation of DR Refill-FSSW, highlighting the sleeve plunge variant and the equal rotation direction for both probe and sleeve.

It was naturally expected that the new conditions of the material flow for DR Refill-FSSW might produce significant changes in the joint mechanical behavior. The positive relation between the PD and LSS found for CR Refill-FSSW could in fact not be true for DR. However, the results regarding the PD were simply transferred to DR Refill-FSSW, without making additional experiments to check the influence of the PD and its optimal value (study suggested for future works). Thus, the reference PD for the entire study was 2.9 mm, threshold value for the SZ pull-out defect for CR Refill-FSSW. Even though the effect of PD wasn't investigated, a preliminary study of the influence of sleeve RS, in the macroscopic flow and joint strength, was conducted. Since the SZ pull-out defect tended to appear for higher heat input, higher sleeve RS and welding time were tested and the results shown in Figure 129. The main goal for DR Refill-FSSW was to decrease the reaction between probe and SZ, reducing for that the probe RS. This is the same strategic concept used in the first two approaches of the preliminary study in section 4.1.3: copper foil as interlayer between the probe and SZ, and replacement of the tool steel probe by a Titanium based. However, this technique had an additional goal of considerably greater importance. It was expected that the reduction of the probe RS could change the material flow behavior, and consequently change the distribution of Mg-Zn region. Different rotation direction might have produced even greater changes in the material flow, which could have positive or negative outputs. However, it wasn't studied because of previous results in similar welding of AM50 Mg alloy, which led to high tool wear and catastrophic failure of several tools. Thus, following the advice of this work's supervisor Banglong Fu, and given the short stock of replacement tools, only the angular speed was reduced, without changing the rotation direction.

4.4.1 Lap Shear Results

The background of this technique is confined to the similar welding by DR Refill-FSSW of AM50-AM50 Mg alloys, previously conducted by Banglong Fu. From his own experimental work, the main conclusions (allowed to reveal) are illustrated in Figure 128 a) - b), and can be summarized as: enhanced lap shear strength; changes in material flow and texture development (studied by stop-action and EBSD techniques); and finally, superior LSS for two DR features: higher Probe RS and different rotation direction, with a change in failure mode when the two are combined. The SZ pull-out failure mode, or just pull-out failure mode, shouldn't be confused with the SZ pull-out defect, previously detailed in section 4.1.3.

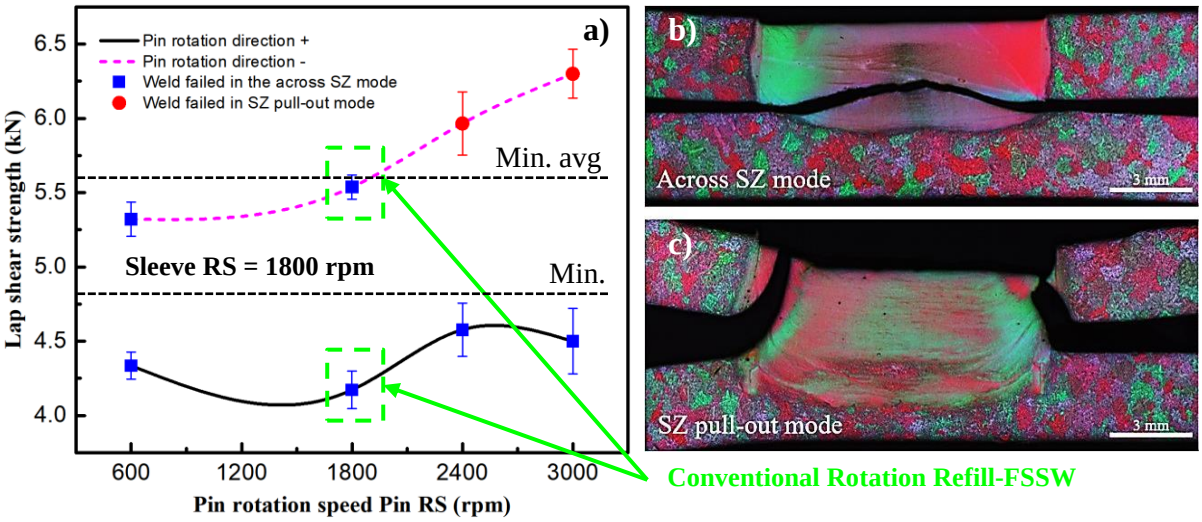

Figure 128- a) Influence of probe RS and probe rotation direction in DR Refill-FSSW of AM50-AM50 Mg alloy. Typical macrostructures for b) Across SZ failure mode; and c) SZ pull-out failure mode.

The results collected in the preliminary studied were summarized in Figure 129. The three highlighted data points correspond to three parameters settings of CR Refill- FSSW, in which nugget pull-out occurred. The SZ pull-out defect was successfully avoided by decreasing the probe RS. The probe RS significant influences the LSS, increasing with the decrease of the probe RS. A possible positive correlation between the LSS and sleeve RS might exist, which is precisely the opposite of what was concluded for the conventional rotation. Also, the total welding time could have a negative effect in the joint strength. However, substantiated conclusions would require a dedicated DoE for DR Refill-FSSW. Additional positive outcomes were achieved:

- Better Surface finish;
- Enhanced joint strength;
- Wider Process Window.

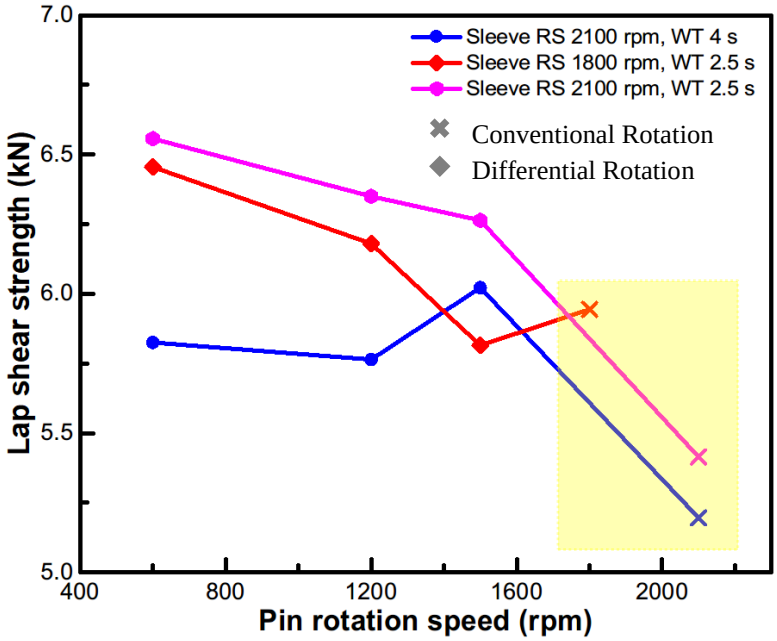

Figure 129- Effect of probe RS in Refill-FSSW of Mg-steel, for PD = 2.9 mm and three different sets of welding parameters

4.4.2 Macro/microstructure and Macro/microanalysis

In order to be able to conduct a comparative study between CR and DR Refill-FSSW, the reference welding parameters used are the same as for CR, and are summarized in Table 69. Only the influence of Probe RS was studied in detail. Optical microscopy was used to check the effect of Probe and Sleeve RS in the distribution of the Mg-Zn rich region as a result of changes in macroscopic flow. SEM macrographs and micrographs, backed with EDS localized analysis, were taken to get a closer look of the layer like Mg-Zn region and check for the existence of the typical crack that follow it, which was observed for CR Refill-FSSW.

Table 69- Summary of the reference welding parameters used for the study of Differential Rotation Refill-FSSW.

Reference Parameters	Studied Parameters
Sleeve RS = 1800 rpm	Probe RS = 1800 rpm
PD = 2.9 mm	Probe RS = 1200 rpm
PT= 1.5 s; DT= 0 s; RT= 1 s	Probe RS = 600 rpm

Macrostructure observations of cross-sectioned joints in Figure 130 and Figure 131 indicate that DR Refill-FSSW changed the material flow behavior. The original layered like material flow observed for CR Refill-FSSW, resulted in a continuous distribution of the Mg-Zn eutectic and solid solution, with minor material intermixing in the axial direction. Whereas for DR Refill-FSSW, it changed into a chaotic flow state, in which the characteristic Mg-Zn region was broken, and is now randomly distributed within the SZ. This macroscopic change was probably the reason why, the SZ pull-out defect was avoided. The material intermixing in the axial direction is even more enhanced with the decrease in Probe RS, Figure 130 a) - c) and Figure 131 a) - c). However, no obvious correlation between the macrostructural features and the Sleeve RS can be observed, Figure 130 and Figure 131. Nevertheless, it seems that the presence of what looks like small voids and lack of refilling decreases with the reduction of Sleeve RS from 1800 rpm to 1500 rpm. Figure 132 a) and b) shows the SEM macrographs of Figure 130 c) and b) respectively. It was already stated that for lower Probe RS the Mg-Zn distribution is more random. However, even when the Mg-Zn region doesn't change completely, such as Figure 132 b), the concentrated layer region is thinner and without visible cracks due to Mg-Zn eutectic liquation, Figure 132 c) - e).

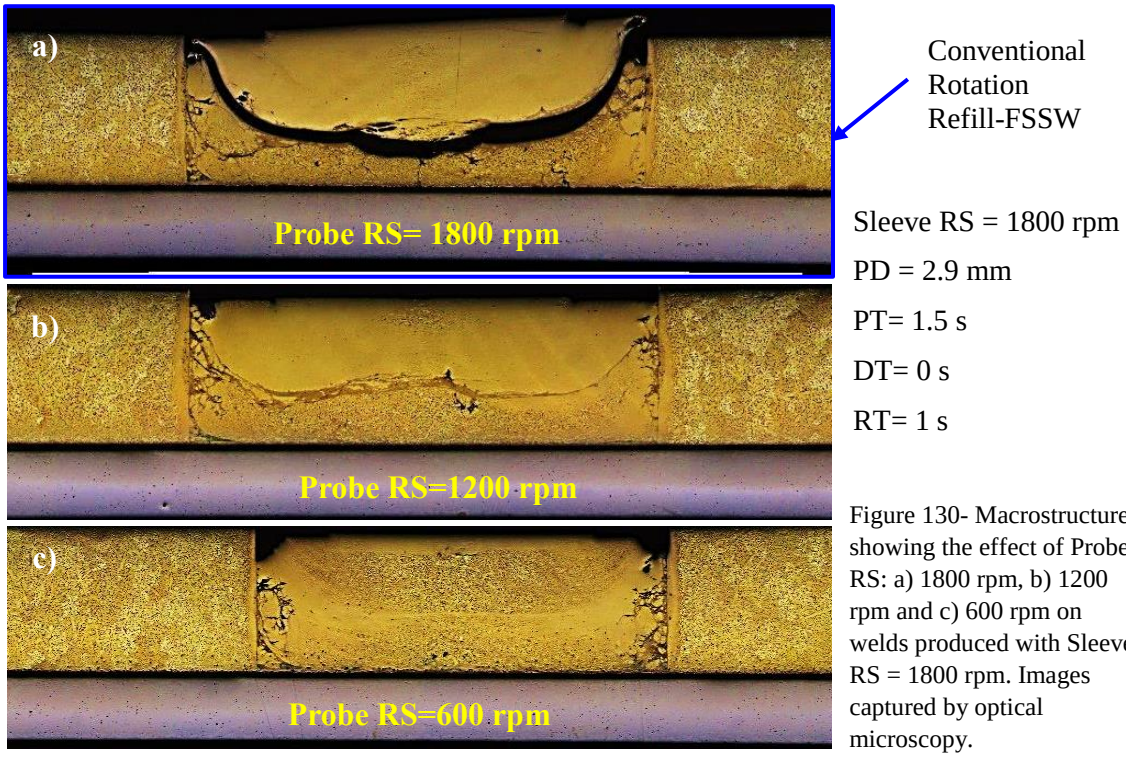

Figure 130- Macrostructures showing the effect of Probe RS: a) 1800 rpm, b) 1200 rpm and c) 600 rpm on welds produced with Sleeve RS = 1800 rpm. Images captured by optical microscopy.

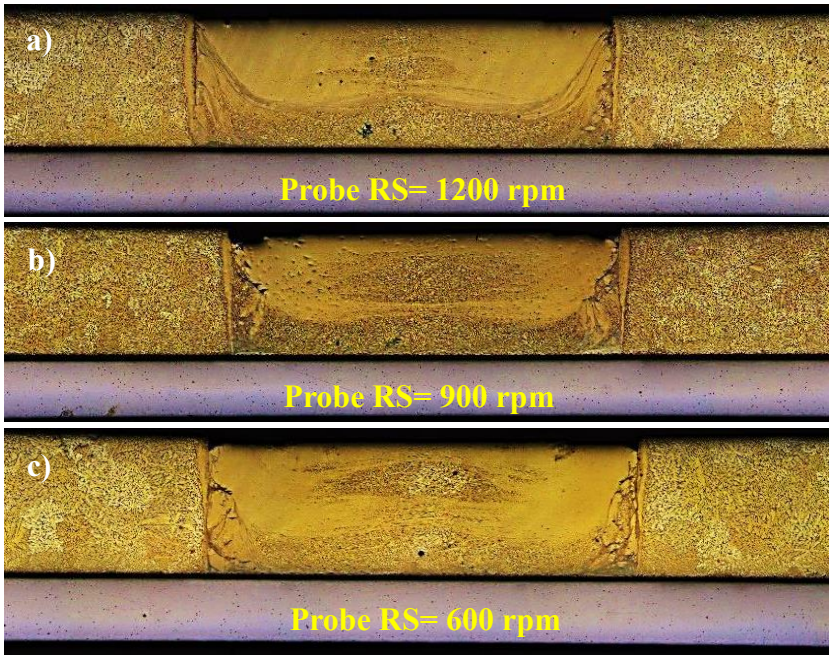

Sleeve RS = 1500 rpm

PD = 2.9 mm

PT= 1.5 s

DT= 0 s

RT= 1 s

Figure 131- Macrostructures showing the effect of Probe RS a) 1200 rpm, b) 900 rpm and c) 600 rpm. Images captured by optical microscopy.

The interfacial features observed for CR Refill-FSSW are also observed for DR Refill-FSSW. Figure 133 a) - f) describes the evolution of the interface heterogeneous reactions, starting away from the SZ center, until the center of the SZ. The four interfaces described for CR Refill-FSSW in Figure 113, are also present in Figure 133: a) interface I, b) - d) interface II, e) interface III and f) interface IV. There are no detectable changes of the structural features in the interface.

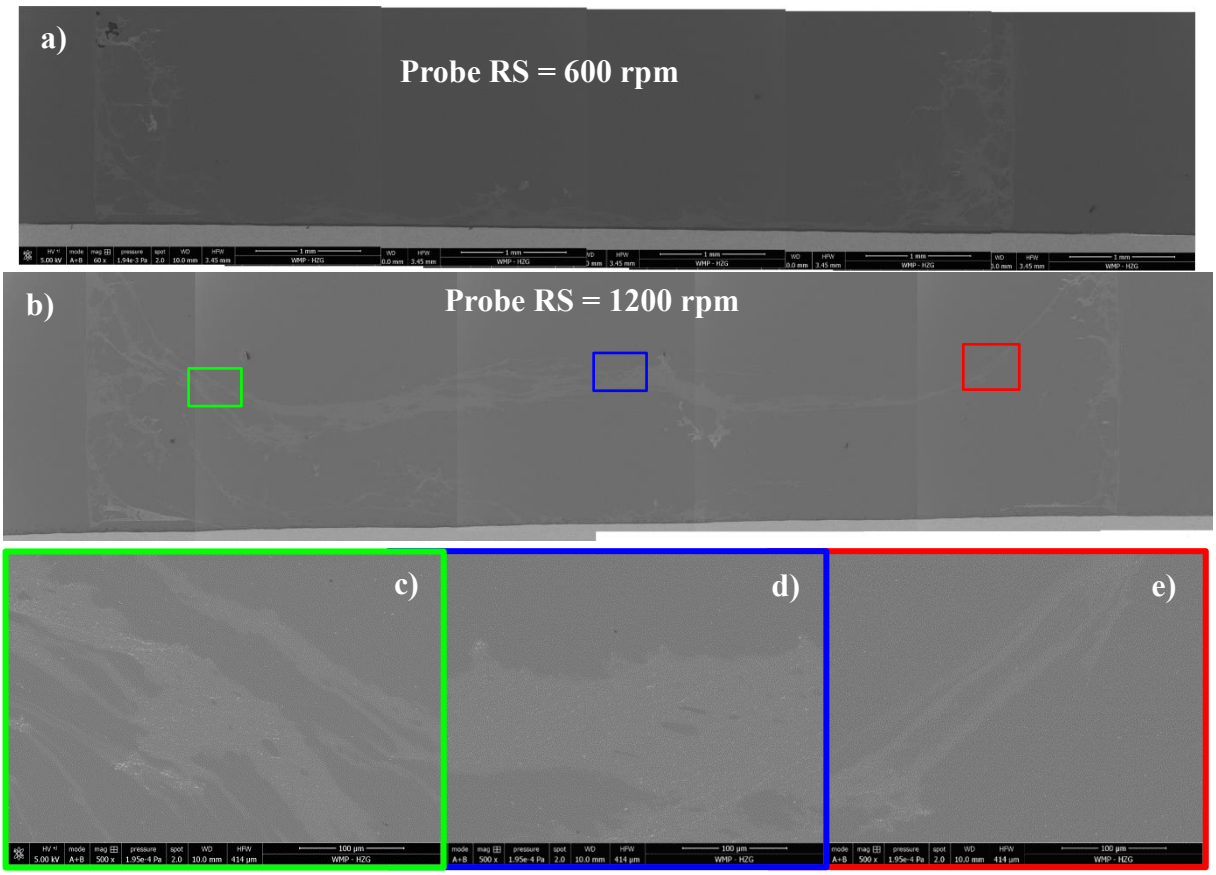

Figure 132- SEM macrographs for DR Refill-FSSW with Probe RS equal to a) 600 rpm; b) 1200 rpm. Cross-sections produced with the following parameters: Sleeve RS= 1800 rpm, PD= 2.9 mm, PT= 1.5 s, DT= 0 s, RT= 1 s.

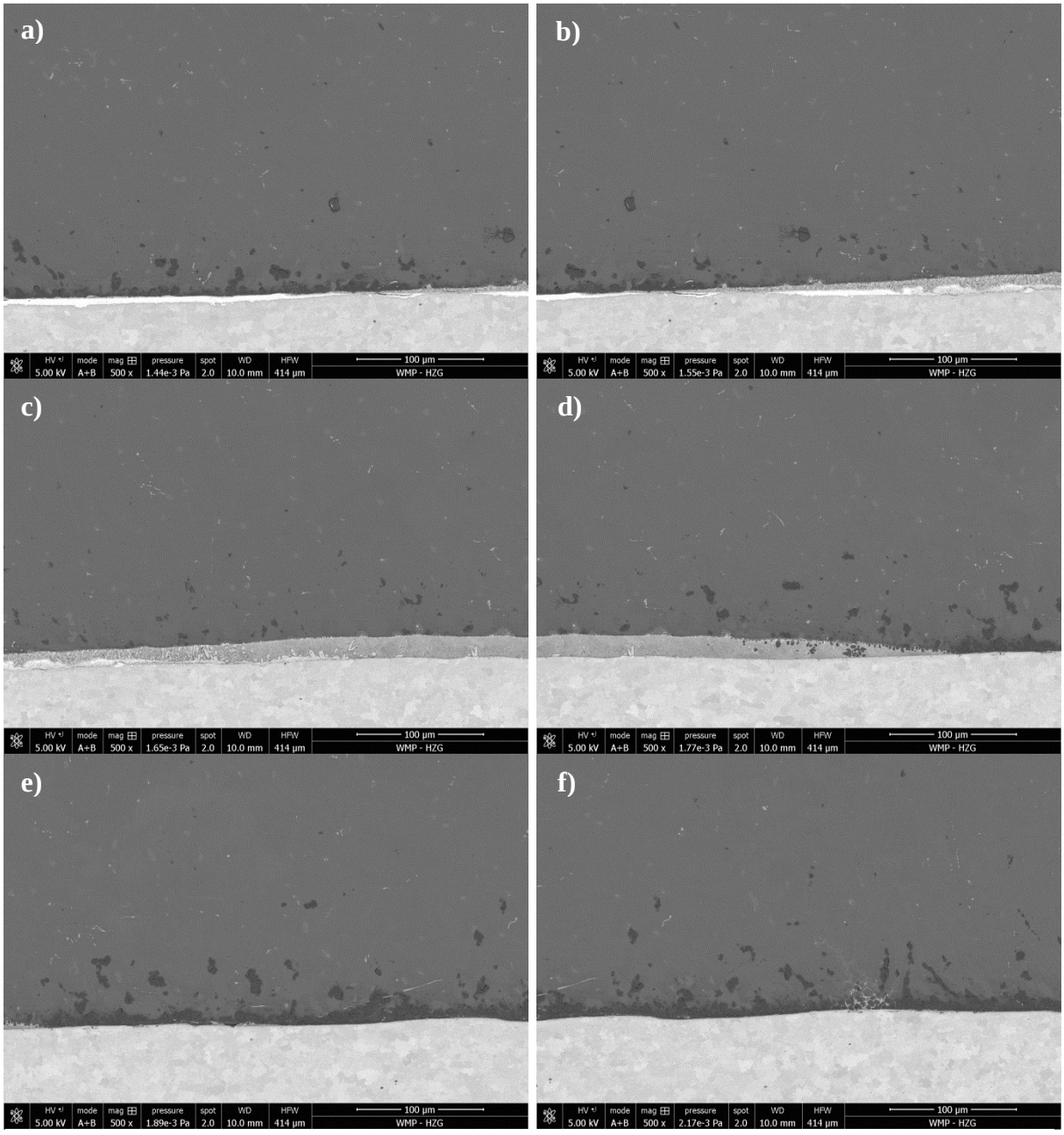

Figure 133- SEM micrographs of the interface features of DR Refill-FSSWed joint. Cross-sectioned spot produced with: PD = 2.9 mm, Sleeve RS = 1800 rpm, Probe RS = 1200 rpm, PT = 1.5 s, DT = 0 s and RT = 1 s.

From the preliminary study detailed in section 4.4.1 it was observed that the LSS increased with the reduction of the Probe RS. The strengthening mechanism of PD found for CR Refill-FSSW was related to the increase in the length of Interface II. Thus, the same assumption was tested for DR Refill-FSSW. The length of the interface II and interface III were measured and detailed in Table 70. However, unlike the effect of PD for CR Refill-FSSW, no significant changes in length of interface II with the reduction in Probe RS were found.

Table 70- Length of the Interfacial Regions I and II for different Probe RS.

Probe RS [rpm]	Interface II Length [µm]	Variation [%]	Interface III Length [µm]	Variation [%]
1800	830	-	524	-
1200	832	0.2	585	11.6
600	872	5.1	603	15.1

The correlation between the PD and the thickness of the Fe-Al was also tested for conventional rotation, but no significant changes of the IMC's layer at the SZ were detected. So, an EDS line scan was also conducted at the Mg-steel interface near the center of the SZ for DR Refill-FSSW. Figure 134 shows the evolution of the atomic elements composition near the center of the weld for: a) CR Refill-FSSW and b) DR Refill-FSSW with Probe RS = 600 rpm. Contrary to CR, for DR it is possible to observe a significant Al enrichment and growth of the Fe-Al IMC's transition layer. The increase in LSS was correlated with the increase in the Fe-Al thickness, which enhanced the metallurgical bonding in the SZ. However, the critical thickness of 10 μm (Jana, Hovanski, and Grant 2010), wasn't exceeded. Figure 134 a) - b) show the growth of the Fe-Al IMC's layer (horizontal widen of the Al element curve) and the enrichment in Al (higher vertical peak of the Al element curve) when DR Refill-FSSW was used.

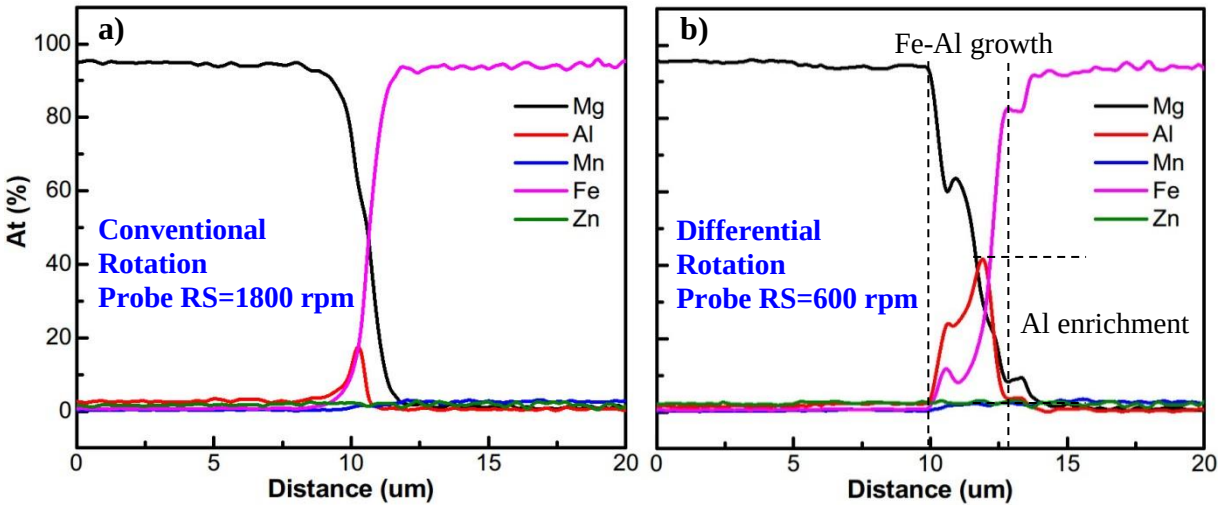

Figure 134- EDS element line scan across the Mg-steel interface near the SZ centre for different Probe RS: a) 1800 rpm and b) 600 rpm. Joints produced with: Sleeve RS = 1800 rpm, PD = 2.9 mm, PT = 1.5 s, DT = 0 s, RT = 1 s.

In order to justify the growth of the Fe-Al IMC's interlayer; temperature measurements at the centre of the weld were collected. Regarding the peak temperature achieved for different Probe RS, no significant differences were observed. A very slight increase in the maximum temperature recorded, which might be entirely related to acquisition errors, can be observed with the decrease in Probe RS. However, a significant correlation between the Probe RS and the total time during which the weld experienced temperatures above 350 ºC was found. The decrease in the Probe RS increases the total time with temperatures above 350 ºC. As indicated in Figure 135, the melting point of Mg-Zn eutectic ($Mg+Mg_7Zn_3$) is about 350 ºC. The growth of the Fe-Al layer might be related to longer exposing times to higher temperatures. However, further studies need to be conducted to correlate the stabilized temperature, the eutectic reactions and the growth of the Fe-Al IMC's layer.

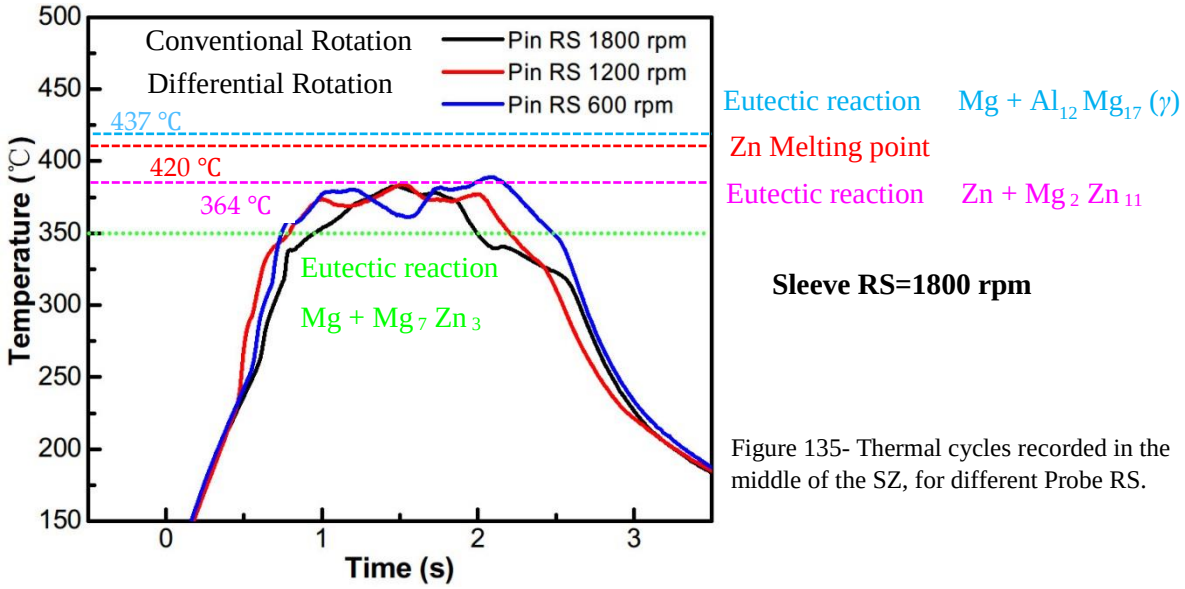

Figure 135- Thermal cycles recorded in the middle of the SZ, for different Probe RS.

4.4.3 Fracture Surface and Fracture Analysis

In CR Refill-FSSW, the strengthening mechanism was related to the widening of interface II, whereas in DR the increase in LSS was attributed to the growth of the Fe-Al IMC's in the SZ. This change is reflected in the fracture surface, Figure 136 a). In the case of DR in the left side: the crack extended along the Fe-Al layer, Figure 136 c), but in this case no Mg-Zn eutectic was observed, Figure 136 e). No significant changes in the right side of the spot were found. However, the crack didn't extend along the Mg-Zn eutectic as observed for some regions in Figure 122 e) - g). Figure 129 indicates that the LSS of the joint produced with Probe RS = 600 rpm and PD = 2.9 mm (6.455 kN), is significantly higher than the CR Refill-FSSWed joint produced with PD = 2.8 mm (5.944 kN). Thus, both fracture surfaces were superimposed in Figure 136 b) to check the difference in the area of fracture along the Mg SZ. Only a slight reduction in the total area can be observed, but the geometry of the fracture along the Mg SZ changed more significantly. Additional studies need to be conducted to correlate the fracture surface geometry and composition, to the strengthening mechanism.

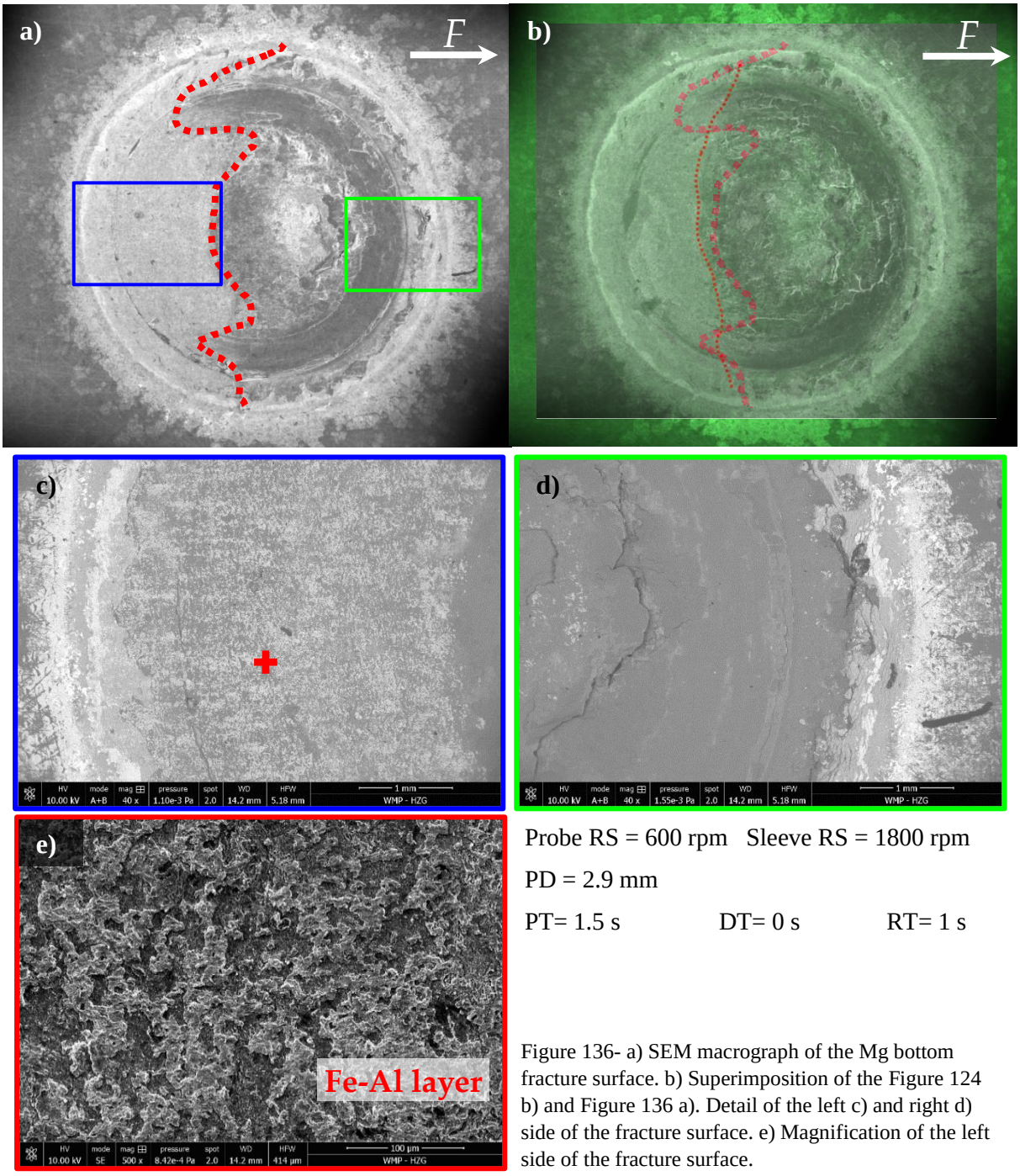

Probe RS = 600 rpm Sleeve RS = 1800 rpm

PD = 2.9 mm

PT= 1.5 s DT= 0 s RT= 1 s

Figure 136- a) SEM macrograph of the Mg bottom fracture surface. b) Superimposition of the Figure 124 b) and Figure 136 a). Detail of the left c) and right d) side of the fracture surface. e) Magnification of the left side of the fracture surface.

5 Final Remarks

5.1 Conclusions

From the experimental work carried out it was possible to conclude that:

Conventional Rotation Refill-FSSW

- The feasibility of CR Refill-FSSW of casting Mg alloy to Zn coated steel was successfully verified, the technical barriers of welding these two disparate alloy systems in nature were overcome. Sound welds with good surface finish and appearance were successfully produced for a wide range of welding parameters;
- Refill-FSSW is a competitive welding technology for dissimilar welding of Mg to steel, achieving comparable or even greater static shear mechanical properties than other solid-state process, and higher than the majority of fusion spot joining techniques. Casting Mg alloy to steel joints achieved higher LSS than the data published so far, concerning dissimilar Refill-FSSW of wrought Mg alloys to steel. Non-optimized welding parameters, for a fairly wide process window, fulfilled the AWS D17.2 requirements for weld quality assessment;
- Overall some insensitivity of the LSS with the welding parameters was observed. For welds outside the inference spaces defects such as voids, lack of refilling, lack of mixing and SZ pull-out defect started to appear. Nevertheless, the LSS didn't experience a steep drop, highlighting the robustness of the process;
- DoE approach was used in order to statistically analyze and evaluate the effect of the individual parameters in the mechanical properties (LSS) of the spot welds. The reasonableness of the base assumptions from the DoE was validated by residual analysis. The mathematical model was established using the commercial software Minitab®, and properly adjusted by model refinement. Good overall model fitting with fairly good predicting capacity of the total variability was achieved. Optimized parameters were obtained to guide the industry production. The optimized parameters were PD= 2.8 mm, RS= 1500 rpm, PT= 1.5 s, DT= 0 s, RT= 2 s;
- ANOVA methodology indicated a strong positive relation between the LSS and sleeve PD (almost 3x the second most statistically significant factor). The effect of PD stood out when compared with the minor effects of the remaining statistically significant parameters, indicating that was the only parameter worth studying, similar to what was concluded by (Dong et al. 2016). (Ding, Shen, and Gerlich 2017), in dissimilar welding of Al and steel;
- A characteristic region with layered distribution that could be easily observed in both OM (dark contrast) and SEM (bright contrast), resulted from particular macroscopic material flow behaviour, along with reactions of Zn from the steel coating. The Zn was probably transferred from the steel surface under the combined effects of heat and force during plunging movement, reacting with the Mg matrix. In the SZ, the stable layered material flow had a global straining stage characterized by simple shear (Shen, Lage, et al. 2018). The result was the presence of a continuous Mg-Zn rich region. This characteristic region was formed by Mg-Zn solid solution and Mg-Zn divorced eutectic lamellar structure, which wasn't broke by the diminished vertical flow. None detectable correlation between the distribution of the Mg-Zn region and the PD was found;
- Heterogeneous interfacial reactions resulted from transfer of the reaction products of the materials of the Mg-steel interface. Four interface regions were cataloged, starting far away from the spot

center. Interface I was characterized by the absence of welding with the preservation of the original Zn coating. Interface II was formed by Mg-Zn IMC's and Mg-Zn divorced eutectic that progressively developed over the fading Zn coating. Interface III was formed by the squeezing of Mg-Zn during plunging movement to Interface II, and extrusion into the interior of the SZ. Interface IV in the SZ, features no Zn coating, Mg-Zn eutectic, or Mg-Zn IMC's, and the metallurgical bonding was ensured by the original Fe-Al IMC's layer;

- Mg-Zn solid solution and eutectic was formed during welding due to the reaction of Mg with Zn. The Mg-Zn eutectic distributed along the interface offered a weld brazing bonding mechanism. The strengthening mechanism by PD increasing is correlated with the size of interface II; higher PD increases the interface II length, which on its turn increases LSS by increasing the weld brazing area. The original Fe-Al layer did not grow in the case of CR Refill-FSSW;
- Only the bottom view of the Mg fracture surface was observed in detail. The fracture in the side of the spot close to the free plate end was mainly through the Fe-Al layer and along Mg-Zn eutectic. In the side of the spot close to the loaded plate end, the fracture was mainly through the Mg SZ, but also extended along the Mg-Zn eutectic region, showing traces of liquation. For higher PD the area of fracture, along the Mg SZ increased;
- The role of the Zn interlayer was studied by studying the fracture surface of joints welded with steel plates in bare surface conditions. When the Zn coating layer of the steel was absent, no macro or micro plastic deformation was observed. No traces of diffusion or metallurgical bonding were found by EDS mapping and local analysis. The bonding mechanism was probably adhesion between the two substrates by high pressure and temperature, justifying the reduce LSS (almost half of the load capacity achieved with the same welding parameters for Zn coated steel). On the other hand, since there wasn't Zn in the steel surface, the SZ pull-out defect also wasn't formed for higher PD. In the case of Refill-FSSW of wrought Mg-steel, (Chen 2015) reported similar functions and effects for the Zn coating. However, the results achieved were the opposite of the data reported by (Verastegui et al. 2014), in the study of Al-steel dissimilar welding. In that case, the plates showed interface deformation, causing mechanical anchoring on the interface. In spite of the change in the bonding mechanism, the mechanical strength was about the same. The PD used was 0.5 mm above the steel interface, whereas in this study a higher safety margin of 1 mm was left;
- The presence of the SZ pull-out defect for higher PD was observed. Its importance was related to the correlation indicated by the DoE between the LSS and the PD. In order to further increase the LSS of the joint, it is necessary to avoid the SZ pull-out defect. Small continuous cracks along the concentrated layered structure were identified, and the presence of the SZ pull-out defect attributed to them. Several unsuccessful approaches were tried to avoid this type of defect, being DR Refill-FSSW the last and successful method tried to avoid the SZ pull-out defect.

Differential Rotation Refill-FSSW

- The feasibility of DR Refill-FSSW of casting Mg alloy to Zn coated steel, by reducing the probe RS was successfully verified. The SZ pull-out defect was avoided for higher PD, increasing the process window. Additional outcomes such as enhanced LSS and better surface finish were achieved;
- The macroscopic material flow behaviour changed by enhancing the material intermixing in the axial direction. The distribution of Mg-Zn characteristic region changed continuously with the reduction of the probe RS;
- Heterogeneous interfacial reactions were observed, and similarly to CR Refill-FSSW, four interface regions were identified;
- The strengthening mechanism for DR Refill-FSSW wasn't related to the length of interface II, but to the thickness of the Fe-Al IMC's layer in the SZ. The original Fe-Al IMC's layer grew with the reduction of the probe RS, due to longer exposure time to high temperatures;
- In the side of the spot close to the free plate end, the fracture was mainly through the Fe-Al IMC's layer. It wasn't found any correlation between the area of fracture along the Mg SZ and the probe RS.

Overall Study

- The mechanical properties of Refill-FSSWed Mg-steel dissimilar joints improved with the increase in sleeve PD. (Chen et al. 2015) in Mg-steel, and (Dong et al. 2016) in Al-steel, reported that reaching the critical threshold distance or even plunging the steel sheet could improve drastically the joint strength. However, it was reported by (Dong et al. 2016), that the increase in the sleeve PD until reaching the steel interface, could lead to catastrophic tool wear, reducing the tool service life. The hot topic of plunging in the hard metal lower sheet will be solved in the near future with the progressive technology transfer from FSW and FSSW of wear/temperature-resistant ceramic based tooling;
- The hypothetical difference between casting Mg-steel and wrought Mg-steel dissimilar welding may be only related to the plate thickness. Major differences should be detected in similar welding of casting Mg alloy, in which material flow and texture development play a more important role. However, the study of the influence of the Al content in the Mg alloy (major difference for the compared published data) is essential to draw any substantiated conclusions regarding the influence of the manufacturing process.

5.2 Future work perspective

Research topics in welding of Mg alloys to steel are far from being exhausted. Some fusion welding techniques, such as laser welding based technologies and resistance spot welding have already a modest but solid experimental background in this field. Particularly novel solid-state welding technologies such as Refill-FSSW, still lack a significant input of research power effort, already seen in the more well rooted such as USW or FSSW.

Next Steps

Regarding the project in which this report is integrated, the study of the Aluminum content in the Mg alloy still needs to be done – similar to (Kasai, Morisada, and Fujii 2015) for FSW. The evaluation of fatigue properties (by lap shear fatigue test) and its correlation with macro/microstructure and fracture surface (studied by OM and SEM), still lacks of explanation. The fatigue specimens were already prepared and welded during the thesis internship. However, due to time limitations and availability of the testing machine, the tests weren't performed. The influence of the plunge depth in the fatigue life will be evaluated. SN-curves for PD equal to 2.2 mm, 2.5 mm, and 2.8 mm will be determined. In addition, it is also worth studying the deformation behavior during quasi-static test by Digital Image Correlation (DIC) – which due to time restriction wasn't conducted, even though the proper training was received. Although the Torque and axial force data was collected, a deeper analysis of the response variables still needs to be done. The temperature was recorded for different material combinations - Mg/Mg, Mg/ Zn coated steel and Mg/bare steel; and different locations in the center of the weld and in the mid- thickness of the clamping ring. However, time limitations and technical problems in acquiring repayable data prevented its analysis in due time.

Future Topics

Different scientific topics related to the study developed in the context of this specific project could be further explored:

- Check the correlation between PD and mechanical strength for PD higher than 2.9 mm. For this it would be necessary the acquisition of a Refill-FSSW tool, capable of penetrating into the steel lower sheet. A similar study was conducted by (Liyanage et al. 2014) for FSSW, evaluating the effect in the joint resistance of plunging into the steel lower sheet. With the continuous development of advanced tooling for FSW, in a near future it may be economical viable to use this special type of materials in Refill-FSSW tools for automotive applications;
- DoE of DR Refill-FSSW with a complete study of the influence of the main welding parameters. Final comparative study, with CR Refill-FSSW, of the static and dynamic fatigue;

To further develop and complement the experimental work carried out during this project, a number of new research topics should be explored in the near future. They concern Mg to steel welding with - different steel coating conditions, steel sheets of different automotive alloys, joint properties (fatigue and corrosion) for both conventional and hybrid joining technologies (with adhesive and faying sealants) - and technological transversal topics not necessarily related to Mg-steel welding. The Zn coating developed a ruling roll in the Refill-FSSW of AM50 to DP600 steel. Thus, it would be relevant to study the metallurgical and mechanical influence of the major coating modifications. As preliminary suggestions:

- Comparison of hot-dip galvanized coatings with different Aluminum content in the bath (Galvanized, MicroZinc D4®, Galfan® or Supergalva®, Galvalume®); and its post treatment (general galvanized or galvannealed) – The influence of the Aluminum content in the Mg alloy was already proposed in the project within this report was wrote in, a natural step would be to study Al influence in the main welding mechanisms, when it is located in the coating;
- Study the feasibility of Refill-FSSW Mg to Zn coated steel, by typical industrial coating methods: Hot-dip Galvanizing, Zinc (Thermal) Spraying, Zinc Electroplating, Mechanical Plating, Zinc rich Paint – the coating layer will have different thickness and Zn content, with the formation of different phases with different hardness and elongation, which can influence the material flow and also its composition;

- Comparative study of dissimilar joining of Mg alloys steel sheets, with different coating conditions: aluminized (AlSi), Zn coated, bare cold rolled, and bare hot rolled as performed in GMAW by (Kang, Kim, and Kim 2017);

The majority of Mg-Steel welded joints use dual phase steels with or without Zn coating as a base material to study. This is easily justified by their privileged chronological appearance, and relevance that nowadays have relatively to the remaining AHSS. However, 2nd and 3rd generations of AHSS have considerable different technological properties. In addition, a fraction of steels alloyed to Mn and Al may not be coated, forming a natural protective oxide layer. Since Refill-FSSW of dissimilar steel joints is and interfacial mechanism, this new surface conditions will be a challenge. So, further experiments with novel steels not only have scientific value, but also industrial and technological applicability;

- Study the feasibility of welding Mg alloys to steels with novel AHSS: SS, L-IP, TWIP, etc., similar to the study conducted by (Manladan et al. 2017b) in REW;

Mg and steel have a huge galvanic potential difference, so their joints will definitely suffer from galvanic corrosion. In fact, extruded Mg is mainly used as sacrificial anodes in aggressive environments such as salty water/atmosphere (e.g. ship hulls), high temperatures (e.g. heat exchangers), transport of corrosive compounds (e.g. pipelines, chemical industry), etc. (Agnew 2004). Consequently, it is of extremely importance to quantify and try to predict its corrosion resistance.

- Corrosion behavior and resistance of Mg to steel Refill-FSSWed joints, as it was done by (Pan and Santella 2012a) and (Pan and Santella 2012c) for USW;

Adhesive bonding has many advantages (e.g. larger bonding areas and less stress concentration) and can further benefit from hybrid welding techniques (e.g. through increasing its peeling resistance). Consequently, the combination of Refill-FSSW and adhesive bonding (Refill FSSWeldbonding) in Mg to steel dissimilar joints is worth studying (Chowdhury et al. 2013a). Some topics suggestions:

- Feasibility of Refill Friction Stir Spot Weldbonding of Mg to steel with different types of adhesives – as was done in FSSW/USW by (Chowdhury et al. 2013b) / (Pan et al. 2006); and faying sealant material – as was done for Refill-FSSW of Al alloys by (Brown 2008);
- Corrosion (Pan et al. 2014), (Pan et al. 2013), and fatigue behavior (Lai et al. 2013) of Mg to steel Refill Friction Stir Spot Weldbonding joints as was already studied for USWB;

Finally, even though Refill-FSSW has a series of advantages regarding other solid-state and fusion welding process, it still lacks of industrial significant implementation as FSSW (Pan 2007). Topics regarding the process and technological features are further suggested:

- Proper comparative studies of the two variants probe plunge and sleeve plunge - probe plunge with a probe, with the same diameter of a sleeve, in sleeve plunge;
- Tool durability, design (threaded, grooved, plane surface, etc.), weld stability and process reproducibility in industrial welding cycle's requirements. This type of experiment can be performed in the industrial fitted and sized Kawasaki® ZX300S robot arm from HZG;
- Study the influence of additional external cooling systems for the Refill-FSSW (Mg is a heat sink), allowing to conduct heat to the interface where the metallurgical bonding occurs (Shen, Hou, et al. 2016);
- Develop clamping devices for fixture and work-holding for sound Refill-FSSW of non-flat components (mechanical design team of Refill-FSSW division);
- All welding techniques introduce a specific amount of residual stresses, which have usually thermal and mechanical sources. To the best of the author's knowledge, there are no published literature regarding the study or simulation of residual stresses in Refill-FSSW of any similar or dissimilar joint as done by (Zeng et al. 2011) for hybrid laser-arc welding technology;
- Further development of non-destructive testing/techniques (NDT) detection, evaluation and controlling of manufacturing defects as studied by (Sewell et al. 2015) in FSW and successfully applied in Refill-FSSW by (Santos et al. 2011).

[blank page]

References

Acherjee, Bappa. 2018. "Hybrid laser arc welding: State-of-art review." *Optics & Laser Technology* 99:60-71.

Addison, AC, and AJ Robelou. 2004. "Friction stir spot welding: principal parameters and their effects." Proceedings of the Fifth International Conference on Friction Stir Welding.

Agnew, Sean R. 2004. "Wrought magnesium: a 21st century outlook." *Jom* 56 (5):20-21.

Ahmed, Nasir. 2005. *New developments in advanced welding*: Elsevier.

Akafuah, Nelson K, Sadegh Poozesh, Ahmad Salaimeh, Gabriela Patrick, Kevin Lawler, and Kozo Saito. 2016. "Evolution of the automotive body coating process - A review." *Coatings* 6 (2):24.

Al-Sarraf, Z, and M Lucas. 2012. "A study of weld quality in ultrasonic spot welding of similar and dissimilar metals." Journal of Physics: Conference Series.

Al-Zubaidy, Basem. 2017. "Material interactions in a novel refill friction stir spot welding approach to joining Al-Al and Al-Mg automotive sheets." University of Manchester.

Amancio-Filho, Sergio T, Ana PC Camillo, Luciano Bergmann, Jorge F Dos Santos, Sebastião E Kury, and Nelson GA Machado. 2011. "Preliminary investigation of the microstructure and mechanical behaviour of 2024 aluminium alloy friction spot welds." *Materials Transactions* 52 (5):985-991.

Amancio-Filho, ST, C Bueno, JF Dos Santos, N Huber, and E Hage Jr. 2011. "On the feasibility of friction spot joining in magnesium/fiber-reinforced polymer composite hybrid structures." *Materials Science and Engineering: A* 528 (10-11):3841-3848.

Antony, J. 2014. *Design of Experiments for Engineers and Scientists*. Vol. 2: Elsevier Science.

Araki, Toshio, Masaki Koba, Shoichi Nambu, Junya Inoue, and Toshihiko Koseki. 2011. "Reactive Transient Liquid Phase Bonding between AZ31 Magnesium Alloy and Low Carbon Steel." *Materials Transactions* 52 (3):568-571.

Arizmendi, A, A Salinas, E Nava, and R Garza. 2003. "Microstructure of Al-Zn-Si coatings on steel substrates." Materials Science Forum.

Armstrong, RL, Brent L Adams, and Mark A Arnold. 2018. *ASM Handbook Volume 10: Materials Characterization*. Vol. 10: ASM International.

Arul, SG, SF Miller, GH Kruger, T-Y Pan, PK Mallick, and AJ Shih. 2008. "Experimental study of joint performance in spot friction welding of 6111-T4 aluminium alloy." *Science and Technology of Welding and Joining* 13 (7):629-637.

ASTM International Standards. 2005. ASTM B 275 - 05 Standard Practice for Codification of Certain Nonferrous Metals and Alloys, Cast and Wrought. USA.

ASTM International Standards. 2011. ASTM E3 - 11(2017) Standard Guide for Preparation of Metallographic Specimens. USA.

Badarinarayan, H, F Hunt, and K Okamoto. 2006. "Friction stir stitch welding–process development and mechanical property evaluation." 6th International Symposium of Friction Stir Welding ISFSW6.

Baker, LJ, JD Parker, and SR Daniel. 2002. "Mechanism of bake hardening in ultralow carbon steel containing niobium and titanium additions." *Materials Science and Technology* 18 (5):541-547.

Baluch, Nazim, Zulkifli Mohamed Udin, and Che Sobry Abdullah. 2014. "Advanced high strength steel in auto industry: An overview." *Engineering, Technology & Applied Science Research* 4 (4):686-689.

Basuki, Eddy A, Muhammad I Yuliansyah, Farhan M Rahman, Fadhli Muhammad, and Djoko Prajitno. 2016. "Interdiffusion Behavior of Aluminide Coated Two-Phase α2-Ti3Al/γ-TiAl Alloys at High Temperatures." *Journal of Engineering and Technological Sciences* 48 (5):534-549.

Bergmark, Hans, Jessica Bergmark, and Anders Eliasson. 2015. "Friction stir welding." accessed 26/06/2018. https://www.manufacturingguide.com/en/friction-stir-welding-fsw.

Bestetti, Massimiliano, and Anna Da Forno. 2011. "Electroless and Electrochemical Deposition of Metallic Coatings on Magnesium Alloys Critical Literature Review." *Magnesium Alloys-Corrosion and Surface Treatments, Rijeka: InTech*:153-184.

Bettles, Colleen, and Matthew Barnett. 2012. *Advances in wrought magnesium alloys: fundamentals of processing, properties and applications*: Elsevier.

Bhat, Shrikant P. 2011. "Advances in high strength steels for automotive applications." Great Designs in Steel Seminar - Acerlor Mittal, Chicago.

Billur, E, and T Altan. 2013. "Three generations of advanced high-strength steels for automotive applications, Part I." *Stamping Journal*:16-17.

Billur, E, and T Altan. 2014a. "Three generations of advanced high-strength steels for automotive applications, Part II." *Stamping Journal*:12-13.

Billur, E, and T Altan. 2014b. "Three generations of advanced high-strength steels for automotive applications, Part III." *Stamping Journal*:12-13.

Binjiang, Lu, Peng Jian, Tong Xiaoshan, and Pan Fusheng. 2013. "Effects of Extruding Temperature on Microstructure and Mechanical Properties of Mg-2.0 Zn-0.3 Zr-0.9 Y Alloy." *Rare Metal Materials and Engineering* 42 (4):841-844.

Blanchard, Patrick J, DJ Hill, Greg T Bretz, and Robert C McCune. 2016. "Evaluation of corrosion protection methods for magnesium alloys in automotive applications." In *Essential Readings in Magnesium Technology*, 593-598. Springer.

Blawert, C, N Hort, and KU Kainer. 2004. "Automotive applications of magnesium and its alloys." *Trans. Indian Inst. Met* 57 (4):397-408.

Blawert, Carsten, Wolfgang Dietzel, Edward Ghali, and Guangling Song. 2006. "Anodizing treatments for magnesium alloys and their effect on corrosion resistance in various environments." *Advanced Engineering Materials* 8 (6):511-533.

Böhler, Elmar, Gerd Kronsteiner, Hans H. Priebsch, Michael Bauer, and Gernot Wagner. 2008. "Alternative vehicle bodies." *ATZ Worldwide* 110 (10):14-19. doi: 10.1007/bf03225032.

Bowles, Amanda L, Qingyou Han, and JA Horton. 2016. "Castability of magnesium alloys." In *Essential Readings in Magnesium Technology*, 187-192. Springer.

Bozzolo, Guillermo, Ronald D Noebe, and Phillip B Abel. 2007. *Applied computational materials modeling: theory, simulation and experiment*: Springer Science & Business Media.

Brown, Jeremy Micah. 2008. "The effects of sealants and surface treatments on the faying surface of swept friction stir spot welds." Wichita State University.

Buffa, G., L. Fratini, and M. Piacentini. 2008. "On the influence of tool path in friction stir spot welding of aluminum alloys." *Journal of Materials Processing Technology* 208 (1):309-317. doi: https://doi.org/10.1016/j.jmatprotec.2008.01.001.

C.Schilling, A.V. Strombeck, J.F. dos Santos, and N.V. Heesen. 2000. "Proceedings of 2nd Symposium on Friction Stir Welding." Gothenburg, Sweden, May 26-28.

Calcagnotto, Marion, Dirk Ponge, and Dierk Raabe. 2010. "Effect of grain refinement to 1 μm on strength and toughness of dual-phase steels." *Materials Science and Engineering: A* 527 (29-30):7832-7840.

Campanelli, Leonardo Contri, Uceu Fuad Hasan Suhuddin, Armando Ítalo Sette Antonialli, Jorge Fernandez dos Santos, Nelson Guedes de Alcântara, and Claudemiro Bolfarini. 2013. "Metallurgy and mechanical performance of AZ31 magnesium alloy friction spot welds." *Journal of Materials Processing Technology* 213 (4):515-521. doi: https://doi.org/10.1016/j.jmatprotec.2012.11.002.

Campanelli, Leonardo Contri, Uceu Fuad Hasan Suhuddin, Jorge Fernandez dos Santos, and Nelson Guedes de Alcântara. 2012. "Parameters optimization for friction spot welding of AZ31 magnesium alloy by Taguchi method." *Soldagem & Inspeção* 17 (1):26-31.

Campbell, A.S. 1985. *Thermodynamic Analysis of Combustion Engines*: R.E. Krieger Publishing Company.

Campbell, Flake C. 2008. *Elements of metallurgy and engineering alloys*: ASM International.

Cao, JY, M Wang, L Kong, and LJ Guo. 2016. "Hook formation and mechanical properties of friction spot welding in alloy 6061-T6." *Journal of Materials Processing Technology* 230:254-262.

Cao, JY, M Wang, L Kong, HX Zhao, and P Chai. 2017. "Microstructure, texture and mechanical properties during refill friction stir spot welding of 6061-T6 alloy." *Materials Characterization* 128:54-62.

Cao, R, JY Yu, JH Chen, and Pei-Chung Wang. 2013. "Feasibility of cold-metal-transfer welding magnesium AZ31 to galvanized mild steel." *Welding journal* 92 (9).

Cardillo, Maria E. B., Junjun Shen, Nelson G. de Alcântara, Conrado R. M. Afonso, and Jorge F. dos Santos. 2018. "Effect of friction spot welding parameters on the joint formation and mechanical properties of Al to Cu." *Welding in the World*. doi: https://doi.org/10.1007/s40194-018-0632-4.

Cavazzuti, M. 2012. *Optimization Methods: From Theory to Design Scientific and Technological Aspects in Mechanics*: Springer Berlin Heidelberg.

Chatterjee, Debasish. 2017. "Behind the Development of Advanced High Strength Steel (AHSS) Including Stainless Steel for Automotive and Structural Applications - An Overview." *Materials Science and Metallurgy Engineering* 4 (1):1-15.

Chen, J, B Shalchi Amirkhiz, and R Zhang. 2017. "Continuous nanoscale Al2Fe transition layer strengthened magnesium-steel spot joints." *Materials Letters* 196:242-244.

Chen, Kai, Xun Liu, and Jun Ni. 2017. "Keyhole refilled friction stir spot welding of aluminum alloy to advanced high strength steel." *Journal of Materials Processing Technology* 249:452-462. doi: https://doi.org/10.1016/j.jmatprotec.2017.06.039.

Chen, Y, J Chen, B Shalchi Amirkhiz, MJ Worswick, and AP Gerlich. 2015. "Microstructures and properties of Mg alloy/DP600 steel dissimilar refill friction stir spot welds." *Science and Technology of Welding and Joining* 20 (6):494-501.

Chen, YC, and K Nakata. 2009. "Effect of tool geometry on microstructure and mechanical properties of friction stir lap welded magnesium alloy and steel." *Materials & Design* 30 (9):3913-3919.

Chen, YC, and K Nakata. 2010. "Effect of surface states of steel on microstructure and mechanical properties of lap joints of magnesium alloy and steel by friction stir welding." *Science and Technology of Welding and Joining* 15 (4):293-298.

Chen, Yuyang. 2015. "Refill Friction Stir Spot Welding of Dissimilar Alloys." University of Waterloo.

Chowdhury, S. H., D. L. Chen, S. D. Bhole, X. Cao, and P. Wanjara. 2013a. "Lap shear strength and fatigue behavior of friction stir spot welded dissimilar magnesium-to-aluminum joints with adhesive." *Materials Science and Engineering: A* 562:53-60. doi: https://doi.org/10.1016/j.msea.2012.11.039.

Chowdhury, SH, DL Chen, SD Bhole, X Cao, and P Wanjara. 2013b. "Lap shear strength and fatigue behavior of friction stir spot welded dissimilar magnesium-to-aluminum joints with adhesive." *Materials Science and Engineering: A* 562:53-60.

Committee, ASM International. 2004. *ASM Handbook: Metallography and Microstructures*. Vol. 9, *Scanning Electron Microscopy*: ASM International.

Conrardy, C. 2008. "US industry's top materials joining technology needs." 8th International Conference on Trends in Welding Research.

Crolla, D.A. 2009. *Automotive Engineering: Powertrain, Chassis System and Vehicle Body*: Butterworth-Heinemann.

Czerwinski, Frank. 2011. "Welding and joining of magnesium alloys." In *Magnesium Alloys-Design, Processing and Properties*. InTech.

Da Silva, AAM, E Aldanondo, P Alvarez, E Arruti, and A Echeverria. 2010. "Friction stir spot welding of AA 1050 Al alloy and hot stamped boron steel (22MnB5)." *Science and Technology of Welding and Joining* 15 (8):682-687.

da Silva, AAM, JF dos Santos, TR Rosendo, FD Ramos, CCP Mazzaferro, MAD Tier, L Bergmann, JAE Mazzaferro, and TR Strohaecker. 2007. Performance evaluation of 2-mm thick alclad AA2024 T3 aluminium alloy friction spot welding. SAE Technical Paper 2007-01-3812.

Dahle, Arne K, Young C Lee, Mark D Nave, Paul L Schaffer, and David H StJohn. 2001. "Development of the as-cast microstructure in magnesium–aluminium alloys." *Journal of Light Metals* 1 (1):61-72.

de Rincón, O., A. Rincón, M. Sánchez, N. Romero, O. Salas, R. Delgado, B. López, J. Uruchurtu, M. Marroco, and Zephir Panosian. 2009. "Evaluating Zn, Al and Al–Zn coatings on carbon steel in a special atmosphere." *Construction and Building Materials* 23 (3):1465-1471. doi: https://doi.org/10.1016/j.conbuildmat.2008.07.002.

de Souza, Helder Jose Celani, Messias Borges Silva, Cinthia B Moyses, Fernando Lopes Alberto, Fabrício J Pontes, Ubirajara R Ferreira, Roberto N Duarte, and Carlos Eduardo

Sanches da Silva. 2013. "Robust Design and Taguchi Method Application." In *Design of Experiments-Applications*. InTech.

Demeri, Mahmoud Y. 2013. *Advanced High-Strength Steels: Science, Technology, and Applications*: ASM International.

Ding, Y., Z. Shen, and A. P. Gerlich. 2017. "Refill friction stir spot welding of dissimilar aluminum alloy and AlSi coated steel." *Journal of Manufacturing Processes* 30:353-360. doi: https://doi.org/10.1016/j.jmapro.2017.10.006.

Dong, Honggang, Su Chen, Yang Song, Xin Guo, Xiaosheng Zhang, and Zhiyang Sun. 2016. "Refilled friction stir spot welding of aluminum alloy to galvanized steel sheets." *Materials & Design* 94:457-466.

Dosdat, L, J Petitjean, T Vietoris, and O Clauzeau. 2011. "Corrosion Resistance of Different Metallic Coatings on Press-Hardened Steels for Automotive." *Steel Research International* 82 (6):726-733.

Dubourg, L, and P Dacheux. 2006. "Design and properties of FSW tools: a literature review." Proceedings of the 6th International Symposium on Friction Stir Welding, Saint Sauveur, Quebec, Canada.

Effertz, P.S., L. Quintino, and V. Infante. 2017. "The optimization of process parameters for friction spot welded 7050-T76 aluminium alloy using a Taguchi orthogonal array." *The International Journal of Advanced Manufacturing Technology* 91 (9):3683-3695. doi: 10.1007/s00170-017-0048-0.

Egbue, Ona, and Suzanna Long. 2012. "Barriers to widespread adoption of electric vehicles: An analysis of consumer attitudes and perceptions." *Energy Policy* 48:717-729. doi: https://doi.org/10.1016/j.enpol.2012.06.009.

El Rehim, S. S. Abd, E. E. Fouad, S. M. Abd El Wahab, and Hamdy H. Hassan. 1996. "Electroplating of zinc-nickel binary alloys from acetate baths." *Electrochimica Acta* 41 (9):1413-1418. doi: https://doi.org/10.1016/0013-4686(95)00327-4.

Elsayed, Fady Refaat, Norbert Hort, Mario Alberto Salgado Ordorica, and Karl Ulrich Kainer. 2011. "Magnesium permanent mold castings optimization." *Materials Science Forum* 690:65-68. doi: https://doi.org/10.4028/www.scientific.net/MSF.690.65.

Elthalabawy, Waled M, and Tahir I Khan. 2010. "Microstructural development of diffusion-brazed austenitic stainless steel to magnesium alloy using a nickel interlayer." *Materials Characterization* 61 (7):703-712.

Elthalabawy, Waled M, and Tahir I Khan. 2011. "Eutectic bonding of austenitic stainless steel 316L to magnesium alloy AZ31 using copper interlayer." *The International Journal of Advanced Manufacturing Technology* 55 (1-4):235-241.

Escobar, José C., Electo S. Lora, Osvaldo J. Venturini, Edgar E. Yáñez, Edgar F. Castillo, and Oscar Almazan. 2009. "Biofuels: Environment, technology and food security." *Renewable and Sustainable Energy Reviews* 13 (6):1275-1287. doi: https://doi.org/10.1016/j.rser.2008.08.014.

Fadaeifard, Firouz, Khamirul Amin Matori, Meysam Toozandehjani, Abdul Razak Daud, Mohd Khairol Anuar Mohd Ariffin, Norinsan Kamil Othman, Farhad Gharavi, Abdul Hadi Ramzani, and Farhad Ostovan. 2014. "Influence of rotational speed on mechanical properties of friction stir lap welded 6061-T6 Al alloy." *Transactions of Nonferrous Metals Society of China* 24 (4):1004-1011.

Fanelli, Pierluigi, Francesco Vivio, and Vincenzo Vullo. 2012. "Experimental and numerical characterization of Friction Stir Spot Welded joints." *Engineering Fracture Mechanics* 81:17-25.

Federer, W.T., and F. King. 2007. *Variations on Split Plot and Split Block Experiment Designs*: Wiley.

Feng, M, Y Li, C Zhao, and Z Luo. 2016. "Mechanical properties and interface morphology of Mg/Al ultrasonic spot weld bonding welds." *Science and Technology of Welding and Joining* 21 (8):688-699.

Feng, Yueqiao, Yang Li, Zhen Luo, Zhanxiang Ling, and Zhengming Wang. 2016. "Resistance spot welding of Mg to electro-galvanized steel with hot-dip galvanized steel interlayer." *Journal of Materials Processing Technology* 236:114-122.

Feraboli, Paolo, and Attilio Masini. 2004. "Development of carbon/epoxy structural components for a high performance vehicle." *Composites Part B: Engineering* 35 (4):323-330.

Filho, Sergio de Traglia Amancio, P.H.F. de Oliveira, Carlos Bueno, A. Hoppe, Jorge Fernandez dos Santos, and E. Hage Jr. 2010. "Proceedings for ANTEC 2010." ANTEC 2010, Orlando World Center Marriott Resort & Convention Center, Orlando. FL, USA.

Firouzdor, V, and S Kou. 2009. "Al-to-Mg friction stir welding: effect of positions of Al and Mg with respect to the welding tool." *Weld. J* 88 (11):213-224.

Fonstein, N. 2015. *Advanced High Strength Sheet Steels: Physical Metallurgy, Design, Processing, and Properties*: Springer International Publishing.

Fox, Sean Long. 2010. "Refill friction stir spot weld repair of a fatigue crack." *Research experience for undergraduates. Rapid City (USA): South Dakota School of Mines and Technology*.

Franklin, Teresa J. 2013. "Fatigue Behavior and Life Estimations for Dissimilar Ultrasonic Welds in Lap-shear Specimens of Magnesium and Galvanized Steel Sheets." PhD, Mechanical Engineering, University of Michigan.

Franklin, Teresa J, Jwo Pan, Michael Santella, and Tsung-Yu Pan. 2011. "Fatigue behavior of dissimilar ultrasonic spot welds in lap-shear specimens of magnesium and steel sheets." *SAE International Journal of Materials and Manufacturing* 4 (2011-01-0475):581-588.

Friedrich, H.E., and B.L. Mordike. 2006. *Magnesium Technology: Metallurgy, Design Data, Automotive Applications*: Springer Berlin Heidelberg.

Fujimoto, M, T Hyoe, M Inuzuka, H Kashiki, U Nagao, R Sakano, and K Yamashita. 2001. "Development of spot FSW robot system for automobile body members." Proceedings of the Third International Symposium of Friction Stir Welding, Kobe, Japan.

Fukada, S, R Ohashi, M Fujimoto, and H Okada. 2014. "Refill friction stir spot welding of dissimilar materials consisting of A6061 and hot dip zinc-coated steel sheets." Proceedings of the 1st international joint symposium on joining and welding.

Gándara, María Josefa Freiría. 2011. "Recent growing demand for magnesium in the automotive industry." *Materials and Technology* 45 (6):633-637.

Ghosh, Pampa, and Chiradeep Ghosh. 2009. "Precipitation in interstitial free high strength steels." *The Iron and Steel Institute of Japan International* 49 (7):1080-1086.

Giancarlo, Genta, and Morello Lorenzo. 2009. *The Automotive Chassis–Volume 1: Components Design*: Springer Netherlands.

Gilles, T. 2015. *Automotive Service: Inspection, Maintenance, Repair*: Cengage Learning.

Goebel, Jannik, Martin Reimann, Andrew Norman, and Jorge F. dos Santos. 2017. "Semi-stationary shoulder bobbin tool friction stir welding of AA2198-T851." *Journal of Materials Processing Technology* 245:37-45. doi: https://doi.org/10.1016/j.jmatprotec.2017.02.011.

Gonçalves, J., J. F. dos Santos, L. B. Canto, and S. T. Amancio-Filho. 2015. "Friction spot welding of carbon fiber-reinforced polyamide 66 laminate." *Materials Letters* 159:506-509. doi: https://doi.org/10.1016/j.matlet.2015.08.036.

Gonçalves, Joel, Jorge Fernandez dos Santos, Leonardo Bresciani Canto, and Sergiode Traglia Amancio Filho. 2016. "Improvement of friction spot welding (FSpW) to join polyamide 6 and polyamide 66/carbon fibre laminate." *Welding International* 30 (4):247-254.

CES Edupack 17.1.0 (Database). Granta Design Limited, Cambridge.

Graudenz, M., and M. Baur. 2013. "21 - Applications of laser welding in the automotive industry." In *Handbook of Laser Welding Technologies*, edited by Seiji Katayama, 555-574. Woodhead Publishing.

Gupta, H.N. 2006. *Fundamentals of Internal Combustion Engines*: Prentice-Hall of India Pvt. Limited.

Gupta, I, and P-H Chang. 1984. "Effect of Compositional and Processing Parameters on the Variability of the Tensile Strength of Continuously Annealed Water Quenched Dual Phase Steels." *Technology of Continuously Annealed Cold-Rolled Sheet Steel*:263-276.

Han, Q, and S Viswanathan. 2003. "Analysis of the Mechanism of Die Soldering in Aluminum Die Casting." *Metallurgical and Materials Transactions* 34 (1):139-146.

Hancock, Ross. 2004. "Friction welding of aluminum cuts energy costs by 99%." *Welding Journal* 83 (2):40-43.

Happian-Smith, J. 2001. *An Introduction to Modern Vehicle Design*: Butterworth-Heinemann.

Hilgert, Jakob. 2012. "Knowledge based process development of bobbin tool friction stir welding." Citeseer.

Hovanski, Yuri, Piyush Upadhyay, John Carsley, Tom Luzanski, Blair Carlson, Mark Eisenmenger, Ayoub Soulami, Dustin Marshall, Brandon Landino, and Susan Hartfield-Wunsch. 2015. "High-speed friction-stir welding to enable aluminum tailor-welded blanks." *Jom* 67 (5):1045-1053.

Hu, Rong-Gang, Su Zhang, Jun-Fu Bu, Chang-Jian Lin, and Guang-Ling Song. 2012. "Recent progress in corrosion protection of magnesium alloys by organic coatings." *Progress in Organic Coatings* 73 (2):129-141. doi: https://doi.org/10.1016/j.porgcoat.2011.10.011.

Huang, Guang-Sheng, Hua Zhang, Xiao-Yun Gao, SONG Bo, and Lei Zhang. 2011. "Forming limit of textured AZ31B magnesium alloy sheet at different temperatures." *Transactions of Nonferrous Metals Society of China* 21 (4):836-843.

Huang, M. 2002. *Vehicle Crash Mechanics*: CRC Press.

Huang, YX, L Wan, SX Lv, and JC Feng. 2013. "Novel design of tool for joining hollow extrusion by friction stir welding." *Science and Technology of Welding and Joining* 18 (3):239-246.

Hussey, Robert John, and Josephine Wilson. 2013. *Light Alloys: Directory and Databook*: Springer Science & Business Media.

IMA. 2012. "The Impact of Chinese Production, Costs and Shipments."

Jana, S., and Y. Hovanski. 2012. "Fatigue behaviour of magnesium to steel dissimilar friction stir lap joints." *Science and Technology of Welding and Joining* 17 (2):141-145. doi: 10.1179/1362171811Y.0000000083.

Jana, Saumyadeep, Yuri Hovanski, and Glenn J Grant. 2010. "Friction stir lap welding of magnesium alloy to steel: a preliminary investigation." *Metallurgical and Materials Transactions A* 41 (12):3173-3182.

Jeon, J, S Mironov, YS Sato, H Kokawa, SHC Park, and S Hirano. 2011. "Friction stir spot welding of single-crystal austenitic stainless steel." *Acta Materialia* 59 (20):7439-7449.

Ji, Shude, Yuxiao Wang, Jin Zhang, and Zhengwei Li. 2017. "Influence of rotating speed on microstructure and peel strength of friction spot welded 2024-T4 aluminum alloy." *The International Journal of Advanced Manufacturing Technology* 90 (1-4):717-723.

John, Chambers, William Cleveland, Beat Kleiner, and Paul Tukey. 1983. "Graphical methods for data analysis." *Wadsworth, Ohio*:128-129.

Kah, P, R Suoranta, and J Martikainen. 2013. "Advanced gas metal arc welding processes." *The International Journal of Advanced Manufacturing Technology* 67 (1-4):655-674.

Kamal, Haidar, Abdul Wahab, Abdulwahab Khuder, Muhammed M, and Muhammed. 2017. *Effects of Rotational Speeds and Tool Pin Geometry on Microstructure and Mechanical Properties of Refilled Friction Stir Spot Welds of Similar AA2024-T3 Aluminum Alloy Sheets*. Vol. Vol. 6.

Kang, Minjung, Cheolhee Kim, and Young-Min Kim. 2017. "Joining of AZ31 Magnesium Alloy and Steel Sheet under Four Different Coating Conditions Based on Gas Metal Arc Weld-Brazing." *Materials transactions* 58 (1):95-102.

Karthikeyan, R, and V Balasubramanian. 2010. "Predictions of the optimized friction stir spot welding process parameters for joining AA2024 aluminum alloy using RSM." *The International Journal of Advanced Manufacturing Technology* 51 (1-4):173-183.

Kasai, H, Y Morisada, and H Fujii. 2015. "Dissimilar FSW of immiscible materials: steel/magnesium." *Materials Science and Engineering: A* 624:250-255.

Katayama, Seiji. 2013. *Handbook of laser welding technologies*: Elsevier.

Katayama, Seiji, Yousuke Kawahito, and Masami Mizutani. 2012. "Recent Advances in Laser Welding." Laser and Tera-Hertz Science and Technology.

Kennard, Kirtis Frankland. 2015. "A Simple Method for Evaluating Wear in Different Grades of Tooling Applied to Friction Stir Spot Welding."

Khan, MI, ML Kuntz, P Su, A Gerlich, T North, and Y Zhou. 2007. "Resistance and friction stir spot welding of DP600: a comparative study." *Science and Technology of Welding and Joining* 12 (2):175-182.

Khan, Shehzad Saleem, Norbert Hort, Ingo Steinbach, and Siegfried Schmauder. 2008. "Castability of magnesium alloys." In *Magnesium Technology 2018*, edited by Wiley, 197-202. Minerals, Metals and Materials Society.

Khedkar, Pranay, Rohit Motagi, Paras Mahajan, and Gitansh Makwana. 2016. "A review on advance high strength steels." *International Journal of Current Engineering and Technology* (Special Issue 6):240-243.

Kiełbus, Andrzej, Tomasz Rzychoń, and R Cibis. 2006. "Microstructure of AM50 die casting magnesium alloy." *Journal of Achievements in Materials and Manufacturing Engineering* 18 (1-2):135.

Kim, Hyung Chul, and Timothy J Wallington. 2013. "Life-cycle energy and greenhouse gas emission benefits of lightweighting in automobiles: review and harmonization." *Environmental Science & Technology* 47 (12):6089-6097.

Kim, Young-Gon, In-Ju Kim, Ji-Sun Kim, and Jae-Hyun Park. 2014. "Mechanical Properties and Tool Life of Friction-Stir-Welded DP590 Using the Si3N4 Tool." *Materials Transactions* 55 (10):1557-1563.

Kimapong, Kittipong, and Takehiko Watanabe. 2005. "Effect of welding process parameters on mechanical property of FSW lap joint between Aluminum alloy and steel." *Materials Transactions* 46 (10):2211-2217.

Kinsey, B., and X. Wu. 2011. *Tailor Welded Blanks for Advanced Manufacturing*: Elsevier Science.

Kluz, Rafał, Andrzej Kubit, and Dawid Wydrzyński. 2017. "Analysis of structure and shear/peel strength of refill friction stir spot welded 7075-T6 aluminium alloy joints." *Advances in Science and Technology Research Journal* 11.

Koba, Masaki, Toshio Araki, Shoichi Nambu, Junya Inoue, and Toshihiko Koseki. 2012. "Bonding interface formation between Mg alloy and steel by liquid-phase bonding using the Ag interlayer." *Metallurgical and Materials Transactions A* 43 (2):592-597.

Kolba, Tom. 2016. "Experimental investigation of the weldability of aluminum alloys using friction spot welding." Master, Electrical Energy, systems and automation, Universiteit Gent.

Korchynsky, M, and H Stuart. 1970. "Symposium low alloy high strength steels." *Dusseldorf Metallurgy Companies*:17.

Kubit, Andrzej, Magdalena Bucior, Dawid Wydrzyński, Tomasz Trzepieciński, and Maciej Pytel. 2018. "Failure mechanisms of refill friction stir spot welded 7075-T6 aluminium alloy single-lap joints." *The International Journal of Advanced Manufacturing Technology* 94 (9-12):4479-4491.

Kubit, Andrzej, Dawid Wydrzynski, and Tomasz Trzepiecinski. 2018. "Refill friction stir spot welding of 7075-T6 aluminium alloy single-lap joints with polymer sealant interlayer." *Composite Structures* 201:389-397. doi: https://doi.org/10.1016/j.compstruct.2018.06.070.

Kulekci, Mustafa Kemal. 2008. "Magnesium and its alloys applications in automotive industry." *The International Journal of Advanced Manufacturing Technology* 39 (9-10):851-865.

Kumar, D Sameer, C Tara Sasanka, K Ravindra, and KNS Suman. 2015. "Magnesium and its alloys in automotive applications–a review." *American Journal of Materials Science and Technology* 4 (1):12-30.

Kumar, Nitesh, Anjani Kumar Singh, Ajit Kumar, and Sshil Patel. 2014. "High Strength Hot Rolled Steel Sheet for Automobile." *Journal of Mechanical and Civil Engineering* II (3):14.

Kuziak, R, Rudolf Kawalla, and Sebastian Waengler. 2008. "Advanced high strength steels for automotive industry." *Archives of Civil and Mechanical Engineering* 8 (2):103-117.

Lacki, P, A Derlatka, and T Gałaczyński. 2017. "Selection of basic position in Refill Friction Stir Spot Welding of 2024-T3 and D16UTW aluminum alloy sheets." *Archives of Metallurgy and Materials* 62 (1):443-449.

Lai, Wei-Jen, and Jwo Pan. 2014. "Stress intensity factor solutions for adhesive-bonded lap-shear specimens of magnesium and steel sheets with and without kinked cracks for

fatigue life estimations." *Engineering Fracture Mechanics* 131:454-470. doi: https://doi.org/10.1016/j.engfracmech.2014.09.002.

Lai, Wei-Jen, and Jwo Pan. 2015. "Failure mode and fatigue behavior of weld-bonded lap-shear specimens of magnesium and steel sheets." *International Journal of Fatigue* 75:184-197.

Lai, Wei-Jen, Jwo Pan, Zhili Feng, Michael Santella, and Tsung-Yu Pan. 2013. "Failure mode and fatigue behavior of ultrasonic spot welds with adhesive in lap-shear specimens of magnesium and steel sheets." *SAE International Journal of Materials and Manufacturing* 6 (2013-01-1020):279-285.

Lawson, Richard D., David K. Matlock, and George Krauss. 1980. "An etching technique for microalloyed dual-phase steels." *Metallography* 13 (1):71-87. doi: https://doi.org/10.1016/0026-0800(80)90023-3.

Lazarz, Kimberly, Robert C. McCune, Wenchao Wang, and P. K. Mallick. 2009. Effect of Surface Pretreatments on Adhesive Bonding and Corrosion Resistance of AM60B, AZ31-H24, and AM30 Magnesium. In *SAE Technical Paper 2009-01-0037*.

Li, W. Y., T. Fu, L. Hütsch, J. Hilgert, F. F. Wang, J. F. dos Santos, and N. Huber. 2014. "Effects of tool rotational and welding speed on microstructure and mechanical properties of bobbin-tool friction-stir welded Mg AZ31." *Materials & Design* 64:714-720. doi: https://doi.org/10.1016/j.matdes.2014.07.023.

Li, Wenya, Jinfeng Li, Zhihan Zhang, Dalu Gao, Weibing Wang, and Chunlin Dong. 2014. "Improving mechanical properties of pinless friction stir spot welded joints by eliminating hook defect." *Materials & Design (1980-2015)* 62:247-254. doi: https://doi.org/10.1016/j.matdes.2014.05.028.

Li, Zhengwei, Shude Ji, Yinan Ma, Peng Chai, Yumei Yue, and Shuangsheng Gao. 2016. "Fracture mechanism of refill friction stir spot-welded 2024-T4 aluminum alloy." *The International Journal of Advanced Manufacturing Technology* 86 (5-8):1925-1932.

Li, Zhengwei, Zhiwu Xu, Liguo Zhang, and Zhongjie Yan. 2017. "Friction spot welding of dissimilar 6063/5083 aluminium alloys." *Materials Science and Technology* 33 (14):1626-1634. doi: 10.1080/02670836.2017.1303563.

Lienert, T, T Siewert, S Babu, V Acoff, and Standard Welding Procedure Specifications. 2011. *ASM Handbook, Volume 6A: Welding Fundamentals and Processes*. Vol. 6: ASM International.

Liu, Huijie, J. C. Feng, H. Fujii, and K. Nogi. 2005. "Wear characteristics of a WC-Co tool in friction stir welding of AC4A+30 vol%SiCp composite." *International Journal of Machine Tools and Manufacture* 45 (14):1635-1639. doi: 10.1016/j.ijmachtools.2004.11.026.

Liu, L. 2010a. "The joining of magnesium alloy to steel." In *Welding and Joining of Magnesium Alloys*, 63-79e. Elsevier.

Liu, L, L Xiao, DL Chen, JC Feng, S Kim, and Y Zhou. 2013. "Microstructure and fatigue properties of Mg-to-steel dissimilar resistance spot welds." *Materials & Design* 45:336-342.

Liu, L, L Xiao, J Feng, L Li, S Esmaeili, and Y Zhou. 2011. "Bonding of immiscible Mg and Fe via a nanoscale Fe2Al5 transition layer." *Scripta Materialia* 65 (11):982-985.

Liu, L, L Xiao, JC Feng, YH Tian, SQ Zhou, and Y Zhou. 2010. "The mechanisms of resistance spot welding of magnesium to steel." *Metallurgical and Materials transactions A* 41 (10):2651-2661.

Liu, L. 2010b. "Adhesive bonding of magnesium alloys." In *Welding and Joining of Magnesium Alloys*, 149-159. Woodhead Publishing.

Liu, Lei, Guisheng Zou, Hiroaki Mori, Shahrzad Esmaeili, and Y Norman Zhou. 2016. "Nanostructure of immiscible Mg–Fe dissimilar weld without interfacial intermetallic transition layer." *Materials & Design* 92:445-449.

Liu, Liming, and Xiaodong Qi. 2010. "Strengthening effect of nickel and copper interlayers on hybrid laser-TIG welded joints between magnesium alloy and mild steel." *Materials & Design* 31 (8):3960-3963.

Liu, Liming, Daxin Ren, and Fei Liu. 2014. "A Review of Dissimilar Welding Techniques for Magnesium Alloys to Aluminum Alloys." *Materials* 7 (5):3735-3757. doi: 10.3390/ma7053735.

Liu, LM, and Xu Zhao. 2008. "Study on the weld joint of Mg alloy and steel by laser-GTA hybrid welding." *Materials Characterization* 59 (9):1279-1284.

Liyanage, T, S Abu-Zahra, AP Gerlich, M Yamamoto, and T Shibayanagi. 2014. "Friction stir spot welding of AM60 magnesium alloy to DP600 steel." 4th International Symposium on Aerospace Materials and Manufacturing Processes: Advances in Processing and Repair of Aerospace Materials 2008 Winnipeg, Manitoba, Canada, 24-27 August 2008.

Liyanage, T, J Kilbourne, AP Gerlich, and TH North. 2009. "Joint formation in dissimilar Al alloy/steel and Mg alloy/steel friction stir spot welds." *Science and Technology of Welding and Joining* 14 (6):500-508.

Logan, Stephen D, Joy H Forsmark, and Richard Osborne. 2016. Development and Demonstration of a Magnesium-Intensive Vehicle Front-End Substructure. United States Automotive Materials Partnership LLC, Southfield, MI (United States).

Louda, P. 2007. "Applications of thin coatings in automotive industry." *Journal of Achievements in Materials and Manufacturing Engineering* 24 (1):51-56.

Luo, Alan A. 2013. "Magnesium casting technology for structural applications." *Journal of Magnesium and Alloys* 1 (1):2-22.

MacKenzie, Donald, Stephen Zoepf, and John Heywood. 2014. "Determinants of US passenger car weight." *International Journal of Vehicle Design* 65 (1):73-93.

Manladan, SM, F Yusof, S Ramesh, Y Zhang, Z Luo, and Z Ling. 2017a. "Microstructure and mechanical properties of resistance spot welded in welding-brazing mode and resistance element welded magnesium alloy/austenitic stainless steel joints." *Journal of Materials Processing Technology* 250:45-54.

Manladan, SM, F Yusof, S Ramesh, Y Zhang, Z Luo, and Z Ling. 2017b. "Resistance Element Welding of Magnesium Alloy/austenitic Stainless Steel." Joining and Welding Symposium, Universiti Malaysia Pahang, Malaysia, 11 July 2017.

Manual, Minitab User. 2001. "Making data analysis easier." *MINITAB Inc., UsA.*

Manzie, Chris, Harry Watson, and Saman Halgamuge. 2007. "Fuel economy improvements for urban driving: Hybrid vs. intelligent vehicles." *Transportation Research Part C: Emerging Technologies* 15 (1):1-16.

Marder, AR. 2000. "The metallurgy of Zinc-coated steel." *Progress in Materials Science* 45 (3):191-271.

Martin, J P, C Stanhope, and S Gascoyne. 2011. "Novel Techniques for Corner Joints Using Friction Stir Welding." In *Friction Stir Welding and Processing VI*.

Mathews, P.G. 2005. *Design of Experiments with MINITAB*: ASQ Quality Press.

Matlock, David K, John G Speer, E De Moor, and Paul J Gibbs. 2012. "Recent developments in advanced high strength sheet steels for automotive applications: an overview." *Engineering Science and Technology, an International Journal* 15 (1):1-12.

Mead, R. 1990. *The Design of Experiments: Statistical Principles for Practical Applications*: Cambridge University Press.

Medina, GY, E Hurtado Delgado, AF Pérez, and H Lopez Ferreira. 2017. "Phases quantification in DP600 steel welded by GTAW process using SEM and atomic force microscopy." *Materials Research* 20 (5):1161-1165.

Meschut, G, O Hahn, V Janzen, and T Olfermann. 2014. "Innovative joining technologies for multi-material structures." *Welding in the World* 58 (1):65-75.

Meschut, G, V Janzen, and T Olfermann. 2014. "Innovative and highly productive joining technologies for multi-material lightweight car body structures." *Journal of Materials Engineering and Performance* 23 (5):1515-1523.

Mesquita, Rodrigo Marschner, Uceu Fuad Hasan Suhuddin, and Jorge Fernandez dos Santos. 2012. "Parameters Optimization for Friction Spot Welding of Aluminium 6082 by the Taguchi Method." *International Refeered Journal of Engineering and Science*.

Meyer, Lutz, Friedrich Heisterkamp, and Wolfgang Mueschenborn. 1975. "Columbium, Titanium, and Vanadium in normalized, thermo-mechanically treated and cold-rolled steels." Proceedings of an international symposium on HSLA steels, Microalloying, Washington D.C., 1-3 October.

Mezbahul-Islam, Mohammad, Ahmad Omar Mostafa, and Mamoun Medraj. 2014. "Essential magnesium alloys binary phase diagrams and their thermochemical data." *Journal of Materials* 2014:33. doi: http://dx.doi.org/10.1155/2014/704283.

Mileiko, ST. 1969. "The tensile strength and ductility of continuous fibre composites." *Journal of Materials Science* 4 (11):974-977.

Milton, B.E. 1995. *Thermodynamics, Combustion and Engines*: Chapman & Hall.

Min, Ding, Zhen Yong, and Lian Jie. 2016. "Dissimilar spot welding joints of AZ31-443 ferritic stainless steel with cover plate." *The International Journal of Advanced Manufacturing Technology* 85 (5-8):1539-1545.

Mishra, R. S., and Z. Y. Ma. 2005. "Friction stir welding and processing." *Materials Science and Engineering: R: Reports* 50 (1):1-78. doi: https://doi.org/10.1016/j.mser.2005.07.001.

Mishra, R.S., and M.W. Mahoney. 2007a. *Friction Stir Welding and Processing*: ASM International.

Mishra, Rajiv Sharan, Partha Sarathi De, and Nilesh Kumar. 2014. *Friction stir welding and processing: science and engineering*: Springer.

Mishra, RM, and MW Mahoney. 2007b. *Friction Stir Welding and Processing*: ASM International.

Miyamoto, Kenji, Shigeyuki Nakagawa, Shingo Iwatani, Shinji Hojo, Takahiro Tachibana, Tomo Ogura, Akio Hirose, and Kojiro Kobayashi. 2012. "Dissimilar Joining of Magnesium Alloy and Steel by Resistance Spot Welding." *Transactions of JWRI*:33-35.

Monas, Alexander, Oleg Shchyglo, Se-Jong Kim, Chang Dong Yim, Daniel Höche, and Ingo Steinbach. 2015. "Divorced Eutectic Solidification of Mg-Al Alloys." *Journal of The*

Minerals, Metals & Materials Society 67 (8):1805-1811. doi: 10.1007/s11837-015-1418-4.

Montag, Tobias, Jens-Peter Wulfsberg, Henry Hameister, and Rodrigo Marschner. 2014. "Influence of Tool Wear on Quality Criteria for Refill Friction Stir Spot Welding (RFSSW) Process." *Procedia CIRP* 24:108-113. doi: https://doi.org/10.1016/j.procir.2014.08.015.

Montgomery, D.C. 2010. *Design and Analysis of Experiments, Minitab Manual*: John Wiley & Sons.

Montgomery, Douglas C. 2017. *Design and analysis of experiments*: John Wiley & Sons.

Moore, David S, and Stephane Kirkland. 2007. *The basic practice of statistics*. Vol. 2: WH Freeman New York.

Moscovitch, N, D Eliezer, and E Aghion. 2005. "The effect of high pressure die casting process characteristics on the properties and performance of advanced MG alloys." *Magnesium Technology 2005*:357-363.

Muci-Küchler, Karim H, Sindhura Kalagara, and William J Arbegast. 2010. "Simulation of a refill friction stir spot welding process using a fully coupled thermo-mechanical FEM model." *Journal of Manufacturing Science and Engineering* 132 (1):014503.

Nakada, N, K Mizutani, T Tsuchiyama, and S Takaki. 2014. "Difference in transformation behavior between ferrite and austenite formations in medium manganese steel." *Acta Materialia* 65:251-258.

Nakata, K. 2009. "Friction stir lap welding of magnesium alloy and zinc-coated steel." *Materials Transactions* 50 (11):2598-2603.

Nakata, Kazuhiro, and Masao Ushio. 2002. "Needs and prospects of dissimilar metal joining and welding." *Journal of the Japan Welding Society*:71-6.

Nandan, R, T DebRoy, and HKDH Bhadeshia. 2008. "Recent advances in friction-stir welding–process, weldment structure and properties." *Progress in Materials Science* 53 (6):980-1023.

Nasiri, Ali M, Zhikang Shen, Jeff Shao Chun Hou, and Adrian P Gerlich. 2018. "Failure analysis of tool used in refill friction stir spot welding of Al 2099 alloy." *Engineering Failure Analysis* 84:25-33.

National Research Council. 2013. *Transitions to alternative vehicles and fuels*: National Academies Press.

Neumann, Tomasz. 2009. "Friction stir welding of Al 2024-T351 using a self-reacting bobbin tool." PhD, Hochschule Mainz.

Okamoto, K, F Hunt, and S Hirano. 2005a. Development of Friction Stir Welding Technique and Machine for Aluminum Sheet Metal Assembly-Friction Stir Welding of Aluminum for Automotive Applications (2). SAE Technical Paper 2005-01-1254.

Okamoto, K, F Hunt, and S Hirano. 2005b. Friction stir welding of magnesium for automotive applications. SAE Technical Paper 2005-01-0730.

Oliveira, PHF, ST Amancio-Filho, JF Dos Santos, and E Hage Jr. 2010. "Preliminary study on the feasibility of friction spot welding in PMMA." *Materials Letters* 64 (19):2098-2101.

Olson, D.L., T.A. Siewert, S. Liu, and G.R. Edwards. 1993. *ASM Handbook Volume 6: Welding, Brazing, and Soldering*. Vol. 6: ASM International.

Overbagh, William H. 1995. Use of Aluminum in Automotive Space Frames. SAE Technical Papaer 950721.

Ozgowicz, Wojciech, Agnieszka Kurc-Lisiecka, and Adam Grajcar. 2012. "Corrosion behaviour of cold-deformed austenitic alloys." In *Environmental and Industrial Corrosion-Practical and Theoretical Aspects*. InTech.

Ozturk, F, A Polat, S Toros, and RC Picu. 2013. "Strain hardening and strain rate sensitivity behaviors of advanced high strength steels." *Journal of Iron and Steel Research, International* 20 (6):68-74.

Pan, Dr Tsung-Yu, Teresa Franklin, Elliot Brown, and Michael L Santella. 2010. Ultrasonic Spot Welding of AZ31B to Galvanized Mild Steel. Oak Ridge National Lab.(ORNL), Oak Ridge, TN (United States).

Pan, Fu Sheng, Ming Bo Yang, Ding Fei Zhang, Ling Yun Wang, and Pei Dao Ding. 2005. "Research and development of wrought magnesium alloys in China." *Materials Science Forum* 488-489:413-418. doi: https://doi.org/10.4028/www.scientific.net/MSF.488-489.413.

Pan, T, WJ Schwartz, KA Lazarz, and ML Santella. 2006. "Spot Friction Weldbonding for Sheet Aluminum Joining." Proceedings of Sixth International Symposium on Friction Stir Welding, Paper.

Pan, Tsung-Yu. 2007. Friction Stir Spot Welding (FSSW) - A Literature Review SAE Technical Paper 2007-01-1702.

Pan, Tsung-Yu, Zhili Feng, Michael Santella, and Jian Chen. 2013. "Corrosion behavior of mixed-metal joint of magnesium to mild steel by ultrasonic spot welding with and without adhesives." *SAE International Journal of Materials and Manufacturing* 6 (2013-01-1017):271-278.

Pan, Tsung-Yu, Zhili Feng, Michael L Santella, and Jian Chen. 2014. "Corrosion of Ultrasonic Spot Weldbonds of Magnesium to Steel." In *Magnesium Technology 2014*, 491-496. Springer.

Pan, Tsung-Yu, and Michael Santella. 2012a. Corrosion behavior of mixed-metal joint of magnesium to mild steel by ultrasonic spot welding. SAE Technical Paper 2012-01-0472.

Pan, Tsung-Yu, and Michael Santella. 2012b. Ultrasonic spot welding of galvanized mild steel to magnesium AZ31B. SAE Technical Paper 2012-01-0474.

Pan, Tsung-Yu, and Michael L Santella. 2012c. "Corrosion of Ultrasonic Spot Welded Joints of Magnesium to Steel." In *Magnesium Technology 2012*, 265-269. Springer.

Parra, Bruno, Vinícius Toledo Saccon, Nelson Guedes de Alcântara, Tonilson Rosendo, and Jorge Fernandes dos Santos. 2011. "An investigation on friction spot welding in AA6181-T4 alloy." *Tecnologia em Metalurgia, Materiais e Mineração* 8 (3):184.

Pasha, Aleem, Ravinder Reddy, P Laxminarayana, and Ishtiaq Ahmad Khan. 2014. "Influence of Process and Tool Parameters on Friction Stir Welding - Overview." *International Journal of Applied Engineering and Technology* 4 (3):54-69.

Patel, V. K., S. D. Bhole, and D. L. Chen. 2013. "Formation of zinc interlayer texture during dissimilar ultrasonic spot welding of magnesium and high strength low alloy steel." *Materials & Design* 45:236-240. doi: https://doi.org/10.1016/j.matdes.2012.09.018.

Patel, VK, DL Chen, and SD Bhole. 2014. "Dissimilar ultrasonic spot welding of Mg-Al and Mg-high strength low alloy steel." *Theoretical and Applied Mechanics Letters* 4 (4).

Peer, Andrea J, and Jacob J. Rindler. 2015. Coldwater Machine Company.

Pieta, G, J dos Santos, TR Strohaecker, and T Clarke. 2014. "Optimization of friction spot welding process parameters for AA2198-T8 sheets." *Materials and Manufacturing Processes* 29 (8):934-940.

Plaine, A. H., A. R. Gonzalez, U. F. H. Suhuddin, J. F. dos Santos, and N. G. Alcântara. 2015. "The optimization of friction spot welding process parameters in AA6181-T4 and Ti6Al4V dissimilar joints." *Materials & Design* 83:36-41. doi: https://doi.org/10.1016/j.matdes.2015.05.082.

Plaine, AH, AR Gonzalez, UFH Suhuddin, JF dos Santos, and NG Alcântara. 2016. "Process parameter optimization in friction spot welding of AA5754 and Ti6Al4V dissimilar joints using response surface methodology." *The International Journal of Advanced Manufacturing Technology* 85 (5-8):1575-1583.

Plaine, AH, UFH Suhuddin, CRM Afonso, NG Alcântara, and JF dos Santos. 2016. "Interface formation and properties of friction spot welded joints of AA5754 and Ti6Al4V alloys." *Materials & Design* 93:224-231.

Plaine, AH, UFH Suhuddin, NG Alcântara, and JF dos Santos. 2016. "Fatigue behavior of friction spot welds in lap shear specimens of AA5754 and Ti6Al4V alloys." *International Journal of Fatigue* 91:149-157.

Pleanjai, Somporn, Shabbir H Gheewala, and Savitri Garivait. 2007. "Environmental evaluation of biodiesel production from palm oil in a life cycle perspective." *Asian J. Energy Environ* 8 (1):15-32.

Potzies, Carsten, and Karl Ulrich Kainer. 2004. "Fatigue of magnesium alloys." *Advanced Engineering Materials* 6 (5):281-289.

Prakash, S John, and S Muthukumaran. 2011. "Refilling probe hole of friction spot joints by friction forming." *Materials and Manufacturing Processes* 26 (12):1539-1545.

Prém, László, Zoltán Bézi, and András Balogh. 2017. "Development of complex spot welding technologies for automotive DP steels with FEM support." In *Vehicle and Automotive Engineering*, 407-423. Springer.

Qi, Xiaodong, and Gang Song. 2010. "Interfacial structure of the joints between magnesium alloy and mild steel with nickel as interlayer by hybrid laser-TIG welding." *Materials & Design* 31 (1):605-609.

Qiao, Fengbin, Kai Cheng, Lianfeng Wang, and Lijie Guo. 2016. "An experimental investigation on the dissimilar joining of AA6061 and 1Cr18Ni9Ti by refill friction stir spot welding and its mechanical properties." *Proceedings of the Institution of Mechanical Engineers, Part B: Journal of Engineering Manufacture* 230 (4):779-785.

Rana, Radhakanta, and Shiv Brat Singh. 2016. *Automotive Steels: Design, Metallurgy, Processing and Applications*: Woodhead Publishing.

Reimann, Martin, Thomas Gartner, Uceu Suhuddin, Jannik Göbel, and Jorge F dos Santos. 2016. "Keyhole closure using friction spot welding in aluminum alloy 6061–T6." *Journal of Materials Processing Technology* 237:12-18.

Reimann, Martin, Jannik Goebel, Thomas M Gartner, and Jorge F dos Santos. 2017. "Refilling termination hole in AA 2198–T851 by refill friction stir spot welding." *Journal of Materials Processing Technology* 245:157-166.

Ren, Daxin, and Liming Liu. 2014. "Interface microstructure and mechanical properties of arc spot welding Mg–steel dissimilar joint with Cu interlayer." *Materials & Design* 59:369-376.

Rosendo, T, B Parra, MAD Tier, AAM Da Silva, JF Dos Santos, TR Strohaecker, and NG Alcântara. 2011. "Mechanical and microstructural investigation of friction spot welded AA6181-T4 aluminium alloy." *Materials & Design* 32 (3):1094-1100.

Rosendo, T, M Tier, J Mazzaferro, C Mazzaferro, TR Strohaecker, and JF Dos Santos. 2015. "Mechanical performance of AA6181 refill friction spot welds under Lap shear tensile loading." *Fatigue & Fracture of Engineering Materials & Structures* 38 (12):1443-1455.

Rosendo, Tonilson de Souza. 2009. "Estudo do desempenho mecânico de solda (s) ponto por fricção (FSpW) da liga AA6181-T4." Doctor, Departamento de Metalurgia, Escola de Engenharia UFRGS.

Ryan, Barbara F, Brian L Joiner, and Jonathan D Cryer. 2012. *MINITAB Handbook: Update for Release*: Cengage Learning.

Ryan, T.P. 2007. *Modern Experimental Design*: Wiley.

SAE. 2007. Welding, Resistance: Spot and Seam. United States of America: SAE International.

Sajed, Moosa. 2016. "Parametric study of two-stage refilled friction stir spot welding." *Journal of Manufacturing Processes* 24:307-317.

Santana, LM, UFH Suhuddin, MH Ölscher, TR Strohaecker, and JF dos Santos. 2017. "Process optimization and microstructure analysis in refill friction stir spot welding of 3-mm-thick Al-Mg-Si aluminum alloy." *The International Journal of Advanced Manufacturing Technology* 92 (9-12):4213-4220.

Santella, M, E Brown, M Pozuelo, TY Pan, and JM Yang. 2012. "Details of Mg–Zn reactions in AZ31 to galvanised mild steel ultrasonic spot welds." *Science and Technology of Welding and Joining* 17 (3):219-224.

Santos, Jorge Fernandez dos, and Sergio de Traglia Amancio Filho. 2013. Method for joining metal and plastic workpieces edited by European Patents. Washington, USA: U.S. Patent and Trademark Office.

Santos, Telmo G, Pedro VilaCca, Luisa Quintino, Jorge Dos Santos, and Rosa M Miranda. 2011. "Application of eddy current techniques to inspect friction spot welds in aluminium alloy AA2024 and a composite material." *Welding in the World* 55 (9-10):12-18.

Schilling, Christoph, and Jorge dos Santos. 2004. Method and device for joining at least two adjoining work pieces by friction welding. Washington, U.S.A: U.S. Patent and Trademark Office.

Schneider, Christof, Thomas Weinberger, J Inoue, Toshihiko Koseki, and Norbert Enzinger. 2011. "Characterisation of interface of steel/magnesium FSW." *Science and Technology of Welding and Joining* 16 (1):100-107.

Schubert, E, M Klassen, I Zerner, C Walz, and G Sepold. 2001. "Light-weight structures produced by laser beam joining for future applications in automobile and aerospace industry." *Journal of Materials Processing Technology* 115 (1):2-8.

Schwartz, Mel. 2010. *Innovations in materials manufacturing, fabrication, and environmental safety*: CRC Press.

Selvi, S, A Vishvaksenan, and E Rajasekar. 2017. "Cold metal transfer (CMT) technology-An overview." *Defence Technology* 14 (1):28-44.

Seo, Eun Jung, Lawrence Cho, and Bruno Charles De Cooman. 2014. "Application of quenching and partitioning (Q&P) processing to press hardening steel." *Metallurgical and Materials Transactions A* 45 (9):4022-4037.

Sewell, NT, JCS Wright, JR Wright, and TD Mottram. 2015. "Automated non-linear acoustic NDT of Friction Stir Welds."

Shah, LH, and M Ishak. 2014. "Review of research progress on aluminum–steel dissimilar welding." *Materials and Manufacturing Processes* 29 (8):928-933.

Shah, LH, NH Othman, and Adrian Gerlich. 2018. "Review of research progress on aluminium–magnesium dissimilar friction stir welding." *Science and Technology of Welding and Joining* 23 (3):256-270.

Shashikala, AR, R Umarani, SM Mayanna, and AK Sharma. 2008. "Chemical conversion coatings on magnesium alloys—a comparative study." *Int J Electrochem Sci* 3:993-1004.

Shaw, Jody, and Richard Roth. 2002. Achieving An Affordable Low Emission Steel Vehicle; An Economic Assessment of the ULSAB-AVC Program Design. SAE Technical Paper 2002-01-0036.

Shen, Junjun, Sara B. M. Lage, Uceu F. H. Suhuddin, Claudemiro Bolfarini, and Jorge F. dos Santos. 2018. "Texture Development and Material Flow Behavior During Refill Friction Stir Spot Welding of AlMgSc." *Metallurgical and Materials Transactions A* 49 (1):241-254. doi: 10.1007/s11661-017-4381-6.

Shen, Junjun, Uceu FH Suhuddin, Maria EB Cardillo, and Jorge F dos Santos. 2014. "Eutectic structures in friction spot welding joint of aluminum alloy to copper." *Applied Physics Letters* 104 (19):191901.

Shen, Z, Y Chen, JSC Hou, X Yang, and AP Gerlich. 2015. "Influence of processing parameters on microstructure and mechanical performance of refill friction stir spot welded 7075-T6 aluminium alloy." *Science and Technology of Welding and Joining* 20 (1):48-57.

Shen, Z, Y Ding, J Chen, and AP Gerlich. 2016. "Comparison of fatigue behavior in Mg/Mg similar and Mg/steel dissimilar refill friction stir spot welds." *International Journal of Fatigue* 92:78-86.

Shen, Z, J Hou, K Chan, N Scotchmer, N Zhou, and AP Gerlich. 2016. "Spot welding aluminum 6022-T4 to galvanized DP600 sheet by refill friction stir spot welding." SWMC XVII conference.

Shen, Z., J. Chen, Y. Ding, J. Hou, B. Shalchi Amirkhiz, K. Chan, and A. P. Gerlich. 2018. "Role of interfacial reaction on the mechanical performance of Al/steel dissimilar refill friction stir spot welds." *Science and Technology of Welding and Joining* 23 (6):462-477. doi: 10.1080/13621718.2017.1414022.

Shen, Z., Y. Ding, O. Gopkalo, B. Diak, and A. P. Gerlich. 2018. "Effects of tool design on the microstructure and mechanical properties of refill friction stir spot welding of dissimilar Al alloys." *Journal of Materials Processing Technology* 252:751-759. doi: https://doi.org/10.1016/j.jmatprotec.2017.10.034.

Shen, Zhikang, Xinqi Yang, Shuo Yang, Zhaohua Zhang, and Yuhuan Yin. 2014. "Microstructure and mechanical properties of friction spot welded 6061-T4 aluminum alloy." *Materials & Design* 54:766-778. doi: https://doi.org/10.1016/j.matdes.2013.08.021.

Shen, Zhikang, Xinqi Yang, Zhaohua Zhang, Lei Cui, and Tielong Li. 2013. "Microstructure and failure mechanisms of refill friction stir spot welded 7075-T6 aluminum alloy

joints." *Materials & Design* 44:476-486. doi: https://doi.org/10.1016/j.matdes.2012.08.026.

Shi, Yao, Yumei Yue, Liguo Zhang, Shude Ji, and Yue Wang. 2017. "Refill Friction Stir Spot Welding of 2198-T8 Aluminum Alloy." *Transactions of the Indian Institute of Metals*:1-7.

Shibli, S. M. A., B. N. Meena, and R. Remya. 2015. "A review on recent approaches in the field of hot dip zinc galvanizing process." *Surface and Coatings Technology* 262:210-215. doi: https://doi.org/10.1016/j.surfcoat.2014.12.054.

Shome, Mahadev, and Muralidhar Tumuluru. 2015. *Welding and Other Joining Technologies (AHSS), Welding and Joining of Advanced High Strength Steels (AHSS)*: Woodhead Publishing.

Shuangming, Du, Gao Yang, and Hu Jie. 2016. "Transient Liquid Phase Bonding of Magnesium Alloy AZ31B and 304 Stainless Steel." *Rare Metal Materials and Engineering* 45 (8):2064-2070.

Sierens, Arne, Jasmien Vanvooren, K Deplus, Koen Faes, and Wim De Waele. 2014. "Review on the possible tool materials for friction stir welding of steel plates." Sustainable Construction and Design (SCAD-2013).

Silva, Lucas Filipe Martins da, Fernando Jorge Lino Alves, and António Torres Marques. 2013. *Materiais de Construção*: Pubindústria.

Sinha, VC, S Kundu, and S Chatterjee. 2016. "Microstructure and mechanical properties of similar and dissimilar joints of aluminium alloy and pure copper by friction stir welding." *Perspectives in Science* 8:543-546.

Skszek, Tim, Jeff Conklin, Matt Zaluzec, and David Wagner. 2014. Multi-Material Lightweight Vehicles: Mach-II Design. Vehma International & Ford Motor.

Smith, W. J., and F. E. Goodwin. 2010. "4.06 - Hot Dipped Coatings A2 - Cottis, Bob." In *Shreir's Corrosion*, edited by Michael Graham, Robert Lindsay, Stuart Lyon, Tony Richardson, David Scantlebury and Howard Stott, 2556-2576. Oxford: Elsevier.

Snow, Jonathan. 2011. *The complete research suite: a step-by-step guide to using Qualtrics*.

Song, Gang, Taotao Li, Zhaodong Zhang, and Liming Liu. 2017. "Investigation of unequal thickness Mg/steel butt-welded plate by hybrid laser-tungsten inert gas welding with a Ni interlayer." *Journal of Manufacturing Processes* 30:299-302.

Song, Gang, Jingwei Yu, Taotao Li, Jifeng Wang, and Liming Liu. 2018. "Effect of laser-GTAW hybrid welding heat input on the performance of Mg/Steel butt joint." *Journal of Manufacturing Processes* 31:131-138.

Southwick, PD, PH Chang, AG Preban, and RW Thompson. 1985. "Development of high strength steels on Inland's No. 3 continuous annealing line (Cal)." The Metallurgical Society Paper Selection, Detroit, USA, 16-20 Septermber.

Sovacool, Benjamin K., and Richard F. Hirsh. 2009. "Beyond batteries: An examination of the benefits and barriers to plug-in hybrid electric vehicles (PHEVs) and a vehicle-to-grid (V2G) transition." *Energy Policy* 37 (3):1095-1103. doi: https://doi.org/10.1016/j.enpol.2008.10.005.

Sprovieri, John. 2016. "Friction Stir Spot Welding." accessed 29/07/2018. https://www.assemblymag.com/articles/93337-friction-stir-spot-welding.

Struers. 2015. "Abrasive Wet Cutting." accessed 13/02/2018. https://www.struers.com/en/Knowledge/Cutting#cutting-about.

Styczynski, A, Ch Hartig, J Bohlen, and D Letzig. 2004. "Cold rolling textures in AZ31 wrought magnesium alloy." *Scripta Materialia* 50 (7):943-947.

Suhuddin, U., L. Campanelli, M. Bissolatti, H. Wang, R. Verastegui, and J. F. dos Santos. 2013. "A review on microstructural and mechanical properties of friction spot welds in Al-based similar and dissimilar joints." In *Proceedings of the 1st International Joint Symposium on Joining and Welding*, edited by Hidetoshi Fujii, 15-21. Woodhead Publishing.

Suhuddin, U. F. H., V. Fischer, and J. F. dos Santos. 2013a. "The thermal cycle during the dissimilar friction spot welding of aluminum and magnesium alloy." *Scripta Materialia* 68 (1):87-90. doi: https://doi.org/10.1016/j.scriptamat.2012.09.008.

Suhuddin, U., V. Fischer, F. Kroeff, and J. F. dos Santos. 2014. "Microstructure and mechanical properties of friction spot welds of dissimilar AA5754 Al and AZ31 Mg alloys." *Materials Science and Engineering: A* 590:384-389. doi: https://doi.org/10.1016/j.msea.2013.10.057.

Suhuddin, Uceu, Vanessa Fischer, and Jorge F dos Santos. 2013b. "Microstructure in Dissimilar Friction Spot Weld of Al to Mg Alloys Observed by Stop-Action Technique." In *Friction Stir Welding and Processing VII*, 263-270. Springer.

Suhuddin, UFH, V Fischer, A Kostka, and JF dos Santos. 2017. "Microstructure evolution in refill friction stir spot weld of a dissimilar Al–Mg alloy to Zn-coated steel." *Science and Technology of Welding and Joining* 22 (8):658-665.

Sun, YF, H Fujii, N Takaki, and Y Okitsu. 2011. "Novel spot friction stir welding of 6061 and 5052 Al alloys." *Science and Technology of Welding and Joining* 16 (7):605-612.

Swarnkar, Ashish, Rahul Kumar, Atul Suri, and Ankit Saha. 2016. "A review on Friction Stir Welding: An environment friendly welding technique." Humanitarian Technology Conference (R10-HTC), 2016 IEEE Region 10.

Tamarelli, CM. 2011. "AHSS 101: the evolving use of advanced high strength steels for automotive applications." *AUTOSTEEL (e-book available from http://www. autosteel. org/en/sitecore/content/Global/Document% 20Types/News/2012/~/media/Files/Autosteel/Research/AHSS/AHSS% 20101% 20-% 20The% 20Evolving% 20Use% 20of% 20Advanced% 20High-Strength% 20Steels% 20for% 20Automotive% 20Applications% 20-% 20lr. ashx).*

Tan, Caiwang, Liqun Li, Yanbin Chen, and Wei Guo. 2013. "Laser-tungsten inert gas hybrid welding of dissimilar metals AZ31B Mg alloys to Zn coated steel." *Materials & Design* 49:766-773.

Tasan, Cemal Cem, Martin Diehl, Dingshun Yan, Marion Bechtold, Franz Roters, Lars Schemmann, Chengwu Zheng, Nicola Peranio, Dirk Ponge, and Motomichi Koyama. 2015. "An overview of dual-phase steels: advances in microstructure-oriented processing and micromechanically guided design." *Annual Review of Materials Research* 45:391-431.

Teker, T. 2013. "Effect of synergic controlled pulsed and manual gas metal ARC welding processes on mechanical and metallurgical properties of AISI 430 ferritic stainless steel." *Archives of Metallurgy and Materials* 58 (4):1029-1035.

Ten Broek, Cees, Harry Singh, and Martin Hillebrecht. 2012. "Lightweight design for the future steel vehicle." *ATZ Worldwide* 114 (5):4-11. doi: 10.1007/s38311-012-0203-z.

Thorpe, Michael D., and Henrik Adam. 2002. ULSAB-AVC - Overview and Design. SAE Technical Paper 2002-01-0036.

Tier, MD, JF dos Santos, CW Olea, T Rosendo, CP Mazzaferro, JAE Mazzaferro, TR Strohaecker, AAM da Silva, and J-T Isakovic. 2008. The influence of weld microstructure on mechanical properties of alclad AA2024-T3 friction spot welded. SAE Technical Paper.

Tier, MD, TS Rosendo, JF dos Santos, N Huber, JA Mazzaferro, CP Mazzaferro, and TR Strohaecker. 2013. "The influence of refill FSSW parameters on the microstructure and shear strength of 5042 aluminium welds." *Journal of Materials Processing Technology* 213 (6):997-1005.

Tier, MD, TS Rosendo, JA Mazzaferro, CP Mazzaferro, JF dos Santos, and TR Strohaecker. 2017. "The weld interface for friction spot welded 5052 aluminium alloy." *The International Journal of Advanced Manufacturing Technology* 90 (1-4):267-276.

Toyota Canada Inc. 2016. *Unibody vs Body on frame*. Youtube: Toyota Canada Inc.

Tozaki, Y, Y Uematsu, and K Tokaji. 2010. "A newly developed tool without probe for friction stir spot welding and its performance." *Journal of Materials Processing Technology* 210 (6-7):844-851.

Tweedy, B, CA Widener, and DA Burford. 2007. "The effect of surface treatments on the faying surface of friction stir spot welds." *Friction Stir Welding and Processing IV, RS Mishra, MW Mahoney, TJ Lienert, & KV Jata, The Minerals, Metals & Materials Society (TMS), ISBN*:978-0.

TWI. 2017. Joint Industry Project Outline - Refill Friction Stir Spot Welding for Aerospace Applications. edited by The Welding Institute.

Uchihara, Masato. 2011. "Joining technologies for automotive steel sheets." *Welding International* 25 (04):249-259.

Uddeholm. 2011. Uddeholm Hotvar. edited by Uddeholm.

Uematsu, Y, K Tokaji, Y Tozaki, T Kurita, and S Murata. 2008. "Effect of re-filling probe hole on tensile failure and fatigue behaviour of friction stir spot welded joints in Al–Mg–Si alloy." *International Journal of Fatigue* 30 (10-11):1956-1966.

Upadhyay, Vinod, Zachary Bergseth, Brett Kelly, and Dante Battocchi. 2017. "Silica-based sol-gel coating on magnesium alloy with green inhibitors." *Coatings* 7 (7):86.

Vacchi, G. S., A. H. Plaine, R. Silva, V. L. Sordi, U. F. H. Suhuddin, N. G. Alcântara, S. E. Kuri, and C. A. D. Rovere. 2017. "Effect of friction spot welding (FSpW) on the surface corrosion behavior of overlapping AA6181-T4/Ti-6Al-4V joints." *Materials & Design* 131:127-134. doi: https://doi.org/10.1016/j.matdes.2017.06.005.

Venukumar, S, S Yalagi, and S Muthukumaran. 2013. "Comparison of microstructure and mechanical properties of conventional and refilled friction stir spot welds in AA 6061-T6 using filler plate." *Transactions of Nonferrous Metals Society of China* 23 (10):2833-2842.

Verastegui, Roger Navarro, José Antonio Esmerio Mazzaferro, Cíntia Cristiane Petry Mazzaferro, Telmo Roberto Strohaecker, and Jorge Fernandez Dos Santos. 2014. "Welding of Aluminum to DP600 Steel Plates by Refill Friction Stir Spot Welding Process (Refill FSSW): Preliminary Results." *Advanced Materials Research* 1082.

Vogt, W.P., and R.B. Johnson. 2015. *The SAGE Dictionary of Statistics & Methodology: A Nontechnical Guide for the Social Sciences*. 5 ed: SAGE Publications.

Wan, Long, and Yongxian Huang. 2017. "Microstructure and Mechanical Properties of Al/Steel Friction Stir Lap Weld." *Metals* 7 (12):542.

Wang, Lei, Qi Qiao, Yang Liu, and Xiu Song. 2013. "Formability of AZ31 Mg alloy sheets within medium temperatures." *Journal of Magnesium and Alloys* 1 (4):312-317.

Wang, Peisheng, Jingrui Zhao, Yong Du, Honghui Xu, Tie Gang, Jicai Fen, Lijun Zhang, Cuiyun He, Shuhong Liu, and Hongwu Ouyang. 2011. "Experimental investigation and thermodynamic calculation of the Fe–Mg–Mn and Fe–Mg–Ni systems." *International Journal of Materials Research* 102 (1):6-16.

Wang, Pengfei, Xizhang Chen, Qiuhong Pan, Bruce Madigan, and Jiangqi Long. 2016. "Laser welding dissimilar materials of aluminum to steel: an overview." *The International Journal of Advanced Manufacturing Technology* 87 (9-12):3081-3090.

Wang, R.M., A Eliezer, and E. M. Gutman. 2003. "An investigation on the microstructure of an AM50 magnesium alloy." *Materials Science and Engineering* 355 (1-2):201-207. doi: https://doi.org/10.1016/S0921-5093(03)00065-0.

Wang, Xi Jing, Yu Lian Wu, Zhong Ke Zhang, Ting Kai Guo, Yong Xin Lu, and Ji Peng Shi. 2013. "The Study of the Microstructure and Mechanical Properties of Friction Stir Spot Welding Joint between AZ31B Magnesium Alloy and Steel." *Advanced Materials Research* 668:818-822.

Wang, Xi Jing, Chang Qing Zhang, Bo Qiang Li, and Tian Li. 2011. "A preliminary investigation on friction stir spot welding of steel/Mg." *Applied Mechanics and Materials* 84.85:529-533. doi:

https://doi.org/10.4028/www.scientific.net/AMM.84-85.529.

Wang, Xiao-yong, Da-qian Sun, Shi-qiang Yin, and Dong-yang Liu. 2015. "Microstructures and mechanical properties of metal inert-gas arc welded Mg–steel dissimilar joints." *Transactions of Nonferrous Metals Society of China* 25 (8):2533-2542.

Wang, Xijing, Gang Zhao, Zhongke Zhang, and Peichung Wang. 2012. "Process research on friction stir spot welding without key hole between magnesium and steel dissimilar alloys." *Hot Working Technol* 41 (17):153-155.

Wang, XJ, WH Li, and G Zhao. 2014. "Connection mechanism research on friction stir spot welding without keyhole between magnesium and steel dissimilar alloys." *Materials Research Innovations* 18 (sup2):S2-1063-S2-1066.

Wang, XY, DQ Sun, and Y Sun. 2016. "Influence of Cu-interlayer thickness on microstructures and mechanical properties of MIG-welded Mg-steel joints." *Journal of Materials Engineering and Performance* 25 (3):910-920.

Watanabe, Takehiko, Kazuhiko Kagiya, Atushi Yanagisawa, and Hiroshi Tanabe. 2006. "Solid state welding of steel and magnesium alloy using a rotating pin." *Quarterly Journal of The Japan Welding Society* 24 (1):108-115.

Wei, Yanni, Jinglong Li, Jiangtao Xiong, Fu Huang, and Fusheng Zhang. 2012. "Microstructures and mechanical properties of magnesium alloy and stainless steel weld-joint made by friction stir lap welding." *Materials & design* 33:111-114.

WordAutoSteel. 2009. "Facing the Challenge for Crash Safety." accessed 26/03/2018. https://www.worldautosteel.org/why-steel/safety/facing-the-challenge-for-crash-safety/.

Xin, Qianfan. 2013. "3 - Optimization techniques in diesel engine system design." In *Diesel Engine System Design*, edited by Qianfan Xin, 203-296. Woodhead Publishing.

Xu, L, YY Cui, YL Hao, and R Yang. 2006. "Growth of intermetallic layer in multi-laminated Ti/Al diffusion couples." *Materials Science and Engineering: A* 435:638-647.

Xu, W., D. L. Chen, L. Liu, H. Mori, and Y. Zhou. 2012. "Microstructure and mechanical properties of weld-bonded and resistance spot welded magnesium-to-steel dissimilar joints." *Materials Science and Engineering: A* 537:11-24. doi: https://doi.org/10.1016/j.msea.2011.12.096.

Yang, XW, T Fu, and WY Li. 2014. "Friction stir spot welding: a review on joint macro-and microstructure, property, and process modelling." *Advances in Materials Science and Engineering* 2014.

Yao, Zong Xiang, De Ping Jiang, Chao Pan, and Xiao Ming Wang. 2012. "Analysis about the jointing status for dissimilar metals of steel with magnesium." *Applied Mechanics and Materials* 233:374-379. doi:

https://doi.org/10.4028/www.scientific.net/AMM.233.374.

Yuan, Xin-jian, Guang-min Sheng, LUO Jun, and LI Jia. 2013. "Microstructural characteristics of joint region during diffusion-brazing of magnesium alloy and stainless steel using pure copper interlayer." *Transactions of Nonferrous Metals Society of China* 23 (3):599-604.

Yue, Yumei, Yao Shi, Shude Ji, Yue Wang, and Zhengwei Li. 2017. "Effect of Sleeve Plunge Depth on Microstructure and Mechanical Properties of Refill Friction Stir Spot Welding of 2198 Aluminum Alloy." *Journal of Materials Engineering and Performance* 26 (10):5064-5071.

Zeng, Zhi, Xunbo Li, Yugang Miao, Gang Wu, and Zijun Zhao. 2011. "Numerical and experiment analysis of residual stress on magnesium alloy and steel butt joint by hybrid laser-TIG welding." *Computational Materials Science* 50 (5):1763-1769. doi: https://doi.org/10.1016/j.commatsci.2011.01.011.

Zhang, YN, X Cao, S Larose, and P Wanjara. 2012. "Review of tools for friction stir welding and processing." *Canadian Metallurgical Quarterly* 51 (3):250-261.

Zhang, Yuankun, and Shichao Ding. 2013. "Parametric study on chain-die forming for advanced high strength steels." *International Journal of Materials and Product Technology 15* 47 (1-4):138-149.

Zhang, Zhong-ke, Xi-jing Wang, Pei-chung Wang, and ZHAO Gang. 2014. "Friction stir keyholeless spot welding of AZ31 Mg alloy-mild steel." *Transactions of Nonferrous Metals Society of China* 24 (6):1709-1716.

Zhao, J., and Z. Jiang. 2017. *Rolling of Advanced High Strength Steels: Theory, Simulation and Practice*: CRC Press, Taylor & Francis Group.

Zhao, YQ, HJ Liu, SX Chen, Z Lin, and JC Hou. 2014. "Effects of sleeve plunge depth on microstructures and mechanical properties of friction spot welded alclad 7B04-T74 aluminum alloy." *Materials & Design (1980-2015)* 62:40-46.

Zheng, WC, Shuang-shou Li, Bin Tang, and DB Zeng. 2006. "Microstructure and properties of Mg-Al binary alloys." *China Foundry* 3 (4):270-274.

Zhou, L, D Liu, K Nakata, T Tsumura, H Fujii, K Ikeuchi, Y Michishita, Y Fujiya, and M Morimoto. 2012. "New technique of self-refilling friction stir welding to repair keyhole." *Science and Technology of Welding and Joining* 17 (8):649-655.

Zuidema, Blake K., Stephen G. Denner, Bernhard Engl, and Jan-Olof Sperle. 2001. New High Strength Steels Applied to the Body Structure of ULSAB-AVC. SAE Technical Paper 2001-01-3042.

Annex A Summary of steel automobile body-frames

Table 1- Main automobile chassis types, designations, advantages and disadvantages (Happian-Smith 2001), (Giancarlo and Lorenzo 2009), (Crolla 2009).

Chassis Type	Description	Applications	Advantages	Disadvantages
Full-Frame chassis or Conventional Frame or Body on Frame (BoF)	Independent frame and body Body and chassis part bolted to the frame (by mounting brackets) Ladder/grillage, Perimeter and X frames types (bolted and riveted elements)	Industrial vehicles, large trucks and SUV's	Simpler design (2D element) Enhanced off road performance - best suspension tuning (suspension in series with body mounts) Easy and cheaper body aesthetics update (without structural changes) and repair	Poor torsion resistance Higher overall height (floor pan above the frame, and not integrated)
Backbone Tube or Central tunnel	Tubular backbone (usually a box section) Connects the front and rear axle (drivetrain, the engine and the suspensions) Provides nearly all the mechanical strength.	Strong enough for small sports cars,	Very simple chassis construction	Not suitable for high performance sports cars Does not provide any protection against side impact and off-set crash
Unibody on frame, partial frame or semi-integral frame	Sub-frames assemblies are used at the front and rear section while the unibody supports the middle area	Small Pickups	Easy sub-frames replacement in case of extensive damage Noise and vibration of the powertrain isolation	Difficult alignment between the front and rear sub-chassis
Unibody, unit body, unitized body, semi-*monocoque* or integral frame	Combination of rails (compressive structure), sheet steel pressings and panels (tensile stressed skin) joined mainly by spot welding Body with aesthetic and structural functions	Conventional cars, vans, crossovers	High structural stiffness, space efficiency and easy access Applicable for mass production Weight reduction Enhanced handling and balance (low floorpan with lower CG)	Complex design (only by FEA) Difficult to repair Not strong nor light enough for sport cars Not compatible for small-volume production
Tubular Space frame, roll cage, or *superleggera*	3D tubular load-bearing chassis cage (fully triangulated planes)	Luxury cars and high-end sports cars	Good stiffness/weight ratio Isotropic load-bearing behavior of the whole structure	Complex, costly and time consuming assembly Incompatible for mass production Difficult access to the cabin due to high door sills

Annex B Summary of Advanced High Strength Steels

Table 1- Automotive industry main classification of conventional steels (Schwartz 2010), (Baker, Parker, and Daniel 2002), (Ghosh and Ghosh 2009).

Classification	Grade	Description
Mild Steel Single phase ferrite steel Main strengthening mechanism: - Basic solid-solution of Carbon	Interstitial –Free (IF) or Ultra Low Carbon (ULC)	Ultra low carbon (C) and Nitrogen (N) content Stabilized to Titanium and/or Niobium Extremely High ductility formability - ideal for deep-drawn products Produced by a vacuum degassing process (remove CO_2, N_2, H_2)
	Low Carbon (LC) or Plain Carbon (PC) or Deep Drawing	Low content of Carbon and other alloying elements Aluminum killed steel Good ductility and formability
Conventional **High Strength Steels (HSS)** Single phase ferrite steel Main Strengthening mechanism: - Solid-Solution Hardening by alloying - Grain refinement - Precipitation Hardening (HSLA)	Interstitial-Free High Strength (IF-HS) or High Strength Interstitial Free (HSIF) or	Interstitial –Free based steel Strengthened by P (0.06-0.10 wt %) and Mn as solid solution elements
	Isotropic (IS)/(ISO) Isotropic Quality (IQ)	Ferritic type of microstructure – HSLA steel based Ultra clean steel with rigorous quality control – small and isolated inclusions Grain refining by Ti alloying Plastic strain ratio (r) near zero – minimized earing tendencies No dependence of the material values on the rolling direction
	Bake Hardenable (BH) or Dent Resistance (DR)	Carbon in solution throughout the forming processing Increase in dislocation density during forming Diffusion of carbon atoms to these dislocations
	Carbon-Manganese (CMn)	Low carbon solid-solution steels Strengthened by Mn alloying
	High Strength Low Alloy (HSLA) or Microalloyed (MA)	CMn based steel Microalloying to Ti, V, Nb, Cb, Mo, etc. …

Table 2- Summary of the 1st Generation of advanced high strength steels (1st AHSS) (Kuziak, Kawalla, and Waengler 2008), (Seo, Cho, and De Cooman 2014), (Kuziak, Kawalla, and Waengler 2008), (Chatterjee 2017), (Shome and Tumuluru 2015).

Grade	Description
Ferrite-Bainite (FB)	Ferritic matrix second phase hardened by fine bainite structures Mechanical properties improved by Mo and bainite hardening by Ti and Nb alloying (precipitating hardening) Some authors consider the FB steels a specific case of dual phase steels (FBDP). However, it's more common to leave that designation to ferritic-martensitic steels (also FMDP). They are sometimes also referred by their drawing properties for which they were specially designed: Stretch Flangeable (SF) or High Hole Expansion (HHE) capabilities in favor of improved edge stretch capability. The improved formability of FB steels is due the less likelihood of cracks nucleation/propagation in bainite structure during shearing operations (blanking or hole punching)
Dual phase (DP) or **Partial Martensite (PM)** (for higher vol. fractions of M)	Their microstructure consists in a ferritic matrix with strengthen martensitic islands Mn, Ni, Cr, Mo, V and Si and P (martensite strengthening) The ferritic and martensitic phases create a balance between ductility (given by the ferritic matrix) and strength (martensite).
Transformation-Induced Plasticity (TRIP) **or** **Low Manganese TRIP (LMn TRIP)** **or** **Strain-Induced Martensite Transformation (SIMT)**	Ferrite-matrix with embedded second phases mixture of bainite, retained austenite, and martensite (post to TRIP mechanism) TRIP mechanism consists of metastable martensite transformation from room temperature plastically deformed austenite. This deformation can be imposed during drawing (usually low C alloy with higher initial work-hardening ratios), or due to the presence of some retained austenite before crash impact (at higher C content the martensite transformation begin at strain levels beyond those produced during the forming stages). The phase transformation is instantaneous, diffusionless, and favorable by tensile tension. It helps to distribute strain (dispersion hardening) and resistance to localized deformation. It also enhances bake-hardening capacity. Strengthening by Mn (< 2 wt.%), Ti, Ni and V alloying; Si, Al (avoid carbide formation and accelerate the ferritic bainite formation); Mn and higher C content (<0.4 wt %) as austenite stabilizers.

Complex Phase (CP)	Fine grain ferrite-bainite matrix with second phases mixture of martensite, pearlite, and possible retained austenite Grain refinement and fine precipitating hardening by micro alloying to Ti, V, and Nb, in addition to the alloys used in TRIP/DP Heat treatment similar to TRIP steels, with a final stage less rigorous (no need to control the amount of retained austenite)
Martensitic Steels (MS / MART)	Needlelike microstructure essentially composed by a martensitic matrix lath (single phase) and may contain a small fraction of ferritic and bainitic phases mixture. Hardenability increase by C content and alloying to B and Mn, but also, Mo, Ni, V, Cr, and Si (the last 2 also stabilize austenite) Martensitic steels can be produced by roll forming (profiles). Specific alloys design for Hot stamping or post-forming heat treatment usually fall in the next classifications. Post-quench tempering imporves ductility and formability
Post-Forming Heat Treatable (PFHT) **Press Hardened Steel (PHS) or** **Hot Press Forming (HPF) or** **Hot-Formed/Stamped (HF/HS)**	MS based composition with the higher yield and ultimate tensile strength. In some literature are included in the MS grade. The mechanical strength and C content can be progressively higher in PFHT and HF steel grades. PFHT Treatment (forming-heating-quenching) the forming stage is done in room temperature, but the quenching is performed with the piece fixtured Two types of HS: Direct (heating-forming-quenching); Indirect (forming-heating-forming-quenching), usually more adequate to Zn based coatings. The cooling stage is done in pressure, in die-quenching

Main Features	**Main Strengthening Mechanisms**
Low alloy	Multiphase concept – but with primarily ferritic based microstructure
Complex and stringent thermomechanical processing	Strengthening by hard second phases precipitation (perlite, bainite, martensite)
Small net cost increase when compared to **HSS**	Grain refinement and precipitation hardening by microalloying

Table 3- Summary of the 2nd and 3rd Generations of AHSS (Billur and Altan 2014a), (Billur and Altan 2014b), (Demeri 2013), (Matlock et al. 2012), (Zhao and Jiang 2017), (Ozgowicz, Kurc-Lisiecka, and Grajcar 2012), (Nakada et al. 2014).

Generation of AHSS	Grade	Description
AHSS 2nd Generation • Austenite (γ) base steels • High alloying content (austenite stabilizers) • High Cost • Exceedingly high deformation levels required to get maximum strength • Poor weldability • Manufacturing and casting technologic issues • Very limited application SFE (Stacking Fault Energy) Higher Mn and Al content increase the SFE, changing the plastic deformation mechanism Phase transformation-Twinning-Dissociated dislocation-Undissociated dislocation	Light Steel with Induced Plasticity (L-IP) or Shear-band (formation/strengthened) Induced Plasticity (SBIP)/(SIP) or Triplex	Different possible microstructures (single-phase austenite, austenite based, austenite-ferrite and ferrite based). SFE of γ 40-90 mJ / m^2 and C content 0.5-1.8 wt.% Highly alloyed to Mn (15-30 wt.%) - for austenite stabilizing; and Al (2-12 wt.%) -for precipitation of coherent Nano sized $FeMn_3$ AlC (also called κ-carbides) Mechanical strengthening by dissociated and undissociated dislocation glide mechanism with micro-band formation (for higher SEF)
	Austenitic Stainless Steel (ASS/ AUST. SS)	Austenitic crystal structure as primary phase (100%). Corrosion resistance by the formation of an invisible, adherent passive Cr-rich strong oxide surface film that develops in the presence of oxygen (continuous protection) Highly alloyed to Cr (16-26 wt.%) and Ni (<35%), and also alloyed to Mo, Cu, Ti, Al, Si and Nb. Strengthening by cold working (transformation of austenite in martensite–TRIP mechanism and TWIN for high strain rates and low temperatures)
	Twinning Induced Plasticity (TWIP) or High Manganese TWIP (HMn TWIP)	Austenitic crystal structure as primary phase (100%). SFE of γ 20-40 mJ / m^2 Highly alloyed to Mn (22-30 wt%) to fully stabilize the γ at room temperature Solid-solution hardening by C (< 1 wt.%), Al (< 10 wt.%) and Si (< 3 wt.%) alloying. Microalloying to V, Ti, Nb for grain controlling (Hot working conditions) Mechanical strengthening by typical dislocation glide mechanism (typical) and TWIP mechanism. TWIP is a non-thermally activated plastic deformation mechanism, and consists of
	High Manganese TRIP (HMn TRIP)	Austenitic crystal structure as primary phase (100%). SFE of γ < 20 mJ / m^2 Highly alloyed to Mn (<18 wt.%) Mechanical strengthening by TRIP mechanism
Generation	**Grade**	**Description**

Four under development approaches:

- Modification of 1st and 2nd Gen. AHSS (X-AHSS)
- Multiphase (A+M) Steel by novel processing methods (Q&P, DSTC) and small alloying – stabilization of austenite by Carbon partitioning
- NanoSteel®

Objectives:

- Reduce the alloying and Carbon content to improve weldability and cost reduction (of the raw material and production process), when compared to the 2nd Gen.
- Reduce the Carbon content to improve weldability
- Avail from the existing infrastructure of steel (consistence with the current sheet steel production practice)
- Bridging solution between the ductility of the 2nd Gen. and the mechanical strength of the 3rd Gen. of AHSS

Ferrite-Bainite TRIP (FB-TRIP), TRIP aided Bainitic Ferritie (TBF), Carbide-Free Bainite (CFB), Super Bainite TRIP (SB-TRIP)	Carbide-free-lath Bainite with inter-lath retained γ with C content (0.2-0.3 wt%) Alloyed to Al, Si, Mn and Cr and microalloyed to Nb, B and Ti Strengthening by TRIP effect and bainite plates grain size refinement During an isothermal bainite transformation γ is enriched in C and Mn
Medium Mn Steels (MMnS) or Medium Mn TRIP (MMnTRIP)	Retained γ (15-30 wt%) embedded in a complex ultra-fine microstructure of M/F Medium alloyed to Mn (4-10 wt%) , Si(< 2wt%) and Al (< 2 wt%) and microalloyed to Nb, Ti, V, Mo Microstructure controlled by heat treatment in order to concentrate Mn and C in the austenite (γ) phase. Partial reversion transformation by intercritical annealing (austenization-quenching-reaustenization-intercritical annealing-cooling) Strengthening by TRIP/(TWIP) effect and alternate arrangement of ultra-fine lamellar γ and acicular martensite structure
Quenching and Partitioning (Q&P) process and Double Stabilization Thermal Cycling (DSTC) process Martensite based TRIP (M-TRIP)	Small interlath films of retained Austenite between tempered wider Martensite laths Alloying based on CMn steels with addition of, Al (1-1.5 wt%), and Si (1-1.5 wt%) to avoid carbide formation and help stabilize the austenite Thermal treatments based on Dynamic Carbon Partitioning (DCP) mechanism. Deposition of C into the austenite (enriched) through C depletion from the martensite 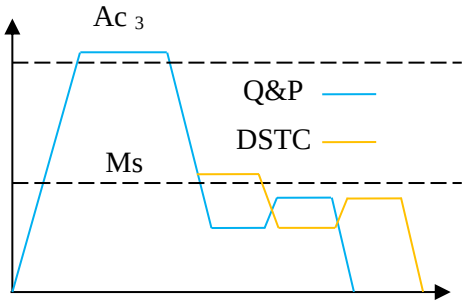
NanoSteel® or UltraSteel® or XPF®	Single phase refined ferrite matrix reinforced with nanoprecipitates Static NanoPhase refinement - new mechanism to create nanoscale structures at elevated temperature Strengthening by new room temperature strain hardening mechanism (nanosize behavior governed by surface atoms properties) - dynamic strain nanoscale phase transformation. And also by grain refinement

Annex C Steel microstructure design by composite modeling

The curves plotted in Figure 10, were based on a composite modeling technique applied to microstructure design of steel. Each phase is assumed to be a component of the composite (either matrix or fiber). The original plastic instability model of fiber reinforced composites (under loading parallel to the fiber) is further detailed in (Mileiko 1969).

The nomenclature used is summarized below:

Uniform True Strain	$\ddot{\varepsilon}$	Uniform Engineering Strain	$\bar{\varepsilon}$
Ultimate Tensile Strength	UTS	Volume Fraction	V

M subscript refers to Martensite phase

F subscript refers to Ferrite phase but can be readily substitute by Austenite properties data

When no subscript is specified, the parameter refers to the steel alloy as a whole

The model used is based on the following constitutive equations:

Rule of mixtures applied to the composite/multiphase steel alloy strength:

$$\sigma = V_M \cdot \sigma_M + (1 - V_M) \cdot \sigma_F \tag{1}$$

It will be assumed Isotrain state (instantaneous strain):

$$\varepsilon = \varepsilon_M = \varepsilon_F \tag{2}$$

Computing of the true uniform strain and the ultimate tensile strength of the alloy:

$$solve\left[V_M = \frac{1}{1 + \frac{UTS_M}{UTS_F} \cdot \frac{\ddot{\varepsilon}_F^{\ddot{\varepsilon}_F}}{\ddot{\varepsilon}_M^{\ddot{\varepsilon}_M}} \cdot \frac{e^{\ddot{\varepsilon}_M}}{e^{\ddot{\varepsilon}_F}} \cdot \frac{\ddot{\varepsilon} - \ddot{\varepsilon}_M}{\ddot{\varepsilon}_F - \ddot{\varepsilon}} \cdot \ddot{\varepsilon}^{\,\ddot{\varepsilon}_M - \ddot{\varepsilon}_F}}\right] for\ \ddot{\varepsilon} \tag{3}$$

$$UTS = V_M \cdot \lambda_M \cdot UTS_M + (1 - V_M) \cdot \lambda_F \cdot UTS_F \tag{4}$$

$$\bar{\varepsilon}\,[\%] = 100 \cdot \left(e^{\ddot{\varepsilon}} - 1\right)\lambda_F = \left(\frac{\ddot{\varepsilon}}{\ddot{\varepsilon}_F}\right)^{\ddot{\varepsilon}_F} \cdot e^{\ddot{\varepsilon}_F - \ddot{\varepsilon}}\lambda_M = \left(\frac{\ddot{\varepsilon}}{\ddot{\varepsilon}_M}\right)^{\ddot{\varepsilon}_M} \cdot e^{\ddot{\varepsilon}_M - \ddot{\varepsilon}} \tag{5}$$

Annex D Types of Common Zinc Coatings

Table 1- Summary of typical Zinc coating processes (Marder 2000, Smith and Goodwin 2010, Shibli, Meena, and Remya 2015).

Zinc Coating Process	Description
Hot-Dip Galvanization	Metallurgical reaction of the Fe from the steel and molten Zn to form a tightly-bonded alloy coating Can be classified according to its production process: batch galvanization or general galvanization (immersion of a prefabricated or bulk article into a molten Zn bath) and continuous galvanization (continuous galvanization of sheets, coils/strips and wires of metal) with a possible variation called galvannealed (posterior annealing treatment in the last stages of the line)
Zinc Electroplating	Electro-deposition of Zn metal on positively charged steel (cathode) by chemical reduction of Zn ions The reaction occurs between a anode (lead/silver or pure soluble Zn) and a cathode (steel), through a electrolyte solution (Zn sulfate) When coatings are applied to sheet steels and wire is usually referred as electro-galvanization, when used in small parts such as fasteners, crank handlers, springs, etc. is referred as Zn plating
Zinc Mechanical Plating	Tumbling of small flash Cu-coated parts in a drum loaded with Zn powder, proprietary chemicals, glass beads Metallurgical bonding by zinc powder peening (by the glass beads) onto the components Used almost exclusively for hard to HDG coat components, such as high strength fasteners and hardened self-drilling screws
Sherardizing or Dry Galvanization or Vapor Galvanizing	Tumbling of small components in a zinc and filler (sand) mixture at a temperature of around 400/500 ºC Diffusion bonding by Zn evaporation and diffusion into the steel substrate (forming Zn-Fe IMC) Process with small applications - time consuming and with low Zn recovery
Zinc (Thermal) Spraying or Metalizing	Spraying of melted zinc by feeding zinc wire or powder into a heated gun, using combustion gases and/or auxiliary compressed air as projection medium
Zinc rich Paint or Cold Galvanizing	Application by brushing or spraying, of a mixture of zinc powder with an organic or inorganic binder The paints are classified by the nature of the binder in either: organic (polymers based) or inorganic (alkyl silicates based) Zinc-rich paints contain 65-95% metallic zinc in dry film

Annex E Background in Magnesium-Steel Research

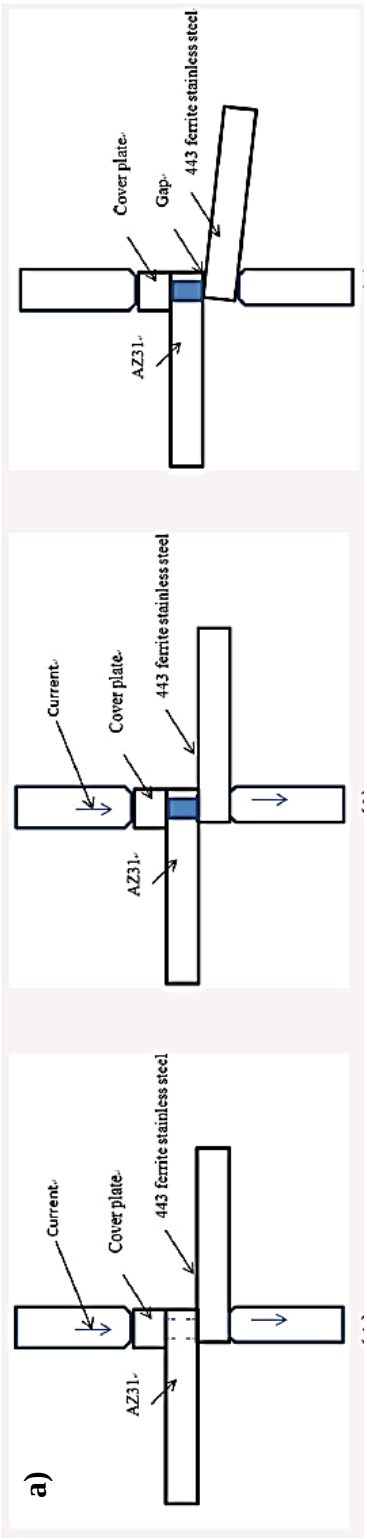

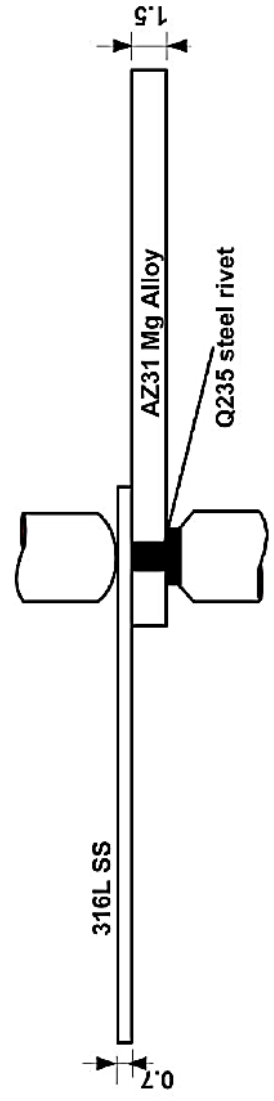

Figure 1- a) Schematic description of the novel RSW process using a steel cover plate (Min, Yong, and Jie 2016). b) Illustration of the Resistance Element Welding (Manladan et al. 2017a).

Annex F Evolution of different “Refilling” techniques applied to the FSSW Concept

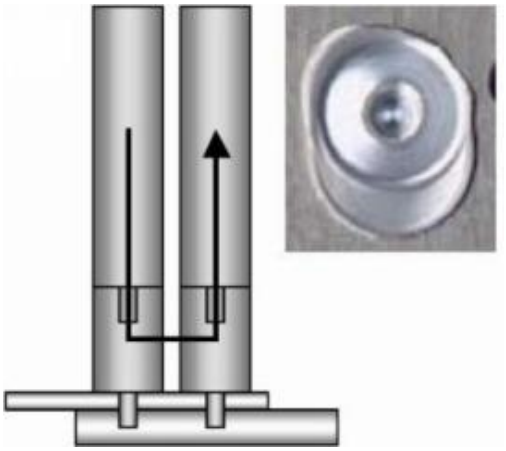

Figure 1- Short FSW based, Stitch FSSW (C.Schilling et al. 2000).

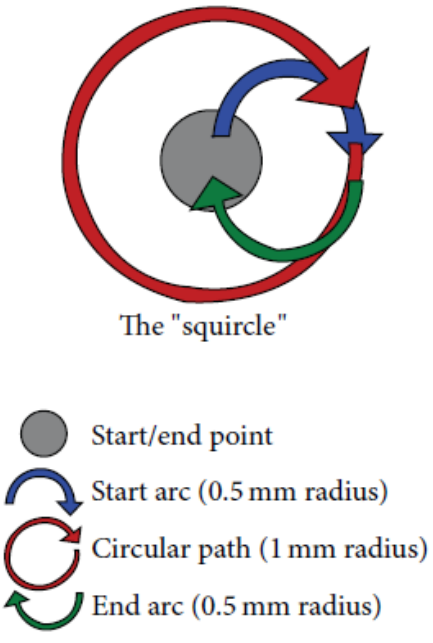

Figure 2- Squircle Friction Stir Spot Welding (Squircle FSSW) (Addison and Robelou 2004)

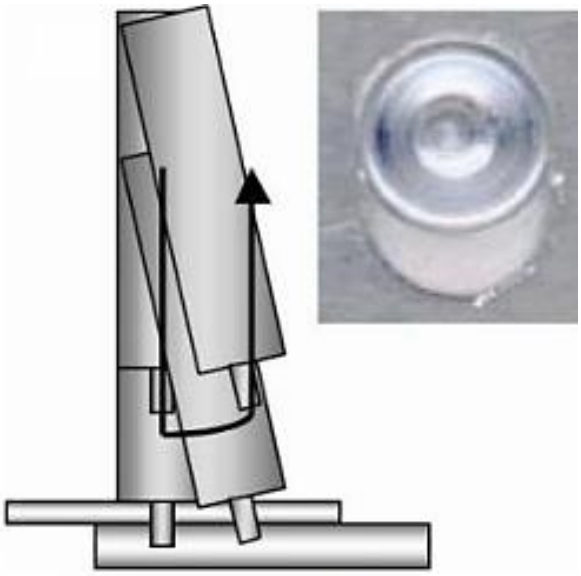

Figure 3- Swing Friction Stir Spot Welding (Swing FSSSW). Short FSW process (Okamoto, Hunt, and Hirano 2005b), (Okamoto, Hunt, and Hirano 2005a), (Badarinarayan, Hunt, and Okamoto 2006)

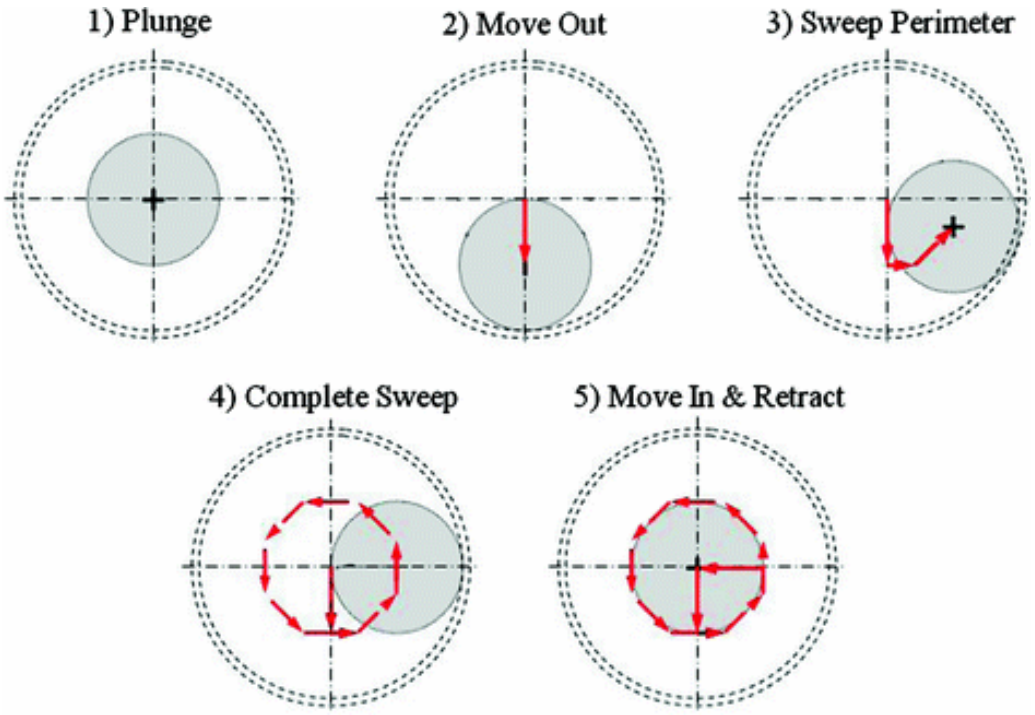

Figure 4- Swept or octaspot Friction Stir Spot Welding(Tweedy, Widener, and Burford 2007)

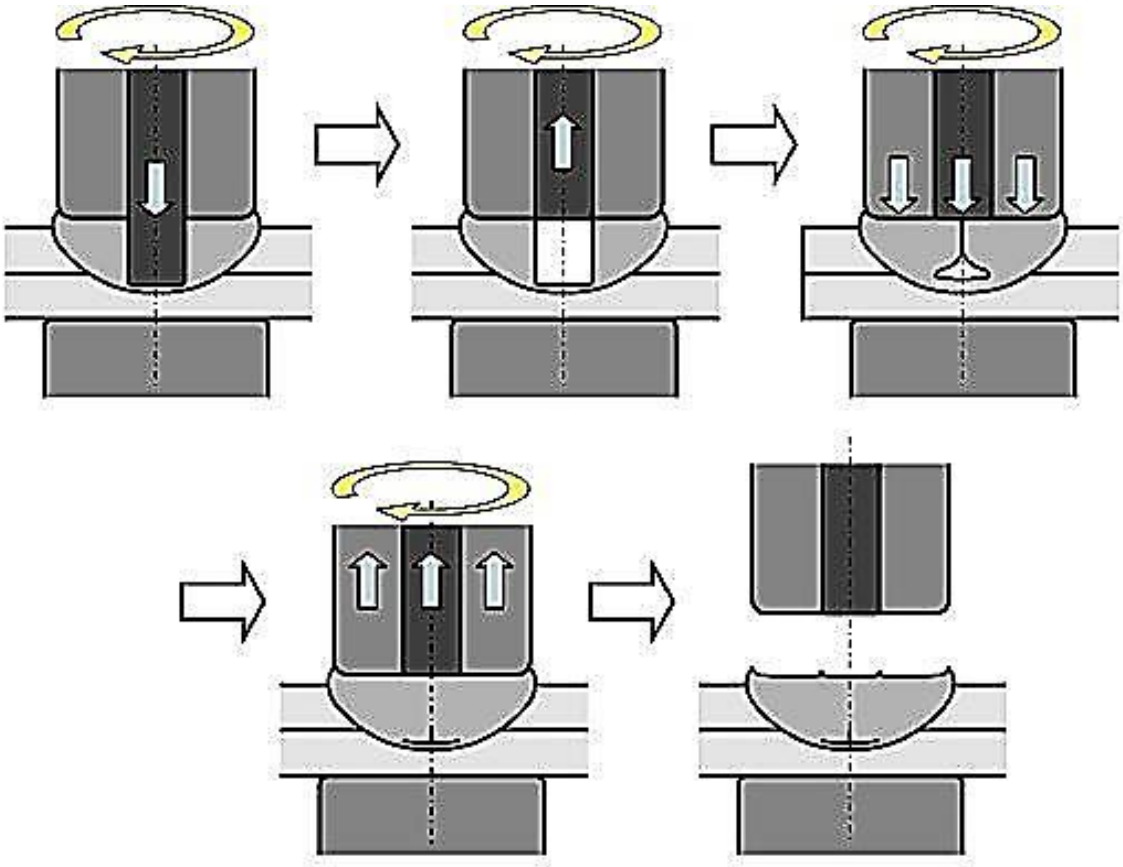

Figure 5- Re-fill FSSW (Uematsu et al. 2008)

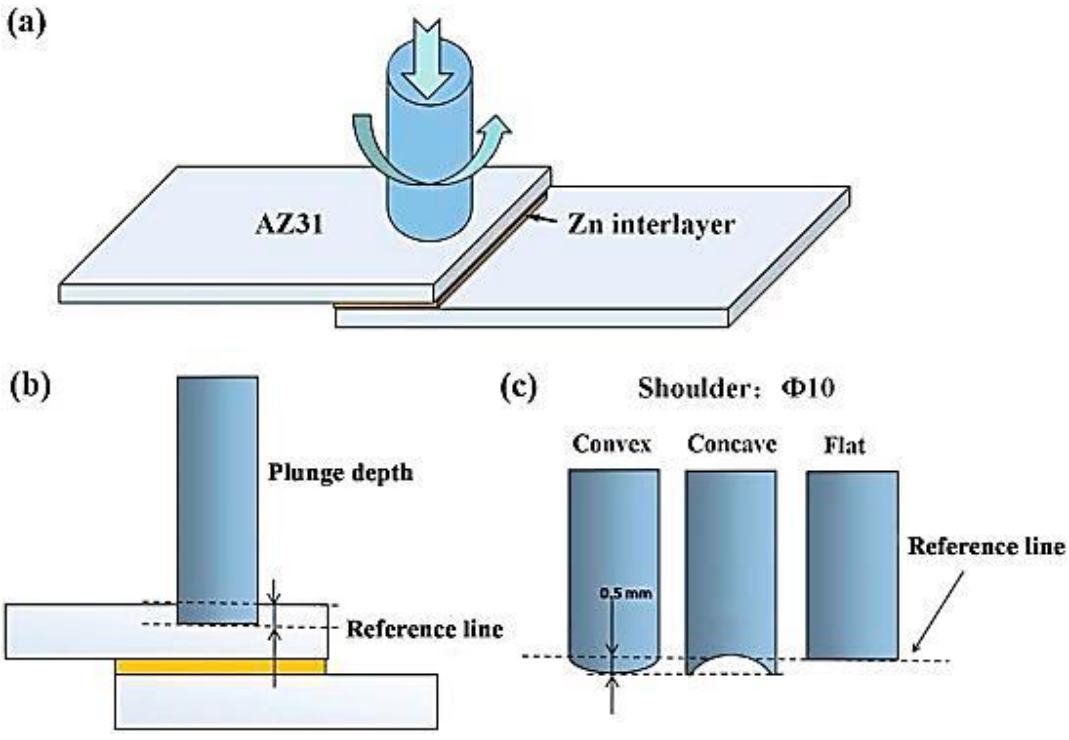

Figure 6- Pinless-Friction Stir Spot Welding (P-FSSW) (Tozaki, Uematsu, and Tokaji 2010)

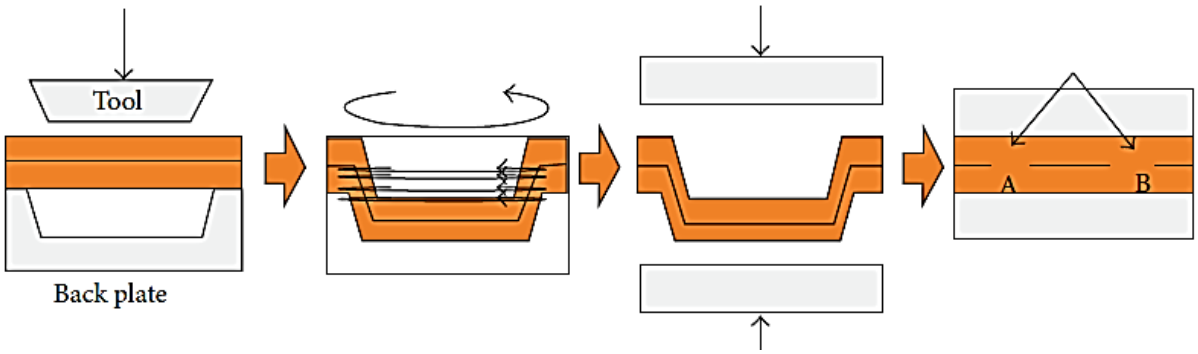

Figure 7- Two-step FSSW refilling technique with initial backing plate with dent. (Sun et al. 2011)

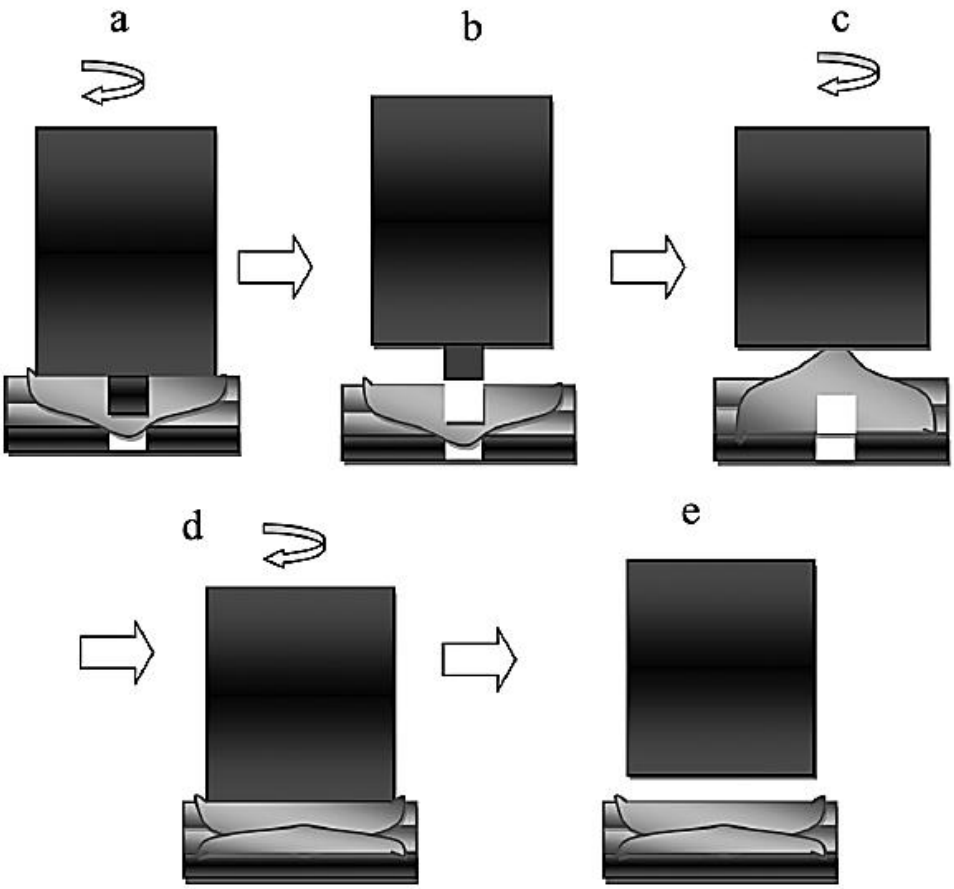

Figure 8- A Friction stir spot welding, with refilling by the friction forming process (FSSW-FFP) (Prakash and Muthukumaran 2011)

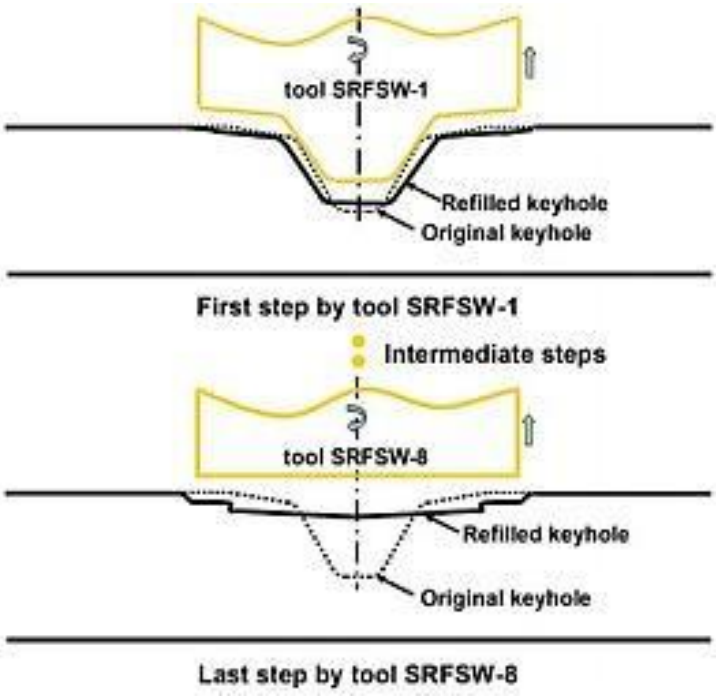

- Combination of plastic deformation and flow of the material around the keyhole,
- Step by step process that resorts on specifically designed consumable tools

Figure 9- Self-Refilling Friction Stir Welding (SRFSW) (Zhou et al. 2012).

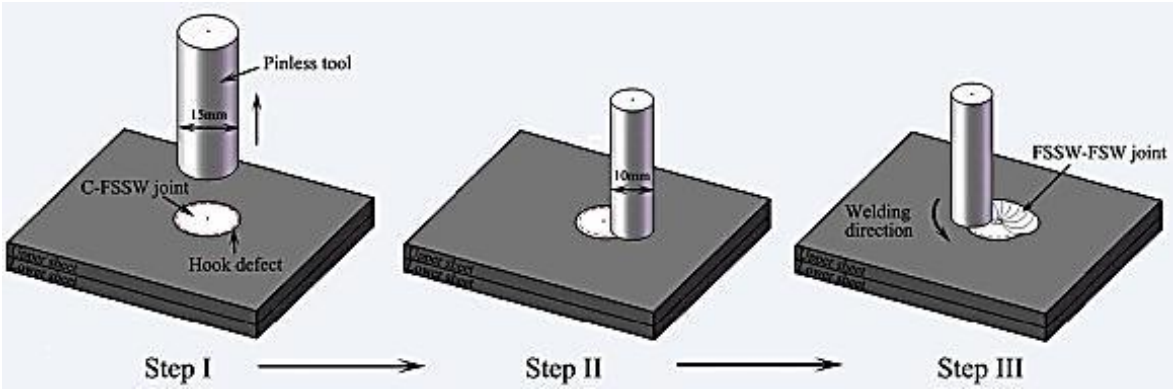

Figure 10- Pinless FSSW plus subsequent FSW (FSSW-FSW) (Li, Li, et al. 2014)

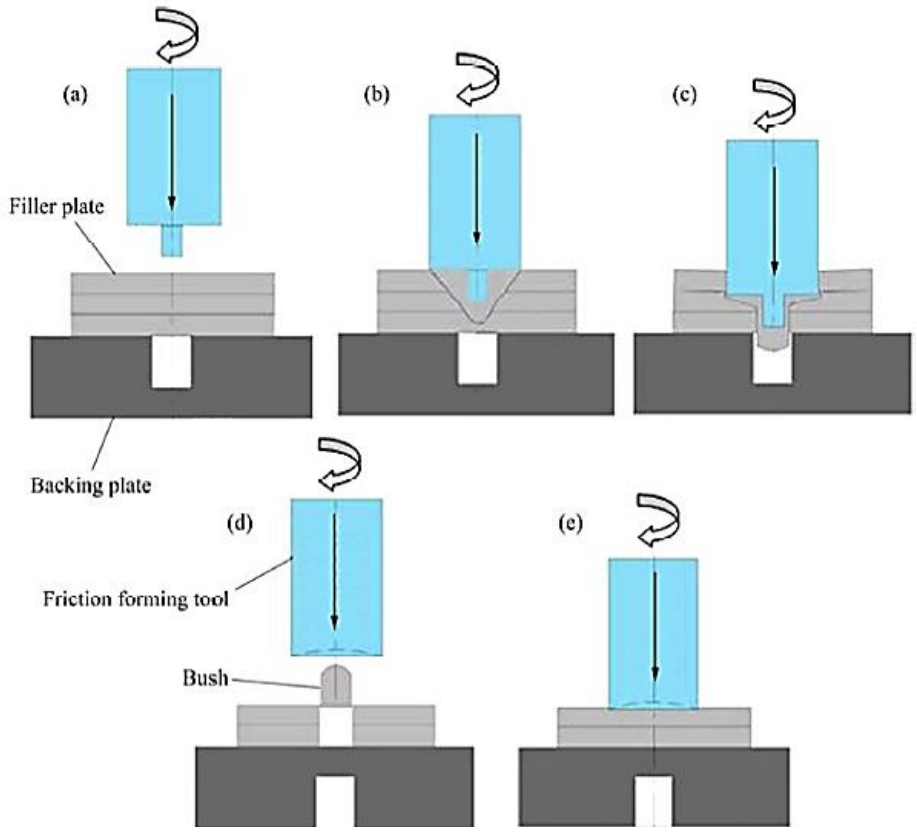

Figure 11- A Friction stir spot welding with refilling by friction forming process using filler plate (Venukumar, Yalagi, and Muthukumaran 2013)

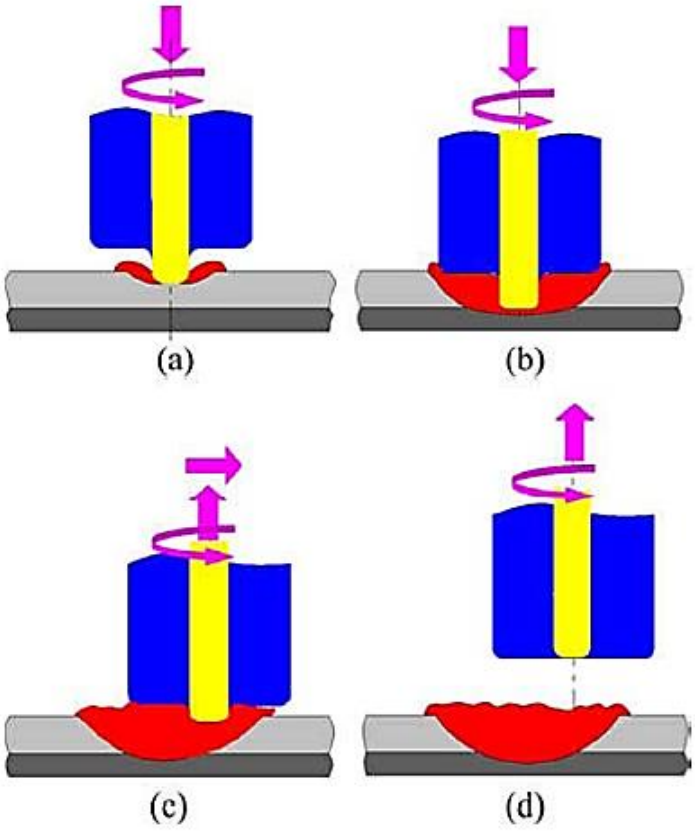

Figure 12- Friction Stir Keyholess Spot Welding (FSKSW) (Zhang et al. 2014).

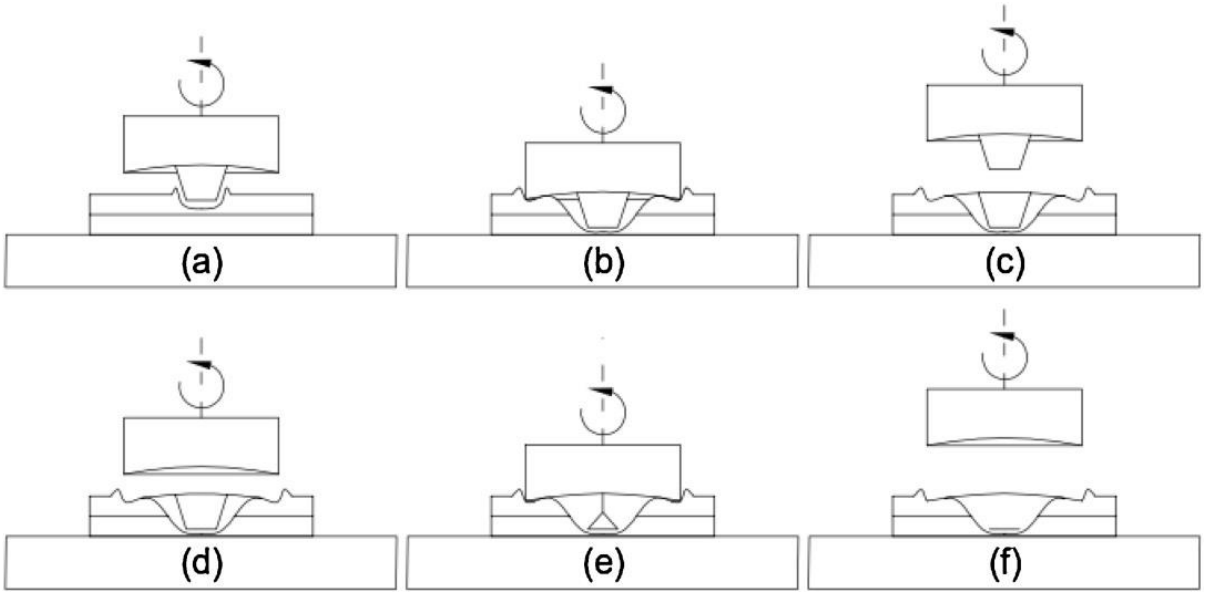

Figure 13- Two-Stage refilled FSSW (TSFSSW) (Sajed 2016).

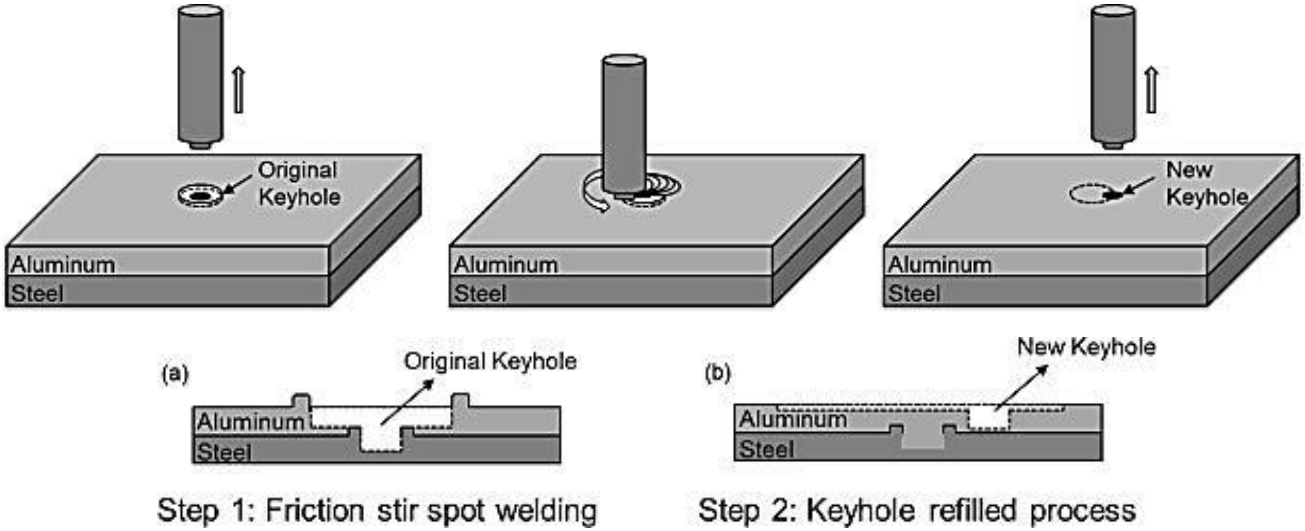

Figure 14- A keyhole refilled Friction Stir Spot Welding (FSSW) (Chen, Liu, and Ni 2017)

Annex G Direct chill permanent molding casting process

This direct chill permanent molding casting process was developed and optimized by (Elsayed et al. 2011), HZG. Briefly, the main steps of the process are: melting and mixing the alloy, pre-heating the permanent mold, pouring the molten metal into the permanent mold, and final controlled cooling of permanent mold. It can be briefly described as:

- The magnesium alloy is prepared from liquid mixtures of their individual elements. A purity higher than 99.85% is used;
- A three zone resistance furnace, with a tubular shape is used to heat up to 720 ºC a 8 kg stainless steel crucible;
- The commercially pure magnesium is first melted before adding the alloying elements;
- To ensure complete mixing (after 5 min of holding time), a six-blade boron nitride coated stainless steel propeller, rotating at 150 rpm during 30 min is used;
- During the melting and stirring stages, a constant flux of Argon and SF_6 mixture is assured;
- A boron nitride coated stainless steel paddle is used to remove the oxides that segregated to the upper surface (even after stirring);
- After the alloy preparation, the permanent mold is pre-heated to 720 ºC;
- The molten metal is poured into the permanent mold at 720 ºC;
- Holding the permanent molding for 30 min at 700 ºC;
- Finally, the bottom hatch is opened, and with a pulling velocity of 10 cm/min was used to control the macro and microstructure of the ingot.

[blank page]

Annex H Technical drawing of the tensile test specimens used for material characterization

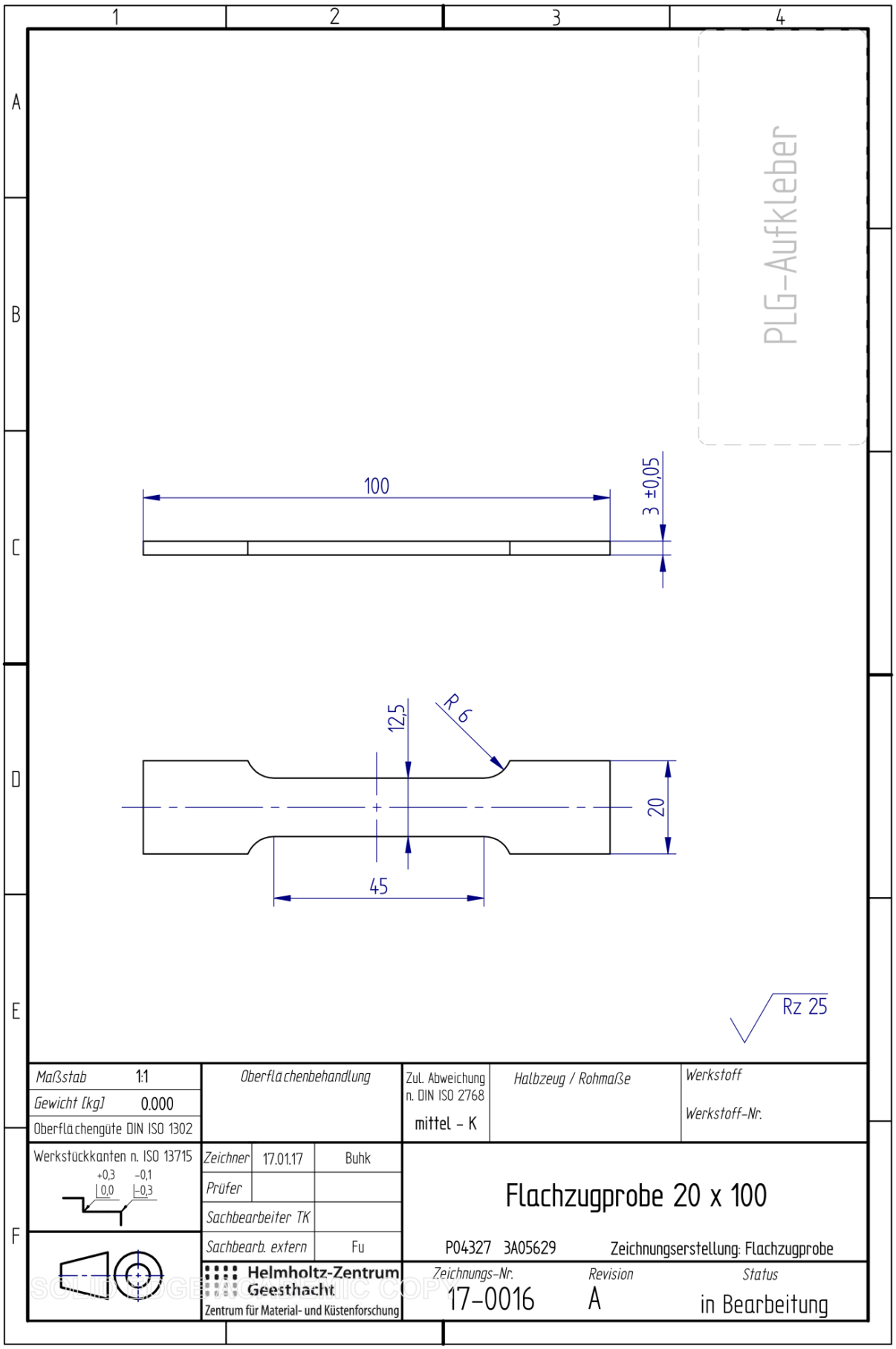
1
2
3
4
A
B
C
D
E
F
PLG-Aufkleber
100
3 ±0,05
12,5
R 6
20
45
Rz 25
Maßstab 1:1
Gewicht [kg] 0.000
Oberflächengüte DIN ISO 1302
Oberflächenbehandlung
Zul. Abweichung n. DIN ISO 2768 mittel - K
Halbzeug / Rohmaße
Werkstoff
Werkstoff-Nr.
Werkstückkanten n. ISO 13715
+0,3 −0,1
0,0 −0,3
Zeichner 17.01.17 Buhk
Prüfer
Sachbearbeiter TK
Sachbearb. extern Fu
Helmholtz-Zentrum Geesthacht
Zentrum für Material- und Küstenforschung
Flachzugprobe 20 x 100
P04327 3A05629 Zeichnungserstellung: Flachzugprobe
Zeichnungs-Nr. 17-0016
Revision A
Status in Bearbeitung

Annex I Binary Phase Diagrams

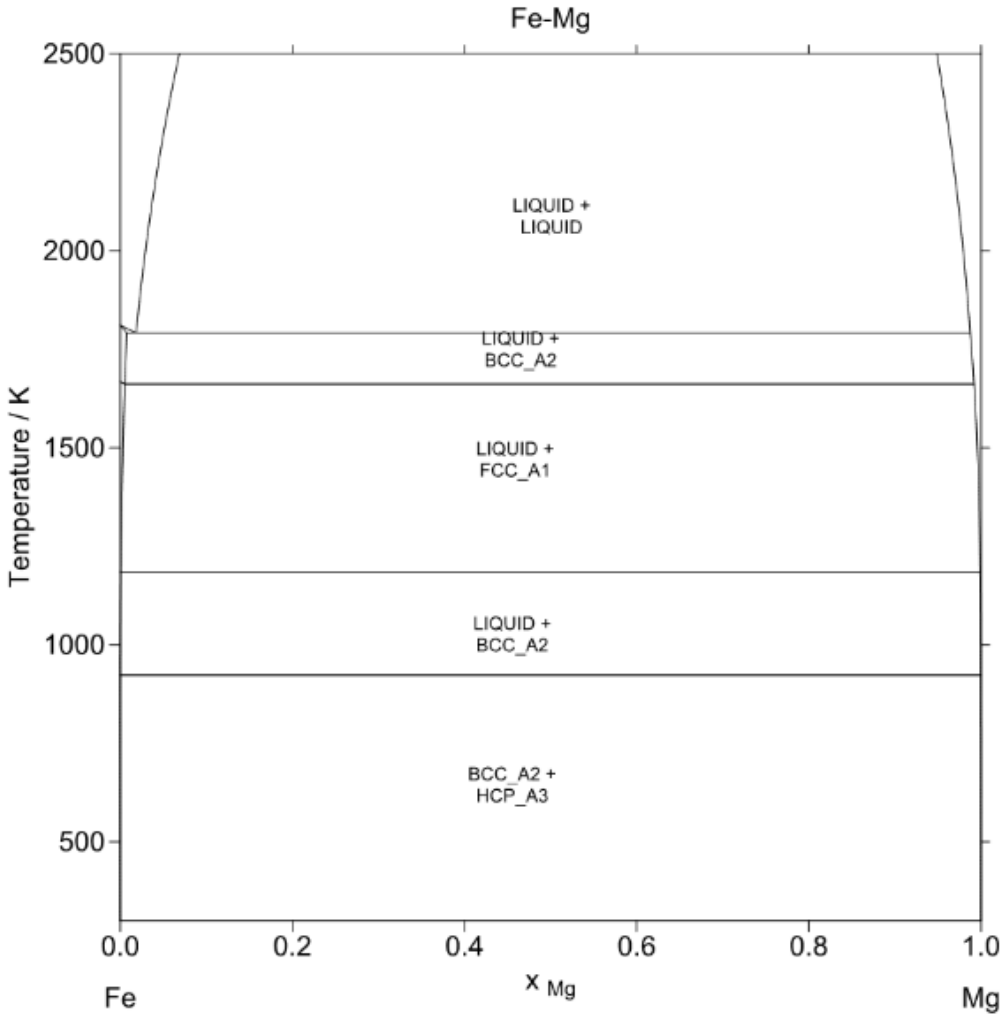

Figure 1- Fe-Mg binary phase diagram, adapted from (Wang, Zhao, et al. 2011).

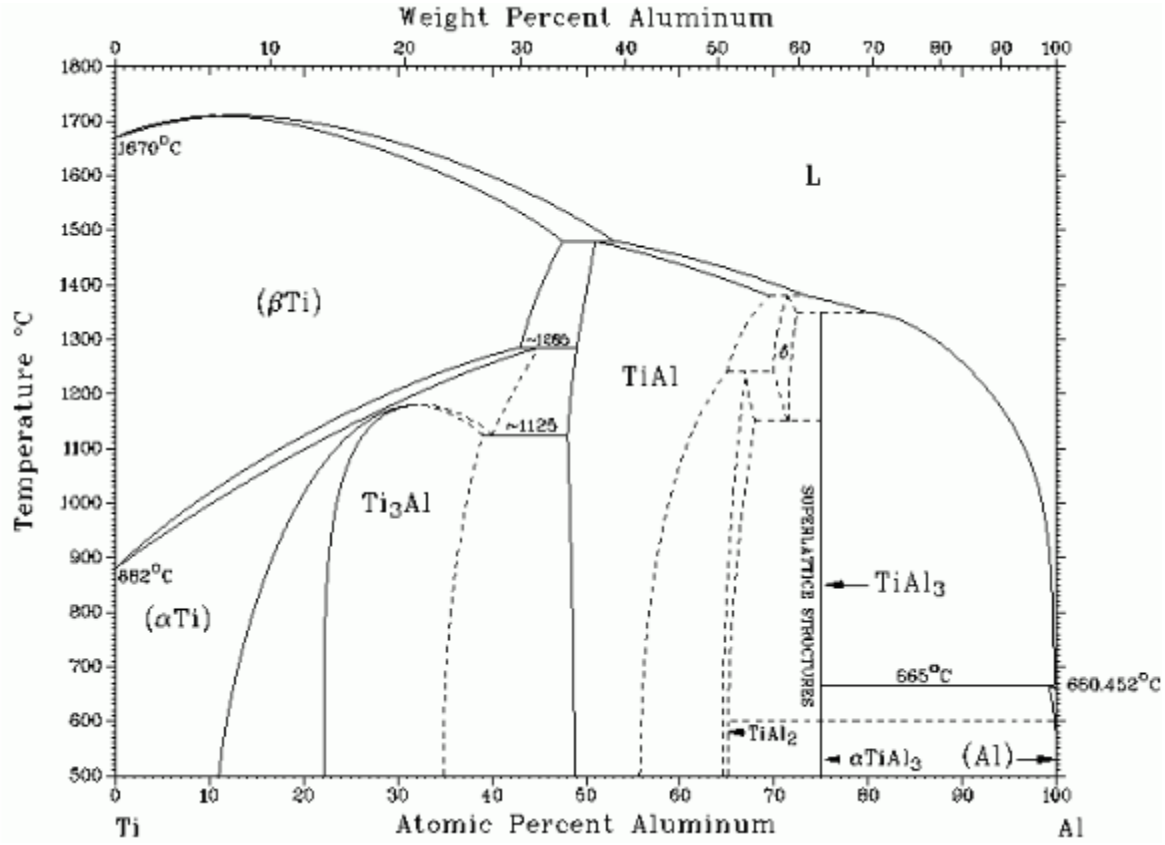

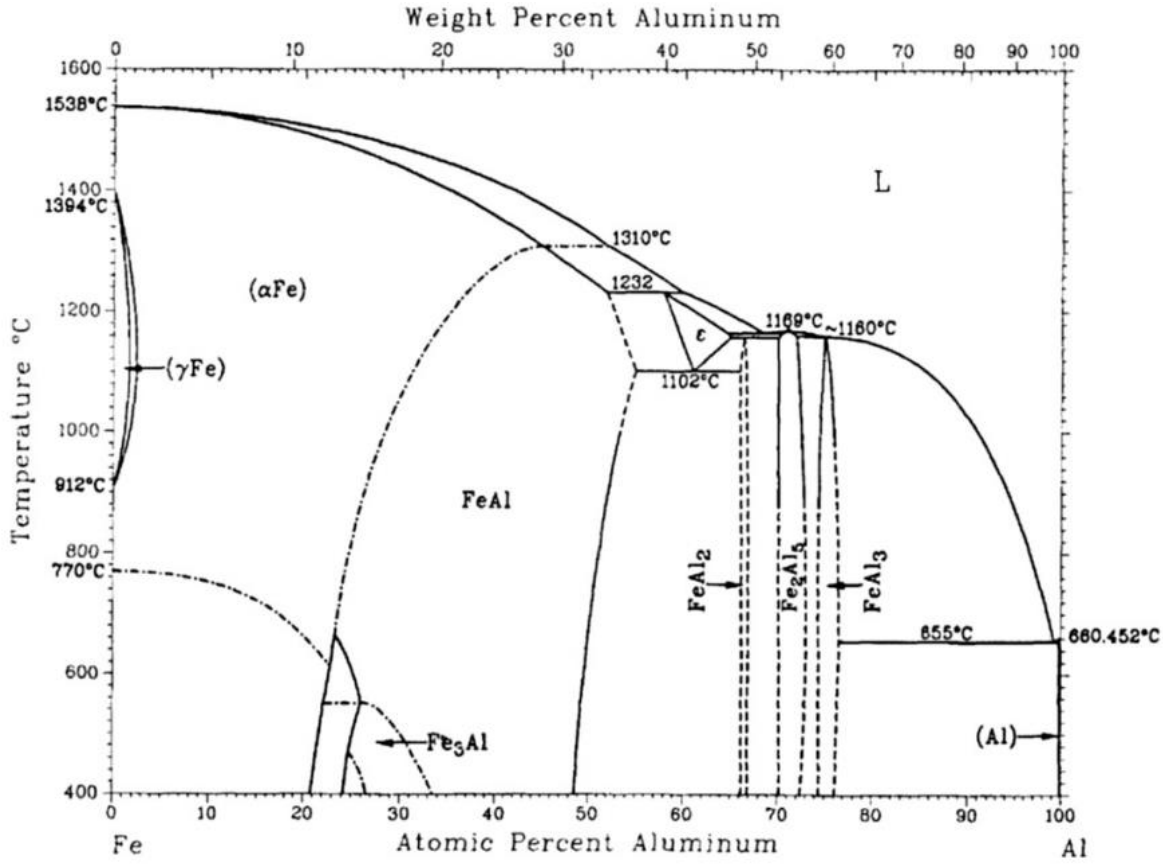

Figure 2- a) Ti-Al (Basuki et al. 2016) and b) Fe-Al (Han and Viswanathan 2003) binary phase diagrams.

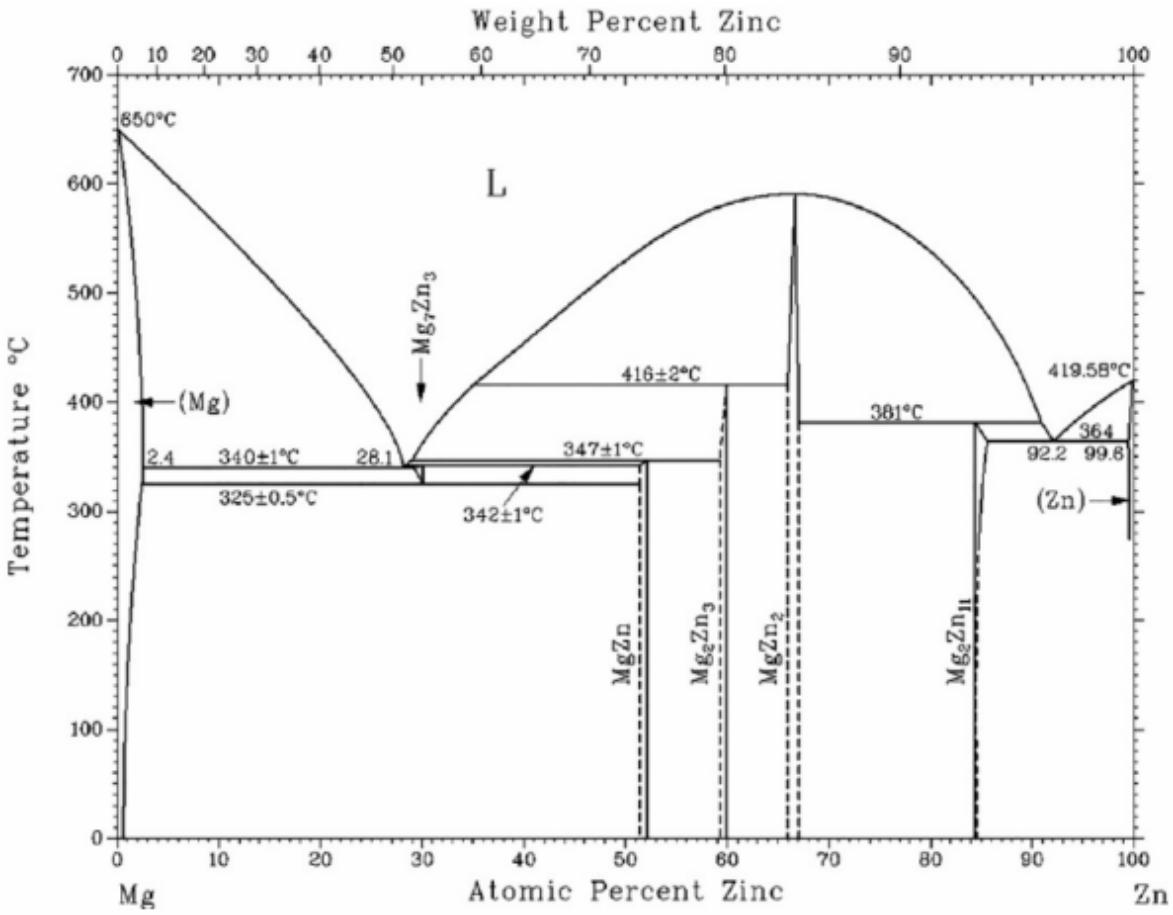

Figure 3- Mg-Zn binary phase diagram, adapted from (Binjiang et al. 2013).

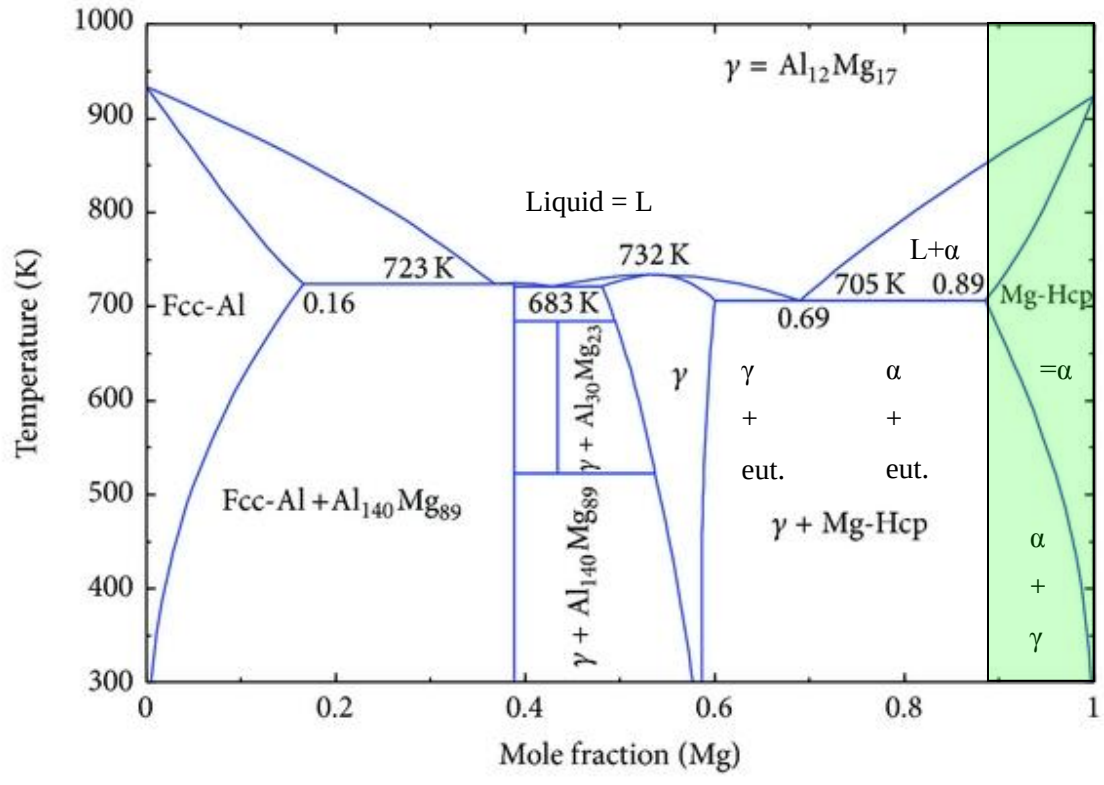

Figure 4- Mg-Al binary phase diagram, adapted from (Mezbahul-Islam, Mostafa, and Medraj 2014).

[blank page]

Annex J Features of the Scanning Electron Microscope

Table 1- Summary of the main features of the Quanta™ 650 FEG SEM microscope used.

Hardware	Schottky Field Emission	
	Accelerating Voltage [kV]	0.2 – 30
	Beam Deceleration	Plasma Cleaner
	3 Vacuum Modes	HiVac (10^{-4} – 10^{-2}) LoVac (10-200 Pa) ESEM (10-4000 Pa)
	Navigation Camera	
	Stage Control	Eucentric position
	Anti-Vibratory Table	Anti-Magnetic Frame
Detector	Everhart-Thornley (ETD)	SE+BSE
	Large Field (LFD)	SE
	Gaseous Secondary Electron (GSED)	SE
	Concentric Backscattered (CBS)	BSE
	Gaseous Analytical Electron (GAD)	BSE
	CCD Camera (CCD)	Light +Infra-red
	Energy Dispersive X-ray Spectrometer (EDS)	X-ray
	Electron Backscattered Diffraction (EBSD)	BSE

SE – Secondary Electrons; BSE – Backscattered Electrons;